Gesellschaft für Mikro- und Nanoelektronik

The Society for Micro- and Nanoelectronics

Annual Report

2002

Vienna, September 2003

Gesellschaft für Mikro- und Nanoelektronik

The Society for Micro- and Nanoelectronics

Annual Report

2002

Society for Micro- and Nanoelectronics
c/o Vienna University of Technology
Institute of Industrial Electronics and Material Science
Gusshausstrasse 27-29/366, A-1040 Vienna, Austria

Vienna, September 2003

Editor: Karl Riedling

Layout: Claudia Benedela
Karl Riedling

ISBN: 3-901578-11-0

c/o Technische Universität Wien
Institut für Industrielle Elektronik und Materialwissenschaften
Gusshausstraße 27-29/366, A-1040 Wien

The Society for Micro- and Nanoelectronics (GMe — Gesellschaft für Mikro- und Nanoelektronik)

E. Gornik, K. Riedling

Gesellschaft für Mikro- und Nanoelektronik,
c/o Institut für Industrielle Elektronik und Materialwissenschaften,
TU Wien
Gußhausstraße 27 – 29, A-1040 Wien

Goals of the Society for Micro- and Nanoelectronics

The Society for Micro- and Nanoelectronics (GMe) has been founded in 1985 as "*Society for Microelectronics - Gesellschaft für Mikroelektronik*" with the aim to "*support microelectronics technology and its applications*" in Austria. With the shift of the focus in research from micro to nano technologies the goals of the GMe changed accordingly. In 2003, therefore, the GMe changed its name into "*Society for Micro- and Nanoelectronics - Gesellschaft für Mikro- und Nanoelektronik*".

The GMe defines its tasks as follows:

- Support of university-based "high-tech" research in the areas of micro- and nanoelectronics, semiconductor technology, sensors, and opto-electronics;
- Operation of research facilities;
- Support and consulting for industry, in particular, for small and medium enterprises, within the area of micro- and nanoelectronics.

The central task of the GMe is to provide an internationally competitive *infra-structure* in the area of micro- and nanoelectronics technology. The GMe allocates funds to maintain research projects in the fields of semiconductor technology, sensors, opto-electronics, and ASIC design. Thus the infra-structure support generates a base for research projects that are funded by other funding agencies.

Activities of the Society

Due to funding constraints, the present focal point activity of the GMe is exclusively the operation of university-based laboratories for micro- and nanoelectronics technology. Nevertheless, the GMe tries to support the other activities mentioned above in their submission and administration of certain projects.

The main task of the GMe is the operation of the cleanroom laboratories in Vienna and Linz. The GMe has coordinated the construction of the Microstructure Center (MISZ — Mikrostrukturzentrum) in Vienna; the funds were supplied by the Austrian Federal Ministry of Science and Research. The GMe now finances a significant part of the operation costs for the cleanroom laboratories in Vienna and Linz.

Microelectronics Technology — Cleanroom Vienna

The following university institutes receive support within this focal point activity:

- TU Wien:
  - Institut für Festkörperelektronik
  - Institut für Industrielle Elektronik und Materialwissenschaften

Microelectronics Technology — Cleanroom Linz

The following university institutes receive support within this focal point activity:

- Johannes Kepler Universität Linz:
  - Institut für Halbleiter- und Festkörperphysik
  - Institut für Mikroelektronik

Other Activities of the Society

In 2002, the GMe has prepared its biennial seminar, the "*GMe Forum*", which meanwhile has taken place at the Vienna University of Technology on April 10 and 11, 2003. The intention of the "*GMe Forum*" is to present application-oriented results of international industrial and academic research and to indicate trends for future applications of research results. The "*GMe Forum 2003*" focused on the technologies and issues involved in the transition from a micro- to an nanotechnology.

One of the declared tasks of the GMe is to provide information on current Austrian academic activities in the field of micro- and nanoelectronics to industry, in particular to Austrian small- and medium enterprises (SMEs). To enhance the distribution of the results of the research work done with GMe support, the GMe has put the contents of its annual reports — 1995 through 2002 — and the proceedings of the latest seminars organized by the GMe on its Web server. This server provides a variety of search facilities into the reports, thus acting as a Micro- and Nanoelectronics Knowledge Base. The GMe Web server is available under the address:

http://gme.tuwien.ac.at/

The Annual Report for 2002 of the Society for Micro- and Nanoelectronics

The GMe is currently supporting the microelectronics technology activities of the cleanroom laboratories in Vienna and Linz. All projects described in this report were carried out in the cleanrooms in Vienna and Linz, respectively. They are *not* specific projects of the GMe but were funded by a variety of other sources. They all have in common that they use the infra-structure provided by the GMe. It would therefore not have been possible to carry out these projects without the support by the GMe.

Contents

Microelectronics Technology — Cleanroom Vienna

Cleanroom Vienna

G. Strasser

**Mikrostrukturzentrum der Technischen Universität Wien,
Floragasse 7, A-1040 Vienna, Austria**

This annual report contains a summary of the major research activities represented by national and international projects carried out in the MISZ TU Wien (Mikrostrukturzentrum der Technischen Universität Wien) during the year 2002. In this year an important step in the direction of future technologies was taken by implanting new equipment into the MISZ to fabricate nanodevices. To keep the mission of the MISZ TU Wien alive (state of the art growth, processing and structuring of novel devices) new downscaling processes for nanoscale and ultrafast devices have to be developed. High-risk projects as well as the improvement of standard devices are running in the framework of the cleanroom and the available technologies within. Top down and bottom up approaches are investigated in parallel, making partly intensive use of the cleanroom and the existing technologies. After a short introduction an overview of the main research efforts with a high need of technological input is presented.

Introduction

The cleanroom of the MISZ TU Wien holds a variety of technologies capable to fabricate and characterize novel artificial materials and devices. These technologies include growth of III-V nanostructures, silicon processing, structuring techniques like contact lithography, the production of patterned masks, ion milling, dry etching, plasma enhanced chemical vapor deposition, electron beam writing, focused ion beam etching and depositing, metallization techniques, transport measurements, spectroscopic techniques for optoelectronic devices, scanning tunneling microscopy, and atomic force microscopy.

Within the last year new equipment as well as upgrades of existing one was installed in the MISZ. These systems are a spectroscopic ellipsometer, a high resolution x-ray diffraction (HRXRD) system, a reactive ion etching with inductive coupled plasma, rapid thermal annealers, a wafer bonder, a spray coater, an upgraded surface profiler, MBE pumping and cell upgrades, and a scanning probe microscope. It takes some time to take full advantage of new equipment and although the additional technologies started to pay off already, we expect a peak in the productivity within the next 18 months.

To satisfy the mission of the MISZ and demonstrate novel materials and devices for semiconductor industries all the technologies implemented in the cleanroom have to be kept at state of the art performance. This includes an operable cleanroom environment (purified air, constant temperature and humidity, cooling, purified water, various inert gases) as well as periodic maintenance of the equipment and the cleanroom itself, e.g. pumping systems (rotary pumps, turbo pumps), exhaust filtering, liquid nitrogen, and cleaning and repair. Testing of the cleanroom quality and adjustment (laminar airflow, filters, cooling, humidity, and temperature) is done periodically. A detailed project information naming all the people making use the cleanroom, scientific publications resulting from samples processed in the cleanroom, talks presented at international conferences, finished diploma and PhD works and national and international cooperations are listed below. The listed projects and the attached publication list may give more insides on the broad range of activities in our facility and offer a more general overview.

This scientific report wants to highlight projects with a high need of technological input carried out within the cleanroom of the MISZ TU Wien during the last twelve months. A selected number of projects describe the achieved results in detail to show some of the major research activities and offer a deeper inside in the scientific work. All projects described below in detail take full advantage of the technologies installed in our cleanroom.

Research Activities

Opto-Electronics

J. Darmo et al.: New Generation of Photoconductive Terahertz Emitters

W. Schrenk et al.: Quantum Cascade Lasers

F.F. Schrey et al.: Modification of the Photoresponse by Energy Level Engineering in InAs Quantum Dot Nanostructures

P. Schwaha et al.: Electrically Pumped Quantum Cascade Ring Lasers

Transport Phenomena

M. Kast et al.: Transport through Wannier-Stark States in Biased Finite Superlattices

T. Müller et al.: Time-Resolved Measurement of Intersubband Population Dynamics

Power Devices

M. Blaho et al.: Study of Internal Behavior of BCD ESD Protection Devices under TLP and Very-Fast TLP Stress

D. Pogany: Local Thermal and Current Imaging in Power Devices

Direct Write Processes

W. Brezna et al.: Scanning Capacitance Microscopy Investigations of Focused Ion Beam Damage in Silicon

A. Lugstein et al.: Post-Process CMOS Channel Profile Tailoring With Focused Ion Beams

H.D. Wanzenboeck et al.: Deposition Mechanism of Direct-write Processes – An Application-Oriented Approach to Custom-Tailored Material Properties

Insulating Films

S. Harasek et al.: Zirconium Dioxide Thin Films for Microelectronics Deposited by Metal Organic Chemical Vapor Deposition

Project Information

Project Manager

Reinraum MISZ TU Wien, G. Strasser

Floragasse 7, A-1040 Wien

Project Group

Last Name	First Name	Status	Remarks
Anders	Solveig	postdoc	
Auer	Erwin	student	
Basnar	Bernhard	postdoc	
Beiter	Klaus	student	
Bertagnolli	Emmerich	o. prof.	
Blaho	Matej	dissertation	
Boxleitner	Winfried	postdoc	
Bychikhin	Sergey	postdoc	
Bratschitsch	Rudolf	dissertation	
Brezna	Wolfgang	dissertation	
Coquelin	Michael	student	
Darmo	juraj	postdoc	
Dubec	Viktor	dissertant	
Dzigal	Elvira	technician	
Fasching	Gernot	dissertant	
Fürnhammer	Felix	dissertant	
Gornik	Erich	o. prof.	
Gruber	Karl	student	
Harasek	Stefan	dissertation	
Hobler	Gerhard	ao. prof.	
Kamvar	Parvis	student	
Kast	Michael	dissertation	
Kröll	Josef	student	
Kröll	Peter	technician	
Kreuter	Johann	student	
Kuzmik	Ian	postdoc	
Langfischer	Helmut	dissertation	GMe
Litzenberger	Martin	dissertation	
Lugstein	Alois	univ. ass.	
Müller	Thomas	dissertation	

Last Name	First Name	Status	Remarks
Otto	Gustav	dissertation	
Pacher	Christoph	dissertation	
Pogany	Dionyz	univ. ass.	
Prinzinger	Johannes	technician	
Pflügl	Christian	dissertation	
Rebohle	Lars	postdoc	
Rakoczy	Doris	dissertation	
Riegler	Erich	technician	
Roch	Tomas	postdoc	
Schinnerl	Markus	technician	
Schenold	Helmut	technician	
Schrenk	Werner	cleanroom director	
Schrey	Frederik	dissertation	
Schwaha	Philipp	student	
Smoliner	Jürgen	ao. prof.	
Steinesberger	Gernot	dissertant	
Strasser	Gottfried	ao. prof.	
Tamosiunas	Vincas	postdoc	
Ulrich	Jochen	dissertation	
Unterrainer	Karl	ao. prof.	
Wanzenböck	Heinz	univ. ass.	
Zobl	Reinhard	dissertation	

Books and Contributions to Books

1. R. Bratschitsch and K. Unterrainer, “Terahertz physics of semiconductor heterostructures”; Encyclopedia of Modern Optics, Academic Press, to be published February 2002
2. C. Kranz, B. Mizaikoff, A. Lugstein, E. Bertagnolli, “Integrating an Ultramicroelectrode in an AFM Cantilever: Towards the Development of Combined Microsensing Imaging Tools”, Enviromental Electrochemistry, Analysis of Trace Element Biogeochemistry, American Chemical Society (ISBN 0-8412-3774-3), pp. 320, (2002)

Patents

1. E. Gornik, D. Pogany, Innovationsagentur, “Verfahren und Einrichtung zum optischem Testen von Halbleiterbauelementen”, submitted Jan 2002.
2. T. Le, A. Stingl, G. Tempea, J. Darmo, G. Strasser, and K. Unterrainer, “Einrichtung zur Erzeugung von Terahertz-Strahlung sowie Halbleiterbauelement” (A312/2002 H01S).

Publications in Reviewed Journals

1. D. Rakoczy, G. Strasser, J. Smoliner, “Ballistic electron emission microscopy of ‘on-surface’ self assembled InAs dots and wetting layers”, J. Vac. Sci. Technol. B **20**, 373 (2002), Selected for the *Virtual Journal of Nanoscale Science & Technology **5**(8) 2002*
2. S. Anders, W. Schrenk, E. Gornik, G. Strasser, “Room-temperature emission of GaAs/AlGaAs superlattice quantum cascade lasers at 12.6 μm”, Appl. Phys. Lett. 80, 1864 (2002), Selected for the Virtual Journal of Nanoscale Science & Technology 5(12) 2002
3. A. Lugstein, E. Bertagnolli, C. Kranz, B. Mizaikoff, Fabrication of a ring nanoelectrode in an AFM tip: novel approach towards simultaneous electrochemical and topographical imaging, Surf. Interface Analysis 33, 146 (2002)
4. R. Bratschitsch, T. Müller, G. Strasser, K. Unterrainer; “Intersubband relaxation dynamics in semiconductor quantum structures”; Physica E 13, 908 (2002).
5. J. Ulrich, G. Strasser, K. Unterrainer; “Terahertz quantum cascade emitters based on AlAs/GaAs”; Physica E 13, 900 (2002).
6. W. Schrenk, E. Gornik, H. Page, C. Sirtori, V. Ortiz, G. Strasser; “High performance single mode GaAs quantum cascade lasers”; Physica E 13, 840 (2002).
7. M. Kast, C. Pacher, M. Coquelin, G. Fasching, G. Strasser, E. Gornik; “Narrow electron injector for hot electron spectroscopy”; Physica E 13, 728 (2002).
8. S. Hofer, H. Hirner, R. Bratschitsch, G. Strasser, K. Unterrainer; “Photoconductive Response of InAs/GaAs quantum dot stacks”; Physica **E 13**, 190 (2002).
9. M. Kast, C. Pacher, M. Coquelin, G. Fasching, G. Strasser, E. Gornik; “LO-phonon assisted hot electron transport in biased superlattices”; Physica B **314**, 409 (2002).
10. D. Rakoczy, G. Strasser, J. Smoliner; “Ballistic Electron Emission Microscopy for Local Measurements of Barrier Heights on InAs Self-assembled Quantum Dots on GaAs”; Physica **B 314**, 81 (2002)
11. C. Pacher, G. Strasser, E. Gornik, F. Elsholz, G. Kießlich, A. Wacker, and E. Schöll, “Optics with ballistic electrons: antireflection coatings for GaAs/AlGaAs superlattices”, Physica E **12**, 285 (2002).
12. T. Müller, R. Bratschitsch, G. Strasser, K. Unterrainer, “Direct measurement of intersubband dynamics”, Physica **B 314**, 259 (2002).
13. G. Strasser, W. Schrenk, S. Anders, E. Gornik; “Single mode GaAs Quantum Cascade Laser”; Microelectronic Engineering **63**, 179 (2002)
14. D.Rakoczy, R.Heer, G.Strasser, J.Smoliner, High Energy Ballistic Transport in Hetero- and Nanostructures, to be published in Physica E (2002)
15. J. Ulrich, J. Kreuter, W. Schrenk, G. Strasser, K. Unterrainer, “Long wavelength (15 and 23 μm) GaAs/AlGaAs quantum cascade lasers”, Appl. Phys. Lett. **80**, 3691 (2002), Selected for the *Virtual Journal of Nanoscale Science & Technology **5**(12) 2002*
16. K. Unterrainer, R. Colombelli, C. Gmachl, F. Capasso, H.Y. Hwang, L. Sivco, A. Y. Cho,”Quantum cascade lasers with double metal-semiconductor waveguide resonators”, Appl. Phys. Lett. **80**, 3060 (2002).
17. D.Rakoczy, G.Strasser, J.Smoliner, L-Valley Electron Transport in GaAs-AlAs Double Barrier Resonant Tunneling Structures Studied by Ballistic Electron Emission Microscopy, Phys. Rev. B **66**, 033309 (2002), selected for the *Virtual Journal of Nanoscale Science and Technology **6**(7), 2002*

18. H. Langfischer, E. Bertagnolli, B. Basnar, H. Hutter, “Evolution of Tungsten Film Deposition Induced by Focused Ion Beam”, J. Vac. Sci. Technol. **A 20(4)**, Jul/Aug 2002, p. 1408

19. W. Brezna, S. Harasek, H. Enichlmair, E. Bertagnolli, E. Gornik, J. Smoliner, “Scanning Capacitance Microscopy With ZrO_2 as Dielectric Material”, J. Appl. Phys. **92**, 2144 (2002)

20. S. Harasek, H.D. Wanzenboeck, B. Basnar, J. Smoliner, J. Brenner, H. Stoeri, E. Gornik, and E. Bertagnolli, “Metal-organic chemical vapor deposition and nanoscale characterization of zirconium oxide thin films”, Thin Solid Films **414**, 199 (2002)

21. D. Pogany, S. Bychikhin, M. Litzenberger, E. Gornik, G. Groos and M. Stecher, “Extraction of spatio-temporal distribution of power dissipation in semiconductor devices using nanosecond interferometric mapping technique”, Appl. Phys. Lett, **81**, 2881-2883 (2002).

22. D. Pogany, V. Dubec, S. Bychikhin, C. Fürböck, M. Litzenberger, G. Groos, M. Stecher, E. Gornik, “Single-shot thermal energy mapping of semiconductor devices with the nanosecond resolution using holographic interferometry”, IEEE Electron. Dev. Lett., **23,** 606-608, (2002).

23. K. Kempa, Y. Zhou, J. R. Engelbrecht, P. Bakshi, H. I. Ha, J. Moser, M.J. Naughton, J. Ulrich, G. Strasser, E. Gornik, K. Unterrainer; “Transport signatures of intersubband electron-electron scattering in quantum wells in strong magnetic fields”; Phys. Rev. Lett. **88**, 226803 (2002), selected for the *Virtual Journal of Nanoscale Science & Technology **5**(22) 2002*

24. F. Eickemeyer, R. Reimann, M. Woerner, T. Elsaesser, S. Barbieri, C. Sirtori, G. Strasser, T. Müller, R. Bratschitsch, K. Unterrainer; “Ultrafast coherent electron transport in semiconductor quantum cascade structures”; Phys. Rev. Lett. 89, 047402 (2002), selected for the *Virtual Journal of Nanoscale Science & Technology **6**(3) 2002*

25. J. Darmo, G. Strasser, T. Müller, R. Bratschitsch, K. Unterrainer, “Surface-modified Gaas terahertz plasmon emitter”, Appl. Phys. Lett. **81**, 871 (2002).

26. F. Capasso, R. Paiella, R. Martini, R. Colombelli, C. Gmachl, T. L. Myers, M. S. Taubman, R. M. Williams, C. G. Bethea, K. Unterrainer, H.Y. Hwang, D. L. Sivco, A. Y. Cho, A. M. Sergent, H. C. Liu, E. A. Whittaker, “Quantum Cascade Lasers: Ultrahigh-Speed Operation, Optical Wireless Communication, Narrow Linewidth, and Far-Infrared Emission”, IEEE J. Quantum Electron. **38**, 511 - 532 (2002).

27. L. Rebohle, F.F. Schrey, S. Hofer, G. Strasser, K. Unterrainer, “Energy level engineering in InAs quantum dot nanostructures”; Appl.Phys. Lett. **81**, 2097(2002), selected for the *Virtual Journal of Nanoscale Science & Technology **6**(12) 2002*

28. M. Blaho, D. Pogany, E. Gornik, L. Zullino, A. Andreini, “Experimental and simulation analysis of a BCD ESD protection element under the DC and TLP stress conditions”, Microel. Reliab. 2002., **42**, pp.1281-1286, (2002).

29. D. Pogany, J. Kuzmik, J. Darmo, M. Litzenberger, S. Bychikhin, K. Unterrainer, E. Gornik, Z. Mozolova, S. Hascik, T. Lalinsky, “Electrical field mapping in InGaP HEMTs and GaAs teraherz emitters using backside infrared OBIC technique”, Microel. Reliab. 2002., **42**, pp. 1673-1677 (2002).

30. W. Stadler, K. Esmark, H. Gossner, M. Streibl, M. Wendel, W. Fichtner, M. Litzenberger, D. Pogany, E. Gornik, Device Simulation and Backside Laser Interferometry - Powerful Tools for ESD Protection Development”, Microel. Reliab. 2002., **42**, pp. 1267-1274 (2002).

31. J. Darmo, R. Bratschitsch, T. Müller, R. kersting, G. Strasser, and K. Unterrainer, “Few-cycle THz generation for imaging and tomography applications”, Phys. Med. and Biology **47**, 3691-3697 (2002).

32. J. Darmo, T. Müller, G., Strasser, K. Unterrainer, T. Le, G. Tempea, and A. Stingl, “Voltage-controlled intracavity terahertz generator for self-starting Ti:sapphire lasers”; Optics. Lett. **27**, 1941-1943 (2002).

33. A. Lugstein, E. Bertagnolli, C. Kranz, A. Kueng, B. Mizaikoff, “Integrating Micro- and Nanoelectrodes into Atomic Force Microscopy Cantilevers using Focused Ion Beam Techniques”, Appl. Phys. Lett., **81**, 349 (2002), selected for the *Virtual Journal of Nanoscale Science & Technology **6**(2) 2002*

34. A. Lugstein, B. Basnar, G. Hobler, and E. Bertagnolli, “A novel approach for current density profile extraction of focused ion beams based on AFM contour profiling of nanodots”, Journal of Applied Physics **92**, 4037 (2002), selected for the *Virtual Journal of Nanoscale Science & Technology **6**(14) 2002*

35. M. Kast, C. Pacher, G. Strasser, WSM Werner, E. Gornik, “Wannier-Stark States in Finite Superlattices”, Physical Review Letters **89**, 136803 (2002).

36. S. Anders, W. Schrenk, E. Gornik, G. Strasser; “Room temperature lasing of electrically pumped quantum cascade microcavities”; Appl. Phys. Lett. **80**, 4094 (2002), selected for the *Virtual Journal of Nanoscale Science & Technology **5**(22) 2002*

37. C. Brink, D. Schneider, G. Ploner, G. Strasser, E. Gornik; “Magnetophonon resonance in the confinement of an n-GaAs/AlGaAs-heterojunction, tuned to a quasi-one-dimensional quantum wire”; Physica **E 12**, 446 (2002)

38. R. Ascazubi, O.C. Akin, T. Zaman, R. Kersting, G. Strasser; “Dephasing in modulation-doped quantum structures probed by THz time-domain spectroscopy”; Appl. Phys. Lett. **81**, 4344 (2002), selected for the *Virtual Journal of Nanoscale Science & Technology **6**(24) 2002*

39. A. Lugstein, B. Basnar, E. Bertagnolli, “Study of focused ion beam response of GaAs in the nanoscale regime”, J. Vac. Sci. Technol. B **20**(6), 2238 (2002).

40. D. Pogany, S. Bychikhin, C. Fürböck, M. Litzenberger, E. Gornik, G. Groos, K. Esmark, M. Stecher, “Quantitative internal thermal energy mapping of semiconductor devices under short current stress using backside laser interferometry”, IEEE Trans. Electron Dev., **49**, 2070 (2002).

41. R. Colombelli, F. Capasso, K. Unterrainer, C. Gmachl, A. M. Sergent, D. L. Sivco, A.Y. Cho, “Quantum Cascade Lasers and Metal Waveguides at λ>20μm”, SPIE Proceedings, **4651**, .146-156 (2002).

42. D.Rakoczy, G.Strasser, J.Smoliner Measuring the Energetic Distribution of Ballistic Electrons after their Refraction at an Au-GaAs Interface, to be published in Appl-Phys. Lett. (2003)

43. C.Pflügl, M.Litzenberger, W.Schrenk, D.Pogany, E.Gornik, G.Strasser Interferometric study of thermal dynamics in GaAs-based quantum cascade lasers, to be published in Appl. Phys. Lett (2003)

44. S. Anders, W, Schrenk, A. Lugstein, and G. Strasser, “Room temperature lasing of electrically pumped quantum cascade microcylinders”, to be published in Physica E (2003)

45. M. Lackner, C. Forsuch, F. Winter, S. Anders, and G. Strasser, “Investigation of biomass steam gasification gas using a GaAs based quantum cascade laser emitting at 11 μm”, to be published in Optics Communications.

46. G. Otto, G. Hobler, and K. Gärtner, “Defect characterization of low-energy recoil events in silicon using classical molecular dynamics simulation”, *Nucl. Instr. Meth.* B, (accepted for publication).

47. A. Lugstein, B. Basnar, and E. Bertagnolli, “FIB processing of silicon in the nanoscale regime”, Appl. Physics A. (accepted for publication)

48. A. Lugstein, W. Brezna, M. Stockinger, B. Goebel, L. Palmetshofer, E. Bertagnolli, “Nonuniform Channel MOS Device”, Applied Phys. A. (accepted for publication)

49. S. Anders, W. Schrenk, C. Pflügl, E. Gornik, G. Strasser, C. Becker, and C. Sirtori, “Room temperature operation of Gaas-based quantum cascade lasers processed as ridge and microcavity waveguides”, to be published in IEE opto-electronics 09/2002.

50. S. Harasek, H.D. Wanzenboeck, E. Bertagnolli, “Compositional and electrical properties of zirconium dioxide thin films chemically deposited on silicon”, accepted for publication in J. Vac. Sci. Technol.

Presentations & Conference Proceedings

1. K. Unterrainer (invited), “Ultrafast Spectroscopy of Intersubband Transitions”, “Workshop on Quantum Heterostructures and THz Electronics”, 17.1. 2002, Univ. Regensburg, Regensburg

2. G. Strasser (invited); “Prospects of intersubband laser action in GaAs cascaded quantum dots”; Photonics West, San Jose, USA, 19.-25.1.2002

3. W. Schrenk, E. Gornik, G. Strasser; “Room temperature DFB GaAs quantum cascade lasers”; Photonics West, San Jose, USA, 19.-25.1.2002

4. J.N. Heyman, H. Wrage, C. Lind, D. Hebert, P. Neocleous, P.A. Crowell, T. Müller, K. Unterrainer; “Terahertz Emission from Magneto-plasma Oscillations in Semiconductors”; Photonics West, San Jose, USA, 19.-25.1.2002, *in SPIE Proceedings Photonics West (to be published).*

5. R. Colombelli, F. Capasso, K. Unterrainer, C. Gmachl, A. M. Sergent, D. L. Sivco, A.Y. Cho, “Quantum Cascade Lasers and Metal Waveguides at λ>20μm”, Photonics West, San Jose, USA, 19.-25.1.2002, *in SPIE Proceedings, Photonics West (to be published)*.

6. W. Schrenk (invited), “GaAs-based quantum cascade lasers”, Workshop Light Emitters Based on Intersubband Transitions, Berlin, Germany, February 2002.

7. J.Smoliner (invited), High Energy Ballistic Transport in Hetero- and Nanostructures, 12th International Winterschool on New Developments in Solid State Physics, Mauterndorf (Feb. 2002)

8. G. Steinlesberger, M. Engelhardt, G. Schindler, J. Kretz, W. Steinhögl, E. Bertagnolli, “Processing Technology for the Investigation of Sub-50 Nanometer Copper Damascene Interconnects”, 3rd European Workshop on **UI**timate **I**ntegration of **S**ilicon, ULIS´3, Munich, March 2002.

9. G. Schindler, G. Steinlesberger, M. Engelhardt, Steinhögl, “Electrical Characterization of Copper Interconnects with End of Roadmap Feature Sizes”, 3rd European Workshop on **UI**timate **I**ntegration of **S**ilicon, ULIS´3, Munich, March 2002.

10. C. Kranz, E. L. Heinz, B. Mizaikoff, A. Lugstein, E. Bertagnolli,” Simultaneous Surface Modification and Imaging with Integrated Scanning Electrochemical/Atomic Force Microscopy, Pittcon , Pittsburgh, 17-22.3. 2002.

11. A. Kueng, C. Kranz, B. Mizaikoff, A. Lugstein, E. Bertagnolli, “Integrating an Ultramicroelectrode in an AFM Cantilever for In-Situ Imaging of Enzyme Activities”. 201st Meeting of The Electrochemical Society, 12.5. 2002.
12. F. Eickemeyer, K. Reimann, M. Wörner, T. Elsässer, S. Barbieri, C. Sirtori, G. Strasser, T. Müller, R. Braschitsch, and K. Unterrainer, “Ultrafast coherent electron transport in quantum cascade structures”, 13th International Conference on Ultrafast Phenomena, Vancouver, Canada, 12.-17. 5. 2002, *F. Eickemeyer, R. Reimann, M. Woerner, T. Elsaesser, S. Barbieri, C. Sirtori, G. Strasser, T. Müller, R. Bratschitsch, K. Unterrainer; “Ultrafast coherent electron transport in semiconductor quantum cascade laser structures in OSA Trends in Optics and Photonics Vol.72, The Thirteenth International Conference on Ultrafast Phenomena, OSA Technical Digest, Postconference Edition (Optical Society of America, Washington DC, 2002), pp. 183-184.*
13. T. Müller, R. Bratschitsch, G. Strasser, and K. Unterrainer, “Population dynamics in quantum structures”, 13th International Conference on Ultrafast Phenomena, Vancouver, Canada, 12.-17. 5. 2002, *T. Müller, R. Bratschitsch, G. Strasser, and K. Unterrainer, “Population dynamics in quantum structures”, in OSA Trends in Optics and Photonics Vol.72, The Thirteenth International Conference on Ultrafast Phenomena, OSA Technical Digest, Postconference Edition (Optical Society of America, Washington DC, 2002), pp. 334-335.*
14. T. Müller, R. Bratschitsch, G. Strasser, and K. Unterrainer, “Time-resolved measurement of subband population dynamics”, CLEO/QELS 2002, Long Beach, USA, 19.-24.5.2002, *T. Müller, R. Bratschitsch, G. Strasser, and K. Unterrainer, “Time-resolved measurement of subband population dynamics”, in OSA Trends in Optics and Photonics Vol.74, Quantum Electronics and Laser Science Conference, OSA Technical Digest Postconference Edition (Optical Society of America, Washington DC, 2002), pp. 262-263.*
15. W. Schrenk, S. Anders, E. Gornik, G. Strasser; “Room temperature operation of distributed feedback AlGaAs/GaAs quantum cascade lasers”; CLEO/QELS 2002, Long Beach, USA, 19.-24.5.2002, *W. Schrenk, S. Anders, E. Gornik, and G. Strasser, “Room Temperature Operation of Distributed Feedback AlGaAs/GaAs Quantum Cascade Lasers”, in OSA Trends in Optics and Photonics Vol.73, Conference on Lasers and Electro-Optics, OSA Technical Digest, Postconference Edition (Optical Society of America, Washington DC, 2002), pp. 155.*
16. F. Eickemeyer, K. Reimann, M. Wörner, T. Elsässer, S. Barbieri, C. Sirtori, G. Strasser, T. Müller, R. Braschitsch, and K. Unterrainer, “Ultrafast coherent electron transport in quantum cascade structures”, CLEO/QELS 2002, Long Beach, USA, 19.-25.5.2002, *F. Eickemeyer, R. Reimann, M. Woerner, T. Elsaesser, S. Barbieri, C. Sirtori, G. Strasser, T. Müller, R. Bratschitsch, K. Unterrainer; “Ultrafast coherent electron transport in semiconductor quantum cascade laser structures”; ”, in OSA Trends in Optics and Photonics Vol.73, Conference on Lasers and Electro-Optics, OSA Technical Digest, Postconference Edition (Optical Society of America, Washington DC, 2002), pp. 183.*
17. J. Darmo, T. Müller, G. Strasser, K. Unterrainer, T. Le, A. Stingl; “Voltage-controlled intracavity THz generator for self-starting Ti:Sapphire lasers”; CLEO/QELS 2002, Long Beach, USA, 19.-24.5.2002, *J. Darmo, T. Müller, G. Strasser, K. Unterrainer, T. Le, and A. Stingl, “Voltage-controlled intracavity THz generator for self-starting Ti:Sapphire lasers”, in OSA trends in Optics and Photonics Vol.73, Conference on Lasers and Electro-optics, OSA Technical Digest Postdeadline Papers (Optical Society of America, Washington DC, 2002) paper CPDA6.*
18. A. Kueng, C. Kranz, B. Mizaikoff, A. Lugstein, E. Bertagnolli, “Integrated Ultramicroelectrode/AFM Cantilever for In-Situ Imaging of Enzyme Activity”, 4th

Conference on Scanning Probe Microscopy, Sensors and Nanostructures, Las Vegas, 26-29.5.2002.

19. G. Otto, G. Hobler, and K. Gärtner, “Defect characterization of 10-200 eV recoil events in silicon using classical molecular dynamics simulation, 6th Intl. Conf. Computer Simulation of Radiation Effects in Solids (COSIRES 2002), Dresden, Germany, 23.-27.6.2002.
20. K. Unterrainer, R. Bratschitsch, T. Müller, R. Kersting, J.N. Heyman, and G. Strasser (invited talk), “Few-Cycle THz Pulse Generation and Spectroscopy of Semiconductor Nanostructures”, 12th Semiinsulating and Insulating Materials Conference (SIMC XII), Smolenice Castle, Slovakia, 30.6.-5.7.2002.
21. J. Darmo, T. Müller, G. Strasser, and K. Unterrainer, “ Terahertz Generation in GaAs:As Photoconductive Emitters”, 12th Semiinsulating and Insulating Materials Conference (SIMC XII), Smolenice Castle, Slovakia, 30.6.-5.7.2002.
22. L. Rebohle, F. Schrey, S. Hofer, G. Strasser, K. Unterrainer; “Energy level engineering in InAs quantum dot stacks embedded in AlAs/GaAs superlattices”; Int. Conf. on Superlattices, Nanostructures and Nanodevices (ICSNN), Toulouse, France, 22-26 7.2002
23. S. Anders, W. Schrenk, G. Strasser; “Room temperature lasing of electrically pumped quantum cascade micro-cylinders”; Int. Conf. on Superlattices, Nanostructures and Nanodevices (ICSNN), Toulouse, France, 22-26 7. 2002
24. J. Darmo, G. Strasser, T. Müller, K. Unterrainer; “THz plasmon emission from an LT-GaAs/GaAs homojunction”; 26th Int. Conf. on the Physics of Semiconductors (ICPS), Edinburgh, Scottland, 29.7.-2.8.2002.
25. T. Müller, R. Bratschitsch, W. Parz, G. Strasser, K. Unterrainer; “Intersubband Polarization and Carrier Dynamics”; 26th Int. Conf. on the Physics of Semiconductors (ICPS), Edinburgh, Scottland, 29.7.-2.8.2002.
26. M. Kast, C. Pacher, G. Strasser, E. Gornik, “Transport through Wannier-Stark states in biased finite superlattices”, 26th International Conference on the Physics of Semiconductors (ICPS26), Edinburgh, Scotland, 29.7.–2.8.2002, *M. Kast, C. Pacher, G. Strasser, E. Gornik, “Transport through Wannier-Stark states in biased finite superlattices”, Proceedings of the 26th International Conference on the Physics of Semiconductors (ICPS26), Edinburgh, Scotland, 29.7.–2.8.2002, to be published.*
27. C. Pacher, G. Fasching, M. Kast, G. Strasser, E. Gornik, “Study of Electron-Phonon Scattering in wide GaAs Quantum Wells utilizing Hot Electron Spectroscopy”, 26th International Conference on the Physics of Semiconductors (ICPS26), Edinburgh, Scotland, 29.7.–2.8.2002, C. Pacher, G. Fasching, M. Kast, G. Strasser, E. Gornik, “Study of Electron-Phonon Scattering in wide GaAs Quantum Wells utilizing Hot Electron Spectroscopy”, Proceedings of the 26th International Conference on the Physics of Semiconductors (ICPS26), Edinburgh, Scotland, 29.7.–2.8.2002, to be published.
28. M. Coquelin, C. Pacher, M. Kast, G. Strasser, E. Gornik, “Transport studies on double period superlattices utilizing Hot Electron Spectroscopy”, 26th International Conference on the Physics of Semiconductors (ICPS26), Edinburgh, Scotland, 29.7.–2.8.2002, *M. Coquelin, C. Pacher, M. Kast, G. Strasser, E. Gornik, “Transport studies on double period superlattices utilizing Hot Electron Spectroscopy”, Proceedings of the 26th International Conference on the Physics of Semiconductors (ICPS26), Edinburgh, Scotland, 29.7.–2.8.2002, to be published.*

29. L. Rebohle, F. Schrey, S. Hofer, G. Strasser, K. Unterrainer; “InAs/GaAs quantum dot stacks and their suitability as infrared photodetectors”; 26th Int. Conf. on the Physics of Semiconductors (ICPS), Edinburgh, Scottland, 29.7.-2.8.2002
30. D. Rakoczy, G. Strasser, C. Strahberger, and J. Smoliner; “BEEM/BEES in Hetero- and Nanostructures: Electron Refraction and Higher Valleys”; 26th Int. Conf. on the Physics of Semiconductors (ICPS), Edinburgh, Scottland, 29.7.-2.8.2002
31. G. Strasser, W. Schrenk, S. Anders, J. Ulrich, E. Gornik, K. Unterrainer; “High performance AlGaAs/GaAs quantum cascade lasers 26th Int. Conf. on the Physics of Semiconductors (ICPS), Edinburgh, Scottland, 29.7.-2.8.2002
32. F. Eickemeyer, R. Reimann, M. Woerner, T. Elsaesser, S. Barbieri, C. Sirtori, G. Strasser, T. Müller, R. Bratschitsch, K. Unterrainer; “Ultrafast gain dynamics in quantum cascade laser structures”; 26th Int. Conf. on the Physics of Semiconductors (ICPS), Edinburgh, Scottland, 29.7.-2.8.2002
33. T. Elsaesser, R.A. Kaindl, F. Eickemeyer, K. Reimann, M. Woerner, S. Barbieri, C. Sirtori, G. Strasser, T. Müller, R. Bratschitsch, K. Unterrainer, R. Hey (invited); “Ultrafast intersubband coherences in quantum wells and quantum cascade structures”; OSA Nonlinear Optics Conference, Maui, USA, 29.7.-2.8.2002
34. M. Blaho, D. Pogany, E. Gornik, M. Denison, G. Groos, M. Stecher; “Investigation of the internal behavior of a vertical DMOS transistor under short duration, high current stress by an optical thermal mapping method”; 6th Int. seminar on power semiconductors (ISPS), Prague, 4.-6. 9. 2002, *M. Blaho, D. Pogany, E. Gornik, M. Denison, G. Groos, M. Stecher; “Investigation of the internal behavior of a vertical DMOS transistor under short duration, high current stress by an optical thermal mapping method”; in Proc. of 6th Int. seminar on power semiconductors, Editor V. Benda (IEE Czech Centre, Prague 2002), pp. 63-67*
35. A. Lugstein, W. Brezna, E. Bertagnolli, “Impact of focused Ion Beam Assisted Front End Processing on n-MOSFET Degradation” 40th IEEE, Int. Reliability Physics Symposium (IRPS), Dallas, April 2002, *A. Lugstein, W. Brezna, E. Bertagnolli, “Impact of focused Ion Beam Assisted Front End Processing on n-MOSFET Degradation” in Proc. Of 40th IEEE, Int. Reliability Physics Symposium IRPS, Dallas, 2002, pp 369-375*
36. G. Strasser (invited); “ GaAs-based quantum cascade DFB lasers and Microcavities”; Workshop Quantum Cascade Lasers Technology & Application; Frauenhofer Institut f. phys. Messtechnik IPM, Freiburg, Germany, 19.9.2002
37. H.D. Wanzenboeck, S. Harasek, G. Hobler, H. Hutter, H. Stoeri, P. Pongratz, E. Bertagnolli; “Dielectric Nanostructure Fabrication using a Focused Ion Beam”; 13th International Conference on Ion Beam Modification of Materials (IBMM2002), Kobe, Japan, 1.-6. 10. 2002
38. H.D. Wanzenboeck, G. Hobler, H. Langfischer, S. Harasek, B. Basnar, W. Brezna, J. Smoliner and E. Bertagnolli; “Characterization of Doping and Intermixing Effects of Focused Ion Beam Processing”, 13th International Conference on Ion Beam Modification of Materials (IBMM2002), Kobe, Japan, 1.-6. 10. 2002
39. D. Pogany, M. Litzenberger, S. Bychikhin, E. Gornik, G. Groos, M. Stecher,”A method for extraction of power dissipating sources from interferometric thermal mapping measurements”, 32nd European Solid State Device Research Conference (ESSDERC 2002), Florence, 24-26 Sept. 2002, *D. Pogany, M. Litzenberger, S. Bychikhin, E. Gornik, G. Groos, M. Stecher,”A method for extraction of power dissipating sources from interferometric thermal mapping measurements”, in Proc. 32nd European Solid State Device Research Conference (ESSDERC 2002), Editors G. Baccarani, E. Gnani, M. Rudan, (Florence, Italy, 2002), pp. 243-246.*

40. A. Lugstein, W. Brezna, B. Goebel, L. Palmetshofer, E. Bertagnolli, “Post-Process CMOS Front End Engineering With Focused Ion Beams”, ESSDERC’2002, 24-26 Sept. 2002, Florence, Italy, *Lugstein, W. Brezna, B. Goebel, L. Palmetshofer, E. Bertagnolli, “Post-Process CMOS Front End Engineering With Focused Ion Beams”, in Proc. 32nd European Solid State Device Research Conference (ESSDERC 2002), Editors G. Baccarani, E. Gnani, M. Rudan, (Florence, Italy, 2002), pp. 111-114.*
41. S. Bychikhin, V. Dubec, M. Litzenberger, D. Pogany, E. Gornik, G. Groos, K. Esmark, W. Stadler, H. Gieser, H. Wolf, “Investigation of ESD protection elements under high current stress in CDM-like time domain using backside laser interferometry”, EOS/ESD Symp’2002, Charlotte, Oct 8-10, 2002, *S. Bychikhin, V. Dubec, M. Litzenberger, D. Pogany, E. Gornik, G. Groos, K. Esmark, W. Stadler, H. Gieser, H. Wolf, “Investigation of ESD protection elements under high current stress in CDM-like time domain using backside laser interferometry”, in Proc. 24th Electrical Overstress/ Electrostatic Discharge Symposium (EOS/ESD 2002), (Charlotte, USA, 2002) pp.387-395*
42. M. Blaho, D. Pogany, E. Gornik, L. Zullino, A. Andreini, “Experimental and simulation analysis of a BCD ESD protection element under the DC and TLP stress conditions”, 13th European Symposium on Reliability of Electron Devices, Failure Physics and Analysis (ESREF’2002), Rimini, Italy, October 7-11, 2002
43. W. Stadler (invited), K. Esmark, H. Gossner, M. Streibl, M. Wendel, W. Fichtner, M. Litzenberger, D. Pogany, E. Gornik, Device Simulation and Backside Laser Interferometry - Powerful Tools for ESD Protection Development”, invited paper, 13th European Symposium on Reliability of Electron Devices, Failure Physics and Analysis (ESREF’2002), Rimini, Italy, October 7-11, 2002
44. D. Pogany, J. Kuzmik, J. Darmo, M. Litzenberger, S. Bychikhin, K. Unterrainer, E. Gornik, Z. Mozolova, S. Hascik, T. Lalinsky, “Electrical field mapping in InGaP HEMTs and GaAs teraherz emitters using backside infrared OBIC technique”, 13th European Symposium on Reliability of Electron Devices, Failure Physics and Analysis (ESREF’2002), Rimini, Italy, October 7-11, 2002
45. G. Strasser (invited); “Technology of quantum cascade lasers”; Crystal Growth and Epitaxy, Review Conf. on scientific cooperation between Austria and Poland, Vienna, Austria, 20.-24.10.2002
46. G. Strasser (invited); “Quanten-Kaskaden-Laser – ein leuchtendes Beispiel für Nanodesign”; Nanoforum 2002; Johannes Kepler Universität Linz, Austria, 14.-16.11.2002
47. H.D. Wanzenboeck (invited), S. Harasek and E. Bertagnolli; “ Local Nanodeposition of Dielectric Materials for Microelectronics”, 19th International VLSI Multilevel Interconnection Conference (VMIC2002), Singapore, 18.-20. 11. 2002, *H.D. Wanzenboeck, S. Harasek and E. Bertagnolli; “ Local Nanodeposition of Dielectric Materials for Microelectronics”, Proceedings of the 19th International VLSI Multilevel Interconnection Conference (02IMIC-400); (Library of Congress 89-644090), 2002*
48. T. Elsaesser, R.A. Kaindl, F. Eickemeyer, K. Reimann, M. Woerner, S. Barbieri, C. Sirtori, G. Strasser, T. Müller, R. Bratschitsch, K. Unterrainer, R. Hey, K.H. Ploog (invited); “Ultrafast intersubband coherences in semiconductor quantum wells and quantum cascade structures”; MRS (Material Research Society) Fall Meeting 2002, Boston, USA, 2.-6.12.2002
49. K. Unterrainer, R. Bratschitsch, T. Müller, R. Kersting, J.N. Heyman, G. Strasser, (invited talk) “Few-Cycle THz pulse generation and spectrscopy of semiconductor nanostructures”, 12th Int. Semiconducting and Insulating Materials Conference, Smolenice Castle, Slovakia, 30.6.-5.7.2002

50. D. Pogany , S. Bychikhin, J. Kuzmik , V. Dubec , N. Jensen , M. Denison, G. Groos, M. Stecher and E. Gornik, “Investigation of thermal distribution during destructive pulses in ESD protection devices using a single-shot, two-dimensional interferometric method”, IEEE International Electron Device Meeting, San Francisco, USA, December 9 -11, 2002, *D. Pogany , S. Bychikhin, J. Kuzmik , V. Dubec , N. Jensen , M. Denison, G. Groos, M. Stecher and E. Gornik, “Investigation of thermal distribution during destructive pulses in ESD protection devices using a single-shot, two-dimensional interferometric method”, IEDM 2002 Technical Digest (IEEE International Electron Device Meeting, San Francisco, USA 2002), pp.345-348.*

51. G. Hobler and G. Otto, “Detailed modeling of ion implantation damage in silicon using a binary collision approach with information from molecular dynamics simulations”, poster at *13th Intl. Conf. Ion Beam Modification of Materials* (IBMM2002), Kobe, Japan, 1.-6-9-2002.

52. H.D. Wanzenboeck, S. Harasek, H. Langfischer, W. Brezna, J. Smoliner, E. Bertagnolli, “ Deposition Mechanism of oxide thin films manufactured by a focused energetic beam process”, MRS (Material Research Society) Fall Meeting 2002, Boston, USA, 2.-6.12.2002

53. H.D. Wanzenboeck, S. Harasek, H. Langfischer, E. Bertagnolli, U. Grabner, G. Hammer, P. Pongratz, “FIB-TEM characterization of locally restricted implantation damage”, MRS (Material Research Society) Fall Meeting 2002, Boston, USA, 2.-6.12.2002

54. H.D. Wanzenboeck, H. Langfischer, S. Harasek, E. Bertagnolli, “Versatile Nanodeposition of Dielectrics and Metals by noncontact direct-write technologies” MRS (Material Research Society) Fall Meeting 2002, Boston, USA, 2.-6.12.2002

55. S. Harasek, H.D. Wanzenboeck, H. Langfischer, E. Bertagnolli: “Ultrathin zirconium dioxide chemically deposited at a low thermal budget”, MRS (Material Research Society) Fall Meeting 2002, Boston, USA, 2.-6.12.2002

56. 9. H. Langfischer, S. Harasek, H.D. Wanzenboeck, B. Basnar, E. Bertagnolli; “time-resolvedstudies of Focused Ion Beam Induced Tungsten Deposition”; MRS (Material Research Society) Fall Meeting 2002, Boston, USA, 2.-6.12.2002

57. J.Smoliner, “Charaktrisierung von Halbleitern mittels Rastersonden Mikroskopie”, Chemietage Linz 17.09.2002

58. J. Ulrich, V. Tamosiunas, J. Kreuter, G. Strasser, K. Unterrainer, R. Colombelli, C. Gmachl, F. Cappasso, H. Y. Hwang, D.L. Sivco, A.Y. Cho, “Waveguides for long wavelength quantum cascade lasers”, 10th Int. IEEE Conf. on Terahertz Electronics, Cambridge, UK, September 9-10, 2002.

59. T. Müller, R. Bratschitsch, W. Parz, G. Strasser, K. Unterrainer, “Coherent and incoherent intersubband dynamics”. 10th Int. IEEE Conf. on Terahertz Electronics, Cambridge, UK, September 9-10, 2002, *T. Müller, R. Bratschitsch, W. Parz, G. Strasser, and K. Unterrainer, “Coherent and incoherent intersubband dynamics”, in IEEE Tenth International Conference on Terahertz Electronics Proceedings, Editors: J.M. Chamberlain, P. Harrison, R.E. Miles, A.G. Davies, E.H. Linfield, S. Withington (IEEE, Piscataway 2002), p.41-44.*

60. J. Darmo, T. Müller, G. Strasser, K. Unterrainer, T. Le, G. Tempea, A. Stingl, “Intra- and extra – cavity THz generation from optically and electrically confined photoconducting layers”, 10th Int. IEEE Conf. on Terahertz Electronics, Cambridge, UK, September 9-10, 2002, *J. Darmo, T. Müller, G. Strasser, K. Unterrainer, T. Le, G. Tempea, and A. Stingl, “Intra- and extra-cavity THz generation from optically and electrically confined photoconducting layers”, in IEEE Tenth International*

Conference on Terahertz Electronics Proceedings, Editors: J.M. Chamberlain, P. Harrison, R.E. Miles, A.G. Davies, E.H. Linfield, S. Withington (IEEE, Piscataway 2002), p.67-69.

61. S. Anders, W. Schrenk, C. Pflügl, E. Gornik, and G. Strasser, C. Becker, C. Sirtori; "Room-temperature operation of GaAs-based quantum cascade lasers processed as ridge and microcavity waveguides"; 5th Int. Conf. On Mid-Infrared Optoelectronics Materials and Devices (MIOMD-V2002), Annapolis, USA, 8.-11. 9. 2002.
62. G. Strasser, W. Schrenk, S. Anders, C. Pflügl, E. Gornik; "Growth of GaAs based quantum cascade lasers "; 12th Int. Conf. on Molecular Beam Epitaxy (MBE-XII); San Francisco, 15.-21.9. 2002
63. K. Unterrainer, (invited talk), "THz emission from semiconductors", INFM School on "Progress in Laser Sources and Photonic Devices", Capri, Italy, October 1-8, 2002.
64. C. Pflügl, M. Litzenberger, W. Schrenk, S. Anders, D.Pogany, E. Gornik, G. Strasser; "Interferometric Temperature Mapping Of GaAs-based Quantum Cascade Laser Ridges"; 29th Int. Symp. on Comp. Semicond. (ISCS 2002); Lausanne, Switzerland, 7.-10. 10. 2002
65. W. Schrenk, S. Anders, C. Pflügl, E. Gornik, C. Becker, C. Sirtori, G. Strasser; "Room Temperature Operation Of GaAs/AlGaAs Quantum Cascade Lasers"; 29th Int. Symp. on Comp. Semicond. (ISCS 2002); Lausanne, Switzerland, 7.-10. 10.
66. G. Hobler, "Status and open problems in silicon implant damage modeling", 3rd Intl. Meeting Challenges in Predictive Process Simulation, Prague, Czech Republic, 13.-17.10.2002.
67. J. Darmo, T. Müller, G. Strasser, T. Le, G. tempea, and A. Stingl, " Photoconductive terhertz Emitter with an Integrated Semiconductor Bragg Mirror", 4th Int. Conf. on Advanced Semiconductor Devices and Microsystems (ASDAM 2002), Smolenice Castle, Slovakia, October 14-16, 2002, *J. Darmo, T. Müller, G. Strasser, T. Le, G. tempea, and A. Stingl, " Photoconductive terhertz Emitter with an Integrated Semiconductor Bragg Mirror", in Conference Proc. of 4th Int. Conf. on Advanced Semiconductor Devices and Microsystems, Editors: J. Breza and D. Donoval (IEEE, Piscataway 2002) pp. 179-182.*
68. R. Ascazubi, O.C. Akin, T. Zaman, R. Kersting, G. Strasser; "Scattering and dephasing in semiconductor heterostructures"; MRS (Material Research Society) Fall Meeting 2002, Boston, USA, 2.-6.12.2002
69. C. Kranz, E.L. Heintz, B. Mizaikoff, A. Lugstein, E. Bertagnolli, "Simultaneous Surface Modification and Imaging with Integrated Scanning Electrochemical/Atomic Force Microscopy",53rd Pittsburgh Conference (PITTCON), Pittsburgh 2002
70. G. Steinlesberger, M. Engelhardt, G. Schindler, W. Steinhögl, A. von Glasow, K. Mosig, E. Bertagnolli, "Electrical Assessment of Copper Damascene Interconnects Down to Sub 50 nm Feature Sizes", submitted to MAM 2002 (Materials for Advanced Metallization) in Vaals (Netherlands) 2002.

Doctor's Theses

1. D.I. Reinhard Zobl, "Far-Infrared Emission From Plasmons In Semiconductor Quantum Structures", March 2002
2. Dipl. Phys. Jochen Ulrich, "Longwavelength Quantum Cascade Lasers", March 2002

3. Mag. Wolfgang Fischler, “Zeitaufgelöste Pump-Probe-Spektroskopie an GaAs/AlGaAs-Halbleiterstrukturen”, Dezember 2002

Diploma works

1. Gernot Fasching, “Untersuchung der Elektron-Phonon-Wechselwirkung mittels ballistischer Elektronenspektroskopie”, Jänner 2002
2. Wolfgang Parz, “Intersubband Relaxation Dynamics in Quantum Structures”, September 2002
3. Johann Kreuter, “Long wavelength GaAs/AlGaAs quantum cascade lasers with low-loss waveguide”, Dezember 2002

Cooperations

1. Universität Linz, G. Bauer, W. Heiss, F. Schäffler, L. Palmetshofer, W. Jantsch
2. Universität Wien, H. Kauffmann, G. Kresse
3. TU Wien, H. Hutter, P. Pongratz, G. Lendl
4. Universität für Bodenkultur Wien, U.Sleytr, D. Pum
5. Montanuniversität Leoben, F. Kuchar
6. AMS-Unterbremstätten, H.Enichlmair, K. Tschernay F. Unterleitner
7. Philips Consumer Electronics, E. Kaun
8. Femtolasers, Wien, A. Stingl
9. High Q Laser, Hohenems, Dr. D. Kopf
10. NMP, Weiz, M. Schatzmeier
11. Siemens AG, E. Wolfgang, G. Sölkner, W. Maurer, A. Felder, Deutschland
12. Infineon München, M. Stecher, W. Stadler, Deutschland
13. ATMEL, Heilbronn, M. Graaf, Deutschland
14. TU-München, G. Abstreiter, P. Vogl, Deutschland
15. Universität Regensburg, W. Wegscheider, Deutschland
16. Friedrich-Schiller-Universität Jena, K. Gärtner, Deutschland
17. TU Braunschweig, D. Schneider, Deutschland
18. Forschungszentrum Jülich, P. Kordos, Deutschland
19. Technische Universität Berlin, A. Wacker, Deutschland
20. Heinrich Hertz Institut, Berlin, H. Künzel, Deutschland
21. Paul Drude Institut, Berlin, H. Grahn, Deutschland
22. Universität Bremen, D. Hommel, Deutschland
23. Forschungszentrum Rossendorf, Dresden, M. Helm, Deutschland
24. Bosch, Reutlingen, W. Wilkening, Deutschland
25. XFAB, Erfurt, C. Foss, Deutschland
26. IZM Frauenhofer Institut, München, H. Grieser, Deutschland
27. Centre National de la Recherche Scientific, Laboratoire de Microstructures et de Microelectronique, B. Etienne, Cedex, Frankreich

28. Thales, Orsay , H. Page, D. Corbin, Frankreich
29. Universite Paris Sud, F. Julien, Frankreich
30. Universite Paris 7, C. Sirtori, Frankreich
31. AMIS, Mietec, K. Reynders, Belgien
32. Interuniversity Microelectronics Center (IMEC), Leuven, Belgien
33. Ioffe Physico-Technical Institute, St. Petersburg, Y. Ivanov, Rußland
34. Sub-Micron Center, Weizmann Institute, Rehovot, M. Heiblum, Israel
35. Avant! Corp., V. Moroz, USA
36. Univ. of California, Lawrence Berkeley Laboratories, E. E. Haller , USA
37. Univ. of California, Los Angeles, S. Prussin, USA
38. Univ. of California, Santa Barbara, J. Allen, A. Gossard, USA
39. Columbia University, New York, H. Störmer, USA
40. Princeton University, S. Lyon, USA
41. IBM Fishkill, C.S. Murthy, USA
42. Lucent Technologies, C. Gmachl, USA
43. Boston College, Boston, MA, K. Kempa, P. Bakshi, USA
44. EPI MBE Components, St. Paul, Minnesota, USA
45. Univ. Osaka, C. Hamaguchi, Japan
46. Univ. Nagoya, N. Sawaki, Japan
47. RIKEN, K. Ishibashi, Japan
48. Herriot Watt University, Edinburgh, C. Pidgeon, Schottland
49. Univ. Glasgow, C. Ironside, Schottland
50. Imperial College, London, C. Phillips, England
51. Univ. Leeds, M. Chamberlain, England
52. University of Sheffield, M. Skolnick, J. Coburn, England
53. University of Surrey, B.N. Murdin, England
54. INFM-SNS Pisa, F. Beltram, Italien
55. TASC Trient, L. Sorba, Italien
56. Universita Bari, G. Scamarcio, Italien
57. STMicroelectronics, A. Andreini, Italien
58. Technische Universität Delft, Wenckebach, Holland
59. University Neuchatel, J. Faist, Schweiz
60. EPFL Lausanne, M. Ilegems, Schweiz
61. ETH Zürich, W. Fichtner, Schweiz
62. Orbisphere Semiconductor Lasers, Schweiz
63. Alpes Lasers, Neuchatel, A. Müller, Schweiz
64. Slovak Academy of Sciences, Bratislava, Slowakei

New Generation of Photoconductive Terahertz Emitters

J. Darmo, G. Strasser, T. Müller, T. Roch, K. Unterrainer

Institute for Solid State Electronics, Vienna University of Technology

A photoconductive Terahertz (THz) emitter based on low-temperature-grown GaAs and integrated with Bragg mirror is presented. The emitter exhibits improved terahertz emission efficiency due to the increased pumping light absorption in the Bragg mirror assisted resonant cavity, due to spatial confinement of the photocurrent, and due to optimized photoconductive response.

Introduction

The generation of few-cycle Terahertz radiation into the free space from a biased photoconductive gap illuminated by an ultrashort laser pulse is known more than a decade [1]. Since then, many attempts were presented to increase the generated THz power without compromising the radiation bandwidth [2], [3].

In this contribution, we report on a low-temperature-grown GaAs (LT GaAs) based photoconductive THz emitter integrated with a Bragg mirror. This design improves the generator's THz output power by about one order of magnitude. The optical resonance and the confinement of the photogenerated carriers in the high electric field region of the LT GaAs layer are responsible for the observed enhancement of the THz emission.

In addition, we have focused on optimization of the growth temperature of the LT GaAs layer with respect to a maximum photoresponse of the material and a maximum breakdown field. It is known that annealed LT GaAs changes its properties (resistivity, carrier lifetime) with the growth temperature. Our experiences from THz emission experiments suggest a decrease of the output THz power when the growth temperature is lowered. Therefore, we designed and tested a multilayer LT GaAs structure to increase the performance of the THz emitters.

Photoconductive THz Emitters

A low-temperature MBE GaAs layer grown at temperatures 220 – 350 °C and annealed in-situ at 600 °C (10 minutes) was used as photoconductive material. The modified THz emitter is made of a 326 nm thick LT GaAs grown directly on a Bragg mirror (Fig. 1). The Bragg mirror itself consisted of 30 pairs of $Al_{0.2}Ga_{0.8}As$/AlAs layers designed for a center wavelength of 800 nm. As reference emitter, a 2 µm thick LT GaAs layer was used grown directly on a high resistive GaAs (100) substrate. Electrical contacts to the LT GaAs layers were made of Ti/Au metal and had the shape of coplanar striplines (20 µm wide and separated by a gap of 300 µm (Fig. 1)). The same contact shape was used also for the reference THz emitter structure made of the semi-insulating GaAs. The emitter chips were mounted onto a highly resistive silicon aplanar extended hemisphere lens to efficiently couple the generated THz radiation into free space.

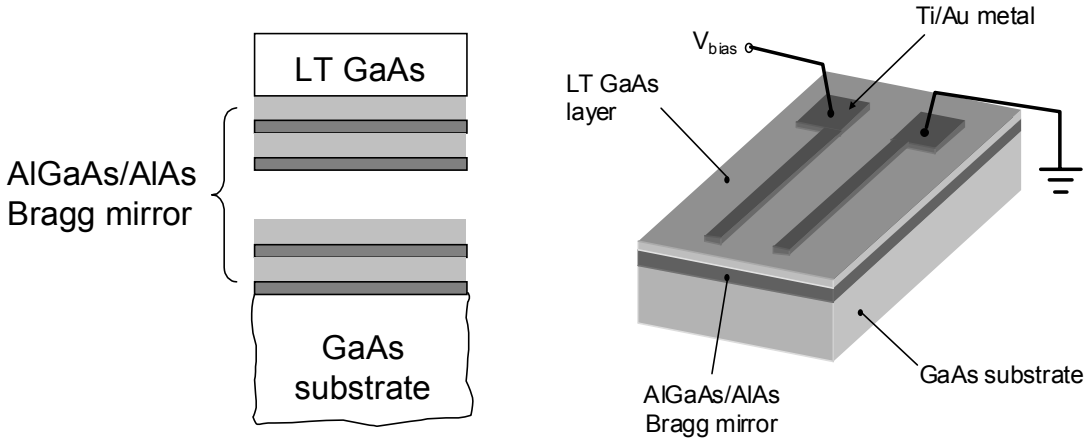

Fig. 1: Schematic of the photoconductive THz emitter.

To access the photoresponse of the LT GaAs layers grown at various temperatures, we used the attenuated unfocused laser beam from a Ti:sapphire laser to homogeneously illuminate the area between the electrodes of the emitter structures. In this configuration, the measured DC photocurrent depends on the lifetime and mobility of the photogenerated charge carriers. As expected, the lagest photocurrent was observed for the emitter structure made of semi-insulating GaAs, a material with the highest carrier lifetime-mobility product (Fig. 2). All structures involving LT GaAs exhibited much lower photocurrent with clear monotonic decrease with decreasing growth temperature.

To compare the emitters with respect to their THz emission efficiency, we have excited the emitter structures with pulses from a *fs* Ti:sapphire oscillator. The repetition rate was 76 MHz and the average excitation power reached about 250 mW. The emitted THz beam was collimated and then focused by a set off-axis parabolic mirrors onto an electro-optic sensor.

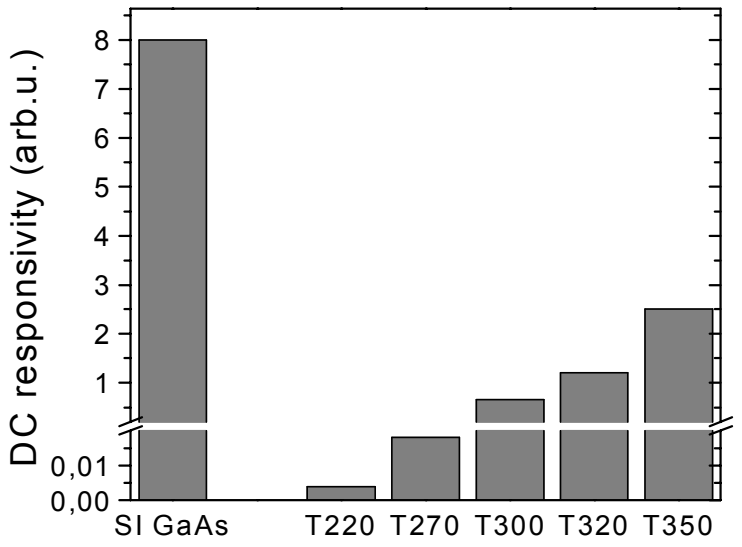

Fig. 2: Photoresponse of the THz emitters.

Figure 3 shows the bias dependence of the amplitude of the THz transients for emitters made of semi-insulating GaAs, a 2 µm thick LT GaAs grown at 220 °C, and a 328 nm thick LT GaAs grown at 220 and 320 °C on the Bragg mirror. The steepest rise of the THz emission with emitter bias was observed for the structure made of semi-insulating GaAs, however, the structure exhibits early breakdown at about 130 V related to heating by the photocurrent. On the other hand, the emitter structure made of 2 µm thick low-temperature GaAs grown at the lowest temperature of 220 °C on semi-insulating GaAs exhibits the weakest increase of the THz radiation with bias. The THz amplitude increases linearly with the applied bias up to 260 V. At biases above 260 V the THz amplitude begins to saturate or even decreases because of Joule heating of the emitter. A heating related device failure is observed for long time operation at these biases. The structure breakdown occurs at biases above 280 V. The lowest THz generation efficiency well correlates with the weakest photoresponse observed for this type of THz emitter (see Fig. 2) and is due to the short lifetime of photogenerated charge carriers and low mobility.

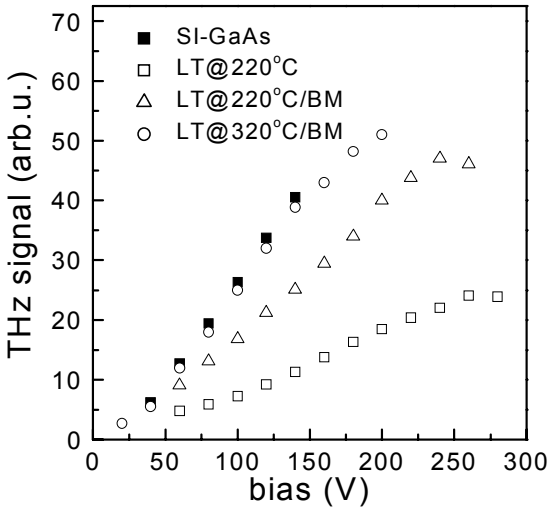

Fig. 3: THz emitter output power as a function of bias.

The emitters based on thin LT GaAs grown on a Bragg mirror exhibit much higher THz generation efficiency in comparison to that based on thick LT GaAs. The presence of the Bragg mirror leads to a doubled THz signal from the same LT GaAs material. The main enhancement is ascribed to the effect of the resonance cavity created by the Bragg mirror, the LT GaAs layer, and the air/GaAs interface. The calculation of the performance of this optical system yields an increased absorption in the LT GaAs [6]. Finally, when we have chosen a LT GaAs material providing a maximum photoresponse (see Fig. 2), the THz generation efficiency has reached a level comparable to that of semi-insulating GaAs. However, the breakdown voltage is higher and so the maximum reachable THz output power. At a bias of 200 V and for an excitation pulse energy of 2.5 nJ the maximum the THz output power was estimated to be 3.8 µW.

Conclusion

The performance of photoconductive antenna THz emitters based on epitaxial GaAs grown at different temperatures on an AlGaAs/AlAs Bragg mirror is presented. The growth occurred at temperatures between 220 and 350 °C. The maximum output THz power was observed for a growth at a temperature of about 320 °C. Moreover, the

resonant cavity effect as well as the effective optical and electrical isolation of the photoconductive layer from the substrate by the Bragg mirror leads to an enhancement of the optical-to-THz conversion efficiency. A photoconductive THz emitter with such a design was recently successfully used as an intra-cavity THz generator in a *fs* oscillator [7].

References

[1] Grischkowsky, D., Keiding, S., van Exter, M., and Fattinger, C.: *J. Opt. Soc. Am. B* **7**, 1990, pp. 2006-2015.

[2] Darrow, J.T., Zhang, X.-C., Auston, D.H., and Morse, J.D.: *IEEE J. Quantum Electron.*, **28**, 1992, pp. 1607-1616.

[3] Cai, Y., Brener, I., Lopata, J., Wynn, J., Pfeiffer, L., and Federici, J., *Appl. Phys. Lett.* 71, 1997, pp. 2076-2078.

[4] Wu, Q. and Zhang, X.-C.: *Appl. Phys. Lett.* **68**, 1996, pp. 1604-1606.

[5] Kersting, R., Unterrainer, K., Strasser, G., Kaufmann, H.F., and Gornik, E.: *Phys. Rev. B* **58**, 1998, pp. 4553-4559.

[6] Darmo, J., and Tempea, G.: unpublished.

[7] Darmo, J., Müller, T., Strasser, G., Unterrainer, K., Le, T., Stingl, A., and Tempea, G.: *Optics. Lett.* **27**, 2002, pp. 1941-1943.

Quantum Cascade Lasers

W. Schrenk, S. Anders, C. Pflügl, E. Gornik, G. Strasser

Institute for Solid State Electronics, Vienna University of Technology

In this work, we intend to present our latest results on the improvement of GaAs/AlGaAs QCLs. The emission wavelength of the mid infrared lasers covers now a range from 8.7 µm up to 23 µm. Room temperature operation is now achieved for several band structure designs.

Introduction

Quantum cascade lasers (QCLs) are powerful light emitters in the mid infrared and, most recently, also in the far infrared [1]. The light generation is based on intersubband transitions, usually within the conduction band. The strong light emission in the mid infrared spectral region is interesting for chemical sensing, and a potential application for far infrared emission is astronomy and tomography in medicine. Recently, continuous wave operation at room temperature of InP based QCLs has been demonstrated [2].

Theory

The design of the band structure of quantum cascade lasers is a challenging task. The population of the individual levels is determined by different scattering processes like electron-electron scattering, LO-phonon emission or absorption, and photon emission or absorption. The population of the energy levels together with the position of the doping atoms modifies the band edge energy. Almost all laser structures are designed so far by very simple one-band calculations, based on an effective mass approximation. The band structures are calculated neglecting the electron population and assuming a constant electric field across each cascade. The non-parabolicity of the energy dispersion is taken into account by an energy dependent effective mass [3]. Only for a few designs more sophisticated calculations were done afterwards, because they are too time consuming to be used as design tool [4], [5].

The advantage of AlGaAs/GaAs grown on GaAs over InGaAs/InAlAs grown on InP is that the $Al_xGa_{1-x}As$/GaAs material system is lattice matched to GaAs for all Al contents x. The Al-content of QCLs working at room temperature in pulsed operation is x=0.45. The emission wavelength of these lasers is in the range of 9 µm [6], [7] up to 12.6 µm [8]. The barrier height in respect to the GaAs wells is 390 meV, large enough to prevent carrier escape into the continuum. In the case of a longer emission wavelength, a lower Al-content is preferred in order to obtain a reasonable thickness of at least one monolayer for the thinnest barrier. Another advantage of GaAs is the far infrared performance. Undoped InP substrates have a rather high background doping which causes free carrier absorption.

The band structure of a chirped superlattice design is shown in Fig. 1 [8]. The laser transition takes place between the lowest level of the second miniband and the highest level of the first miniband. The optical matrix element is large but the total lifetime in the upper laser level is short as LO phonon emission is possible to many final states in the first miniband. In the case of a three well design [6], fewer levels are below the upper laser level, and therefore the total lifetime in the upper laser level is longer. A drawback

of the three well design is the lower optical dipole matrix element in comparison to a chirped superlattice design and the slower carrier extraction form the lower laser level.

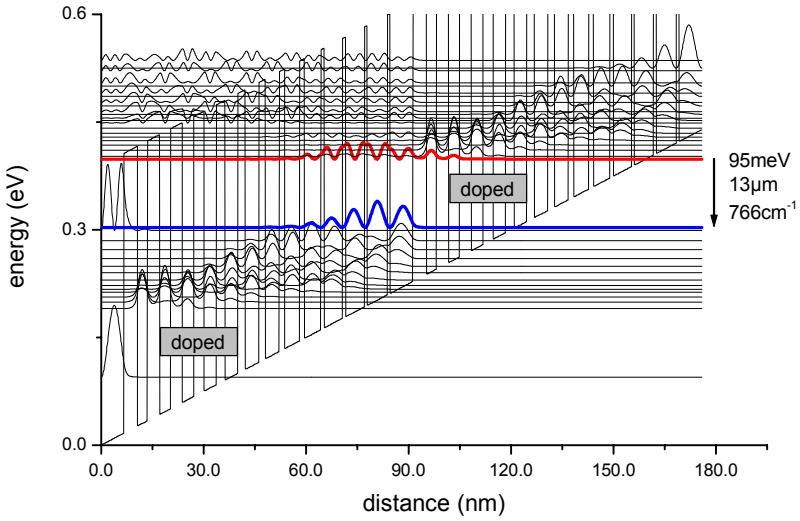

Fig. 1: Calculated conduction band diagram and squared wave functions of a chirped superlattice design for emission at 13 µm wavelength.

Experimental

Sample Preparation

The laser material is grown by molecular beam epitxy on (100) GaAs substrates. The gain media is embedded in the most cases in a double plasmon enhanced waveguide. Such a waveguide consists of ~1 µm thick highly doped cladding layers (~4x10^{18} cm^{-3}), and ~3.5 µm thick low doped spacer layers (~4x10^{16} cm^{-3}). The highly doped layers are used for light confinement and the spacer layers reduce the penetration of the guided mode into the cladding layers as they show huge free carrier absorption. A surface plasmon waveguide [9] is usually used for long wavelength material (λ > 20 µm) because of the reduced thickness, which is important for MBE growth.

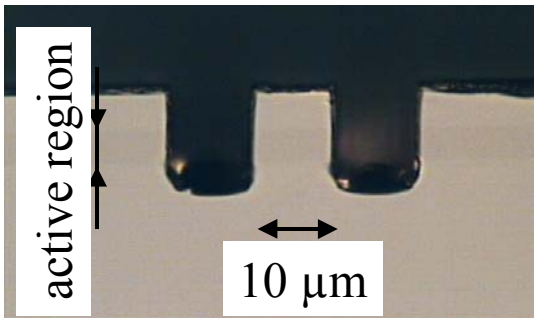

Fig. 2: Image of a laser facet of a 10 µm wide FP laser. The trenches are etched by reactive ion etching.

Different cavity types such as Fabry Perot (FP), distributed feedback (DFB), and cylinder lasers were fabricated. Reactive ion etching was used for directional etching to obtain vertical etch profiles (Fig. 2). SiN is used for insulation and the extended contacts are sputtered. The grating for the DFB lasers was etched into the surface of the top cladding layer and covered with metal. The light is confined by total internal reflection in the case of cylinder shaped lasers. The lasers were soldered with In on Cu plates and wire bonded.

Measurements

Spectral measurements were performed with a Fourier Transform Infrared (FTIR) spectrometer. The absolute light power was measured with a thermopile detector, and the optical power versus current curves were measured in some cases with a DTGS detector or LN_2 cooled MCT detectors, depending on the optical power. Typical operation conditions are 100 ns long pulses and repetition rates in the order of 5 kHz up to several MHz. Pulsed room temperature operation (Fig. 3) was achieved for three different design strategies, a three well design [6], a chirped superlattice design [8], and a bound to continuum design. A bound to continuum design combines the advantages of the three well design and the chirped superlattice and allowed pulsed operation up to 100°C.

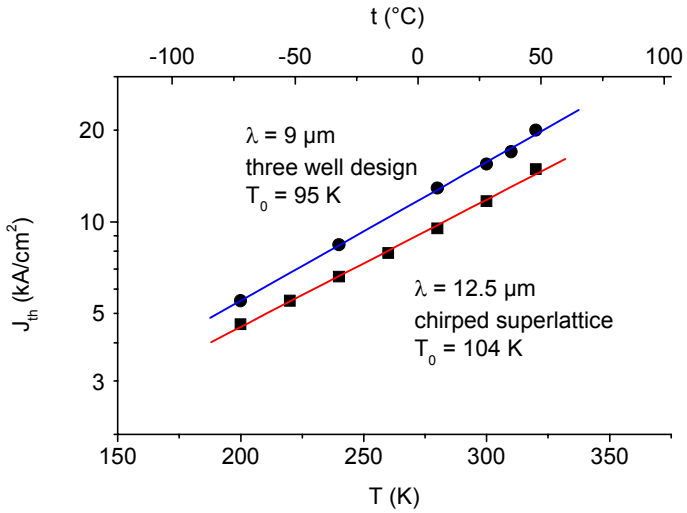

Fig. 3: Threshold current density of cylinder lasers as a function of the heat sink temperature for a three well design (circles) and a chirped superlattice (squares). The lines are fits of the characteristic temperature T_0 ($J_{th} = J_0 \exp(T/T_0)$).

Acknowledgements

This work was supported by the European Community-IST Project SUPERSMILE, and the Austrian FWF (ADLIS).

References

[1] R. Köhler, A. Tredicucci, F. Beltram, H. E. Beere, E. H. Linfield, A. G. Davies, D. A. Ritchie, R. Iotti, F. Rossi: “Terahertz heterostructure laser”, Nature, vol. 417, 2002, pp. 156–159.

[2] M. Beck, D. Hofstetter, T. Aellen, J. Faist, U. Oesterle, M. Ilegems, E. Gini, H. Melchior: “Continuous Wave Operation of a Mid-Infrared Semiconductor Laser at Room Temperture”, Science, vol. 295, 2002, pp. 301–305.

[3] C. Sirtori, F. Capasso, J. Faist, S. Scandolo: “Nonparabolicity and sum rule associated with bound-to-bound and bound-to-continuum intersubband transitions in quantum wells”, Phys. Rev. B, vol. 50, 1994, pp. 8663–8674.

[4] R. Iotti, F. Rossi: “Nature of Charge Transport in Quantum-Cascade Lasers”, Phys. Rev. Lett., vol. 87, 2001, pp. 146603-1–146603-4

[5] A. Wacker, S. C. Lee: “Gain and loss in quantum cascade lasers”, Physica B, vol. 314 (1-4), 2002, pp. 327–331.

[6] H. Page, H. Page, C. Becker, A. Robertson, G. Glastre, V. Ortiz, C. Sirtori: “300 K operation of a GaAs-based quantum-cascade laser at □≈9 μm”, Appl. Phys. Lett., vol. 78, 2001, pp. 3529–3531.

[7] W. Schrenk, E. Gornik, H. Page, C. Sirtori, V. Ortiz, G. Strasseri: “High performance single mode GaAs quantum cascade lasers”, Physica E, vol. 13, 2002, pp. 840–843.

[8] S. Anders, W. Schrenk, E. Gornik, G. Strasser: “Room-temperature emission of GaAs/AlGaAs superlattice quantum-cascade lasers at 12.6 μm”, Appl. Phys. Lett., vol. 80, 2002, pp. 1864–1866.

[9] J. Ulrich, J. Kreuter, W. Schrenk, G. Strasser, K. Unterrainer: “Long wavelength (15 and 23 μm) GaAs/AlGaAs quantum cascade lasers”, *Appl. Phys. Lett.,* vol. 80, 2002, pp. 3691–3693.

Modification of the Photoresponse by Energy Level Engineering in InAs Quantum Dot Nanostructures

F.F. Schrey, L. Rebohle, T. Müller, S. Anders, W. Schrenk, K. Unterrainer and G. Strasser

Institute for Solid State Electronics, Vienna University of Technology

We design the energy structure and the absorption properties of infrared photodetectors based on the combination of quantum dots structures with a surrounding superlattice. By embedding vertically coupled or decoupled quantum dots in a two-dimensional superlattice, the advantages of self-organized growth and band structure engineering can be combined. The transition energies and the form of the transition peaks between the dot levels and the extended states of the superlattice can be adjusted by the period of the superlattice and the dot alignment. We use this scheme in photodetectors made of InAs quantum dots embedded in an AlAs/GaAs superlattice. Besides the reduced dark current compared to devices without a superlattice we can demonstrate clear advantages of vertically coupled dot stacks compared to uncoupled dots in this application.

Introduction

InAs and InGaAs quantum dot (QD) ensembles embedded in GaAs matrices or GaAs quantum well structures offer remarkable properties for fast and efficient optoelectronic devices such as NIR lasers [1]. The energy spacing of electronic states coupled with efficient electron capture capabilities into these discrete states predestine dots to be used as MIR photodetectors and emitters. In contrast to subband transitions in two-dimensional structures, the density of states is peaked at the transition energy, which reduces the phase space for scattering. Thus, QD structures are expected to provide higher photocurrents and lower dark currents than quantum well structures due to the longer lifetime of the excited states [2], [3].

The infrared photoresponse of InAs dots embedded in GaAs was investigated very recently [4] – [9], and transition energies between the dot ground state and the GaAs conduction band were found in the range of 80 to 400 meV. In some cases the existence of the first excited dot state [4] or even higher excited states [6] could be observed. It was also shown that the electronic states within the QD and thus the emission or absorption energies can be tuned by changing the InAs dot size [10]. Further methods to lift the energy levels of the InAs QDs is the incorporation of an AlAs layer close to the QDs [11] or the confinement in an $Al_xGa_{1-x}As$ matrix causing a higher conduction band offset to InAs [12].

In this paper we demonstrate that band gap engineering combined with vertical dot alignment allows tailoring of transition and ionization energies as well as absorption properties for mid-infrared (MIR) and far-infrared (FIR) photodetectors. Because the band structure of the minibands in the superlattice (SL) is not, or only slightly, altered by the embedded QDs, their properties can be tuned independently from each other. While the dot properties are modified by their growth conditions, the SL band structure can easily be estimated by solving the one dimensional Schrödinger equation numerically.

Experimental

The basic device structure and a band structure scheme in growth direction are given in Fig. 1 (a). The devices were grown at 485 °C on a semi-insulating GaAs(001) substrate by molecular beam epitaxy. Three multiple dot (MD) device structures – denoted as MD-A, MD-B and MD-C in the following – were designed, grown and characterized. Device MD-A consists of periodically arranged InAs QD layers, which are spaced by a 10 nm thick GaAs matrix. As shown in [8], this thickness is thin enough to cause a vertical alignment of the QDs due to their strain distribution. Device MD-B is additionally provided with 1 nm thick AlAs barriers at a distance of 1 nm from the QD layer resulting in a SL period of 11 nm and an increase of the absorption energy in comparison with device MD-A. The SL period of MD-C is 14 nm. Single dot (SD) and double dot (DD) devices were fabricated by growing one (SD) or two (DD) SL periods under the same conditions as device MD-B. These layers are followed by 2 SL periods without QD layers preventing the vertical alignment of the QDs. This sequence is repeated several times in such a way that the total number of QD layers in all devices is 20 or 30 (only MD-A).

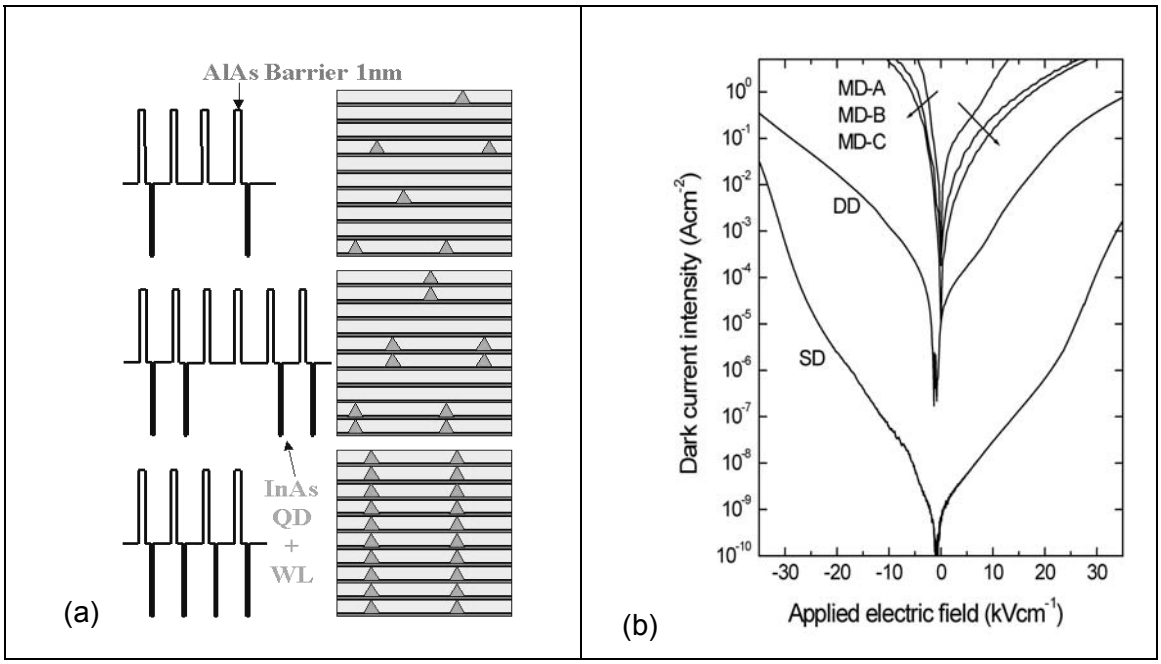

Fig. 1: (a) Device structure; (b) Comparison of dark current behavior.

For characterization of the devices, we performed photoluminescence (PL), photocurrent (PC), and current-voltage (IV) measurements in a LHe flow cryostat system. For the PC measurements, the devices were processed into mesas and provided with a back and front contact made of a thermally alloyed Ni/Ge/Au layer. The spectral photoresponse of the devices is measured in a standard FTIR spectrometer with a glow-bar infrared source.

Results and Discussion

The PL spectra of MD devices at 5 K shown in Fig. 2 are characterized by a PL peak at 1072, 1105, and 1100 meV for device MD-A, MD-B and MD-C, while there is a considerable and continuous shift of the PL peak energy to higher energies in the order of device MD-B, DD and SD in Fig. 2. In the first group, the peak is believed to be due to an electron-hole recombination between the heavy hole and electron ground state of

the QD. The second PL feature at higher energy, which is dominant in the second group, is attributed to higher excited states of the dot ensembles.

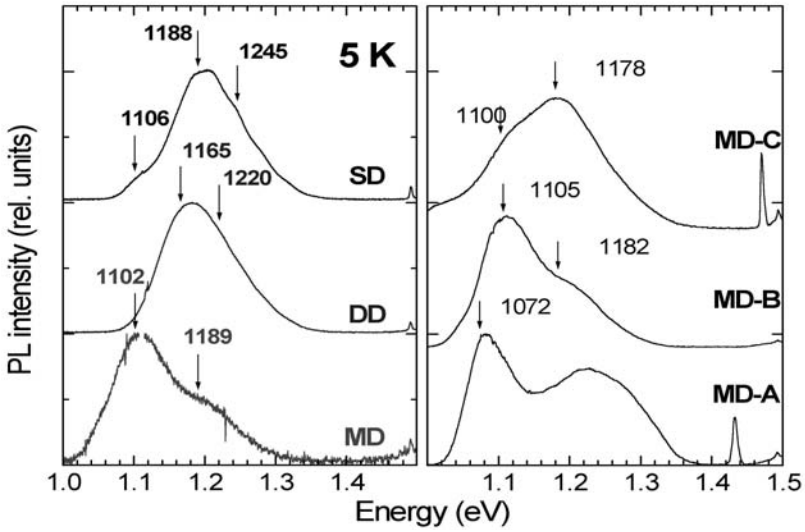

Fig. 2: Photoluminescence spectra of the different device structures.

PC spectra of MD devices at 4 K in Fig. 3 (a) are characterized by a single main peak at around 225 meV (device MD-A, MD-C) and at 247 meV (device MD-B). The full width at half maximum (FWHM) of these peaks amounts approximately to 13, 16 and 11 meV for device A, B and C, respectively. These peaks are assigned to the transition from the dot ground state to the continuum (device A) or to the first miniband of the SL (device B, C). Without vertical coupling of the QDs the situation becomes more complex and several PC peaks in the energy range between 170 and 320 meV can be observed (Fig. 3 (b)). It should be noted that the energy region between 190 and 200 meV is obscured by water absorption lines.

The IV characteristics of the devices at 4 K in Fig. 1 (b) show an asymmetric diode-like behavior. The dark current for the MD devices decreases by one order of magnitude from MD-A to MD-C. A larger decrease of the dark current is even seen in the order of MD-B, DD and SD.

The experimental results are used in the following to reconstruct the energy level scheme of the devices. In the following the heavy hole and electron ground state of the InAs QD are denoted as HH0 and E0, whereas the first excited electron state of the InAs QD and the first miniband of the AlAs SL is indicated with E1 and MB1, respectively.

According to the measurements an energy spacing of 1072 meV between HH0 and E0 and of 224 meV between E0 and the GaAs conduction band (CB) has been found for device MD-A. Although the dot growth conditions are the same for all devices, an enhanced energy spacing of 1105 meV between HH0 and E0 is observed for device MD-B in the PL measurement.

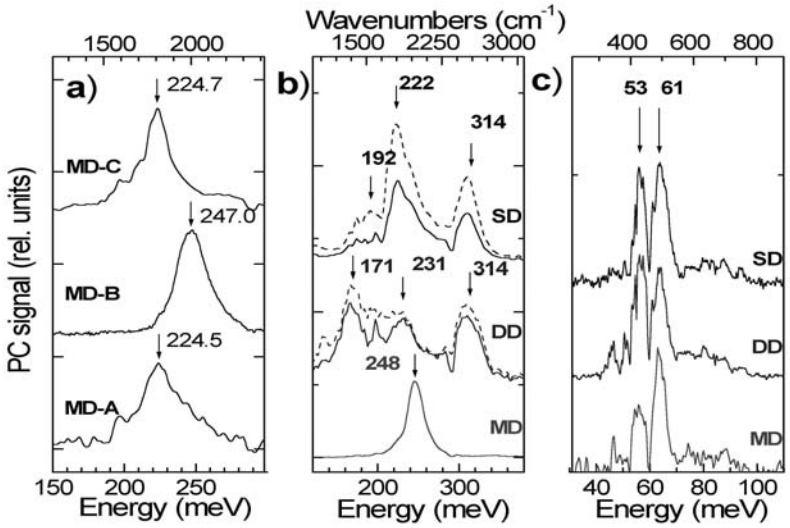

Fig. 3**:** Photocurrent spectra for the MIR region (a) and (b): (c) PC in the FIR region.

In [13] the calculated energy spacing for this transition is blue shifted if the dots are grown close to an AlAs barrier. As a result, the HH0→E0 transition energy increases by 33 meV in our sample. Because of the considerably heavier hole mass, we suppose in a first rough approximation, that the HH0 state remains nearly unchanged, and that the E0 state is lifted by the whole amount of 33 meV [14]. The energy of 247 meV obtained from PC measurements for the E0→MB1 transition can be now split into an energy of 191 meV for the distance E0→CB and an energy of 56 meV for the distance CB→MB1. The position of MB1 was calculated to expand between 48.6 and 53.2 meV above the CB.

The larger SL period of device MD-C lowers and narrows MB1, which now extends between 30.1 and 32.3 meV above the CB. The PC peak at 225 meV leads directly to the experimental value of 29 meV for the CB→MB1 transition. This value and the decrease of the width of the PC peak are in good correspondence with our theoretical prediction. Because of the SL the dark current in MD-C has been decreased by more than one order of magnitude (Fig. 1 (b)) compared to MD-A.

Without or with reduced vertical alignment the description becomes more complicated. Now three different cases have to be distinguished: a SL period without an InAs wetting layer, a SL period with a wetting layer, and a SL period with QD and wetting layer. Additionally to the MB1 in the first case, the wetting layer introduces a ground and first excited state WL0 and WL1. The split up of the former MB1 position in the case of DD and SD devices now enables several transitions to become likely, in good agreement with Figs. 3 (b) and (c). Unfortunately, the rough approximation to describe the QDs by thin quantum wells in our calculation does not allow a quantitative prediction of the PC peak energies in these devices.

The decrease of the dark current can easily be explained by the tunneling behavior of the electrons within the CB or MBs of the materials. Introducing AlAs barriers, the electrons have now to tunnel through the SL structure. Increasing the SL period leads to a decrease of the MB1 energy; thus, the relative barrier height for the electron is increased and the dark current decreases.

The suitability of the various device architectures for infrared photodetectors should be briefly discussed. In comparison with SD and DD devices, there is a clear preference for MD devices. Although SD and DD devices feature an extremely low dark current, their PC spectrum is complex, difficult to predict and of comparatively low intensity. In

contrast, the PC spectra of MD devices are characterized by an intense single peak, whose position can be designed by changing the SL parameters. Even with the crude approximation of a one-dimensional structure and the neglect of strain influences, this peak position can be calculated quite well.

Conclusion

In summary, we present an advanced method to design QD based devices by combining the self-organized growth of QD with band gap engineering. The spectral response was modified by changing the transition energy from the QD ground state to the lowest miniband of the SL. In comparison with isolated QDs, QD stacks are preferable concerning the PC intensity and the possibility to design the spectral dependence of the infrared absorption.

Acknowledgements

We would like to acknowledge the financial support by Gesellschaft für Mikroelektronik (GMe), the Austrian Science Foundation FWF (SFB ADLIS, START Y47) and the European Community-IST project SUPERSMILE.

References

[1] D. Bimberg, N. N. Ledentsov, N. Grundmann, N. Kirstaedter, O. G. Schmidt, M. H. Mao, V. M. Ustinov, A. Y. Egorof, A. E. Zhukov, P. S. Kopev, Z. I. Alferov, S. S. Ruvimov, U. Goesele, and J. Heydenreich, Phys. stat. sol. (b) 194, 159 (1996).

[2] U. Bockelmann and G. Bastard, Phys. Rev. B 42, 8947 (1990).

[3] J. Urayama, T.B. Norris, J. Singh, and P. Bhattacharaya, Phys. Rev. Lett. 86, 4930 (2001).

[4] L. Chu, A. Zrenner, G. Böhm, and G. Abstreiter, Appl. Phys. Lett. 75, 3599 (1999).

[5] N. Horiguchi, T. Futatsugi, Y. Nakata, N. Yokoyama, T. Mankad, and P.M. Petroff, Jpn. J. Appl. Phys. 38, 2559 (1999).

[6] H.C. Liu, M. Gao, J. McCaffrey, Z.R. Wasilewski, and S. Fafard, Appl. Phys. Lett. 78, 79 (2001).

[7] S.F. Tang, S.Y. Lin, and S.C. Lee, Appl. Phys. Lett. 78, 2428 (2001)

[8] S. Hofer, H. Hirner, R. Bratschitsch, G. Strasser, and K. Unterrainer, Physica E 13, 190 (2002).

[9] S. Maimon, E. Finkman, G. Bahir, S.E. Schacham, J.M. Garcia, and P.M. Petroff, Appl. Phys. Lett. 73, 2003 (1998)

[10] L. Chu, M. Arzberger, G. Böhm, and G. Abstreiter, J. Appl. Phys. 85, 2355 (1999).

[11] J.S. Kim, P.W. Yu, J.Y. Leem, M. Jeon, S.K. Noh, J.I. Lee, G.H. Kim, S.K. Kang, J.S. Kim, and S.G. Kim, J. Appl. Phys. 91, 5055 (2002).

[12] K.W. Berryman, S.A. Lyon, and M. Segev, Appl. Phys. Lett. 70, 1861 (1997).

[13] M. Grundmann, O. Stier, and D. Bimberg, Phys. Rev. B 52, 11969 (1995).

[14] L. Rebohle, F.F. Schrey, S. Hofer, G. Strasser, K. Unterrainer, Appl. Phys. Lett. 81, 2079 (2002)

Electrically Pumped Quantum Cascade Ring Lasers

P. Schwaha, S. Anders, T. Roch, W. Schrenk, and G. Strasser

Institute for Solid State Electronics, Vienna University of Technology

Introduction

Circular cavities from a quantum cascade material have been investigated by several groups [1] – [3]. It is generally believed that light propagates as a whispering gallery mode in microcylinder or microdisk [4], [5] cavities. This implies that almost all of the light is at the periphery of the device and the centre of such a device should have little or no influence on the light field. Nevertheless, current will also flow through the centre region and provide gain, which is wasted due to the almost complete absence of a relevant light field. This was a motivation to remove the centre portion of microcylinders and thereby obtain a ring shaped laser cavity (as shown in Fig.1). It was expected that the threshold current required to achieve lasing would drop due to the decreased area of the device.

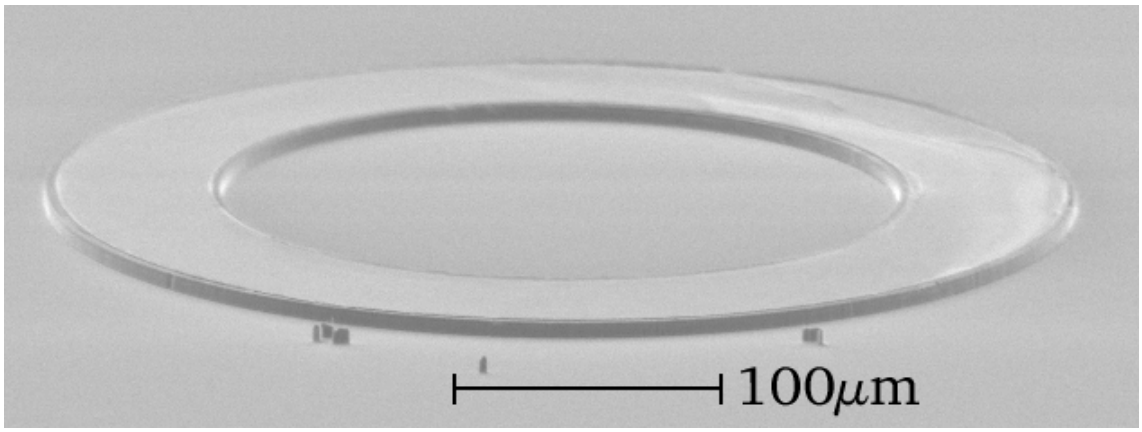

Fig. 1: Ring laser; the height of the laser is approximately 10 μm.

Experimental

The material from which the ring lasers were processed was grown by solid source molecular beam epitaxy. It is based on a three-well design quantum cascade structure. When processed as a standard ridge waveguide, this material functioned at least up to room temperature [6]. An x-ray-rocking curve (shown in Fig. 2) indicates that the actual period of the chosen material is about four percent less than the designed one, but also reveals the accurate periodicity. The deviation between the grown and the simulated period is only 1.8 percent. It thereby denotes the high quality of the material with regard to the cascaded structure and reproducible interfaces.

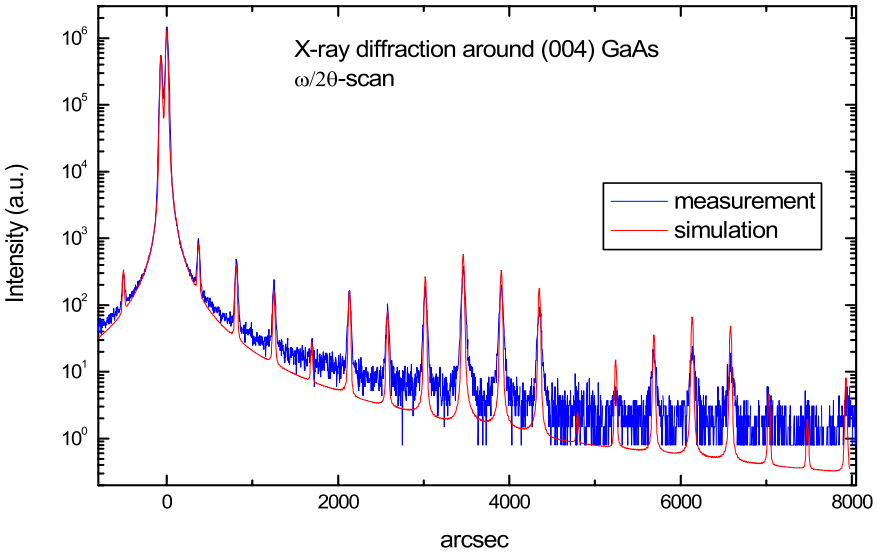

Fig. 2: X-ray-rocking curve.

The rings were processed using standard photolithography and reactive ion etching to achieve smooth and perpendicular sidewalls. These are considered critical for device operation, as deviations from a vertical sidewall will lead to deviations in the length of the optical path. Even small deviations suffice to degrade device performance. This would represent an additional loss mechanism in addition to standard wave-guide losses. Circular cavities that work above room temperature have already been demonstrated [7].

Rings with outer diameters of 200, 300 and 400 µm and various inner diameters were fabricated. Several measurements were conducted, including a temperature dependence of the emitted spectra of the rings (as shown in Fig. 3). It can clearly be seen that the emission wavelength shifts to lower wave numbers and thereby to lower energy as temperature is increased. The frequency shift per Kelvin is somewhat higher than for a Fabry-Perot laser made from the same material where it is in agreement with the temperature dependence of the index of refraction. Presumably, the relatively large shift in emission wavelength indicates an additional loss mechanism in the ring laser. Since the emission wavelengths at higher temperatures approach that of a Fabry-Perot laser from the same material, but shift to smaller wavelengths at lower temperatures, we infer that the additional loss mechanism is less dominant at higher temperatures. But not only the energy of the emitted light changes, but also the number of modes. We note that the number of lasing modes decreases as the temperature increases. This can be attributed to the fact that the lasing threshold increases with temperature and so the same current is not as far above the lasing threshold at different temperatures.

Figure 4 depicts spectra of several rings with a constant outer diameter and different inner diameters. The outer diameter is 400 µm and the inner diameters are varied between 240 and 320 µm in steps of 10 micrometers, with the exception that there is no ring with an inner diameter of 290 µm. The spectra have all been measured at the same temperature of 77 K. The modes are not regularly spaced as would be expected for whispering gallery modes of lowest order. Interestingly, the diameter of the hole influences the emission wavelengths of the lasers, such that the emitted light has a shorter wavelength with decreasing thickness of the ring.

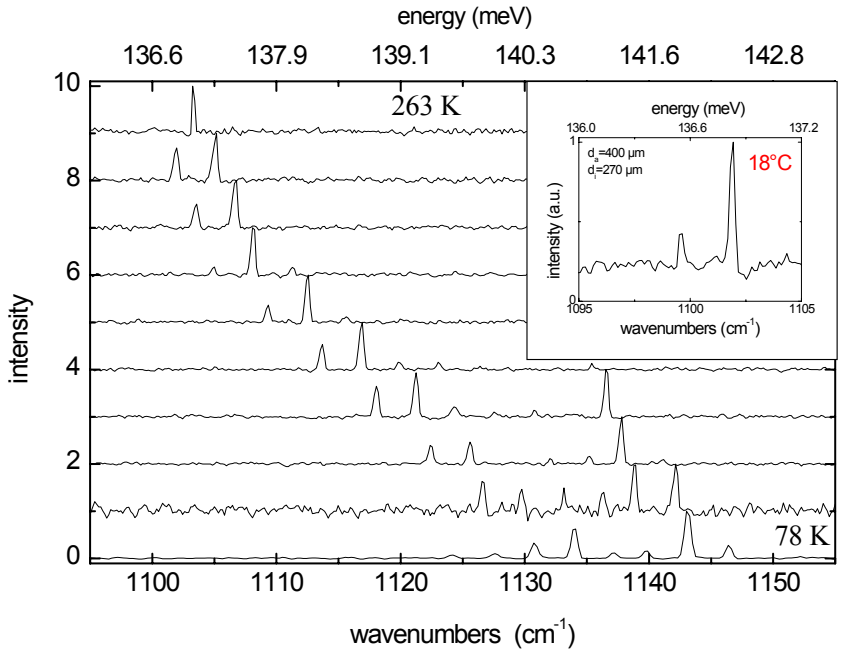

Fig. 3: Temperature dependence of emitted spectra. Temperatures are 78, 98, 118, 138, 158, 178, 198, 218, 238, and 263 K.

This is in contrast to previous assumptions that the light field should not enter the central region of the device and therefore should not be influenced by any changes in the centre section. Considering these facts, it seems necessary to reconsider the idea of whispering gallery modes within these devices.

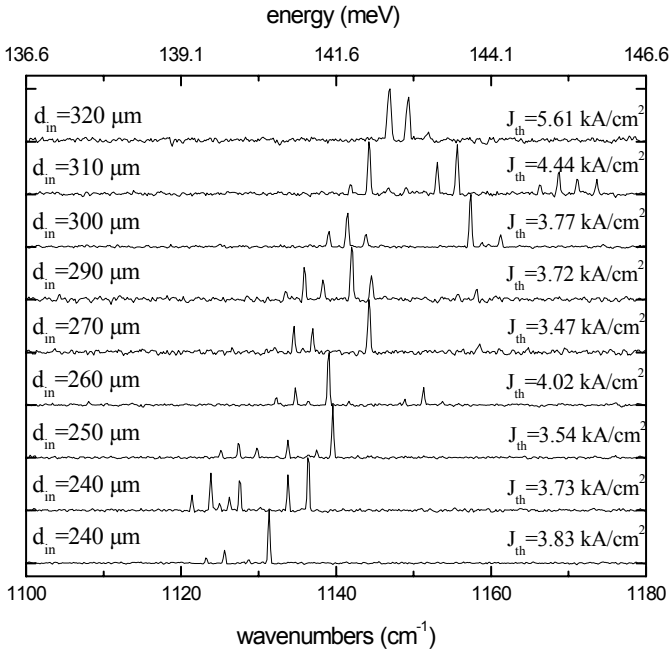

Fig. 4: Spectra of rings of different widths. The outer diameter was 400 µm; the inner diameters are as indicated.

Threshold current densities for the individual lasers are also indicated in Fig. 4. They show a tendency to increase as the inner diameter of the ring increases. We note that the shift in emission wavelength is not caused by a shift in threshold. The threshold current density scatters considerably more than the emission wavelength. Further, we checked that the envelopes of the spectra do not depend on the bias.

Conclusion

We manufactured electrically pumped quantum cascade ring lasers and characterised their optical properties. The emission wavelength was found to be sensitive to changes in the centre section of the device, which is in contrast to the general assumption that circular cavities dominantly support whispering gallery modes. Together with the observation of irregular mode spacing our results suggest that a different mode structure is preferred.

Acknowledgements

We would like to acknowledge the supported by the European Community-IST project SUPERSMILE and the Austrian FWF (ADLIS).

References

[1] J. Faist, C. Gmachl, M. Striccoli, C. Sirtori, F. Capasso, D. L. Sivco, and A. Y. Cho, Appl. Phys. Lett. 69, 2456 (1996).

[2] C. Gmachl, F. Capasso, E. E. Narimanov, J. U. Noeckel, A. D. Stone, J. Faist, D. L. Sivco, and A. Y. Cho, Science 280, 1556 (1998).

[3] S. Gianordoli, L. Hvozdara, G. Strasser, W. Schrenk, K. Unterrainer, and E. Gornik, Appl. Phys. Lett. 75, 1045 (1999).

[4] Y. Yamamoto and R. E. Slusher, Physics Today 46, 66 (1993).

[5] S. C. Hagness, D. Rafizadeh, S. T. Ho, and A. Taflove, Journal of Lightwave Technology 15, 2154 (1997).

[6] W. Schrenk, E. Gornik, H. Page, C. Sirtori, V. Ortiz, and G. Strasser, Physica E 13, 840 (2002).

[7] S. Anders, W. Schrenk, E. Gornik, and G. Strasser, Appl. Phys. Lett. 80, 4094 (2002).

Transport through Wannier-Stark States in Biased Finite Superlattices

M. Kast, C. Pacher, G. Strasser, E. Gornik

Institute for Solid State Electronics, Vienna University of Technology

Individual Wannier-Stark states are resolved in a direct current experiment over a wide electric field range for a 5 and 4 period finite superlattice. A hot-electron transistor is used to probe the transmittance of the superlattices at different bias conditions. The energy level positions are used to determine superlattice parameters with high accuracy. The basic transport through Wannier-Stark states is identified to be coherent. Individual transport channels induced by LO-phonon scattering are observed when the Wannier-Stark states spacing tunes into the optical phonon energy.

Introduction

In an unperturbed superlattice, the strong coupling of the electronic eigenstates of adjacent wells leads to the formation of minibands that are separated by minigaps. In superlattices with a finite number N of periods, each single miniband is formed by N eigenstates, which are delocalized over the whole superlattice length. Applying an external electric field perpendicular to the layer planes alters the quantum mechanical confinement between the neighbouring wells and leads to a splitting and a localization of the states, which are then given by the Wannier-Stark states. In transport experiments, there are two main problems to determine the Wannier-Stark splitting in a semiconductor superlattice: one is the presence of an inhomogeneous electric field unavoidable in two-terminal superlattice structures; the second is the electric field induced localization of the Wannier-Stark states. The localization length inside the superlattice is inversely proportional to the applied electric field, which leads to a quenching of the coherent hot electron transport through the individual Wannier-Stark states.

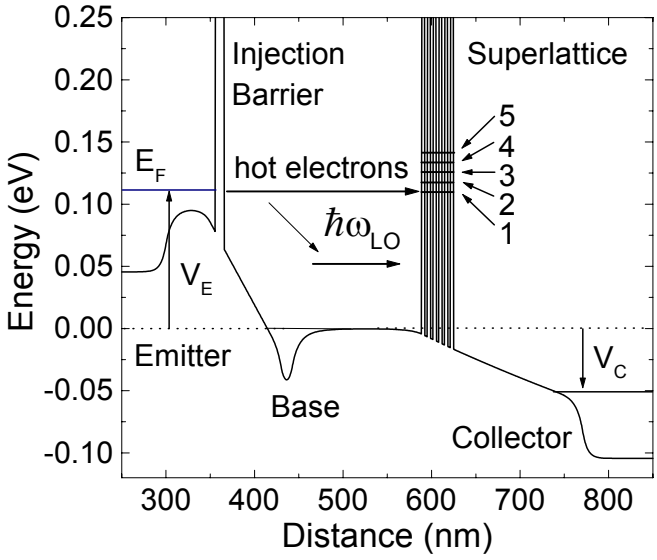

Fig. 1: Conduction band diagram of a hot-electron transistor in growth direction.

In this work, we use the concept of a hot-electron transistor [1] – [4] to study hot electron transport in undoped biased superlattices. The conduction band structure of the device is shown in Fig. 1. An energy tunable electron beam is generated at the tunneling barrier and reaches the superlattice after traversing a highly doped n-GaAs base layer and a slightly n-doped drift region. The static transfer ratio ($\alpha = I_c/I_e$) directly represents the probability of an injected electron to be transmitted through the superlattice. The three terminal device used in this work allows a tuning of the energy of the injected electron distribution independent of the electric field applied to the superlattice.

Experimental

Hot-electron transistors were designed with different undoped superlattice structures between base and collector. The first superlattice consists of 5 periods of 3.5 nm $Al_{0.3}Ga_{0.7}As$ barriers and 3 nm GaAs wells, the second superlattice consists of 4 periods of 4 nm $Al_{0.3}Ga_{0.7}As$ barriers and 3.2 nm GaAs wells. For these superlattice parameters, the lowest miniband is positioned between 122 meV and 158 meV for the 5 period SL and between 120 meV and 143 meV for the 4 period SL. The devices were grown by molecular beam epitaxy and were fabricated by standard photolithographic and wet etching techniques in 30 x 30 μm^2-MESA structures. Standard AuGe/Ni metallization was used to form ohmic contacts. Finally, CrAu pads were evaporated, serving as bonding pads. The emitter and collector currents were measured as a function of negative emitter bias at 4.2 K in a common base configuration using a parameter analyzer.

Results

Figure 2 shows the transfer ratio of the 5 period superlattice in the range of the first miniband as a function of the emitter bias. Below the energy of the first state, we observe no collector current, since the electrons that are injected into the drift region are reflected by the superlattice. This also indicates that no significant leakage current occurs between base and collector. The transfer ratio shows an onset at $V_E = –130$ mV, which indicates electron tunneling through the first resonant state of the miniband. Increasing the emitter bias leads to electron tunneling through the individual resonant states of the miniband. At energies above the first miniband, the ballistic electrons are reflected at the superlattice due to the minigap. In contrast to this behavior, the measured transfer ratio does not drop to zero in this energy range. This is due to the formation of phonon replicas in the drift region and their contribution to the shape of the transfer ratio. To get the energetic positions of the peaks out of the transfer ratios we calculate the second derivatives of the transfer ratios of both samples and take the positions of the corresponding minima. The energetic positions of the 5 (4) individual peaks in the transfer ratio at $V_c = 0$ V fit best to calculated subband energies using superlattice parameters of 3.3 nm AlGaAs barriers and 2.9 nm GaAs wells for the 5 period superlattice and 3.7 nm AlGaAs barriers and 3 nm GaAs wells for the 4 period superlattice. The deviation to the nominal superlattice parameters lies within one monolayer for GaAs and AlGaAs.

Hot electron transport in biased superlattices is investigated as a function of the collector bias up to V_C=400 mV. Figure 3 shows the measured peak positions (symbols) relative to the position of peak 3 for both superlattices as a function of the electric field. The experimental results are in excellent agreement to the theoretical Wannier-Stark splitting (solid lines) up to electric fields of F = 25.9 kV/cm for the 5 period superlattice and F = 27.6 kV/cm for the 4 period superlattice, respectively.

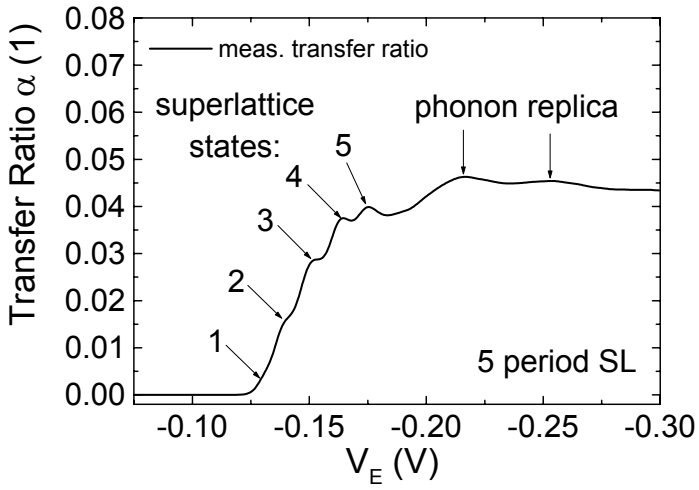

Fig. 2: Measured transfer ratio of the 5 period superlattice as a function of the applied emitter bias V_E.

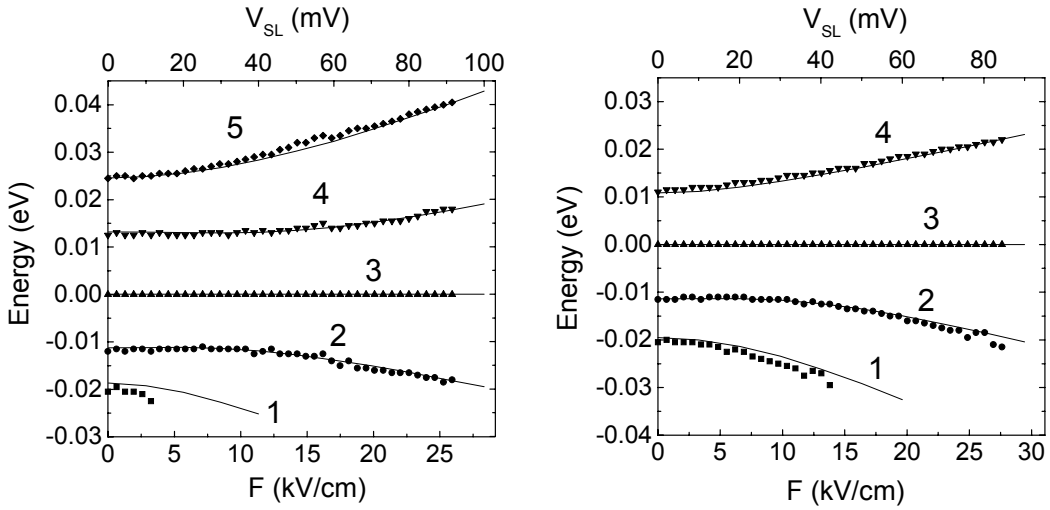

Fig. 3: Measured Wannier-Stark states (symbols) vs. superlattice bias V_{SL} of the 5 (left) and 4 (right) period superlattice compared to the calculated Wannier-Stark splitting (solid lines) vs. electric field F.

In transport experiments, the amplitudes of the current resonances directly resemble the quantum mechanical transmission of the individual states. A comparison of the electric field dependence of the normalized peak amplitudes in the transfer ratios with the expected Wannier-Stark localization amplitudes for the 4 period superlattice is shown in Fig. 4, which directly provides information about the transport mechanisms through each single state. For states 1 and 2, an excellent agreement between measured and calculated transmission is found. For peaks 3 and 4, the experimental findings exceed the coherent predictions: while peak 3 first shows a transmission according to the coherent path an additional contribution to the current starts at 10 kV/cm and becomes larger than the coherent part, passes through a maximum until it decreases at fields above 20 kV/cm. Peak 4 increases above the coherent part already at zero bias and increases in two steps.

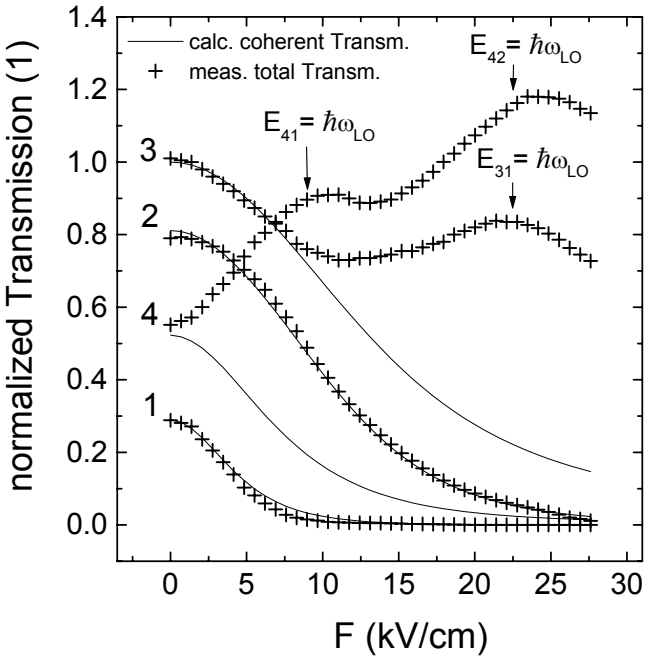

Fig. 4: Measured normalized transmission per states as a function of the electric field (crosses) compared to the calculated normalized coherent transmissions of the individual Wannier-Stark states for the 4 period superlattice (solid lines).

We have previously ruled out interface roughness scattering for a 5 period superlattice [2] as scattering always induces a current component proportional to the electric field which is not observed. Electron-electron scattering can be ruled out due to an extremely low carrier concentration in the device. The only incoherent transmission channel is LO-phonon scattering, which only occurs for transition energies E_{ij} exceeding $\hbar\omega_{LO}$. For the first and second Wannier-Stark state (WSS1, WSS2), LO-phonon scattering can be neglected because the transition energy is much smaller than $\hbar\omega_{LO}$ over the entire bias range. Consequently, transport through these states is purely coherent.

For WSS3 and WSS4, additional current is observed at electric fields where transition energies E_{31}, E_{41} and E_{42} exceed $\hbar\omega_{LO}$ at F_{31} = 21 kV/cm, F_{41} = 9 kV/cm and F_{42} = 22 kV/cm. The increase in the peak amplitude resembles the tuning of the Stark ladder with increasing electric field until the peak of the distribution is resonant with the Stark state splitting of $\hbar\omega_{LO}$. The results clearly show that incoherent transmission channels induced by optical phonons add additional current.

Conclusions

Individual Wannier-Stark states in the first miniband of a 5 (4) period superlattice are resolved up to electric fields of F = 25.9 kV/cm (F = 27.6 kV/cm) in a direct current experiment. From the measured transfer ratios, the exact superlattice parameters are determined. The basic transport through Wannier-Stark states is identified to be coherent. The transport mechanism through higher lying localized states is found to result from an interplay between coherent and incoherent transport as a function of the applied electric field. LO-phonon induced individual channels are found to contribute to the transmitted current. This way we have a method at hand that enables a systematic study of transition rates for different scattering processes in semiconductor heterostructures.

Acknowledgement

This work was supported by the Austrian Science Fund (FWF) Grant No. SFB F016 and Z24.

References

[1] C. Rauch et al., *Appl. Phys. Lett.* **70**, 649 (1997)

[2] C. Rauch et al., *Phys. Rev. Lett.* **81**, 3495 (1998)

[3] M. Kast et al., *Appl. Phys. Lett.* **78**, 3639 (2001)

[4] M. Kast et al., *Phys. Rev. Lett.* **89**, 136803 (2002)

Time-Resolved Measurement of Intersubband Population Dynamics

T. Müller, W. Parz, G. Strasser, K. Unterrainer

Institute for Solid State Electronics, Vienna University of Technology

We apply an interband pump/intersubband probe technique to monitor the temporal evolution of the electron population in the first and second subband of an undoped GaAs/AlGaAs asymmetric double quantum well after interband optical excitation. The spacing between the two subbands is smaller than the longitudinal optical phonon energy. The time dependence of the intersubband absorption can be explained by a simple rate equation model. We extract an intersubband lifetime of T_{21} = 14 ps at an excitation density of $n_S = 1 \times 10^{10}$ cm^{-2}.

Introduction

Semiconductor nanostructures are fascinating quantum systems, which allow engineering of wavefunctions and transition energies. The development of quantum cascade lasers [1] has shown that applying quantum mechanics can lead to new optoelectronic devices. Several other novel devices have been proposed employing intersubband transitions in semiconductor nanostructures [2]. For all these proposals, the population dynamics and the dephasing times are the most crucial parameters. Ultrashort optical pulses with a large spectral width make it possible to study dephasing and relaxation times of carriers in the subbands of quantized structures. The optical pulses can be used to generate ultrashort broadband mid-infrared (MIR) pulses making it possible to measure the complete time-resolved absorption spectrum of a sample with a single pulse, offering simultaneously high resolution in both the time and frequency domains. In our experiment, an interband pump pulse injects electrons into the first and second subband of an undoped asymmetric double quantum well (ADQW) with a level spacing smaller than the LO phonon energy. The time evolution of the electron population in these two subbands is monitored by probing the MIR intersubband transitions to a third (empty) subband. The direct measurement of the subband populations allows us to determine whether there is intersubband THz gain in optically pumped structures.

Experimental

The ADQW sample was grown by molecular beam epitaxy on a semi-insulating (SI)-GaAs substrate. It consists of 40 periods of undoped GaAs wells with widths of 75 Å and 65 Å, separated by a 25 Å $Al_{0.30}Ga_{0.70}As$ barrier. The separation between each double well is 200 Å. A 100 Å AlAs sacrifice layer was grown between the substrate and the ADQW epilayer film. The sample was cleaved into a 1×1 mm^2 piece and etched for about 6 h in 10 % HF. After the QW film had been lifted off the substrate it was bonded via van der Waals forces to the base of a ZnTe prism. The prism forms a waveguide for the mid-infrared probe pulse and enables a considerable electric field component along the growth axis to achieve a strong coupling to the intersubband transition dipoles. Moreover, the ZnTe prism is (in contrast to GaAs) transparent for the probe as well as for the pump light, which allows collinear pumping to achieve a high time-resolution. The difference between the refraction indices of ZnTe in the near- and mid-infrared regions, however, leads to a walk-off between the pump and the probe

pulses that typically amounts to 150 fs. This is the time resolution that can be achieved in this geometry.

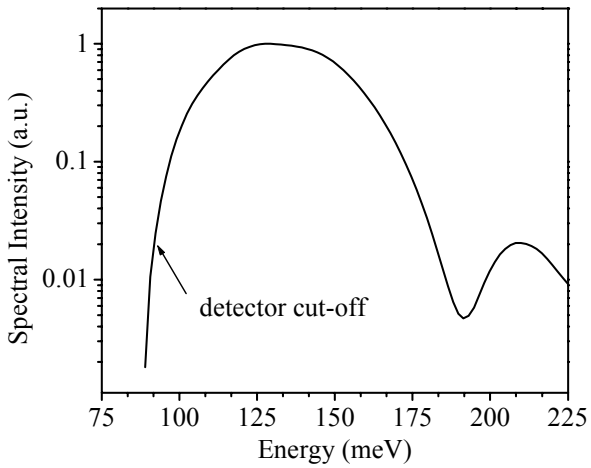

Fig. 1: Intensity spectrum of the MIR probe pulse generated by phase-matched difference frequency mixing in GaSe.

In our time-resolved photoinduced absoption (PIA) setup we use a mode-locked Ti:sapphire laser that delivers 12 fs pulses at a repetition rate of 75 MHz with an average output power of 800 mW. The laser pulses are centered at a wavelength of 780 nm, and the bandwidth is 110 nm (full width at half maximum). The laser beam is split into three parts: *pump*, *probe* and *analysis* beam. The *pump* beam is sent through a variable delay stage and is then used to excite the sample. The desired pump-pulse spectrum is selected through a grating pulse shaper. The sample is mounted on the cold finger of a He continuous flow cryostat and cooled to approximately 5 K. The *probe* is focused on a 30 µm GaSe crystal to generate the linear polarized MIR probe pulse through phase-matched difference mixing [3]. To satisfy the phase-matching condition the polarization of the laser pulse is rotated with a half-wave plate by about 45° out of the horizontal. By changing the orientation of the GaSe crystal it is possible to generate p- or s-polarized light. The MIR radiation transmitted through the sample is then focused on a liquid nitrogen cooled HgCdTe detector. This part of the setup corresponds to a conventional pump-probe experiment in which the total energy of the probe pulse is measured as a function of time delay after excitation. However, the determination of the electric field of the probe pulse requires heterodyne detection. This can be achieved by generating a quasi-single-cycle MIR pulse through optical rectification of the 12 fs *analysis* pulse in a 100 µm ⟨110⟩ SI-GaAs sample. In order to obtain time-resolution, the probe and analysis pulses are mixed at a Si beamsplitter and their superposition is detected as a function of time delay with the time-integrating HgCdTe detector. The signal is collected with a lock-in amplifier phaselocked to an optical chopper which modulates either the pump beam (PIA scan) or the analysis beam (reference scan). Figure 1 shows the intensity spectrum of the MIR probe pulse obtained through Fourier transform of the cross-correlation signal.

Results and Discussion

Figure 2 (a) shows intersubband absorption spectra taken at different time-delays after the excitation by an interband pump pulse. The spectra clearly exhibit two absorption peaks: one around 112 meV, the other one 14 meV above this value. The low-energy peak is due to the (2-3) intersubband absorption, while the second peak is attributed to

the (1-3) absorption. The amplitude of the first peak decreases with time-delay after excitation due to intersubband relaxation, while the amplitude of the second peak first rises slightly, and subsequently decreases due to carrier recombination. Since the area under the peak (*i*-3) (*i* = 1, 2) is directly proportional to the subband population $n_i(t)$, we are able to determine the population dynamics in the quantum well on the basis of the time-resolved absorption spectra [4]. Fig. 2 (b) shows the electron population of the first and second subband as a function of time delay after optical excitation (symbols). About 40% of the photo-excited carriers (1 x 10^{10} cm^{-2}) are injected into the second subband, while the remaining 60% are injected into the first subband at higher k-value. The population in the second subband (squares) shows an exponential decay. The carriers relaxing down from the second subband add to the population in the ground level. Subsequently, the population in the ground level drops due to carrier recombination. The lines in the inset of Fig. 2 (b) are the results obtained from a simple rate equation model. By fitting the calculation to the experimental data we deduce an intersubband relaxation time of T_{21} = 14 ps.

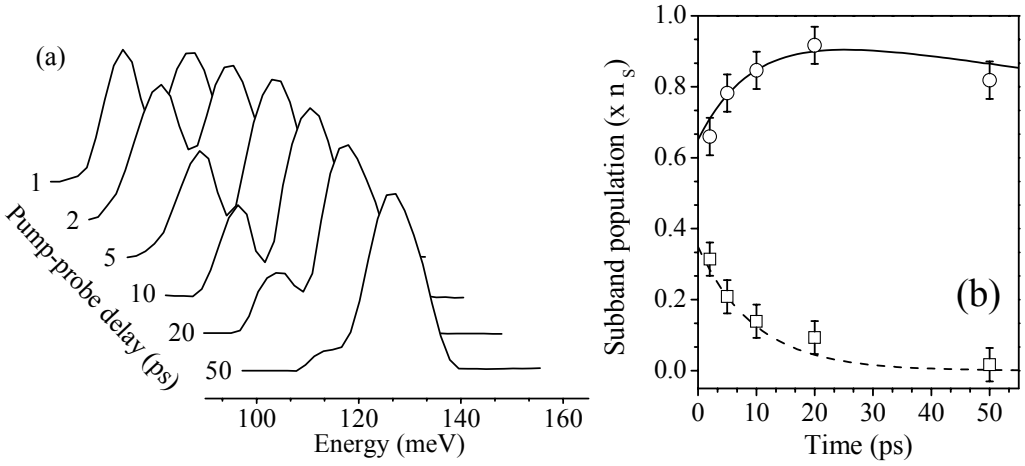

Fig. 2: (a) Time-resolved intersubband absorption spectra for the ADQW sample.
(b) Population in the first (solid line) and second (dashed line) subband.

We will now discuss possible intersubband scattering mechanisms and compare numerical estimates of scattering rates with the experimental results. Since the subband spacing in our sample is smaller than the LO phonon energy the electrons in the second subband do not possess sufficient energy to emit LO phonons and intersubband relaxation can only be due to acoustic phonon emission and electron-electron (e-e) scattering. We calculated the acoustic phonon scattering time to be some hundred ps for our structure. This time is much too long to explain our experimental findings. Recent calculations, however, show that the intersubband e-e scattering rates can be very high, almost approaching in some circumstances the intersubband scattering rate due to LO phonon emission [5]. We calculated the e-e scattering rates in the Born-approximation using static single subband screening within the random phase approximation. The most prominent intersubband e-e scattering processes are labeled 2211 and 2221, where *ijfg* describes an interaction, where an electron in state *i* scatters to *f* under collision with a second electron, which scatters from *j* to *g*. When working out the total population transfer rate between the first and second subband, both scattering processes and the number of electrons that are transferred by each process were taken into account. We calculated an intersubband e-e scattering time of $T_{21} = (2\ W_{2211} + W_{2221})^{-1}$ = 18 ps which is in good agreement with the experimental result. Some authors have also observed a strong reduction of the intersubband relaxation time due to

fast relaxation of electrons in the high-energy tail of the hot carrier distribution in the second subband by emission of LO phonons [6]. Due to the small subband spacing of our sample and the low excitation density, however, the injected electron population in the second subband is cold enough that LO phonon emission is suppressed. Finally, we should also mention our study of the excitation density dependence. We have measured photoinduced intersubband absorption spectra when varying the excitation density from 1 x 10^{10} to more than 1 x 10^{12} cm^{-2}. With increasing densities we observe a significant shortening of the relaxation times. Whereas, in the high density regime we observe a steep increase of the intersubband relaxation times (due to Pauli blocking of the final states). A similar excitation density dependence has been observed by Hartig et al. in a time-resolved photoluminescence experiment [7].

Acknowledgements

This work was sponsored by “Gesellschaft für Mikroelektronik (GMe)” and “Fonds zur Förderung der wissenschaftlichen Forschung (SFB-ADLIS)”.

References

[1] J. Faist et al., Science 264, 553 (1994)

[2] B. F. Levine, J. Appl. Phys. 74, R1 (1993)

[3] R. A. Kaindl, D. C. Smith, M. Joschko, M. P. Hasselbeck, M. Woerner, and T. Elsaesser, Opt. Lett. 23, 861 (1998)

[4] T. Müller, R. Bratschitsch, G. Strasser, and K. Unterrainer, Appl. Phys. Lett. 79, 2755 (2001)

[5] K. Kempa, P. Bakshi, J. Engelbrecht, and Y. Zhou, Phys. Rev. B 61, 11083 (2000)

[6] J. A. Levenson, G. Dolique, J. L. Oudar, and I. Abram, Phys. Rev. B 41, 3688 (1990)

[7] M. Hartig, J. D. Ganiere, P. E. Selbmann, B. Deveaud, and L. Rota, Phys. Rev. B 60, 1500 (1999)

Study of Internal Behavior of BCD ESD Protection Devices under TLP and Very-Fast TLP Stress

M. Blaho[1], D. Pogany[1], L. Zullino[2], A. Andreini[2], E. Gornik[1]

[1]Institute for Solid State Electronics, Vienna Univ. of Technology, Austria
[2]STMicroelectronics, Cornaredo, Italy

The internal behavior of BCD npn electrostatic discharge (ESD) protection devices is analyzed experimentally and by simulation. The device internal thermal and free carrier density distributions during TLP and vf-TLP stresses are studied by a backside transient interferometric mapping technique. Two current paths, one through a lateral npn transistor and one through a vertical npn transistor, are identified. The current flow along the width of the devices is homogeneous. This explains their high ESD ruggedness.

Introduction

The automotive industry requires protection against both the human body model (HBM) and the charged device model (CDM) electrostatic discharge stresses [1, 2]. Monitoring of the internal thermal behavior in such devices is significant for the understanding of device reliability and failure mechanisms [3, 4].

The transient interferometric mapping (TIM) technique is a powerful tool for the investigation of internal device behavior and provides information on thermal and free-carrier concentration dynamics and spatial distribution during an ESD event.

In this paper we investigate the internal device behavior of a bipolar-CMOS-DMOS (BCD) technology ESD protection device under 100 ns TLP and 10 ns vf-TLP stresses.

Device and Measurement Technique

Lateral npn ESD protection devices implemented in an 0.8 µm smart power process (BCD4) are studied. A simplified cross section of the device is shown in Fig. 1. The emitter/body contact was grounded and positive polarity pulses were applied to the collector contact during the investigations.

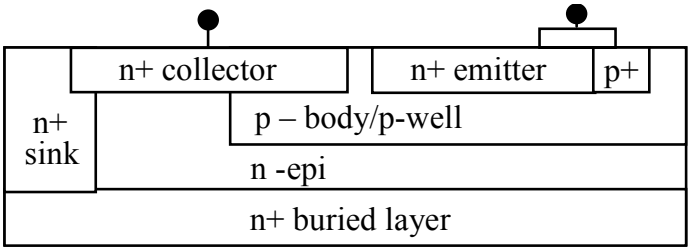

Fig. 1: Simplified cross sections of the studied device.

The high current IV characteristics were measured using 100 ns TLP and 10 ns vf-TLP pulsers.

The backside TIM is carried out by a scanning heterodyne interferometer setup [5]. An infrared laser beam of 1.3 µm wavelength is focused from the backside on a device and scans the device. The temperature and free-carrier induced phase shift of the reflected beam is then interferometrically detected. If the thermal effect dominates the measured phase shift $\Delta\varphi$ can be directly related to the two-dimensional thermal energy density E_{2D} in the device via the relation: $E_{2D}(x,y,t) = 0.88\ \Delta\varphi(x,y,t)$ (nJ/µm^2, rad) [6]. The phase shift is measured with 1.5 µm space and 3 ns time resolution.

Experimental Results

Figure 2 shows the high current IV characteristics of the device of width 100 µm measured by 100 ns TLP and 10 ns vf-TLP. The IV curve obtained by TLP bends from the IV obtained by vf-TLP at currents above 2 A, i.e., the differential resistance (R_{diff}) is higher for TLP stress. This can be attributed to a self-heating effect. The R_{diff} of the device at current levels below 2 A is the same for both TLP and vf-TLP types of stress. The $1/R_{diff}$ scales nearly linearly as a function of the device width in this range as can be seen in Fig. 3.

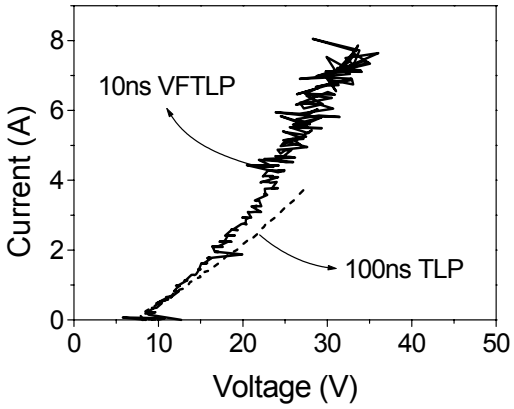

Fig. 2: High current IV characteristics of the device of width 100 µm measured by 10 ns vf-TLP and 100 ns TLP (after [4]).

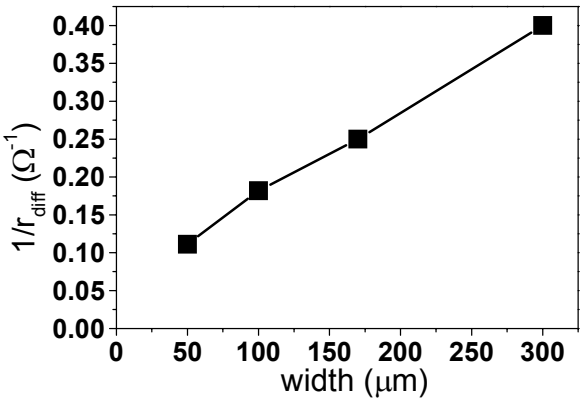

Fig. 3: Inverse differential resistance $1/R_{diff}$ as a function of device width (after [4]).

The ESD ruggedness of the device is high. The 170 µm wide device can sustain 4 A of TLP and 18 A of vf-TLP stress levels. These are the measurement setup limits.

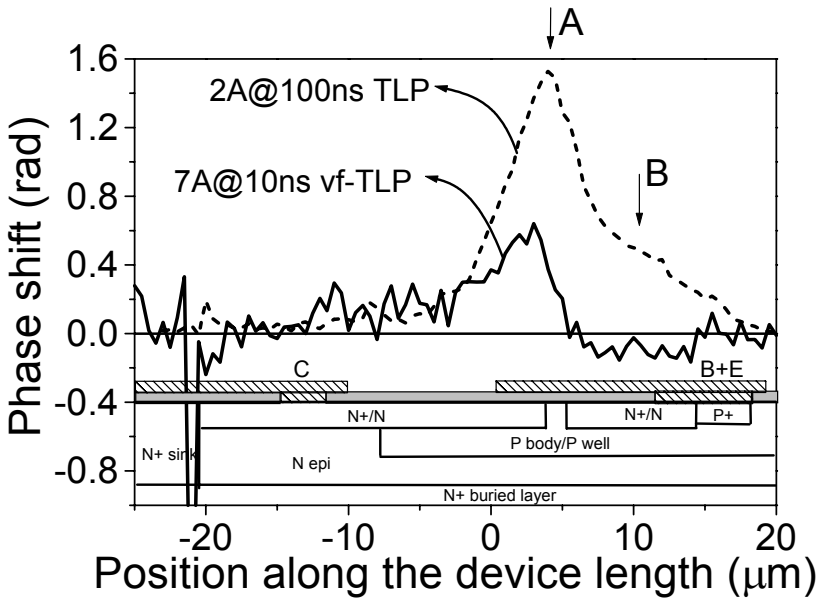

Fig. 4: Phase shift distribution along the device length measured at the pulse end of stresses of 2 A @ 100 ns (TLP) and 7 A @ 10 ns (vf-TLP). Aligned simplified cross section is also indicated (after [4]).

Figure 4 shows the phase shift distribution along the device length at the pulse end of two stress conditions: 100 ns TLP pulse with amplitude of 2 A and 10 ns vf-TLP pulses with amplitude of 7 A. An aligned simplified cross section of the device is also shown in Fig. 4. A dominant positive phase shift peak is located at the collector edge of the lateral npn transistor during both TLP and vf-TLP stresses (see A in Fig. 4). This peak arises from the heat dissipation in the reverse biased n^+-collector/p-body pn junction, which undergoes impact ionization. Another important area is located at the position of the n^+-emitter (see B in Fig. 4). The phase shift at the end of short vf-TLP stress is negative there. It arises from the increased free carrier concentration due to injection in the forward biased n^+-emitter/p-body junction, when the npn transistor is turned on. One can therefore expect also a positive phase shift due to heating related to the activity of a vertical npn transistor being present under the n^+-emitter. However, the temperature rise at pulse duration of 10 ns is insufficient to make the total phase signal positive. A positive thermal side-hump related to the heating in the vertical npn transistor can only be observed under longer pulses, as it can be seen on the phase shift profile measured at the end of a 100 ns long TLP stress pulse (see B in Fig. 4).

The activity of the vertical npn transistor depends on the stress current level. The phase shift distributions along the device length at three different TLP stress current levels are shown in Fig. 5. Let us concentrate on side hump (peak B in Fig. 5). It can be observed only at higher stress levels (I > 2 A). The phase shift peak B is more pronounced at the device corners, compared to the middle of the device. This can be seen on the measurements at I = 4 A, where the phase shift distribution is taken in the device middle (curve “M” in Fig. 5) and at one corner of the device (curve “C” in Fig. 5).

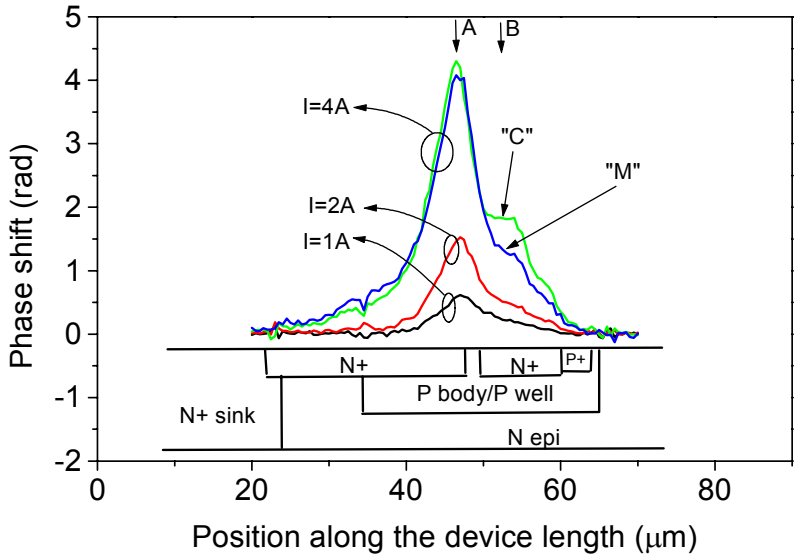

Fig. 5: Phase shift distribution along the device length as a function of TLP stress current. The inset shows a simplified device cross section (after [3]).

Homogeneity of the current flow along the width of the devices stressed by 10 ns vf-TLP pulses was also investigated. Figure 6 shows the phase shift distribution along the dominant hot spot (peak A in Fig. 4) in the devices of different widths stressed by the same current per device width. The optical mapping reveals very homogeneous current flow thus explaining linear scaling of the inverse differential resistance $1/R_{diff}$ as a function of the device width (see Fig. 3) and the high ESD ruggedness of the devices.

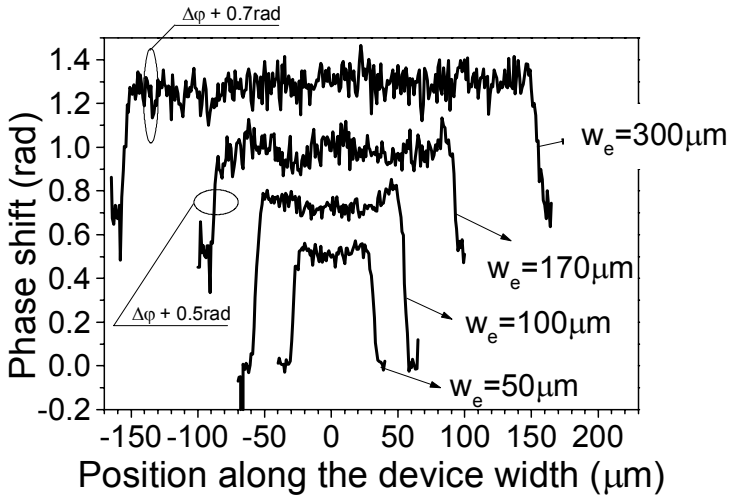

Fig. 6: Phase shift distribution at the end of stress 10 ns vf-TLP along the device width. The current density (current/width) was the same for all devices (after [4]).

Figure 7 shows the simulated heat dissipation in the device at t = 100 ns for the stress current pulse of 2.5 A. The main heat dissipation region is located at the lateral n^+-collector/p-body junction. This agrees with the experiment, because the dominant phase shift peak was observed at this place (see A in Fig. 4). The heat dissipating re-

gion is also observed at the n-epi/p-body junction under the n^+-emitter, which explains the existence of the side-hump observed experimentally at the end of 100 ns TLP pulses in this structure (see B in Fig. 4). This is the second region where the impact ionization takes place.

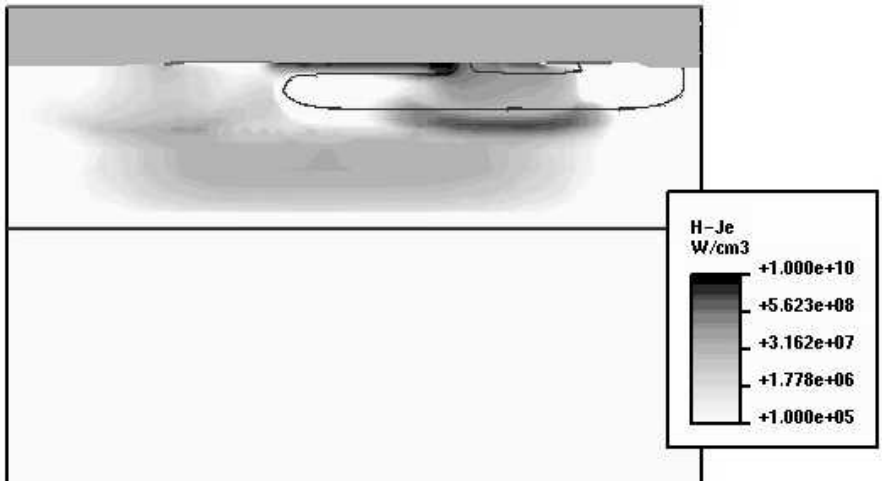

Fig. 7: Simulated heat dissipation due to electron current flow in the device at the end of 2.5 A @ 100 ns stress (after [4]).

Conclusions

The internal behavior of BCD ESD protection devices under TLP and vf-TLP stress was studied and compared. The device operation is dominated by the action of the lateral npn transistor. The n^+-collector/p-base junction of this transistor where impact ionization takes place was identified as the main heat-dissipating source. The activity of the vertical npn transistor is also identified in the device. The optical mapping along the device width has revealed homogeneous current flow. This is consistent with the scaling of the inverse differential resistance of the devices with their width. Thanks to the homogeneous current flow, devices also exhibit excellent ESD ruggedness in both HBM and CDM time domains.

Acknowledgements

This work was performed within the European Community MEDEA+ Project T102 “ASDESE” and was financially supported by the Austrian (Bundesministerium für Verkehr, Innovation und Technologie), German (German research council BMBF) and Italian (Ministero dell’Istruzione, dell’Universita e della Ricerca) national governments.

References

[1] L. Sponton, L. Cerati, G. Croce, F. Chrappan, C. Contiero, G. Meneghesso and E. Zanoni, “ESD protection structures for BCD5 smart power technology,” *Microel. Reliab.*, 41, 2001, pp. 1683-1687

[2] G. Meneghesso, M. Ciappa, P. Malberti, L. Sponton, G. Croce, C. Contiero and E. Zanoni, “Overstress and electrostatic discharge in CMOS and BCD integrated circuits,” *Microel. Reliab.*, 40, 2000, pp.1739-1746.

[3] M. Blaho, D. Pogany, L. Zullino, A. Andreini, E. Gornik, “Experimental and simulation analysis of a BCD ESD protection element under the DC and TLP stress conditions”, *Microel. Reliab.*, 42, 2002, pp. 1281-1286

[4] M. Blaho, D. Pogany, E. Gornik, L. Zullino, E. Morena, R. Stella, A. Andreini, “Internal behavior of BCD ESD protection devices under very-fast TLP stress”, *Proc. of IRPS’03*, 2003, pp. 235-240

[5] C. Fürböck, K. Esmark, M. Litzenberger, D. Pogany, G. Groos, R. Zelsacher, M. Stecher and E. Gornik, “Thermal and free carrier concentration mapping during ESD event in smart power ESD protection devices using an improved laser interferometric technique,” *Microel. Reliab.*, 40, 2000, pp. 1365-1370.

[6] D. Pogany, S. Bychikhin, C. Fürböck, M. Litzenberger, E. Gornik, G. Groos, K. Esmark, M. Stecher, “Quantitative internal thermal energy mapping of semiconductor devices under short current stress using backside laser interferometry,” *IEEE Trans. Electron Devices*, 49, 2002, pp. 2070-2079

Local Thermal and Current Imaging in Power Devices

D. Pogany

Institute for Solid State Electronics, Vienna University of Technology

This paper summarizes recent results obtained at TU Vienna in the field of thermal and free-carrier mapping of semiconductor devices using backside transient interferometric mapping (TIM) technique. The technique is based on measuring optical phase changes due to temperature and free carrier induced variations in semiconductor refractive index. Scanning transient heterodyne and 2D holographic interferometers are used for phase measurements. Thermal distribution, hot spot dynamics, current filament movement, and failure mechanisms are investigated in electrostatic discharge (ESD) protection devices and power vertical DMOS transistors.

Introduction

Experimental access to internal parameters of semiconductor devices as carrier concentration, current densities, power dissipation, temperature, etc. is of great interest for the understanding of device physics and for device optimization. Monitoring of temperature is especially important for power [1] and electrostatic discharge (ESD [2]) protection devices (PDs), where the self-heating effect is a main cause of device failure [3]. These devices operate at high current and power densities where the internal device behavior predicted by device simulation has a limited degree of confidence [4]. This is due to a lack of calibrated physical models at high temperatures. Thermal runaway phenomena in power devices occur in microsecond to millisecond time scale [1]. During an ESD event, large currents (1 – 10 A) and power densities (approx. 100 W) are dissipated in the device during 1 – 100 ns [2].

The backside transient interferometric mapping (TIM) technique has shown its potential in quantitative nanosecond thermal, free carrier and current flow mapping in silicon [5] – [8] and III-V [9] electronic devices and far-infrared quantum cascade lasers [10]. In this paper, recent development in the optical testing and analysis methodology is briefly reviewed. The application of TIM method to study hot spots and current filament dynamics in ESD and power DMOS devices is presented.

Experiments and Methodology

In the TIM method, an infrared non-absorbed laser beam (wavelength λ = 1.3 μm) probes temperature- or free carrier-induced changes in the semiconductor refractive index inside a device [5], [7]. The beam passes through the substrate, is reflected on the device topside and returns. The resulting phase shift is detected interferometrically. In a scanning heterodyne interferometer, a focused laser beam scans the device active area and the device is repetitively electrically stressed for each scan position [5]. Transient phase shift is obtained with 3 ns time resolution. A Michelson-like interferometer is used for phase measurements with 0.4 ns time resolution [11]. In a 2D holographic interferometric version of the TIM method, a broad beam illuminates the whole device area [6]. Figure 1 (a) shows a simplified arrangement of the setup. The phase profile is obtained by analyzing a 2D interference fringe pattern, see Fig. 1 (b), (c). The thermal image in the whole sample can be obtained using a single laser pulse, so non-

repeatable phenomena can be studied. The pulse width of 5 ns determines the time resolution. By varying the delay between the laser and stress pulse, the time evolution of thermal distribution can be obtained.

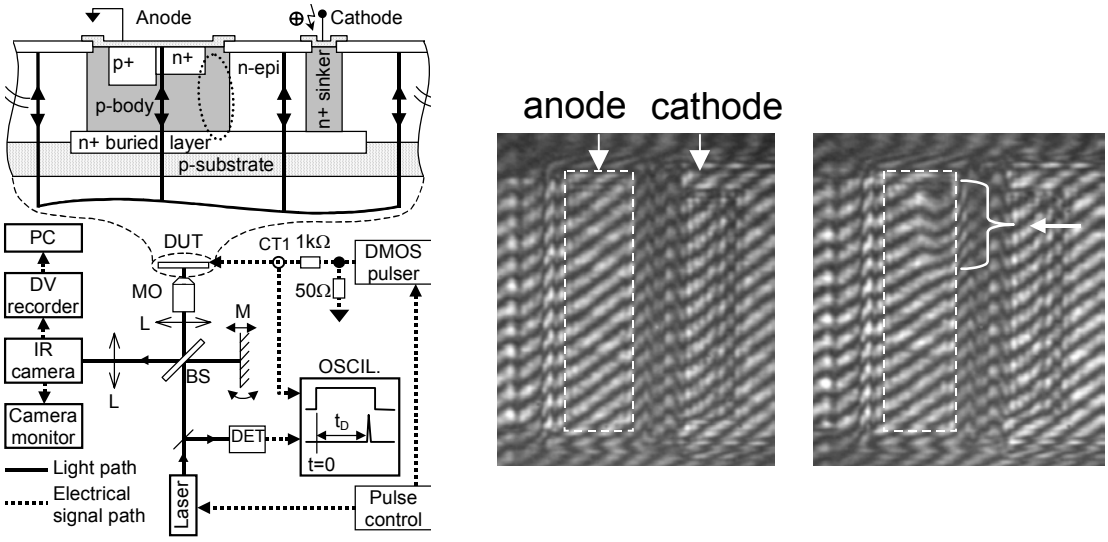

(a) (b) (c)

Fig. 1: Schematics of the 2D TIM method (a). Typical fringe interference pattern in an unstressed (b) and stressed (c) device. The deformation of fringes in (c) marked by an arrow results from local heating causing the phase rise; after [6].

It has been shown that if thermal effects dominate over the free carrier contribution, the measured phase shift $\Delta\varphi(x,y,t)$ can be directly related to a 2D thermal energy density E_{2D} in semiconductor according to the relation [7]:

$$\Delta\varphi(x,y,t) = \frac{4\pi}{\lambda\, c_V}\frac{dn}{dT}E_{2D}(x,y,t) \tag{1}$$

where c_V is the volume specific heat and dn/dT the thermo-optical coefficient. E_{2D} is a "memory" quantity representing the time integration of all the preceding power dissipation. The instantaneous 2D power dissipation density $P_{2D}(x,y,t)$, representing the well the current density if a constant voltage on the device is assumed, can be calculated according to [8]:

$$P_{2D}(x,y,t) = \frac{\lambda}{\frac{dn}{dT}}\frac{c_V}{4\pi}\frac{\partial\Delta\varphi(x,y,t)}{\partial t} - \frac{\lambda}{\frac{dn}{dT}}\frac{\kappa}{4\pi}\left(\frac{\partial^2\Delta\varphi(x,y,t)}{\partial x^2} + \frac{\partial^2\Delta\varphi(x,y,t)}{\partial y^2}\right) \tag{2}$$

where κ is the thermal conductivity.

Smart power ESD and vertical power DMOS devices have been investigated. The devices have a common n^+ buried layer serving as collector of a parasitic npn transistor. The devices were stressed by rectangular current pulses of 100 ns – 1 µs duration. If not specified elsewhere, this drives the devices in a bipolar snapback mode.

Results

The dynamics of current flow in ESD PDs has been studied by analyzing the absolute phase shift itself (representing the temperature), the 2D power dissipating density P_{2D},

(representing the current density) and the device voltage waveform [12]. Strongly localized moving current filaments (see Fig. 2(a)) have been observed in devices exhibiting near zero or NDR part in IV characteristics. The filament characteristics, as starting place, size, speed, travelling mode and its occurrence probability depend strongly on stress magnitude I_S. The filaments exhibit pulse-to-pulse instability in their movement direction and position of origin, i.e. the device internal state differs from pulse to pulse. This is due to fluctuations in carrier densities.

At long pulses of low current magnitude the filament can several time travel over the device width without destroying the device, see Fig. 2(a). The filament passage over the device produces a specific fingerprint across the voltage on the device, see Fig. 2(b). When the filament approaches a region with higher impact ionization, e.g. at terminations, or when it passes from a hot region into a cooler region the voltage decreases due to negative temperature dependence of the impact ionization rate [13]. When the filament does not move, as it is initially in the middle and then at corners, the voltage increases due to the self-heating effect to keep the same impact generation rate under the constant current. When the filament moves, a constant voltage is typically observed, which is due to a stabilizing effect of the movement on the temperature in the filament. The filament localization and persistence is caused by fast cooling to lateral sides.

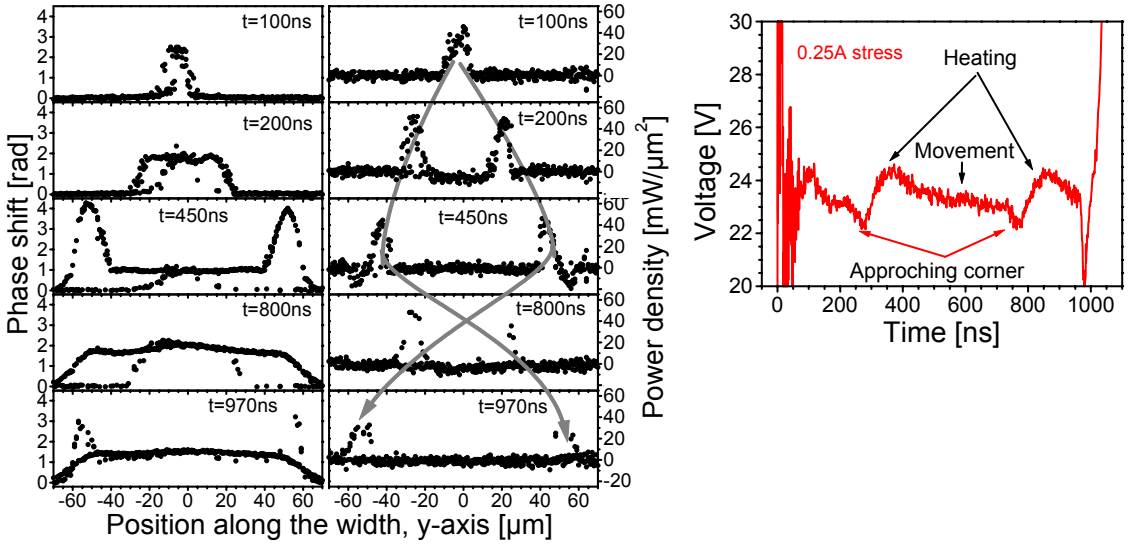

(a) (b)

Fig. 2: (a) Scatter plot of measured phase shift (left) and extracted P_{2D} at several time instants in a silicon controlled rectifier device exhibiting moving filaments at current of 0.15 A. The filament path is marked by the gray lines with arrow. The scattered nature of data is due to pulse-to-pulse instability in the filament movement. (b) Voltage waveform related to the filament movement; after [12].

At higher stress currents, the number of filamentary modes typically increases. Figure 3 shows the 2D thermal distribution at high stress levels, demonstrating the spreading of current flow with time. The high-energy input in the filament exceeds the energy output by cooling to lateral sides. This causes that the current density decreases with time, which leads to a current homogenization or spreading with time [6]. Similar effects have previously been observed indirectly by repetitive photon emission measurements [14].

The speed of the current filaments and of the filament spreading increases with time and with the stress current I_S, see inset of Fig. 3(d). This effect, beneficial for ESD ro-

bustness, is due to a negative temperature dependence of impact ionization rate [13]. The pulse-to-pulse instabilities in the device internal behavior leads to formation of a pattern in IV curves when plotting the IV curve point by point without time or ensemble averaging [12].

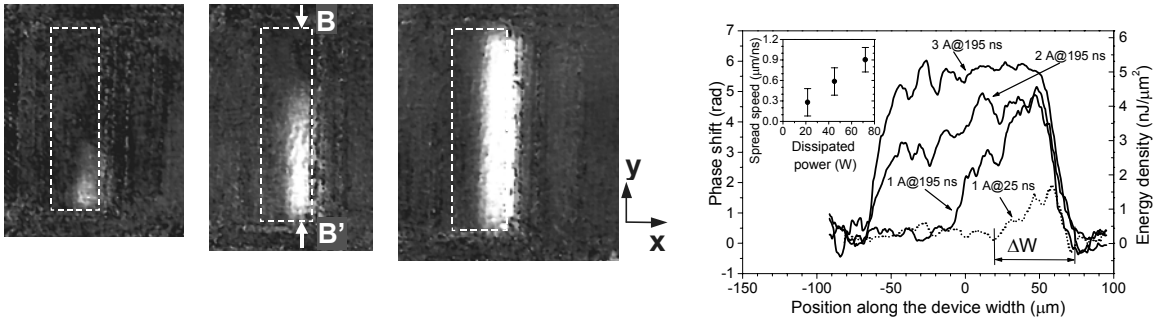

(a) (b) (c) (d)

Fig. 3: Single shot 2D phase profiles in a ESD protection device demonstrating the spreading of current flow with time and I_S: (a) 1 A @ 40 ns, (b) 1 A @ 195 ns, (c) 3 A @ 195 ns. (d) Phase profiles along the B-B' line in (b). Inset: Filament spreading speed as a function of I_S; after [6].

Vertical DMOS transistors with different number of cells were investigated before [15] and in bipolar snapback operation [16], [17] using TIM method. Before snapback, the current sharing between the cells is homogeneous, due to a negative thermal feedback during the avalanche breakdown [15]. Under snapback conditions, the current flow is strongly inhomogeneous, forming localized current filaments, see Fig. 4. The cells at the drain terminations are triggered first due to higher electric field there. With time the neighboring cells trigger as well, causing that the current flow moves toward the device area or along the termination (Fig. 4). The observed feature of DMOS behavior in snapback is qualitatively reproduced by 2D and 3D device simulation [16]. The base-push-out or Kirk effect and the negative temperature dependence of the impact ionization rate were found to play a decisive role in the cell-to-cell hoping of the current flow. This is plausible for ESD robustness.

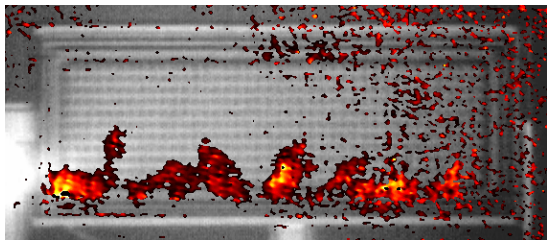

Fig. 4: Phase image in a 440 cell DMOS device recorded at time 150 ns after the beginning of a 7A current stress pulse. The phase image is aligned with the backside infrared device image; after [16], [17].

Finally, failure mechanisms have been studied during single destructive pulses [18]. Fig. 5 shows the device interferogram and extracted phase shift in a diode structure, recorded during a single destructive 2nd BD event. At the destruction, the voltage across the device drops from the pulse beginning, indicating a current density driven instability, see Fig. 5(a). This leads to a formation of a current filament (see Fig. 5(c)),

whose size, taking into account the thermal diffusion length of 4.2 µm for a 200 ns long pulse, was estimated to be 3 – 4 µm. The diameter of the filament correlates with the size of permanent damage at this position (see Fig. 5(d)). A decreased intensity of the interference fringes was observed during this event (see Fig. 5(b)), which indicates the onset of band-to-band absorption (E_G reduction with temperature increase). Taking into account the data of temperature dependence of absorption coefficient for λ = 1.3 µm [19], the temperature in the filament was estimated to exceed 900 K.

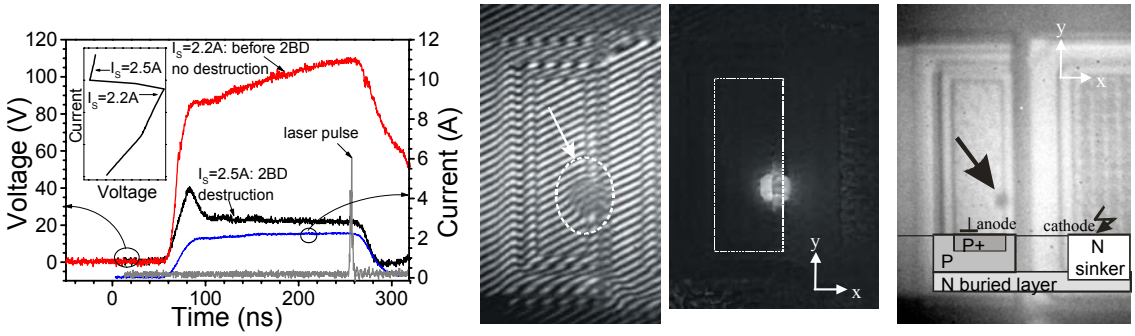

(a) (b) (c) (d)

Fig. 5: Voltage waveform during the destructive event in a diode (a). Fringe pattern (a), extracted phase shift (b) and IR image with defect position (d), after [18].

Conclusion

Current filaments and hot spot dynamics has been investigated in ESD protection and DMOS devices. Using the single shot capability of TIM method, current flow instabilities and destructive mechanisms have been revealed. The movement and spreading of current filaments have been identified as a thermally driven process. The TIM method is a powerful tool providing the design engineer a unique insight into internal device behavior of semiconductor devices and to verify device simulation models.

Acknowledgements

Prof. E. Gornik, S. Bychikhin, M. Blaho, V. Dubec, J. Kuzmik and M. Litzenberger from FKE TU Vienna and M. Denison, N. Jensen and M. Stecher from Infineon Technologies are greatly acknowledged. This work was supported by EU IST Project DEMAND and FWF Wittgenstein award.

References

[1] B. J. Baliga, *Modern power devices*, John Wiley, NY, 1987.

[2] Amerasekera, and C. Duvvury, *ESD in Silicon Integrated Circuits*, J. Wiley & Sons, 1995.

[3] V. M. Dwyer, A. J. Franklin and D. S. Campbell, "Thermal failure in semiconductor devices", *Solid-St. Electron.* vol. 33, pp. 553-560, 1990.

[4] K. Esmark, C. Fürböck, H. Gossner, G. Groos, M. Litzenberger, D. Pogany, R. Zelsacher, M. Stecher, and E. Gornik, "Simulation and experimental study of

temperature distribution during ESD stress in smart-power technology ESD protection devices", In *Proc. IRPS'2000*, pp. 304-309.

[5] C. Fürböck, K. Esmark, M. Litzenberger, D. Pogany, G. Groos, R. Zelsacher, M. Stecher, and E. Gornik, "Thermal and free carrier concentration mapping during ESD event in smart power ESD protection devices using an improved laser interferometric technique", *Microel. Reliab*., vol. 40, pp. 1365-1370, 2000.

[6] D. Pogany, V. Dubec, S. Bychikhin, C. Fürböck, M. Litzenberger, G. Groos, M. Stecher, E. Gornik, "Single-shot thermal energy mapping of semiconductor devices with the nanosecond resolution using holographic interferometry", *IEEE Electron Dev. Lett.*, vol. 23, pp. 606-608, 2002.

[7] D. Pogany, S. Bychikhin, C. Fürböck, M. Litzenberger, E. Gornik, G. Groos, K. Esmark, M. Stecher, "Quantitative internal thermal energy mapping of semiconductor devices under short current stress using backside laser interferometry", *IEEE Trans. Electron Devices*, 2002, vol. 49, pp. 2070-2079, 2002.

[8] D. Pogany, M. Litzenberger, S. Bychikhin, E. Gornik, G. Groos, M. Stecher, "Extraction of spatio-temporal distribution of power dissipation in semiconductor devices using nanosecond interferometric mapping technique", *APL*, vol. 81, pp.2881-2883, 2002.

[9] J. Kuzmik, D. Pogany, E. Gornik, P. Javorka, P. Kordoš: "Electrical overstress in AlGaN/GaN HEMTs: Study of degradation processes", submitted to Solid-State Electronics, 2003.

[10] C. Pflügl, M. Litzenberger, W. Schrenk, D. Pogany, E. Gornik, G. Strasser, "Interferometric study of thermal dynamics in GaAs-based quantum cascade lasers", *Appl. Phys. Lett.*, vol. 82, p.1664-1666, 2003.

[11] S. Bychikhin, V. Dubec, M. Litzenberger, D. Pogany, E. Gornik, G. Groos, K. Esmark, W. Stadler, H. Gieser, H. Wolf," Investigation of ESD protection elements under high current stress in CDM-like time domain using backside laser interferometry" Proc. EOS/ESD Symposium, Charlotte, USE, October 6-10, 2002, pp. 387-395 (2002).

[12] D. Pogany, S. Bychikhin, E. Gornik, M. Denison, N. Jensen, G. Groos and M. Stecher: "Moving current filaments in ESD protection devices and their relation to electrical characteristics", Proc. IRPS'2003, p. 241-248.

[13] K. G. McKay, "Avalanche breakdown in silicon", *Phys. Rev.*, vol. 94, pp. 877-884, 1954.

[14] M. P. J. Mergens, W. Wilkening, S. Mettler, H. Wolf, A. Stricker and W. Fichtner, "Analysis of lateral DMOS power devices under ESD stress conditions", *IEEE Trans. Electron. Dev.,* vol. 47, pp. 2128 - 2137, 2000.

[15] M. Blaho, D. Pogany, E. Gornik, M. Denison, G. Groos, M. Stecher; „Investigation of the internal behavior of a vertical DMOS transistor under short duration, high current stress by an optical thermal mapping method"; *Microel. Reliab*., 2003, in press.

[16] M. Denison, M. Blaho, D. Silber, J. Joos, M. Stecher, V. Dubec, D. Pogany, E. Gornik: "Hot Spot Dynamics in Quasi Vertical DMOS under ESD Stress", *Proc. ISPSD'03*, Cambridge, England, 2003, in press.

[17] M. Blaho, M. Denison, V. Dubec, J. Kuzmik, D. Pogany, M. Stecher, E. Gornik, "Dynamics of current flow in DMOS transistors under bipolar snapback ESD conditions", Submitted to *ESSDERC'2003*.

[18] D. Pogany , S. Bychikhin, J. Kuzmik , V. Dubec , N. Jensen , M. Denison, G. Groos, M. Stecher and E. Gornik, "Thermal distribution during destructive pulses in ESD protection devices using a single-shot, nanosecond resolution, two-dimensional interferometric method", In *IEDM'2002 Techn. Digest*, pp. 345-348.

[19] H. Rogne, P. J. Timans, and H. Ahmed, "Infrared absorption in silicon at elevated temperatures", *Appl. Phys. Lett.*, vol. 69, pp. 2190-2192, 1996.

Scanning Capacitance Microscopy Investigations of Focused Ion Beam Damage in Silicon

W. Brezna, H. Wanzenböck, A. Lugstein, E. Bertagnolli, E. Gornik, J. Smoliner

Institute for Solid State Electronics, Vienna University of Technology

In this article, we explore the application of Scanning Capacitance Microscopy (SCM) for studying focused ion beam (FIB) induced damage in silicon. We qualitatively determine the technologically important beam shape by measuring the SCM image of FIB processed implantation spots and by comparison of topographical and SCM data. Further, we investigate the question how deep impinging ions generate measurable damage below the silicon surface. For this purpose, trenches were manufactured using FIB and analyzed by SCM in cross sectional geometry.

Introduction

Focused ion beam (FIB) techniques are among the most important tools for modification tasks below 100 nanometer. Today, FIB systems are mainly used for device modification, transmission electron microscopy (TEM) sample preparation, scanning probe microscopy (SPM) tip preparation, and deposition of different metals and insulators [1]. Unfortunately, there are mainly two effects that limit the usage of FIB modification to certain applications and areal scales [2]. Difficult to measure, the ion beam diameter and intensity profile defines the lateral resolution and the smallest possible size of a FIB made structure. The other limitation occurs due to ion beam induced damage, which extends far below the modified sample surface.

Various methods such as secondary ion mass spectroscopy (SIMS) and transmission electron microscopy (TEM) have been utilized to measure penetration depths and intensity profiles of FIBs. However, the disadvantage of these methods is their lack of 2D spatial resolution (SIMS) or difficult sample preparation (TEM). For this reason, scanning probe techniques have successfully been applied for FIB intensity profile determination and imaging in other ion beam applications [3]. Topographic atomic force microscopy (AFM) investigations can yield high resolution data from FIB implanted spots via the embossment of FIB amorphisized areas due to the slightly lower density of amorphous silicon compared to crystalline silicon. However, severe degradation of the electronic properties will occur long before the structural changes (amorphization) take place, which cannot be investigated any more with topographic AFM. In this article, we introduce Scanning Capacitance Microscopy (SCM) as a very sensitive tool to investigate the position and extent of FIB induced electronic degradation. SCM is an extension of conventional AFM and a very promising tool for semiconductor device characterization. The current state of the art of this technique can be found in the review article [4]. SCM can detect magnitudes smaller changes in material composition than any other scanning probe method and it is possible to sense as small quantities as 10 – 100 impurity atoms per cubic micron (10^{13} – 10^{14} per cm^3). Where FIB irradiation does not alter the topography of the region of interest, it is still possible to get reliable data of the FIB damaged areas via SCM. We first use this method to determine the ion beam intensity profile by investigating irradiated silicon surfaces. Then we will deal with the damage spread inside the silicon sample beneath a FIB milled trench.

Experimental

To avoid any additional difficulties in data interpretation due to the very complex electrical behavior of pn-junctions [5] we decided to use low p-doped silicon wafers, since our FIB system is equipped with a Ga^+ ion source (acceptors). The low acceptor concentration of the bulk material was an advantage, because SCM yields higher signals on low-doped semiconductors. The samples were prepared in two ways to match the different demands of FIB intensity profile and damage depth determination: For measuring the beam intensity profile, we used the very clean surfaces of freshly cleaved silicon wafers. On the cleaved surface five types of spots were made with the FIB system, which differed from each other in the deposited ion dose (0.025, 0.05, 0.1, 0.5 and 5 pC/spot). The spots were located in close vicinity (a few microns) of the wafer edge to reduce sample tip-holder overlaps and related stray capacitance, which increases the signal to noise ratio in our SCM measurements. The acceleration voltage of the Ga^+ ions was 50 kV and the aperture size was 50 µm. For the investigation of the damage depths, a trench was milled into the polished front side of a wafer. After milling, the sample was cleaved to get cross sections of the damaged area beneath the trench.

Results and Discussion

Although the SCM signal is a complicated function of the semiconductor doping concentration and the applied tip-bias voltage, it is possible to adjust the electrical parameters of the setup in a way to gain a signal that is monotonic with doping concentration [6]. Using such optimized conditions leads to good SCM contrast with big signal in low-doped regions and small signal in higher doped regions. However, besides the p-type doping by Ga^+ ion implantation, the crystalline structure of FIB irradiated samples is damaged heavily which also results in a reduction of the SCM signal. Therefore, we cannot distinguish between high doped or damaged areas. Studies show that ion beam doses magnitudes smaller than the minimum dose for surface modification (e.g. swelling due to amorphization) can already be detected via SCM. We used this fact to determine the beam intensity profile of our FIB system. Figure 1 (a) shows the resulting topographic changes of milling with a moderate dose per spot (0.5 pC/spot). The swelling and subsequent silicon removal due to sputtering can be seen very well and leads to the typical crater-like structures. Figure 1 (b) shows the simultaneously measured SCM picture. In comparison with the topographic image seen in Fig. 1 (a), the recorded SCM picture shows a significantly larger damaged region indicated by the dark circle of low SCM signal. Based on topography, we define the ion beam radius as follows: the radius R_{Topo} is the distance from the deepest milled point (highest intensity in the beam center) to the point where the outer swelling flank is half-decayed. In the case where the ion dose is so small that only swelling is observed, we take the distance between the maximum of the swelling and the point where it is half-decayed. Based on SCM we defined the beam radius R_{SCM} as half the distance between the points where the SCM-signal-flanks rise to half of their maximum.

The two radii R_{Topo} and R_{SCM} are compared in Fig. 1 (c), where cross sections of the image data are plotted along line L. The difference between topography signal and SCM signal, $\Delta R = R_{SCM} - R_{Topo}$, is 250 nm. Figure 1 (d) compares the behavior of the radii R_{Topo} and R_{SCM} with increasing dose per spot. The radii show monotonic growth, however, there are saturation effects in the high dose regime. In addition, both data sets diverge for big ion doses. Whereas for the lowest dose the structures have twice the radius in SCM mode than in topography mode, for the highest dose this ratio is almost four. Our observation that the SCM based beam radius R_{SCM} is always larger than the topographic radius R_{Topo}, and the effect that R_{Topo} and R_{SCM} diverge for big ion doses, can be explained by the following facts. First, as was already published [1], [7], the beam profile consists of (at least) two regions: The region far away from the beam

center, where the overall intensity is very small but decays slowly. The other region is close to the beam center, where the intensity is comparable with the beam center and has the steepest decay. Second, SCM is much more sensitive to ion irradiation effects than the topographic signal, since topographic changes by amorphization need very high ion doses. Because of these two properties, the SCM sensed radius grows quickly with increasing dose per spot in the outer areas of the beam profile, whereas the smaller crater-like structure in the topography grows just slowly.

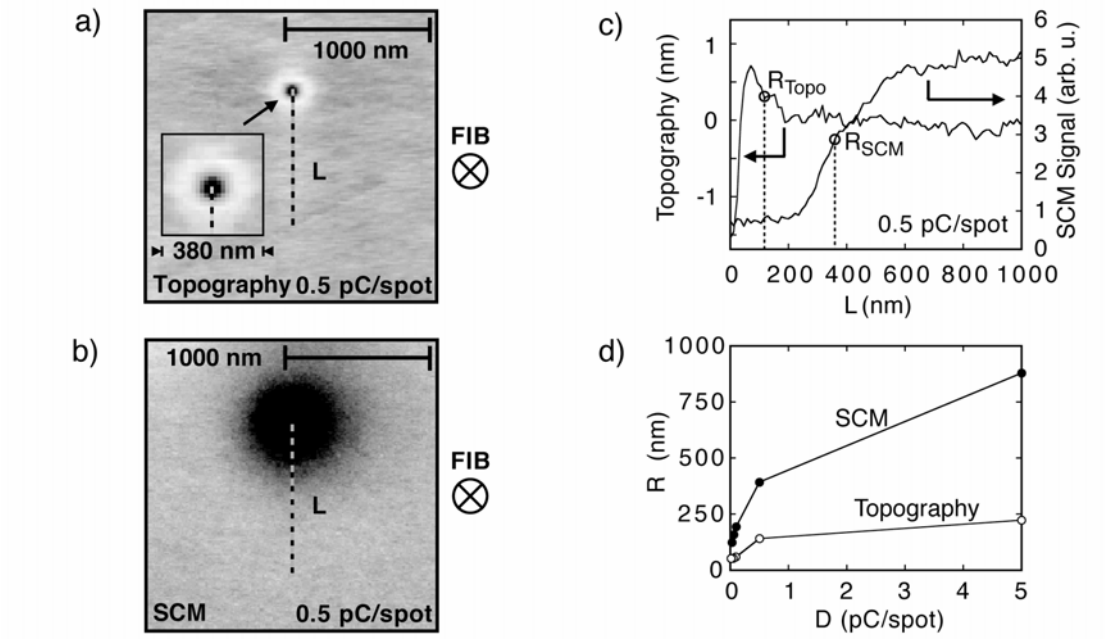

Fig. 1: (a) The topographic image of a FIB irradiated spot with an inset showing a magnification. The beam direction is indicated. (b) Corresponding SCM image. (c) Radial cross sections through the topographic and SCM images along the line L. R_{Topo} and R_{SCM} define the radius of damage as seen in the topographic and the SCM image. (d) R_{Topo} and R_{SCM} versus ion dose D.

A second important subject for FIB application is the determination of the width and depth of FIB induced damage below the sample surface. Figure 2 (a) shows the topography of the cleaved, FIB made trench. The corresponding SCM signal is shown in Fig. 2 (b). Again, we optimized the SCM bias to obtain the largest SCM signals in the unimplanted, low-doped areas. Figure 2 (c) compares the topographic and the SCM signal height plotted along line $L_{||}$ parallel to the incident beam. The distance between the trenches side walls and the SCM signal $\Delta R_{||}$ is approximately 620 nm. Previous TEM investigations of deep FIB milled polysilicon show an amorphisized region that extends about 200 nm in depth [8], which is only a third of the distance we have measured.

This can be explained by comparing the detection sensitivity of TEM and SCM. To get contrast in TEM, a crystalline substrate has to be amorphizised to a high extent, which needs relatively high ion doses. On the other hand, SCM is able to detect impurity concentrations down to 10 – 100 atoms per µm^3 (10^{13} - 10^{14} per cm^3), which is magnitudes more sensitive than TEM. Figure 2 (d) shows plots of the topographic and the SCM signal heights along line L perpendicular to the FIB direction. With a certain probability, ions can be scattered out of their incident direction. In this way, they can reach areas not covered by the beam area. The distance between the trenches sidewall and the SCM signal $\Delta R_{\perp}$ is about 310 nm. A comparison between Fig. 2 (d) and Fig. 2 (c)

shows a ratio $\Delta R_{\perp}/\Delta R_{||}$ of 1/2, which is confirmed by previous TEM investigations of FIB induced damage in polysilicon-gates of MOSFETs [8].

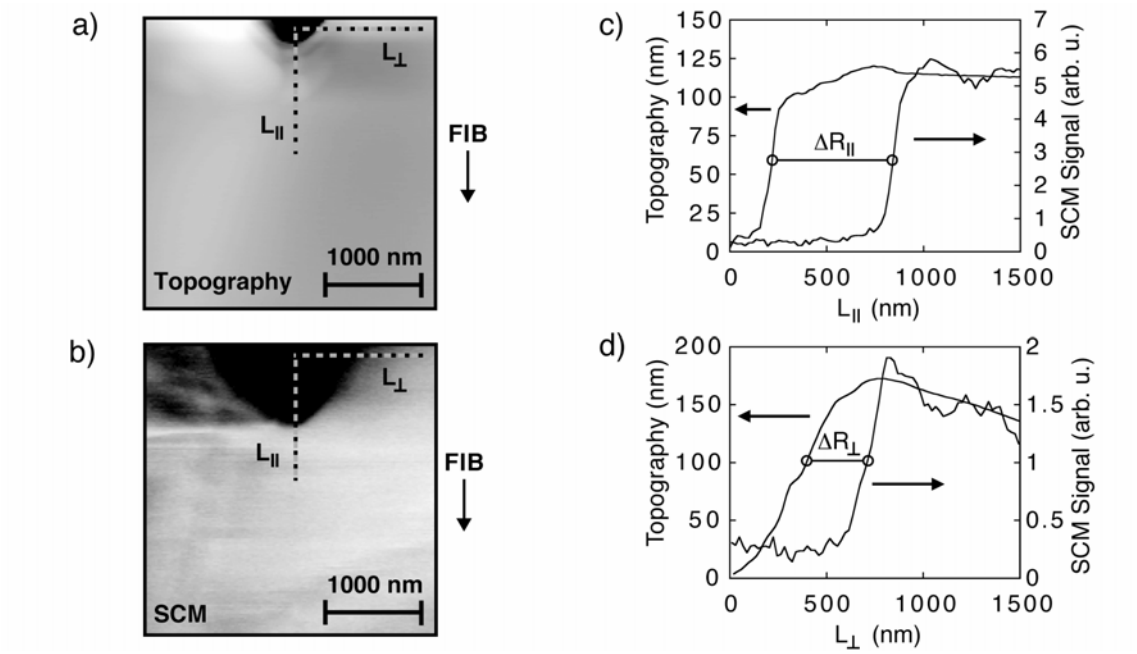

Fig. 2: (a) The topographic image of a FIB milled trench in cross sectional view. The beam direction is indicated. (b) Simultaneously recorded SCM image. (c) Comparison of topographic and SCM signal heights along the line $L_{||}$ parallel to the ion beam. (d) Topographic and SCM signal heights along the line $L_{\perp}$ perpendicular to the incident beam.

Conclusion

In summary, we demonstrated the utilization of SCM for the characterization of FIB processed samples. First, the beam shape of a FIB machine was determined by taking SCM images of spots created by FIB irradiation. Our data indicate a beam shape consisting of a high intensity central region, which decays very quickly when the center is left, and vast tails where the intensity is small but declines more slowly with radial distance. Second, we investigated how deep below the FIB modified surface changes in the structural and electrical properties can be sensed. Damage was detected in much greater depths than reported by other authors, which is probably due to the increased sensitivity of SCM compared to other methods. Finally, the damage depth in the direction parallel to the incident beam and perpendicular to it has been investigated and was found to be in agreement with literature.

Acknowledgements

This work was sponsored by “Fonds für innovative Projekte an der TU Wien”, “Gesellschaft für Mikroelektronik (GMe)” and “Fonds zur Förderung der wissenschaftlichen Forschung (FWF)” project No Z24-TPH.

References

[1] J. Melngailis, J. Vac. Sci. Technol. B5, 469 (1987)

[2] C. Lehrer, L. Frey, S. Petersen, H. Ryssel; J. Vac. Sci. Technol. B19, 2533 (2001)

[3] T. Winzell, S. Anand, I. Maximov, E. L. Sarwe, M. Graczyk, L. Montelius, H. J. Whitlow; Nucl. Instrum. Methods B173, 447 (2001)

[4] D. D. Bugg, P. J. King; J. Phys. E21, 147 (1988)

[5] M. L. O'Malley, G. L. Timp, S. V. Moccio, J. P. Garno, R. N. Kleiman; Appl. Phys. Lett. 74, 272 (1999)

[6] J. Smoliner, B. Basnar, S. Golka, E.Gornik, B.Löffler, M.Schatzmayr, H. Enichlmair; Appl. Phys. Lett. 79, 3182 (2001)

[7] P. D. Rose, S. J. Brown, G. A. C. Jones, D. A. Ritchie; Microelectronic Engineering 41/42, 229 (1998)

[8] A. Lugstein, W. Brezna, E. Bertagnolli; IEEE Internat. Reliability Phys. Symp. IRPS proceedings, 369 (2002)

Post-Process CMOS Channel Profile Tailoring With Focused Ion Beams

A. Lugstein[1], W. Brezna[1], E. Bertagnolli[1], L. Palmetshofer[2]

[1]Institute for Solid State Electronics, Vienna University of Technology
[2]Inst. f. Semiconductor- and Solid State Physics, University Linz, Austria

This paper presents a novel approach of lateral profile engineering addressing sub-lithographic dopant spikes in the MOS channel region. In contrast to conventional approaches, our focused ion beam based method needs only one single dopant activation and damage anneal step avoiding unwanted effects like TED of the implanted species and broadening respective washout of the dopant profiles. We show the viability of this approach to engineer CMOS devices by *in situ* monitoring the impact of the ion beam on device performance, and we prove peak channel implants to gain devices with superior I_{on}/I_{off} ratios and enhanced short channel effect control.

Introduction

In order to overcome the leakage/I_{Dsat} tradeoffs and detrimental short channel effects (SCE) of MOS devices in the deep submicron regime, recent investigations focus on optimized MOSFETs incorporating sharp, sub-lithographic doping peaks, preferably at the source side of the channel [1]. As simulation studies explained [2], the I_{on}/I_{off} ratio of MOS devices can be greatly improved by the introduction of peaking channel dopings. These tripartite channel MOS devices (further on denoted TMOS) should be much less prone to hot carrier degradation due to reduced electric fields, and furthermore less affected by DIBL, thus being easier to scale into the ultra-deep submicron regime. The purpose of this work is to explore the FIB as a high resolution restructuring tool for front end prototyping.

Device Fabrication

In contrast to all work done up to now, in which the doping peaks were implanted during a baseline CMOS process [1] prior to the gate-oxide formation, we implement the doping peak at the very end of the front-end process.

By a masked through-gate implantation, thermal cycling can be reduced to the minimum necessary to eliminate damage and to guarantee dopant activation. The implantation peaks are located at the center of the channel (symmetric device indexed by s) and one quarter off the center (asymmetric device indexed by a) (Fig. 1).

The devices are fabricated relying on preprocessed, fully featured MOS devices with planar silicon gate technology, LDD structure incorporating n^+ polysilicon gates and 9 nm gate oxides. The effective channel length is 0.6 µm for p-MOS and 0.75 µm for n-MOS devices. These n/p-MOS devices are subjected to gallium and phosphorus implants via hard masks, yielding narrow p^+, respectively n^+ regions, dividing the channel into three sections (Fig. 1).

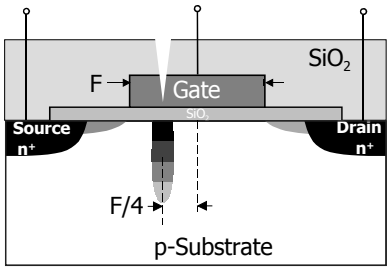

Fig. 1: Schematic of a tripartite n-channel MOSFET (n-TMOS) device with implantation hard mask in an asymmetric configuration.

The implantation windows are formed on top of the gate stack by means of a focused ion beam scheme. The TEM image in Fig. 2 shows a cross section of the implantation trench. All implantation windows for the devices have footprints below 30 nm, thus addressing a sufficiently small aspect ratio respective to the gate related feature sizes.

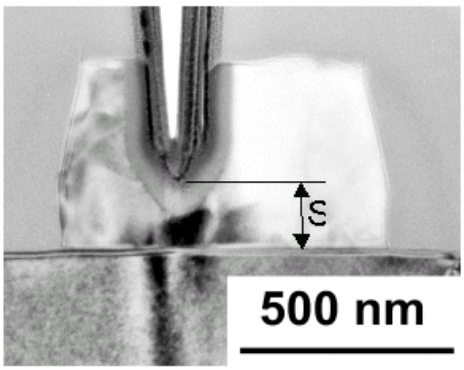

Fig. 2: TEM image of the TMOS with remaining gate seat S

The milling of the implantation trench with Focused Ion Beam is controlled by *in situ* electrical testing. Figure 3 exhibits the drain and gate current during FIB milling of the implantation trench.

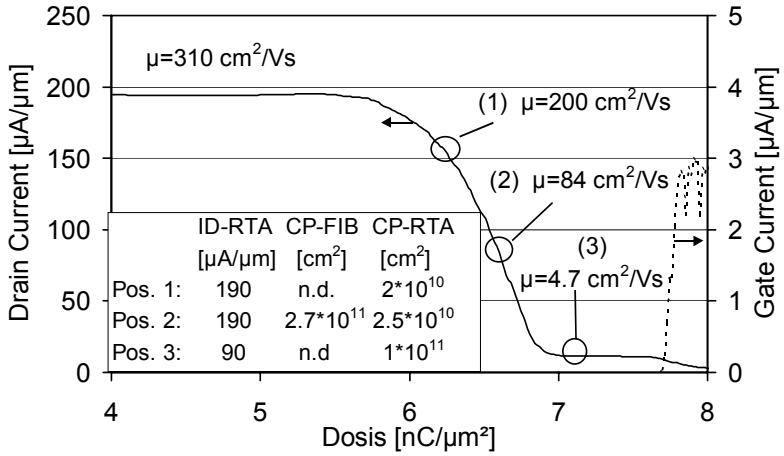

Fig. 3: MOSFET degradation due to FIB milling ($V_G = V_{DS} = 3$ V).

Despite of the fact that the extension of the amorphous region is kept fairly distant to the interface, the transistor begins to degrade due to the decreases of the electron mobility in the disturbed channel region. Charge pumping measurements indicate the formation of interface traps as far as the gate seat approaches 300 nm. Position (2) in Fig. 3 marks the final milling depth with a minimum gate seat of 220 nm. Up to that point, the entire FIB induced damage could be annealed out by an RTA process, and all substantial transistor characteristics could be completely recovered.

Device (dopant)	D[ions/cm^2] E [keV]	V_{th} [mV]	I_{leak} [A/µm]	I_{Dsat} [µA/µm]	SS [mV/dec]
conv. n-MOS	none	509	$1x10^{-13}$	402	82
n-TMOS$_a$ (Ga)	$2x10^{13}$/300	1018	$3x10^{-15}$	319	98
n-TMOS$_s$ (Ga)	$2x10^{13}$/300	1025	$7x10^{-16}$	59	99
n-TMOS$_s$*) (Ga)	5e12/300	842	$5x10^{-14}$	318	103
conv. p-MOS	None	-729	$2x10^{-16}$	196	85,7
p-TMOS$_a$ (P)	$2x10^{13}$/180	-876	$4x10^{-18}$	163	84.6

*) n-TMOS with low dose peak implantation

Tab. 1: Device parameters: implantation dose and energy, threshold voltage, leakage and saturation currents, and the sub-threshold swing.

Electrical Results

Charge pumping was used to determine the interface state density and the residual damage after through-gate implantation and proper post-treatment. Figure 4 exhibits the efficiency of the RTA process for damage anneal.

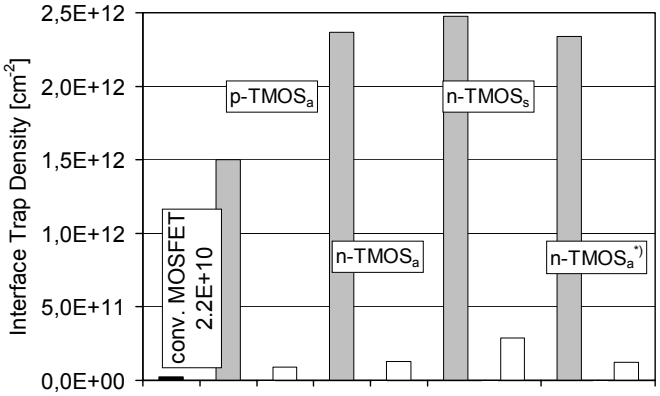

Fig. 4: Interface trap density of MOSFET and TMOS devices after through gate implantation (grey bars) and after RTA processing (white bars).

As expected, the interface trap densities correlate with implantation doses and with ion species, but depend evidently much stronger on the doping peak positioning within the channel. In the asymmetric case the damage cascades overlap with the highly doped S/D region, therefore part of the defects are electrically not detectable. The sub-threshold characteristics shown in Fig. 5 exhibit regular behavior and show off-state leakage currents one to two orders of magnitude lower compared to the conventional MOS devices.

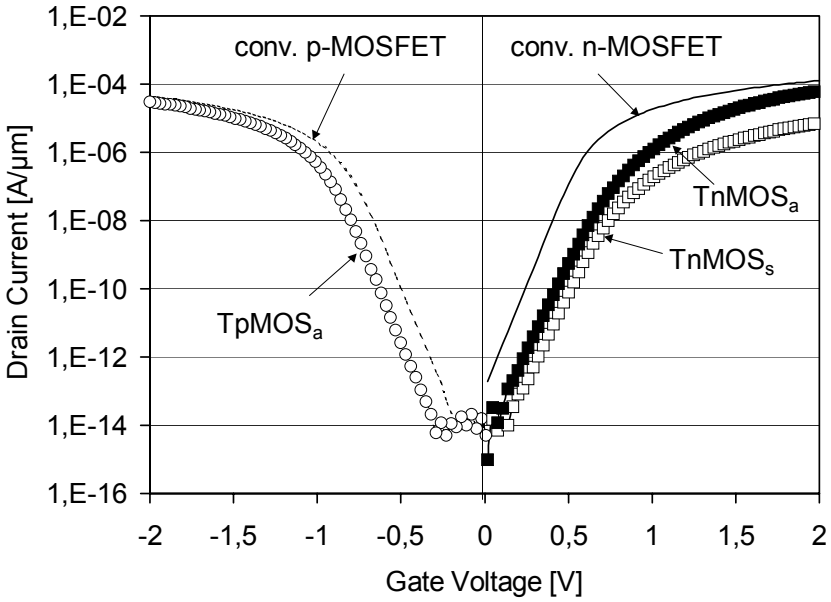

Fig. 5: Comparison of the sub-threshold characteristics for conventional MOSFET and TMOS devices (U_{DS} = 2 V).

The increase of threshold voltage is shown in Tab. 1. The gate drive characteristic in Fig. 6 exhibits the expected improve of the output resistance [1] of the TMOS device with even higher output currents for low gate voltages.

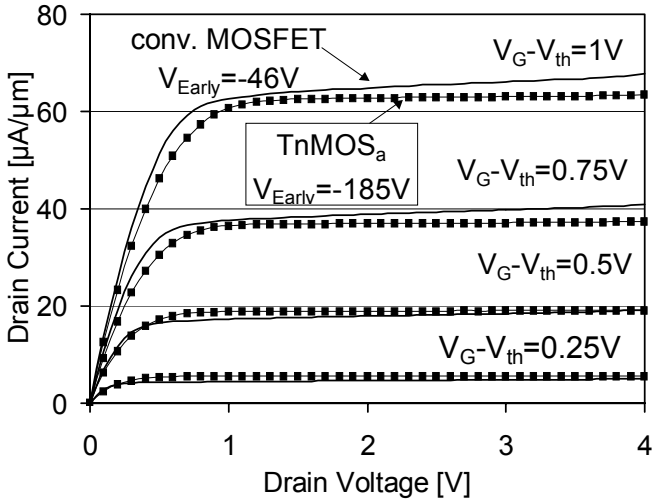

Fig. 6: Gate drive characteristic for the asymmetric n-channel TMOS$_a$ and conventional n-MOSFET device.

Beside the improved device performance, TMOS devices also exhibit enhanced SCE resistance, whereby the placement of the doping peak relative to the LDD extension junction is critical. Figure 7 exhibits the improved DIBL tendency of TMOS. Under reverse biasing conditions, the improved DIBL resistance is kept for the symmetric TMOS devices whereas for the asymmetric device the DIBL gets even worse.

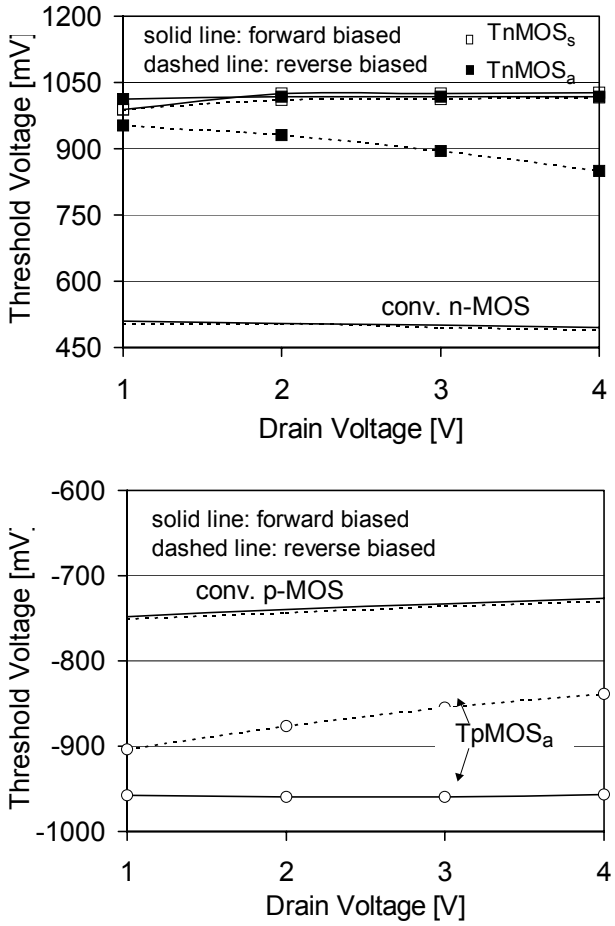

Fig. 7: V_{th}-V_D characteristics of n- and p-MOS devices.

According to the exponential dependence of hot electron degradation on the magnitude of the lateral drain electric field as predicted by simulation results [2] the I_{SUB}/I_{DS} ratio of n- as well as p-channel TMOS devices is 30% lower than that of the conventional MOSFET. The improved resistance to punchthrough of n- and p-TMOS devices is shown in Fig. 8.

Summary

This paper presents a novel technology of lateral profile engineering addressing tripartite channel MOS devices. For the first time MOS devices with highly nonuniform 2-D doping profiles are achieved by post-process implantation of channel doping peaks. In contrast to the conventional approach our focused ion beam based method needs only one moderate dopant activation and damage anneal avoiding unwanted effects like TED of the implanted species and broadening respective washout of the dopant profiles. We have shown, that post implantation can be successfully implemented to form TMOS devices with excellent I_{on}/I_{off} ratios and short channel effect control.

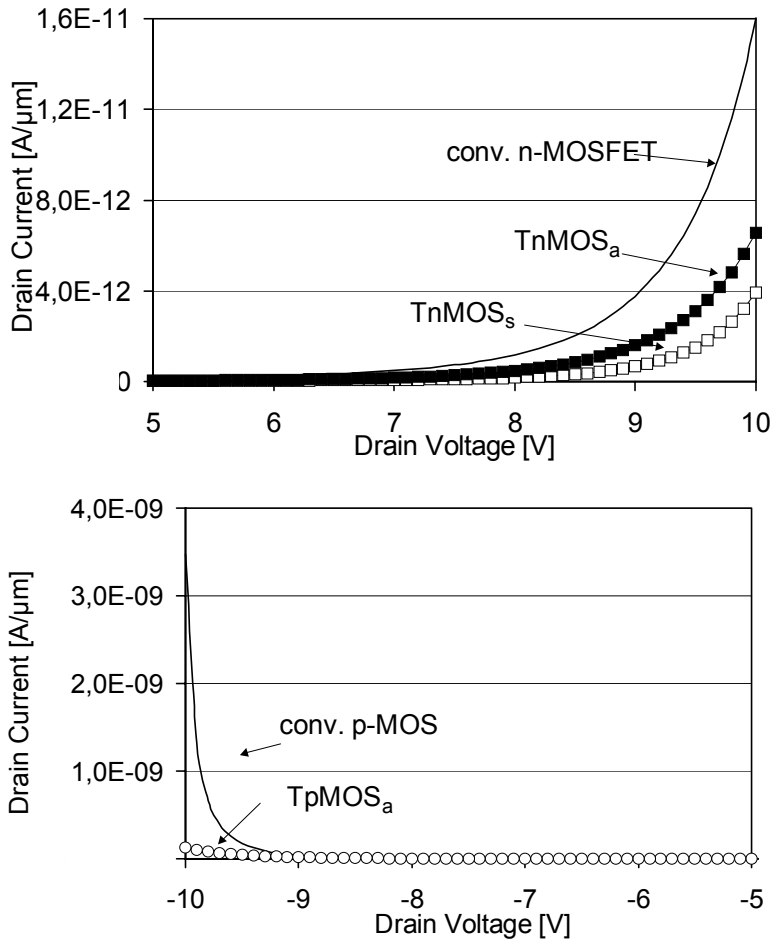

Fig. 8: Punchthrough characteristics of n-MOS devices.

References

[1] C.C. Shen, J. Murguia, N. Goldsman; M. Peckerar, J. Melngailis and D.A. Antoniadis; *IEEE Transactions on Electron Devices*, vol 45, 2, 1998.

[2] M. Stockinger, A. Wild, S. Selberherr; *The Peak Device Microelectronics Journal*, vol. 30, 3, 1999

Deposition Mechanism of Direct-write Processes – An Application-Oriented Approach to Custom-Tailored Material Properties

H.D. Wanzenboeck, S. Harasek, H. Langfischer, E. Bertagnolli

Institute for Solid State Electronics, Vienna University of Technology

Chemical vapor deposition (CVD) utilizes the adsorption and decomposition of a volatile gaseous species on a sample surface. For coating of large areas thermal CVD or plasma enhanced CVD has been established as versatile deposition technique for dielectrics and metals. In contrast to large area coating techniques, a local direct-write technique is introduced using a focused energetic beam to provide the necessary activation energy for CVD. With a focused ion beam, material has been locally deposited within a strictly confined area down to the nanometer range. For this direct-write nanodeposition of silicon oxide, two precursor gases – siloxane and oxygen – have to be added simultaneously. For this local CVD process, an exposure by a scanning beam (FIB) followed by a waiting time allowing for new re-adsorption of the precursor is required. An influence of the different ion exposure times per scan and an effect of the mixture ratio of precursors in the gas phase have been observed. The chemical composition of the solid silicon oxide and the physical properties can be tailored to demand by deliberate changes of process parameters. The beneficial aspects of the process versatility are demonstrated by deposition of insulating layers, structures with smooth surfaces, and 3-dimensional structures.

Introduction

Chemical vapor deposition (CVD) has become extremely popular in microelectronic manufacturing. Due to the versatility of the process CVD is the preferred deposition technique for a wide range of materials – especially for dielectric compound materials. [1]. The requirement for specific shapes of dielectric material in specific functional units has led to the fact that structuring the layer fabricated by CVD is as crucial as the deposition process itself. Multiple process steps including optical lithography followed by chemical etching are the predominantly used approach for structuring. Not only that etching raises the critical issues of material selectivity and etch stop layers, the lithographic approach requiring a specific photomask for every design is very inflexible and time consuming before the first device can be produced. For mass production, the lithographic approach remains unmatched in high throughput and economical value. For rapid prototyping and for 3-dimensional devices an alternative strategy has been sought for a long time.

Recently, direct-write processes utilizing a focused beam of ions, photons or electrons have shifted in the focus of increased interest, as they combine deposition and patterning in a single step [2]. A local gas atmosphere is maintained by introducing the precursor components via a micro-nozzle system [3]. The reaction energy is brought in by energetic ions so that the deposition only occurs in the confined area where the incident ions strike the sample surface [4]. In contrast to large area CVD that needs subsequent lithographic structuring, FIB-CVD allows depositing material while simultaneously obtaining the required structures [5], [6]. This sophisticated technique finally closes the long endured gap between the demand for high-qualitative dielectric material on one hand and a quick prototyping technique for device development on the other hand.

However, the multitude of process parameters with FIB-CVD does not allow a straightforward control of the deposition process, but requires extensive knowledge of the process and the chemical reaction. In this study, both the chemical parameters such as gas phase composition and the beam-related parameters such as pixel spacing have been investigated. The gained process knowledge allows selecting in advance material quality, the deposition rate, and the surface roughness of the deposited layers. An optimum process range has been identified yielding silicon oxide with low contamination and high electrical resistivity [7]. This technique will facilitate the application for fabrication of nanostructured materials in micromachining, MEMS, and for modification of interconnects of microelectronic circuits [8] – [10].

Experimental

Focused beam induced CVD utilizes a focused ion beam with a spot size in the nm regime to initiate the deposition reaction on an arbitrary surface. This maskless direct-write technology facilitates the additive fabrication of dielectric material and structuring towards functional units within a single process step. By guiding the scanned beam, the CVD can be used to deposit pattern designs. Due to the small spot diameter, material deposition can be restricted to the nanometer range so that 3-dimensional nanostructures can be fabricated.

A gas mixture of siloxane (tetramethylcyclotetrasiloxane) and oxygen has been used as chemical precursors to facilitate the deposition of silicon oxide. A focused ion beam of Ga^+ ions has been employed to induce the chemical reaction of the components adsorbed on the substrate surface. As the maintenance of a focused particle beam requires vacuum condition (base pressure 10^{-6} mbar), the chemical precursor compounds were introduced via a micro-nozzle system positioned in close vicinity to the deposition area. The co-adsorbed components are decomposed under formation of silicon oxide by the secondary ions and secondary electrons generated by the impact of the 50 kV Ga^+ ions.

The visual inspection of the deposited structures was performed *in situ* by FIB-imaging recording the secondary electron signal during the beam scan. For purposes of illustration of 3-dimensional structures, the sample surface was tilted during imaging to yield an advantageous view angle. Deposited pads (100 x 100 µm) were used for chemical characterization of the material by secondary ion mass spectroscopy (SIMS) and by Auger electron spectroscopy. The sample surface was pre-cleaned by *in situ* ion milling to remove adsorbed surface species. The characterization of the surface roughness was determined by high resolution transmission electron microscopy (HRTEM) imaging of cross-sections of the deposited layers or by atomic force microscopy (AFM) using tapping mode scans.

Results

With direct-write deposition techniques, arbitrary structures were grown by defining the scan area of the focused beam with a pattern generator. Three-dimensional structures and large layers covering areas up to 1 x 1 µm were deposited without stitching. The dwell time of the beam on a single pixel of the scan was kept short enough to provide a sufficient surface adsorption of precursor for the deposition process. A long exposure of a single spot leads to complete consumption of the adsorbed precursor. This results in increased ion milling and high contamination by Ga and C. The control of the scan area and the scan parameters were shown to be suitable parameters for the custom tailoring of structural features and the surface topology.

Custom-tailoring of structural features

The repetition of the exposure with the energetic beam primarily defines the thickness of the deposited layer. The chemical reaction to deposit material locally is triggered by the energy of the focused energetic beam. By restricting the exposure area on a 2 x 2 µm area and choosing a high repetition of the exposures, pillars with a high aspect ratio of 15:1 could be fabricated (Fig. 1) The efficiency of the deposition was found to depend on the dwell time per exposure cycle and the pixel spacing. By tilting the surface plane during deposition, inclined structures could be deposited (Fig. 1).

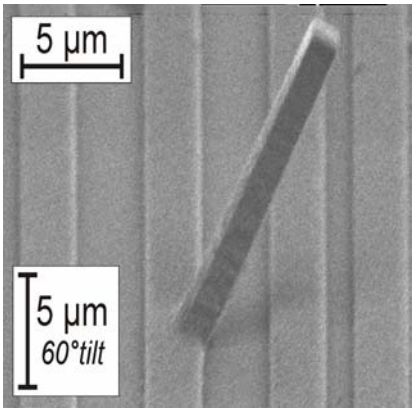

Fig. 1. FIB-deposited 2 x 2 µm pillar made of dielectric material with a total height of 30 µm total. The pillar is deposited with a controlled 30° tilt to the sample surface.

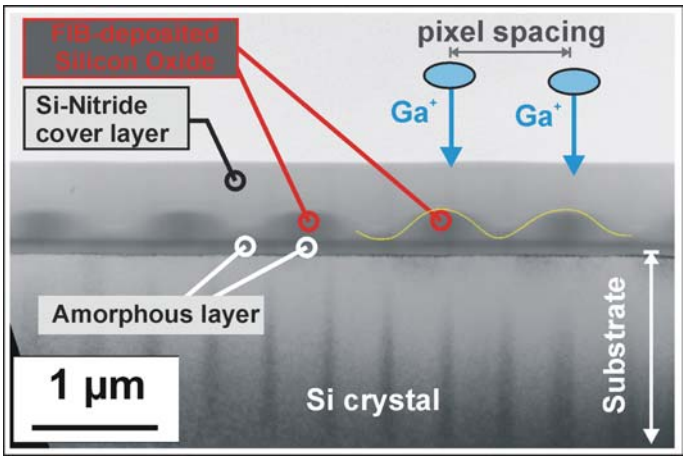

Fig. 2. TEM - cross section (left) Silicon oxide was deposited with a 1 µm pixel spacing of a 300 nm beam. A pattern of deposited bumps was obtained allowing to generate a predefined surface roughness.

In previous studies, the influence of the pixel spacing on the chemical composition of the deposited silicon oxide was confirmed. By choosing a large pixel spacing exceeding the diameter of the focused beam also the morphology can be influenced deliberately. By adjusting the pixel spacing during the deposition scans larger than the beam diameter, an intentional surface roughness can be generated. By depositing silicon oxide with a pixel spacing of 1 µm, a repeated pattern of depositions could be produced. The cross-section of this layer shows distinguishable bumps of silicon oxide

with a periodicity of the pixel spacing and a height of 200 nm (Fig. 2). The FIB-deposited material was covered with a protective layer of silicon nitride to inhibit artifacts during polishing of the ultrathin cross-section for HRTEM-imaging. By adjusting the pixel spacing small enough to produce a beam overlap, smooth surfaces with a RMS roughness of 3.2 nm were obtained according to AFM measurements. However, the deposition efficiency was observed to decrease with narrow pixel spacing. It is assumed that the consumption of precursor in overlapping beam spots exceeds the re-adsorption rate from the gas phase, so that the sufficient precursor coverage is not assured any longer.

Chemical Composition

The gas composition was observed to have a fundamental influence on the deposited material. As mentioned before, refresh times between the single scans were chosen long enough to work under steady-state conditions excluding diffusion-limited kinetics. With two precursor components silicon and oxygen, those substances are undergoing permanent competitive co-adsorption on surface sites. Their mixture ratio in the gas phase and the total gas pressure above the sample is decisive for the adsorption status. The surface concentrations of every precursor species are influencing for the chemical composition of the deposited dielectric (Fig. 3). Using only pure tetramethylcyclotetrasiloxane $Si_4O_4C_4H_{16}$, an atomic ratio of Si:O = 1:1 is already given. Adding molecular oxygen O_2 shifts the ratio towards higher oxide contents.

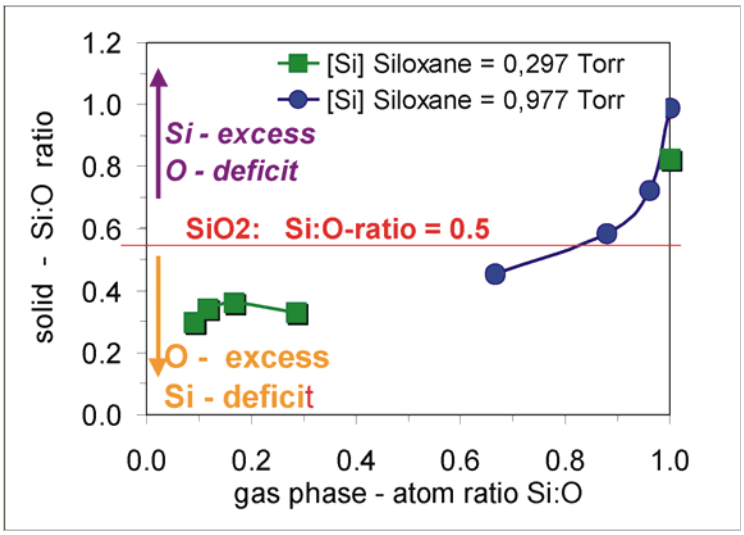

Fig. 3: Si:O atom ratio in deposited solid silicon oxide in correlation to the Si:O atom ratio in the precursor gas mixture. (The siloxane (TMCTS) has a Si:O atom ratio of 1:1. The addition of O_2 changes this ratio.)

The highest purity of deposited silicon oxide could be obtained at a ratio of TMCTS:O_2 = 1:10, reflecting an atomic ratio of Si:O = 1:6. At this mixture ratio, carbon contaminations have dropped below the detection limits of Auger electron spectroscopy, and the Ga implantation is in the range of 10%. In addition, the total pressure of the gas mixture has a significant influence on the deposited material (Fig. 3). A high total pressure was found to be beneficial for the deposition of silicon oxide close to the stoichiometric 1:2 composition of SiO_2. Selecting a precursor gas mixture with a high total pressure and an excess of oxygen, a silicon oxide with low contaminations and a composition close to silicon dioxide was deposited.

Conclusions

Direct-write deposition by a focused energetic beam allows local deposition of dielectric material with a feature size down to the deep sub-µm range. In this work, utilization of a focused ion beam (FIB) for deposition is described as an unorthodox type of chemical vapor deposition (CVD) using the energy of the energetic beam to initiate the chemical reaction only in a confined region.

Experimental results demonstrate the versatility of this method. Direct write deposition allows for custom tailoring of 3-dimensional structures by scanning the beam in a pre-defined pattern. FIB-CVD allows fine-tuning the chemical composition of the deposited material by controlling the gas atmosphere. Furthermore it has been shown that the surface roughness can be modified by deliberate control of the process parameters.

This unmatched flexibility of direct-write deposition of dielectrics bears the potential of becoming a key technology for rapid prototyping of electronic devices as well as for the development of micromechanical systems and for the repair of optical components and photomasks.

Acknowledgement

This work was performed with financial support of the Austrian Society for Microelectronics (Gesellschaft für Mikroelektronik). Erich Gornik (Vienna University of Technology) is thanked for providing the cleanroom of the microstructure center (MISZ) for the fabrication of devices. Herbert Stoeri (Vienna University of Technology) is acknowledged for performing the chemical analysis by Auger spectroscopy. We are grateful for the support of Peter Pongratz for his support in the TEM characterization of sample cross-sections.

References

[1] A. Sherman, In A. Sherman (Ed.) "Chemical Vapor Deposition for Microelectronics: Principles, Technology, and Applications", Noyes Publishing, Park Ridge N J, 1987

[2] J. Melingailis,J. Vac. Sci. & Technol. B 5(2), 469

[3] K. Edinger, J. Melngailis, J. Orloff, J. Vac. Sci. Technol. B 16(6), 3311, (1998)

[4] Y. Tanak., M. Karashima, K. Takanashi; T. Sakamoto, M. Owari, Y. Nihei, Appl. Surf. Sci. 203-204, 205 (2003)

[5] S. Matsui, T. Kaito, J. Fujita, M. Komuro, K. Kanda, Y. Haruyama, J. Vac. Sci. Technol. B, 18(6); 3181 (2000)

[6] S. Reyntjens, R. Puers, J. Micromech. Microengineering 10(2), 181 (2000)

[7] S. Lipp, L. Frey, C. Lehrer, B. Frank, E. Demm, S. Pauthner, H. Ryssel, 14(6), 3920 (1996)

[8] K. Gamo, Microelectronic Engineering 32(1-4), 169 (1996)

[9] M. Langford, G. Dale, P.J. Hopkins, P.J. Ewen, K. Petford-Longi, J. Micromech. Microengineering 12(2), 111 (2002)

[10] J. Fujita, M. Ishida, T. Sakamoto, Y. Ochiai, T. Kaito, S. Matsui; J. Vac. Sci. Technol. B19(6), 2834 (2001)

Zirconium Dioxide Thin Films for Microelectronics Deposited by Metal Organic Chemical Vapor Deposition

S. Harasek, H.D. Wanzenböck, B. Basnar, J. Smoliner, and E. Bertagnolli

Institute for Solid State Electronics, Vienna University of Technology

The metal-organic chemical vapor deposition (MOCVD) of ultrathin zirconium dioxide from $Zr(tfacac)_4$ on (100) silicon is thoroughly investigated. Physical characterization addresses the evolution of surface topography and the impact of processing parameters on the chemical composition of the films to provide a sound basis for the discussion of electrical properties. Electrical investigation by means of MOS structures has been performed to assess the interface quality and the dielectric properties of the layers. Interface trap density is observed to be around 5.10^{11} $cm^{-2}.eV^{-1}$ at midgap for (100)-oriented substrates. Leakage currents in the ultrathin regime are significantly reduced compared to equivalent SiO_2-layers. The temperatures throughout the gate insulator formation process do not need to exceed 650 °C, and thus allow keeping the thermal budget low.

Introduction

Currently the search for a suitable high permittivity dielectric for the forthcoming replacement of SiO_2 as gate dielectric in leading-edge complementary MOS (CMOS) devices provides enormous impetus in this field of materials science. Yet, the identification of a suitable material may only be considered a partial success, since besides the material's properties themselves the entity of material and deposition method must meet the requirements for compatibility with CMOS technology.

While the various methods based on physical vapor deposition (PVD) provide a convenient means for the evaluation of materials systems for alternate dielectric applications, technological considerations concerning device morphology in general rule out such line-of-sight PVD processes as stated by G.D. Wilk *et al.* [1]. On the other hand, different methods of chemical vapor deposition (CVD) have proven quite successful in providing uniform coverage over complicated device topologies. Therefore, our approach utilizes MOCVD, which in general allows processing at lower temperatures than CVD from inorganic precursors.

Group IVB oxides and materials based on these oxides are among the most promising candidates for the succession of SiO_2 as gate dielectric. This is mainly due to their dielectric constants around 20 and – maybe of even higher importance – the sufficient band-offsets provided towards silicon (as displayed in Fig. 1) to suppress tunneling.

We evaluate the properties of thin films of zirconium dioxide with equivalent oxide thicknesses (EOTs) down to the 2 nm range. Chemical composition, surface topography and electrical properties are examined in dependence on thin film processing.

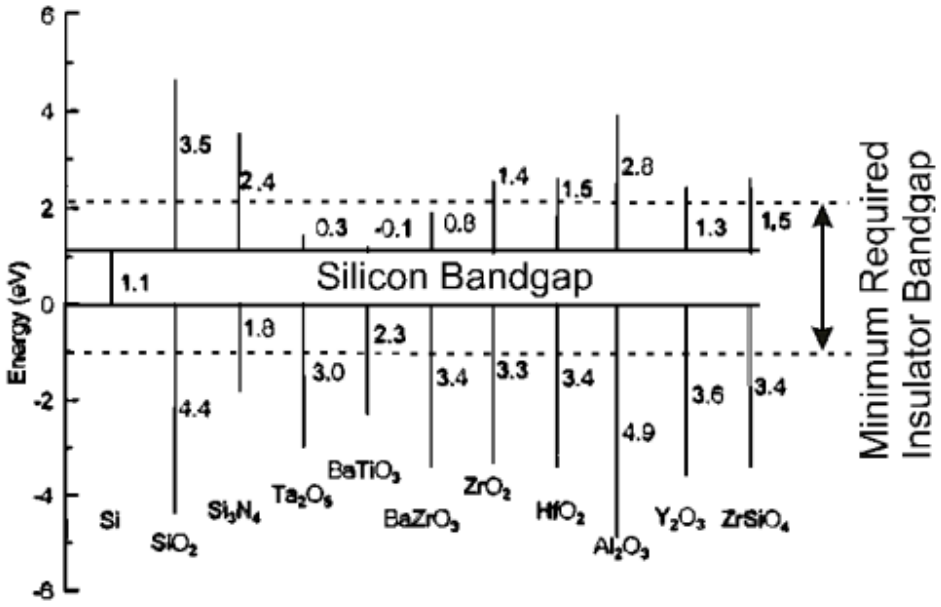

Fig. 1: Band-offsets in respect to silicon provided by several high-k materials. Minimum requirements are indicated (adapted from [2]).

Experimental

Thin films were deposited on p-type silicon (100). The deposition apparatus consisted of a horizontal hot wall reactor with a bubbler system for the delivery of the metal-organic precursor substance. Zirconiumtetrakistrifluoroacetylacetonate was used as precursor due to the favorable properties of this substance in terms of stability and volatility. A detailed description of the deposition process is given in [3]. In order to improve thin film properties different annealing procedures were tested. Oxidizing (20% oxygen in nitrogen) as well as reducing (forming gas, 10% hydrogen in nitrogen) atmospheres were used during annealing at 650 °C. The chemical composition of the films was analyzed by Auger electron spectroscopy (AES) before and after annealing. Surface topography of the deposited films was examined by atomic force microscopy (AFM). For the evaluation of the electrical properties of the thin films, MOS capacitors were constructed. Capacitance-voltage (C-V) and current-voltage (I-V) measurements provided information about EOT, trap and charge densities as well as leakage currents.

Results and Discussion

Topography of the deposited films was evaluated by AFM. The relative roughness ($R_{a,\,rel}$) as the ratio of absolute roughness R_a and total film thickness was used for comparison of the results. This evaluation shows a deposition at 450 °C to result in minimum surface roughness. The graph on the left in Fig. 2 presents the evolution of the relative surface roughness for films with thicknesses up to about 400 nm. The AFM surface plot to the right of Fig. 2 shows that for very low film thicknesses much smoother films – on absolute and relative scale – are obtained. The roughness of the 15 nm thick film amounts to only R_a = 0.135 nm, equaling less than 1 % relative roughness.

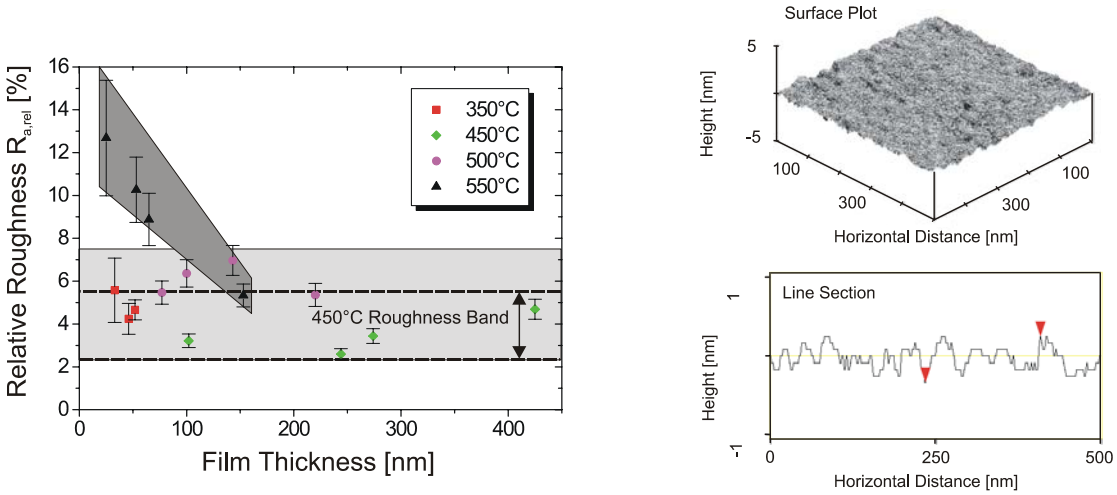

Fig. 2: Left: The evolution of surface roughness with film thickness for thicknesses up to 400 nm. 450 °C deposition temperature leads to smoothest films. Right: AFM surface plot of a 15 nm ZrO_2 thin film deposited at 450 °C. A surface roughness of R_a = 0.135 nm is observed with a peak-to-peak roughness of 0.58 nm in the displayed line section.

This improvement of the film smoothness in the ultrathin film region may be connected to a change in the crystallinity of the films. While transmission electron microscopy (TEM) showed thicker films to be polycrystalline, the smoother surface of the thinnest films possibly points to an amorphous state of these films. However, definitive results are not available by now, and the issue deserves closer attention and clarification by high-resolution TEM examination.

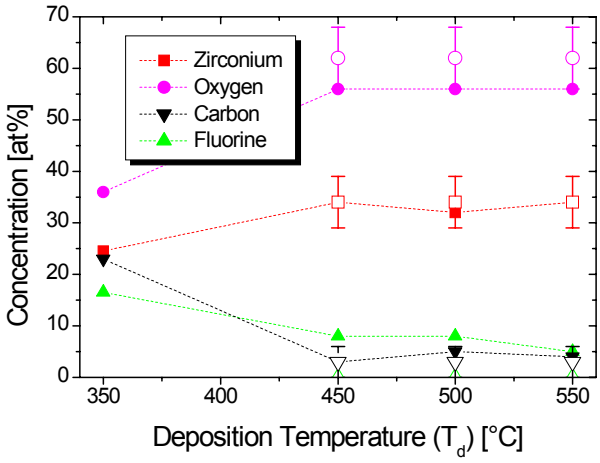

Fig. 3: Chemical composition of thin films deposited at various temperatures (full symbols) and composition achieved after post-deposition annealing (open symbols). For reasons of clarity, the estimated error is indicated for the composition after annealing only.

Figure 3 shows the chemical composition of the films in dependence on the deposition temperature. The unfavorable effect of a too low deposition temperature is clearly discernable, while for medium temperatures a constant film composition is observed only suffering a slight oxygen deficiency. After annealing in either diluted oxygen or forming gas at temperatures of 650 °C or above, the film composition closely approaches the stoichiometric composition ZrO_2. After temperature treatment, the remaining carbon impurities are at a negligible level at the limit of detection.

Al-ZrO_2-p^+Si capacitor structures served as test vehicles for the evaluation of the electrical characteristics of the processed thin films. EOTs down to the 2 nm range have been realized sustaining favorable dielectric and interface properties. Figure 4 displays on the left the C-V curve of a MOSCAP featuring a dielectric with 2 nm EOT of zirconium dioxide as obtained after annealing in diluted oxygen. A flatband voltage shift (ΔV_{FB}) of about –600 mV and minor distortion near midgap is observed in a generally well-behaved curve. The C-V plot on the right side shows that ΔV_{FB} as well as the distortion near midgap are minimized if forming gas is used as annealing atmosphere. However, in this case only EOTs down to about 3 nm are accessible, while post-deposition annealing in an oxidizing atmosphere was found to further reduce EOT.

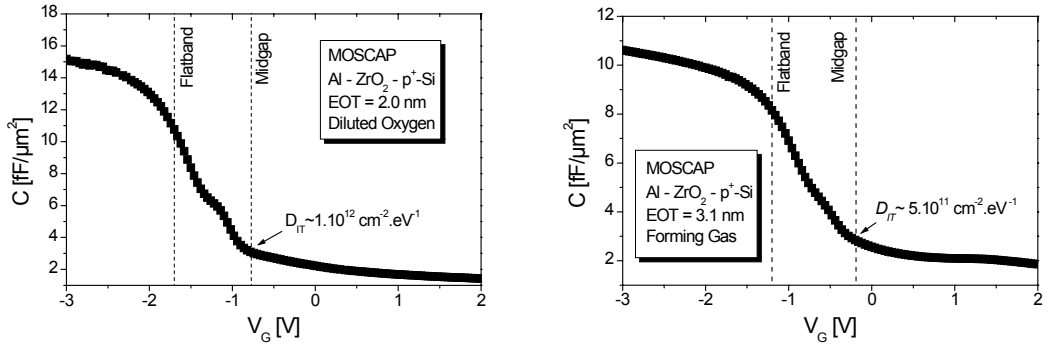

Fig. 4: C-V curves of MOSCAPs with ZrO_2 dielectrics annealed either in diluted oxygen (left) or forming gas (right). Lower EOTs are observed after annealing in oxygen, while electrical characteristics are more favorable after annealing in forming gas.

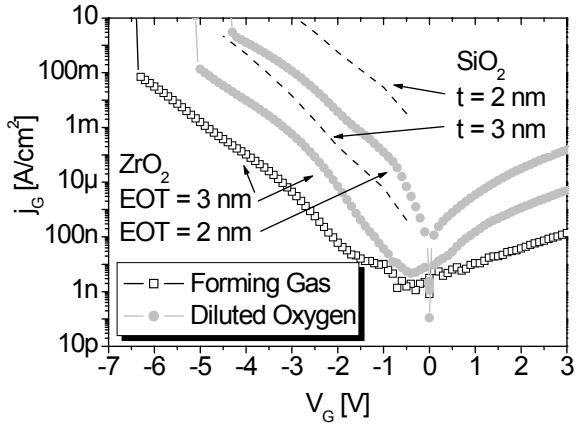

Fig. 5: I-V properties of Al-ZrO_2-p^+Si MOSCAPs. A more than three decades lower leakage than in SiO_2 is observed for ZrO_2 after annealing in forming gas. SiO_2 leakage characteristics are extracted from [4], [5].

Using Terman's method, interface trap densities (D_{IT}) of differently annealed samples were computed. For samples annealed in forming gas, D_{IT} values around 5.10^{11} $cm^{-2}.eV^{-1}$ are usually obtained. Comparable samples annealed in diluted oxygen displayed a higher D_{IT} in all cases. The I-V properties of the thin films are depicted in Fig. 5. For both kinds of anneal ZrO_2 provides a significant decrease in gate leakage compared to SiO_2. A reduction of leakage by more than a factor of 10^3 can be accomplished for 3 nm EOT. Again a forming gas anneal proves advantageous for optimization of the material's performance, suggesting the formation of a large amount of additional charges and traps during annealing in the oxidizing atmosphere. Overall, the impact of the annealing atmosphere on the electrical properties of the films is much stronger than expected from compositional analysis.

Conclusion

The formation of high-quality ZrO_2 thin films on silicon by MOCVD has been successfully demonstrated. Compositional as well as electrical characterization unveils promising properties of the thin films down to the 2 nm EOT range. Throughout the gate insulator formation, processing temperatures do not require to exceed 650 °C, keeping the thermal budget low. Owing to these circumstances, further research to establish film deposition from metal-organic precursor substances in silicon technology is encouraged.

Acknowledgements

The authors would like to thank Josef Brenner and Prof. Herbert Stoeri of the "Institut für Allgemeine Physik" for Auger analysis.

References

[1] G.D. Wilk, R.M. Wallace, J.M. Anthony: *J. Appl. Phys.* **89**, 5243 (2001).

[2] J. Robertson: *J. Vac. Sci. Technol. B* **18 (3)**, 1785 (2000).

[3] S. Harasek, H.D. Wanzenboeck, B. Basnar, J. Smoliner, J. Brenner, H. Stoeri, E. Gornik, and E. Bertagnolli: *Thin Solid Films* **414**, 199 (2002).

[4] K. F. Schuegraf and C. Hu: *Semicond. Sci. Technol.* **9**, 989 (1994).

[5] B. Brar, G. D. Wilk, and A. C. Seabaugh: *Appl. Phys. Lett.* **69**, 2728 (1996).

Microelectronics Technology — Cleanroom Linz

Micro- and Nanostructure Research: Cleanroom Linz

G. Bauer, H. Heinrich, H. Thim, G. Brunthaler

Institut für Halbleiter- und Festkörperphysik, and Institut für Mikroelektronik,

Johannes Kepler Universität Linz, A-4040 Linz, Austria

The micro- and nanostructure research in the cleanrooms of the “Institut für Halbleiter- und Festkörperphysik” and the “Institut für Mikroelektronik” is supported by the Society for Microelectronics (GMe).
For Si/SiGe heterobipolar transistors, the incorporation of carbon was investigated in order to control the contamination for standard Si technology. In addition, self organized growth schemes for the development of nanoscale devices were studied in MBE deposition. In particular, on prepatterned Si substrates two dimensionally ordered Ge islands were deposited and a much narrower size distribution than previously reported was obtained. The interface roughness of Si/SiGe quantum cascade samples was investigated by x-ray reflectivity. The spin properties of Si quantum wells were investigated by electron-spin-resonance in order to contribute to quantum information technology. For two-dimensional GaAlAs structures, a modified ‘Hot Electron Injection Field Effect Transistor’ was developed by utilization of the ‘Gunn’ effect. Also quantum dots were fabricated and studied for the same material system. Optical properties were studied in the light emission of Er-doped Si and in lead-salt based vertical cavity surface emitting lasers. Photocurrent and photoluminescence experiments have been performed on self-assembled Si/SiGe quantum dots and quantum cascade injector structures. The growth of group III-Nitrides for optical applications in the blue region of the visible spectrum was systematically studied in an MOCVD system. The investigation of photonic crystals by a Christian-Doppler laboratory has been started in the same cleanrooms in Linz.

The funding of the activities in the two cleanrooms at the University of Linz, which are jointly used by three groups, is of vital importance for our micro- and nanostructure research activities. This basic funding allows for investigations that are made possible through additional funding coming from the FWF, the FFF, the European Commission, as well as through cooperations with industrial groups as listed in the report.

The activities of the year 2002 in the cleanrooms in Linz are described in a short overview here. The basic equipment that is available in these clean rooms allows for MBE growth of Si-based heterostructures, of II-VI and IV-VI heterostructures, for the deposition of ferromagnetic layers like Fe on II-VI compounds, as well as for MOCVD growth of III-V compounds like GaAs/GaAlAs and GaAs/GaInAs. The latest extension to those material systems happened with a European Project on the in-situ control of GaN deposition by MOCVD. Apart from in-situ and ex-situ structural characterization, lateral patterning is made possible through equipment like optical, holographic and electron beam lithography. Processing includes also facilities for the deposition on insulating as well as contact layers; in particular, a plasma deposition system for Silicon-Nitrides was installed recently. The operation of the transmission electron microscope has been expanded and is intensively used for the characterization of thin SiGeC layers. Research and development of a new Christian-Doppler Laboratory on photonic crystals is also conducted in the same cleanrooms.

The research efforts were mainly concentrated on high frequency and optoelectronic devices and on nanostructures as described in the following.

Si-SiGe heterobipolar transistors are now widely introduced into production for high speed bipolar and BiCMOS circuits, offering a great speed advantage over standard silicon technologies. In Linz, steps towards the optimization of the doping and composition profiles for the SiGeC HBT technology were continued in collaboration with Austria Microsystems, Unterpremstätten. While it is well known that co-doping of the p-type SiGe base layer of an HBT with carbon can completely suppress transient enhanced diffusion of the boron dopants, little is known about the behavior of carbon. Because of the small solid solubility of C in Si and SiGe, its propensity to form complexes, and its diffusion behavior, which follows the same mechanism as boron, C contaminations are usually avoided in standard Si technology. We therefore studied the behavior of 0.2 - 1 at.% of substitutional C in Si and SiGe under annealing conditions. Fourier-transform infrared spectroscopy (FTIR) was employed to measure the intensity of the local vibration modes of substitutional C and of cubic SiC precipitates. We could follow SiC precipitate formation as a function of annealing temperature and time. We found that, as expected, C in Si forms cubic SiC precipitates in thermal equilibrium. However, this process is kinetically impeded and requires long annealing times at elevated temperatures. The results were corroborated by high-resolution transmission electron microscopy to visualize the SiC precipitates in the Si and SiGe matrix material.

With minimum device dimensions of commercial processes already below 100 nm, and with progress being made regarding self-organized growth schemes, selective epitaxy and processing of nano-structured substrates at elevated temperatures become critical issues. During the in situ thermal cleaning step of nano-structured Si substrates before MBE deposition, we found a substantial amount of material transport on the surface. For example, wire structures of rectangular cross section are transformed into trapezoids with {311} facets after 5 min of annealing at 950°C in vacuum. The same mechanism leads to the development of negative slopes on the flanks of SiO_2 wires, which are wetted by mobile surface Si atoms, and desorb after reacting to SiO. To identify the dominating mechanism, we developed a decoration technique for transmission electron microscopy. It provides a means to distinguish oxide-covered and oxide-free surface regions during the course of thermal oxide desorption. It is well known that oxide desorption is not homogeneous, but proceeds via the formation and subsequent expansion of voids in the oxide. With our decoration technique, we were able to exclude any correlation of initial void formation with the presence of the nanostructured template. That means that most of the material transport responsible for facet formation occurs underneath a SiO_2 film, which follows the structural transformation. Once all oxide is desorbed, further mass transport is delayed by orders of magnitude. The results have important consequences for the structural integrity of nanostructured Si surfaces.

Self-organized Ge islands grown in the Stranski-Krastanow growth mode exhibit a statistical distribution of their lateral positions. By growing on prepatterned Si substrates, a two-dimensional periodic positioning of Ge islands can be achieved. In Linz, the patterning was accomplished both by holographic lithography as well as by electron beam lithography and subsequent reactive ion etching. In the laterally periodic pits, first a Si buffer layer was deposited by MBE in order to smoothen the surface and subsequently Ge domes were grown by molecular beam epitaxy at temperatures between 600 °C and 700 °C. Transmission electron microscopy investigations reveal that the islands are dislocation free. With these two-dimensionally periodic islands, by Si overgrowth a 2D pattern of tensely strained Si is formed which might be useful for the realization of the concept of field effect transistors, suggested by O.G. Schmidt and K. Eberl, so-called DOTFET's. The tensile strain in Si above the Ge islands leads to a lifting of the degeneracy of the conduction band states of Si, lowering the two valleys with the smallest transport mass, thus leading to an increase of electron mobility as compared to conventional Si MOS structures. Using x-ray diffraction techniques, we could actually prove the high strain state within the top Si layer.

The interface roughness of Si/SiGe quantum cascade samples, which are promising for the realization of Si-based light emitters and eventually lasers in the mid infrared, was determined from x-ray reflectivity. This is of consequence for quantum well fluctuations and consequently for a broadening of the emission. By growing such structures at temperatures as low as 350 °C, the r.m.s. interface roughness can be kept below 0.3 nm, despite Ge contents as high as 45% in the wells. A study using x-ray diffraction and x-ray reflectivity on a series of samples annealed at 700 °C for times between 10 minutes to several hours reveals the relaxation via interdiffusion of such Si/SiGe quantum cascade structures. Already short annealing times at 700 °C significantly change the structural sample properties.

A method to realize strained Si, which appears in the roadmaps of semiconductor industry for the coming years, is the introduction of SiGe nanostructures into Si. Using self-organized growth, SiGe structures with typical dimensions of 100 nm laterally and 10 to 15 nm vertically can be grown on Si substrates and capped with Si. As a result, the SiGe regions are compressively strained, whereas the Si regions above and below the SiGe islands are tensile strained. The advantage of using this approach is that high strain values up to 0.48% can be achieved without introducing lattice defects such as dislocations that deteriorate the electronic material properties. The particular properties of SiGe islands capped with Si depend sensitively on growth conditions. A study using x-ray diffraction reciprocal space mapping on a series of samples revealed that low substrate temperatures during Si capping are required in order to achieve high strain values in Si, which allow localizing electrons in the Si, while holes can be localized in the adjacent SiGe layers.

The spin properties of electrons in Si quantum wells were investigated making use of electron-spin-resonance (ESR). Here the main motivation is to judge the suitability of Si for spintronics applications, *i.e.*, devices that operate on spin orientation rather than on the displacement of free carriers. Spin-based devices are envisioned to have advantages in some specific applications like in quantum computing and cryptography. For such devices, the spin coherence time should be as long as possible, *i. e.*, much longer than the time required to manipulate spins. Making use of ESR techniques we were able to show that the spin coherence time is limited by the Bychkov-Rashba field which is a consequence of the asymmetric doping of the quantum well. The BR field reduces the spin coherence time to a few microseconds which is still by one or two orders of magnitude longer than the longest life times reported for GaAs, but by a factor of 30..50 shorter than the intrinsic life time implied by the unavoidable Elliott-Yafet mechanism. We conclude that Si is an excellent candidate for spin-based devices: if the Rashba field can be avoided, then the postulated ratio of 10^4 for spin coherence time and manipulation time appears attainable, particularly for quantum dots where quantization additionally limits spin relaxation.

The FECTED (Field Effect Controlled Transferred Electron Device) has been an attractive signal source at millimeter wave frequencies for many years. A remaining severe drawback of the device is its high operating voltage, typically around 7 V. By replacing the Schottky contact, which has been used as the anode up to now, with a combination of an ohmic contact and a Schottky contact, we have been able to reduce this voltage to values between 3 V and 4 V. Consequently, the field strength in the FECTED has been lowered considerably, reducing the risk of device breakdown. First oscillators, which have been realized with this modified FECTED, delivered up to 1 mW at a frequency of 58 GHz.

Quantum dot structures were fabricated by electron beam lithography on two-dimensional AlGaAs layers. The dot structure was defined by metallic gates on top of the layers. Electrical measurements were performed down to 300 mK. The typical Coulomb blockade peaks were observed as well as the strongly non-linear I-V curves for

large source-drain voltages. From the energetical separation of exited states, the size of the electrically active area was estimated to have a diameter of 125 nm.

Light emission from Si making use of Er as optical dopant was further investigated. We demonstrated that the enhanced luminescence yield in samples that were treated also with hydrogen results from an enhanced solubility of optically active Er in Si. Unsolved remains here the problem of avoiding the quenching of photoluminescence. Therefore Si:(Er,O) based light emitting diodes were further optimized for room temperature operation. In addition, we examined also the recently discovered efficient excitation of Erbium in Si-rich Si-oxide. Here Si nano-crystals are formed in SiO_2 surrounding as can be inferred by the observed photoluminescence in the visible. These nano-crystals were reported to act as sensitizers for Er in SiO_2. According to literature and internet announcements, light emitters with external efficiencies of 1-10% are possible. We found that the efficiency under optical excitation is by no means higher than without additional Si. The main effect of the Si nanocrystals apparently arises from their broad absorption band that allows making optimum use of the energy distribution of hot carriers in an electroluminescent device.

Lead-salt based vertical cavity surface emitting lasers with zero, two, and three dimensional laser active zones were grown by molecular beam epitaxy and tested at room temperature under optical excitation. These devices give stimulated emission at wavelength between 3.3 and 3.7 μm and are, therefore, highly suited for gas spectroscopy. Laser operation was demonstrated up to 44 °C, and the devices exhibit an circular output beam with a divergence of about 1°. The minimum effective threshold power, observed at 200 K, amounts 4 kW/cm^2 whereas at room temperature a somewhat higher threshold of 10 kW/cm^2 is found. Surprisingly, the best specifications (threshold power and operation temperature) are achieved by the laser resonators with three dimensional laser active media. The reason for this is that PbSe/PbEuTe quantum dots, used to obtain the zero dimensional laser active zones, exhibit a type 2 band alignment, which is unfortunate for optical transitions. Furthermore, in PbEuTe used as barrier material also for the 2D laser active medium samples, the 4f states of the Eu ions cause the optical transitions across the band gap to be electrically dipole forbidden. Therefore, to obtain laser active zones containing quantum structures other barrier materials than PbEuTe are required.

An alternative to PbEuTe is given by the use of PbSeTe. Therefore, $PbSe_{1-x}Te_x$ epilayers were grown with Te concentrations x varying between 0 and 1 and characterized by atomic force microscopy as well as by X-ray diffraction measurements. By these experiments it is shown that the number of dislocations can be minimized by choosing x in such a way that the epilayers are lattice matched to the BaF_2 substrates. For this concentration, also the best optical properties are expected, so that this alloy could substantially improve the performance of PbTe-PbSe based semiconductor laser structures.

Photocurrent (PC) spectroscopy and photoluminescence (PL) experiments have been performed on self-assembled Si/SiGe quantum dots and Si/SiGe quantum cascade injector structures. The quantum dots have been grown on substrates pre-patterned by both holographic and electron beam lithography. For all quantum dot samples, a clear PL signature of the quantum dots could be observed. For the dots grown on e-beam structured substrates, a narrower linewidth as compared to the dots grown on the substrate structured by holographic lithography is observed. Therefore, we conclude that the size distribution of the quantum dots grown on the former substrate is narrower than that of the dots grown on the latter. These findings are consistent with results obtained by x-ray scattering that also indicate a higher quality of the SiGe dots on the e-beam patterned substrates.

The PC experiments on doped quantum cascade injectors showed that these structures can be used as voltage-tunable 2-color detectors in the 3 – 6 µm region (MIR). The experimental results are in excellent agreement with the model calculations, allowing a detailed understanding of the features observed in the PC spectra of the cascade injectors. Starting with the results obtained on the current samples, improved samples designed for voltage tunable resonant enhanced cavity detection at 3 µm and 6 µm have been designed.

An MOCVD system was used for the growth of group III-Nitrides. Additional sources for Al and In are also available for the fabrication of ternary nitrogen based compounds. As dopant sources we have Si for n-type and Mg for p-type. So we are able to grow single and multilayers of group III nitrides together with the necessary doping profiles to fabricate blue light emitting diodes. However, our main task is the *in situ* growth control of the growth process by spectroscopic ellipsometry. So we can measure the growth rate and the layer composition during growth, which occurs at about 1000 °C in a very pure hydrogen atmosphere. Special software was developed that allows to calculate the Al content of the layers in real time with an accuracy of 1%. This system was tested first on single layers with constant composition. Finally we managed to monitor the concentration profile of superlattices of GaN/GaAlN as well as structures with graded composition profiles between GaN and AlGaN.

First growth runs were performed to grow cubic GaN. The standard and more thermally stable growth occurs in the hexagonal phase, therefore special templates, namely cubic GaN grown by MBE on GaAs, were used to initiate the growth in the cubic phase. The growth parameters were optimised to stabilise the growth in the cubic phase, which offers a much higher growth rate in comparison to MBE.

The ability to control the molecular order in organic thin films consisting of long anisotropic oligomers like oligo-thiophenes or oligo-phenylenes is essential to study the relation between their structure, surface morphology and their optical and electrical properties. We investigated ordered thin films of para-sexiphenyl (PSP) with the possible application in organic light-emitting diodes with polarized blue light emission. A self-organization of PSP molecules occurs during Hot Wall Epitaxy on mica, resulting in well-ordered crystalline needle-like structures with a length to width ratio up to 500. However, the growth regularities of such highly anisotropic films were not clear yet. We have used atomic force microscopy and X-ray diffraction to investigate the morphology, growth kinetic, and crystalline quality of these films in the early growth stages, in order to find the process controlling parameters.

The Christian Doppler Laboratory of Surface Optics is focussing on photonic crystal structures (respectively photonic band-gap materials). PhCs are periodic dielectric (or sometimes metallic) structures that have a photonic band gap (PBG) for photons, i.e. that light propagation is forbidden at certain frequencies. By scaling the size of the periodicity the PBG can be tuned from the microwave to the UV region. This property enables one to control (guide and split) light in a way that is almost impossible with conventional optics or with conventional integrated optics. Christian Doppler laboratories generally serve as a bridge between applied research and basic research. Photonic crystals are described exactly by Maxwell's Equations, which we can (and do) solve by the application of numerical techniques either in reciprocal space or in real space. This group works closely with other groups in the department and is one of the major users of the clean room, especially electron beam lithography and structural processing, evaporation, etc. The company partner of the Christian Doppler Laboratory is Photeon Technologies located in Bregenz, Austria.

Project Information

Project Manager

Reinraum Linz, Gerhard Brunthaler

Institut für Halbleiter- und Festkörperphysik, Johannes Kepler Universität Linz, A-4040 Linz, Austria

Project Group

Last Name	First Name	Status	Remarks
Bauer	Günther	University professor	
Heinrich	Helmuth	University professor	
Jantsch	Wolfgang	University professor	
Schäffler	Friedrich	University professor	
Thim	Hartwig	University professor	
Brunthaler	Gerhard	Associate professor	
Diskus	Christian	Associate professor	
Heiss	Wolfgang	Assistant professor	
Palmetshofer	Leopold	Associate professor	
Springholz	Gunther	Associate professor	ÖAW stipendiary
Sitter	Helmut	Associate professor	
Bonanni	Alberta	Assistant professor	
Fromherz	Thomas	Assistant professor	
Kolmhofer	Erich	Assistant professor	
Lübke	Kurt	Assistant professor	
Stangl	Julian	Assistant professor	
Andreev	Andrej	Assistant professor	
Kocher	Gudrun	Assistant professor	Partly FWF
Binder	Fritz	Technician	
Bräuer	Stephan	Technician	
Fuchs	Othmar	Technician	
Jägermüller	Josef	Mechanic	
Andreeva	Svetlana	Lab Technician	FWF-START
Nusko	Ekkehard	Electronics Engineer	
Halilovic	Alma	Lab Technician	½ paid by GME, since Dec
Haslgrübler	Klaus	Lab Technician	½ paid by GME
Vorhauer	Ernst	Electronics engineer	
Kainz	Ursula	Lab Technician	since Dec
Hingerl	Kurt	Guest researcher	Austrian Academy of Sciences + Company Profactor, until June 30

Last Name	First Name	Status	Remarks
Katzenmayer	Hans	Technician	
Stifter	David	Guest researcher	Company Profactor
Andreev	Andrej	Post Doc	FWF
Zhong	Zhenyang	Post Doc	FWF (P14684), (ECOPro
Chen	Gang	Post Doc	FWF (P14684)
Meduna	Mojmir	Guest Researcher	EC (SigeNET)
Achleitner	Joachim	Ph.D. student	
Berer	Thomas	Ph D student	GMe
Böberl	Michaela	Ph D. student	FWF-START
Kaufmann	Erich	Ph D student	FWF-START
Hesse	Anke	Ph.D. student	EC, Brussels
Lechner	Rainer	Ph D student	FWF
Lichtenberger	Herbert	Ph D student	FWF
Malissa	Hans	Ph D student	FWF
Montaigne-R.	Alberto	Ph.D. student	Eu-Project ISCE-MOCVD
Mühlberger	Michael	Ph.D. student	
Novak	Jri	Ph D student	FWF
Prinz	Adrian	Ph.D. student	OeNB/FWF
Pillwein	Georg	Ph D student	FWF
Raab	Anneliese	Ph.D. student	FWF till Sep 30th
Roch	Thomas	Ph.D. student	FWF
Schülli	Tobias	Ph.D. student	EC, Brussels
Schmidegg	Klaus	Ph.D. student	FWF
Schwarzl	Thomas	Ph.D. student	FWF
Wiesauer	Karin	Ph.D. student	FWF till Sep30th
Griesser	Stefan	Diploma student	
Gruber	Daniel	Diploma student	
Janecek	Stefan	Diploma student	
Kirchschlager	Raimund	Diploma student	
Lindner	Benjamin	Diploma student	
Pachinger	Dietmar	Diploma student	
Pargfrieder	Stefan	Diploma student	
Rauter	Patrick	Dipoma student	
Roither	Jürgen	Diploma student	
Söllinger	Walter	Diploma student	
Schwinger	Wolfgang	Diploma student	
Simma	Matthias	Diploma student	
Wintersberger	Eugen	Diploma student	

Publications in Reviewed Journals

Published:

1. T. Fromherz, W. Mac, A. Hesse, G. Bauer, C. Miesner, K. Brunner, G. Abstreiter, “Intraband absorption and photocurrent spectroscopy of self-assembled p-type Si/SiGe quantum dots”, Appl. Phys. Lett. 80, 2093-2095 (2002).
2. J. Stangl, V. Holy, G. Springholz, G. Bauer, I. Kegel, T.H. Metzger, “Self-organized semiconductor nanostructures: shape, strain and composition”, Materials Science and Engineering C19, 349-358 (2002).
3. V.M. Pudalov, G. Brunthaler, A. Prinz, G. Bauer, “Weak anisotropy and disorder dependence of the in-plane magnetoresistance in high mobility (100) Si-inversion layers”, Phys. Rev. Lett. 88, 076401 (2002).
4. G. Springholz, K. Wiesauer, “Nano-scale dislocation patterning in PbTe/PbSe (001) lattice-mismatched heteroepitaxy”, Phys. Rev. Lett. 88, 015507 (2002).
5. G. Springholz, V. Holy, P. Mayer, M. Pinczolits, A. Raab, R.T. Lechner, G. Bauer, H. Kang, L. Salamanca-Riba, “Self-organized ordering in self-assembled quantum dot superlattices”, Materials Science and Engineering B88, 143-152 (2002).
6. A. Raab, R.T. Lechner, G. Springholz, “Self-organized lateral ordering for vertically aligned PbSe/PbEuTe quantum dot superlattices”, Appl. Phys. Lett. 80, 1273-1275 (2002).
7. G. Dehlinger, L. Diehl, U. Gennser, H. Sigg, E. Müller, S. Stutz, J. Faist, J. Stangl, T. Roch, G. Bauer, D. Grützmacher, “Si/SiGe quantum cascade structures emitting in the 10mm range”, Materials Science and Engineering B 89, 30 (2002).
8. V.M. Pudalov, M.E. Gershenson, H. Kojima, N. Butch, E.M. Dizhur, G. Brunthaler, A. Prinz, G. Bauer, “Low-density spin susceptibility and effective mass of mobile electrons in Si inversion layers”, Phys. Rev. Lett. 88, 196404 (2002).
9. T. Roch, M. Meduna, J. Stangl, A. Hesse, R. Lechner, G. Bauer, G. Dehlinger, L. Diehl, U. Gennser, E. Müller, D. Grützmacher, “Interface roughness in SiGe quantum-cascade structures from x-ray reflectivity studies”, J. Appl. Phys. 91, 8974-8978 (2002).
10. J. Fürst, H. Pascher, T. Schwarzl, M. Böberl, W. Heiss, G. Springholz, G. Bauer, “Midinfrared IV-VI vertical-cavity surface-emitting lasers with zero-, two- and three-dimensional systems in the active regions”, Appl. Phys. Lett. 81, 208-210 (2002)
11. T. Roch, V. Holy, A. Hesse, J. Stangl, T. Fromherz, G. Bauer, T.H. Metzger, S. Ferrer, “Strain in buried self-assembled SiGe wires studied by grazing-incidence x-ray diffraction”, Phys. Rev. B 65, 245324 (2002).
12. G. Grabecki, J. Wrobel, T. Dietl, E. Papis, E. Kaminska, A. Piotrowska, G. Springholz, G. Bauer, “Spin alignment of electrons in PbTe/(Pb,Eu)Te nanostructures”, Physica E 13, 649-652 (2002).
13. W. Jantsch, Z. Wilamowski, N. Sandersfeld, M. Mühlberger, F. Schäffler, “Spin lifetimes and g-factor tuning in Si/SiGe quantum wells”, Physica E 13, 504-507 (2002).
14. M. Mühlberger, C. Schelling, G. Springholz, F. Schäffler, “Step-bunching and strain effects in Si1-xGex layers and superlattices on vicinal Si(001)”, Physica E 13, 990-994 (2002).
15. T. Fromherz, W. Mac, C. Miesner, K. Brunner, G. Bauer, G. Abstreiter, “Intersubband transitions of boron-doped self-assembled Ge quantum dots”, Physica E 13, 1022-1025 (2002).

16. K. Wiesauer, G. Springholz, “Nano-scale dislocation patterning in PbTe on PbSe (100) heteroepitaxy studied by UHV scanning tunneling microscopy”, Physica E 13, 1216-1219 (2002).

17. T. Schwarzl, W. Heiss, G. Springholz, K. Biermann, K. Reimann, “Above-room temperature operation of IV-VI microcavity lasers”, Physica E 13, 888-891 (2002).

18. G. Brunthaler, A. Prinz, G. Pillwein, G. Bauer, V.M. Pudalov, P.E. Lindelof, J. Ahopelto, “On the metallic state in high-mobility silicon inversion and silicon-on-insulator layers”, Physica E 13, 691-694 (2002).

19. G. Springholz, T. Schwarzl, W. Heiss, T. Fromherz, G. Bauer, M. Aigle, H. Pascher, I. Vavra, “Fabrication of 3.9-4.2mm mid-infrared surface emitting PbSe/PbEuTe quantum dot lasers using molecular beam epitaxy”, Physica E 13, 876-880 (2002).

20. H. Beyer, J. Nurnus, H. Böttner, A. Lambrecht, E. Wagner, G. Bauer, “High thermoelectric figure of merit ZT in PbTe and Bi2Te3-based superlattices by a reduction of the thermal conductivity”, Physica E 13, 965-968 (2002).

21. A. Hesse, J. Stangl, V. Holy, T. Roch, G. Bauer, O.G. Schmidt, U. Denker, B. Struth, “Effect of overgrowth on shape, composition and strain of SiGe islands on Si(001)”, Phys. Rev. B 66, 085321 (2002).

22. T. Schwarzl, W. Heiss, G. Springholz, H. Krenn, T. Fromherz, A. Raab, I. Vavra, “Midinfrared absorption of PbSe/Pb1-xEuxTe quantum dot superlattices in IV-VI microcavities”, Phys. Rev. B 65, 245321 (2002).

23. J. Myslivecek, C. Schelling, F. Schäffler, G. Springholz, P. Šmilauer, J. Krug, B. Voigtländer, “On the microscopic origin of the kinetic step bunching instability on vicinal Si(001)”, Surface Science 520, 193-206 (2002).

24. J. Myslivecek, C. Schelling, F. Schäffler, G. Springholz, P. Šmilauer, J. Krug, B. Voigtländer, “Step bunching during Si(001) homoepitaxy caused by the surface diffusion anisotropy”, Cond. Mat. 0212331.

25. A.G. Touryanski, I.V. Pirshin, M.M. Rzaev, M. Mühlberger, F. Schäffler, “Two wave X-ray optical diagnostics of GexSi1-x/Si modulation doped heterostructures”, Physica E 13 2-4, 1063 (2002).

26. M. Mühlberger, C. Schelling, G. Springholz, F. Schäffler, “Step-bunching and strain-effects in Si1-xGex layers and superlattices grown on vicinal Si(001)”, Materials Science & Engineering B 89 1-3, 257 (2002).

27. D. Gruber, M. Mühlberger, T. Fromherz, F. Schäffler, M. Schatzmayr , “Fourier-transform infrared investigations of Si1-yCy structures for hetero bipolar transistor applications”, Materials Science & Engineering B 89 1-3, 97 (2002) .

28. E. Napolitani, D. De Salvador, A. Coati, M. Berti, A.V. Drigo, M.S. Carroll, J.C. Sturm, J. Stangl, G. Bauer, C. Spinella, “Diffusion and clustering of supersaturated carbon in SiGe layers under oxidation”, Nuclear Instruments and Methods in Physics Research B 186, 212-217 (2002).

29. A. Andreev, H. Sitter, N.S. Sariciftci, C.J. Brabec, G. Springholz, P. Hinterdorfer, H. Plank, R. Resel, A. Thierry, B. Lotz, ”A highly ordered anisotropic nano-needles in para-sexiphenyl films”, Thin Solid Films 403, 444-448 (2002).

30. V. Holý, G. Bauer, J. Stangl, G. Springholz, “Processes of self-organization during epitaxial growth of semiconductor superlattices – an x-ray scattering study”, in: “From Semiconductors to Proteins”: Beyond the Averaged Structure, eds. S. J. L. Billinge and M. F. Thorpe, (Kluwer Academic, New York 2002), pp. 67-83.

31. H. Lichtenberger, M. Mühlberger, F. Schäffler, “Transient-Enhanced Surface Diffusion on Native-Oxide-Covered Si(001) Nano-Structures during Vacuum Annealing”, cond-mat/0301074.

32. Z. Wilamowski, W. Jantsch, N. Sandersfeld, M. Mühlberger, F. Schäffler, S. Lyon, “Spin Relaxation and g-Factor of Two-Dimensional Electrons in Si/SiGe Quantum Wells”, Physica E 16, 111 - 120 (2003).

33. G. Springholz, A. Raab, R. T. Lechner, V. Holy, “Dot size dependence of vertical and lateral ordering in self-organized PbSe/Pb1-xEuxTe quantum dot superlattices”, Appl. Phys. Lett. 82, 799-801 (2003).

34. J. Stangl, A. Hesse, T. Roch, V. Holy, G. Bauer, T. Schülli, T.H. Metzger, “Structural investigation of semiconductor nanostructures by x-ray techniques”, Nuclear Instruments and Methods in Physics Research B 200, 11-23 (2003).

35. A. Hesse, Y. Zhuang, V. Holy, J. Stangl, S. Zerlauth, F. Schäffler, G. Bauer, N. Darowski, U. Pietsch, “X-ray grazing incidence study of inhomogeneous strain relaxation in Si/SiGe wires”, Nuclear Instruments and Methods in Physics Research B 200, 267-272 (2003).

36. M.S. Carroll, J.C. Sturm, E. Napolitani, D. De Salvador, M. Berti, J.Stangl, G. Bauer, and D.J. Tweet, “Silicon interstitial driven loss of substitutional carbon from SiGeC structures”, Proc. Symp. Mat. Res. Soc. 669, in print (2001). (presented Symp. MRS, San Francisco, CA, April, 2001, page numbers not avail. yet)

37. H. Plank, R. Resel, A. Andreev, N.S. Sariciftci, H. Sitter, “Structural relationship between epitaxial grown para-sexiphenyl and mica (001) substrates”, J. Cryst. Growth **237-239**, 2076 (2002).

38. A. Andreev, H. Sitter, N.S. Sariciftci, C.J. Brabec, G. Springholz, P. Hinterdorfer, H. Plank, R. Resel, A. Thierry, B. Lotz, “A highly ordered anisotropic nano-needles in para-sexiphenyl films”, Thin Solid Films **403**, 444-448 (2002)

39. T. Schwarzl, W. Heiss, G. Springholz, K. Biermann, K. Reimann, “Above-room-temperature operation of IV-VI microcavity lasers”, Physica E **13**, 888-891 (2002).

40. G. Springholz, T. Schwarzl, W. Heiss, T. Fromherz, G. Bauer, M. Aigle, H. Pascher, I. Vavra, “Fabrication of 3.9 - 4.2 □m mid-infrared surface emitting PbSe/PbEuTe quantum dot lasers using molecular beam epitaxy”, Physica E **13**, 876-880 (2002).

41. G. Springholz, M. Pinczolits, P. Mayer, A. Raab, R. Lechner, V. Holy, G. Bauer, T. Schwarzl, W. Heiss, M. Aigle, H. Pascher, H.H. Kang, L. Salamanca-Riba, “Self-assembled PbSe quantum dot superlattices: Ordering and device applications”, Proc. 10th Int. Conf. NGSC 2001, IPAP Conf. Series 2, pp. 161-164 (2002).

42. G. Springholz, T. Schwarzl, W. Heiss, M. Aigle, H. Pascher, K. Biermann, K. Reimann, “Fabrication of mid infrared vertical cavity surface emitting PbTe quantum well lasers for the 3 - 5 □m spectral region”, Proc. 10th Int. Conf. NGSC 2001, IPAP Conf. Series 2 pp. 142-144 (2002)

43. W. Jantsch, Z. Wilamowski, N. Sandersfeld, M. Mühlberger, F. Schäffler, “Spin lifetimes and g-factor tuning in Si/SiGe quantum wells”, Physica E **13**, 504-507 (2002)

44. T. Schwarzl, W. Heiss, G. Springholz, H. Krenn, T. Fromherz, A. Raab, I. Vavra, “Midinfrared absorption of $PbSe/Pb_{1-x}Eu_xTe$ quantum dot superlattices in IV-VI microwaves”, Phys. Rev. B **65**, 245321, 1-9 (2002)

45. J. Fürst, H. Pascher, T. Schwarzl, M. Böberl, W. Heiss, G. Springholz, G. Bauer, “Midinfrared IV-VI vertical-cavity surface-emitting lasers with zero-, two-, and three-dimensional systems in the active regions”, Appl. Phys. Lett. **81** (2), 208-210 (2002)

46. R.E. Balderas-Navarro, K. Hingerl, D. Stifter, A. Bonanni, H. Sitter, “Reflectance difference spectroscopy during CdTe/ZnTe interface formation”, Appl. Surf. Sci. **190**, 307 (2002)

47. H. Sitter, A. Andreev, G. Matt, N.S. Sariciftci, “Hot-Wall Epitaxy - the method of choice for the growth of highly ordered organic epilayers”, Molecular and Liquid Crystals **385**, 51-60 (2002)

48. A. Andreev, H. Sitter, R. Resel, D.-M. Smilgies, H. Hoppe, G. Matt, N.S. Sariciftci, D. Meissner, D. Lysacek, L. Valek, “Highly aligned organic semiconductor thin films grown by Hot-Wall Epitaxy”, Molecular and Liquid Crystals **385**, 61-70 (2002)

49. G. Kocher-Oberlehner, W. Jantsch, A. Ulyashin, L. Palmetshofer, “Hydrogen enhanced luminescence of Erbium-doped Silicon”, Proc. ICPS 26, Edinburgh 2002

50. G. Kocher-Oberlehner, W. Jantsch, L. Palmetshofer, A. Ulyashin, “Luminescence enhancement by hydrogenation of Si:Er,O”, Proc. E-MRS Spring Meeting, Strasbourg 2002

51. H. Sitter, “Epitaxy - close and far away from thermodynamic equilibrium”, IEEE Catalogue No. 02EX531, ISBN 0-7803-726-x, p 161-174

52. H. Sitter, “Highly ordered organic epitaxial layers”, Proc. “Crystal Growth and Epitaxy”, Vienna 2002.

53. K. Schmidegg, A. Bonanni, A. Montaigne Ramil, D. Stifter, K. Hingerl, H. Sitter, “In-situ growth control and composition determination of MOCVD GaN and related ternary compounds by spectroscopic ellipsometry”, Proc. “Crystal Growth and Epitaxy”, Vienna 2002

54. A. Kozanecki, V. Glukhanyuk, W. Jantsch, B.J. Sealy, “Implantation Erbium doping in 6H SiC for optimum optical efficiency at 1.54 mm”, Proc. CAARI 2002, Denton 2002

55. C. Skierbiszewski, S.P. Lepkowski, P. Perlin, T. Suski, W. Jantsch, J. Geisz, “The effective mass and conduction band states of GaAsN/GaAs quantum wells”, Physica E**13**, 1078-1081 (2002)

Submitted / in print:

1. A. Raab, G. Springholz, R.T. Lechner, I. Vavra, H.H. Kang, L. Salamanca-Riba, “Atomic force microscopy and transmission electron microscopy study of self-organized ordering in vertically aligned PbSe quantum dot superlattices”, MRS Proceedings, in print.

2. A. Hesse, J. Stangl, V. Holy, G. Bauer, O. Kirfel, E. Müller, D. Grützmacher, “Influence of capping on strain, composition and shape of SiGe islands”, Materials Science and Engineering B, in print.

3. G. Brunthaler, A. Prinz, G. Bauer, V.M. Pudalov, “The role of quantum interference for the metallic state in high-mobility Silicon inversion layers”, ICPS 26, Edinburgh, Scotland, UK, 29.07.-02.08.2002, in print.

4. V. Holy, Z. Zhong, G. Bauer, O. Ambacher, “Diffuse x-ray scattering from threading dislocations in hexagonal GaN layers”, Phys. Rev. B, submitted.

5. D. Grützmacher, S. Mentese, E. Müller, L. Diehl, H. Sigg, Y. Campidelli, O. Kermarrec, D. Bensahel, T. Roch, J. Stangl, G. Bauer, “Strain compensated Si/Si0.2Ge0.8 quantum cascade structures grown by low temperature molecular beam epitaxy”, J. Crystal Growth, submitted.

6. J. Stangl, A. Hesse, V. Holy, Z. Zhong, G. Bauer, U. Denker, O. G. Schmidt. “Effect of overgrowth temperature on shape, strain and composition of buried Ge islands deduced from x-ray diffraction”, Appl. Phys. Lett., in print.
7. G. Brunthaler, A. Prinz, G. Pillwein, P.E. Lindelof, J. Ahopelto, M. Prunnila, “On the two-dimensional metallic state in silicon-on-insulator structures”, Phys. Rev. B, submitted.
8. G. Dehlinger, l. Diehl, U. Gennser, H. Sigg, E. Müller, S. Stutz, J. Faist, J. Stangl, T. Roch, G. Bauer, D. Grützmacher, “Si/SiGe quantum cascade structures emitting in the 10 mm range”, Microelectronic Engineering, submitted.
9. Z. Zhong, A. Halilovic, M. Mühlberger, F. Schäffler, G. Bauer, “Positioning of self-assembled Ge islands on stripe-patterned Si (001) substrates”, J. Appl. Phys., submitted.
10. M. Mühlberger, C. Schelling, G. Springholz, F. Schäffler, “Step-bunching in SiGe layers and superlattices on Si(001)”, Surface Science, in print.
11. H.Lichtenberger, M.Mühlberger, F.Schäffler, “Transient-Enhanced Si Diffusion on Native-Oxide Covered Si(001) Nanostructures during Vacuum Annealing”, Appl. Phys. Lett. (in print).
12. H. Kojima, M. E. Gershenson, V. M. Pudalov, G. Brunthaler, A. Prinz, G. Bauer, “Interaction Effects in Electron Transport in Si Inversion Layers”, J. Phys. Soc. Japan, in print.
13. G. Pillwein, A. Prinz, G. Brunthaler, P.E. Lindelof, J. Ahopelto, “Screening behavior of the two-dimensional metallic state in silicon-on-insulator structures”, Proceedings of the 26th Int. Conf. on the Physics of Semiconductors, in print.
14. Z. Wilamowski, W. Jantsch, N. Sandersfeld, M. Mühlberger, F. Schäffler, S. Lyon, “Spin relaxation and g-factor of two-dimensional electrons in Si/SiGe quantum wells”, Physica E, submitted.
15. Z.H. Chen, W. Heiss, G. Springholz, I. Souma, A. Murayama, Y. Oka, ”Anomalous magneto-optical properties of EuTe induced by magnetic polarons”, Physica E, submitted.
16. A. Bonanni, D. Stifter, A. Montaigne-Ramil, K. Schmidegg, K. Hingerl, H. Sitter, “In situ spectroscopic ellipsometry of MOCVD-grown GaN compounds for on-line composition determination and growth control”, J. Cryst. Growth.
17. A. Bonanni, K. Schmidegg, A. Montaigne-Ramil, H. Sitter, K. Hingerl, D. Stifter, “Spectroscopic ellipsometry for one-line composition determination and growth control of GaN and related ternary compounds grown via metal-organic chemical vapor deposition”, Appl. Phys. Lett.
18. A. Andreev, R. Resel, D.-M. Schmilgies, H. Hoppe, G. Matt, H. Sitter, N.S. Sariciftci, D. Meissner, H. Plank, O. Zrzavecka, “Oriented organic semiconductor thin films”, Synth. Metals
19. R. Resel, H. Plank, N.S. Sariciftci, A. Andreev, H. Sitter, G. Hlawacek, C. Teichert, A. Tierry, B. Lotz, “Molecular alignments in epitaxial grown sexiphenyl on mica (001)”, Thin Solid Films.
20. G. Kocher-Oberlehner, W. Jantsch, A. Ulyashin, L. Palmetshofer, “On the influence of Hydrogen on the Erbium related luminescence in Si”, Appl. Phys. Lett.
21. Z. Wilamowski, W. Jantsch, N. Sandersfeld, M. Mühlberger, F. Schäffler, S. Lyon, “Spin relaxation and g-factor of two-dimensional electrons in Si/SiGe quantum wells”, Physica E.

22. Z.H. Chen, W. Heiss, G. Springholz, I. Souma, A. Murayama, Y. Oka, “Anomalous magneto-optical properties of EuTe induced by magnetic polarons”, Physica E.

23. W. Heiss, M. Böberl, T. Schwarzl, G. Springholz, J. Fürst, H. Pascher, “Applications of lead-salt microcavities for mid-infrared devices”, Proc. IEE Optoelectronics.

Presentations

Invited Talks:

1. G. Bauer, “*Semiconductor nanostructures*”, annual meeting of the American Association for the Advancement of Science (AAAS), Boston, Feb. 2002.
2. J. Stangl, A. Hesse, T. Roch, V. Holý, G. Bauer, T. Schülli, T.H. Metzger, “*Structural investigation of semiconductor nanostructures by x-ray techniques*”, invited talk at the E-MRS Strasbourg, Juni 2002.
3. G. Bauer, A. Hesse, T. Roch, J. Stangl, V. Holý, “*Structural invstigations of semicondcutor quantum dots and quantum wires*”, invited talk at the CELDIS Workshop on Low Dimensional and Hybrid Diluted Magnetic Semiconductor Structures, 21.6. - 23.6.2002, Obory, Warsaw, Poland.
4. G. Bauer, “*Structural properties of semiconductor nanostructures*”, invited presentation an the COST meeting, Sevilla, 4. Okt. 2002.
5. G. Brunthaler, A. Prinz, and G. Bauer, “*The role of quantum interference for the metallic state in high-mobility Silicon inversion layers*”, invited talk at the 26th Int. Conf. on the Physics of Semiconductors, Edinburgh, 2002.
6. T. Fromherz, P. Rauter, W. Mac, G. Bauer, C. Miesner, K. Brunner, G. Abstreiter, G. Dehlinger, H. Sigg, D. Grützmacher, “*Intraband absorption and photocurrent spectroscopy of Si/SiGe quantum dots and cascades*”, invited talk at the E-MRS Strasbourg, Juni 2002.
7. H. Kojima, M. E. Gershenson, V. M. Pudalov, G. Brunthaler, A. Prinz, and G. Bauer, “*Interaction Effects in Electron Transport in Si Inversion Layers*”, invited talk at “Localization 2002”, Int. conf. on Quantum Transport and Quantum Coherence, August 16 – 19, Tokyo, Japan, 2002.
8. F. Schäffler, “*Spineffekte in SiGe/Si Elektronenkanälen*”, invited talk at the GMM Workshop: “*Integrierte Silizium-Hetero-Bauelemente*”, München, 25.04.2002.
9. C.Schelling, J.Myslivecek, M.Mühlberger, H.Lichtenberger, Z.Zhong, G.Bauer, and F.Schäffler, “*Kinetic and Strain-Driven Growth Phenomena on Si(001)*”, invited talk at Crystal Growth and Epitaxy, Wien Oct. 2002.
10. T. Schwarzl, W. Heiss, G. Springholz, M. Böberl, M. Aigle, J. Fürst, H. Pascher, K. Biermann, K. Reimann, G. Bauer, “*(Pb,Eu)Te-PbTe based vertical-cavity surface-emitting laser (VCSEL) structures for the 3 - 6 micron range*”, invited talk at the CELDIS Workshop on Low Dimensional and Hybrid Diluted Magnetic Semiconductor Structures, 21.6. - 23.6.2002, Obory, Poland.
11. G. Springholz, “*Molecular beam epitaxy of self-assembled semiconductor quantumd dots*”, Review Conference on Crystal Growth, 20.-24.10.2002, Vienna, Austria.
12. G. Springholz, “*Nanotechnologie – Methoden zur Herstellung von Nanostrukturen*”, Jahrestagung der Östereichischen Physikalischen Gesellschaft, 24.9.2002, Leoben, Austria.

13. G. Springholz, "Vertical and Lateral Ordering in Self-Organized Quantum Dot Superlattices", 35th IUVSTA Workshop on "Pattern Formation and Atomic Processes in Epitaxial Growth and Erosion", Trofaiach, Austria, 9.6. – 13.6.2002.
14. J. Stangl, A. Hesse, T. Roch, Z. Zhong, R.T. Lechner, G. Bauer, M. Meduna, V. Holý, T.H. Metzger, "*X-ray investigation of semiconductor nanostructures*", invited talk at the ESRF User Meeting, Feb. 2002, Grenoble.
15. J. Stangl, A. Hesse, T. Roch, Z. Zhong, R.T. Lechner, G. Bauer, M. Meduna, V. Holý, T. Schülli, T.H. Metzger, "*Investigation of nanoscale self-assembled islands in semiconductor heterostructures*", invited talk at the XTOP 2002, Sept. 2002, Aussois.
16. J. Stangl, A. Hesse, G. Bauer, V. Holý, U. Denker, O.G. Schmidt, O. Kirfel, D. Grützmacher, "*Structural properties of SiGe islands: Effect of capping"*, invited talk at the MRS Fall Meeting, Dec. 2002, Boston.
17. W. Heiss, T. Schwarzl, M. Böberl, G. Springholz, J. Fürst, M. Aigle, H. Pascher, "IV-VI microcavity devices grown by MBE", Crystal Growth and Epitaxy, Vienna, Austria (October 20-24, 2002)
18. W. Heiss, T. Schwarzl, M. Böberl, G. Springholz, "Applications of lead-salt microcavities for mid-Iinfrared devices", 5th International Conference on Mid-Infrared Optoelectronics Materials and Devices (MIOMD V), Annapolis, Maryland, USA (September 8-11, 2002).
19. T. Schwarzl, W. Heiss, M. Böberl, G. Springholz, J. Fürst, M. Aigle, H. Pascher "(Pb,Eu)Te-PbTe VCSEL laser structures", 2nd CELDIS Workshop on Low Dimensional and Hybrid Diluted Magnetic Semiconductor Structures, Warsaw, Poland (June 21-22, 2002)
20. W. Heiss, G. Springholz, T. Schwarzl, M. Böberl, T. Fromherz, A. Raab, "Correlated, self-organized PbSe quantum dots in vertical cavities: Absorption and stimulated emission", E-MRS 2002 Spring Meeting, Strasbourg, France (June 18-21, 2002)
21. W. Heiss, M. Böberl, T. Schwarzl, G. Springholz, J. Fürst, H. Pascher, "Blei-Salz-Mikroresonatoren für das mittlere Infrarot", Physikkolloquiium and der Universität Graz (26. November 2002).
22. H. Sitter, "Highly ordered organic eptaxial layers", Crystal Growth and Epitaxy, Vienna (Oct. 20-23, 2002)
23. H. Sitter, "Epitaxy – Close and away from thermodynamic equilibrium", 4th Int. Conf. on Advanced Semiconductor Devices and Microsystems, Smolenice, Slovakia (Oct. 14-16, 2002)
24. Z. Wilamowski, W. Jantsch, N. Sandersfeld, M. Mühlberger, F. Schäffler, S. Lyon Spin relaxation and g-factor of two-dimensional electrons in Si/SiGe quantum wells 12th International Winterschool on New Developments in Solid State Physics, Mauterndorf, Austria (February 25 – March 1 , 2002)
25. A. Kozanecki, V. Glukhanyuk, W. Jantsch, and B.J. Sealy, "Implantation Erbium doping In 6H SiC for optimum optical efficiency at 1.54 μm", 17th International Conference on the Application of Accelerators in Research and Industry, CAARI 2002, University of North Texas, Department of Physics, Denton, Texas, USA (November 12-16, 2002).

Seminar Talks:

1. G. Bauer, "*Structural investigations of semiconductor quantum dots*", seminar talk at the ETH Zurich, Switzerland, 28. March 2002.

2. G. Bauer, "*Semiconductor Nanostructures*", seminar talk at the Paul Scherrer Institut Villigen, Switzerland, 23. Sept 2002.
3. G. Brunthaler, "*The Role of Quantum Effects on the metallic state in two dimensions*", seminar talk at the Karl-Franzens University, Graz, 2. Dez. 2002.
4. F. Schäffler, "*SiGeC-Heterostrukturen: Wachstum, Eigenschaften und Anwendungen*", Seminar Universität der Bundeswehr, Neubiberg, Germany, 02.02.2002.
5. F. Schäffler, "*Nanoscale Challenges: Growth and Diffusion Phenomena in Si-based Heterostructures*", Seminar Paul-Scherrer-Institut, Villingen, Switzerland, 16.07.2002.
6. F. Schäffler, "*Spin-Effects in SiGe Heterostructures*", Seminar ETH Zürich, Switzerland, 17.07.2002
7. G. Springholz, "*Selbst-organisierte Halbleiter Nanostrukturen: Wachstum, Ordnungsphänomene und Anwendungen*", seminar talk at the Universität Hannover, Germany, 02.07.2002.
8. G. Springholz, "*Selbst-organisierte Halbleiter Nanostrukturen: Wachstum, Ordnungsphänomene und Anwendungen*", seminar talk at the Universität Würzburg, Germany, 18.06.2002.
9. J. Stangl, J. Grenzer, "*Investigation of semiconductor hetero- and nanostructures by x-ray diffraction and reflectivity*", seminar talk at the Forschungszentrum Rossendorf, Okt. 2002, Rossendorf bei Dresden.

Conference presentations (talks and posters):

1. G. Bauer, "Investigation of Si/SiGe cascade structures using x-ray diffraction and reflectivity", SHINE meeting at Cavendish Lab., Cambridge, Feb. 2002.
2. G. Brunthaler, A. Prinz, G. Pillwein, P.E. Lindelof, and J. Ahopelto, "Screening description of the metallic state in Silicon-on-insulator structures", Poster at the 12th Int. Winterschool on New Developments in Solid State Physics, Mauterndorf, Austria, Feb. 2002.
3. G. Brunthaler, G. Pillwein, A. Prinz, P.E. Lindelof and J. Ahopelto, "Screening description of the 2D-metallic state in Silicon-on-insulator structures", Int. Workshop on 2D-MIT, Princeton, USA, May, 2002.
4. L. Diehl, S. Mentese, H. Sigg, U. Gennser, T. Fromherz, D. Grützmacher, E. Müller, I. Sagnes, Y. Campidelli, O. Kermarrec, D. Bensahel, J. Faist, "Strain compensated Si/SiGe quantum well cascade emitters grown on SiGe pseudosubstrates", talk at the 26th International Conference on the Physics of Semiconductors, 29.7.-2.8.2002, Edinburgh, UK.
5. T. Fromherz, "Intersubband transitions in SiSiGe cascade structures", SHINE meeting at Cavendish Lab., Cambridge, Feb. 2002.
6. W. Heiss, R. Kirchschlager, R. T. Lechner, G. Springholz, "Giant magneto-optical effects in EuSe epilayers and EuSe/EuTe superlattices", 26th International Conference on the Physics of Semiconductors (ICPS 2002), Edinburgh, United Kingdom (July 29 - August 2, 2002).
7. W. Heiss, G. Prechtl, G. Springholz; "Giant tunability of excitonic photoluminescence transitions in antiferromagnetic EuTe epilayers induced by magnetic polarons"; poster at the 2nd International Conference on Physics and Application of Spin Related Phenomena in Semiconductors, 22.-26.7.2002,Würzburg, Germany.

8. A. Hesse, V. Holý, J. Stangl, T. Fromherz, G. Bauer, U. Denker, O.G. Schmidt, "Effect of overgrowth temperature on size and shape of SiGe islands", Poster at the 26th Int. Conf. on the Physics of Semiconductors, Edinburgh, 2002.
9. A. Hesse, J. Stangl, V. Holý, G. Bauer, O. Kirfel, E. Müller, D. Grützmacher, "Influence of capping on strain, composition and shape of SiGe islands", poster at the XTOP 2002, Sept. 2002, Aussois.
10. T. Ikaida, Y.H. Matsuda, N. Miura, S. Tsujino, P. Xomalin, S.J. Allen, G. Springholz, M. Pinczolits, G. Bauer, "Angular dependence and photon energy dependence of cyclotron resonance in PbSe/PbEuTe quantum dot crystals", talk at the 26th International Conference on the Physics of Semiconductors, 29.7.-2.8.2002, Edinburgh, UK.
11. R.T. Lechner, G. Springholz, J. Stangl, A. Raab, Z. Zhong, T. Schülli, G. Bauer, "Correlations and ordering in self-organized PbSe quantum dot superlattices", poster at the Spring Meeting of the European Materials Research Society, Strasbourg, 18. – 21.6.2002.
12. R.T. Lechner, T. Schülli, G. Springholz, G. Bauer, D. Lott, A. Schreyer, H. Clemens, H. Krenn, "Structural and magnetic properties of EuSe/PbSe, EuSe/PbTe and EuSe/EuTe superlattices grown by molecular beam epitaxy", talk at the Fall Meeting of the Materials Research Society, 1.-6.12.2002, Boston, USA.
13. R. T. Lechner, G. Springholz, T. Schülli, K. Wiesauer, H. Krenn, G. Bauer, "Structural and magnetic properties of EuSe/PbSe, EuSe/PbTe and EuSe/EuTe superlattices grown by molecular beam epitaxy", poster at the 26th International Conference on the Physics of Semiconductors, 29.7.-2.8.2002, Edinburgh, UK.
14. M. Mühlberger, C. Schelling, G. Springholz, F. Schäffler, "Step bunching and strain effects in SiGe layers and superlattices grown on vicinal Si (001) surfaces", poster at the 35th IUVSTA Workshop on "Pattern Formation and Atomic Processes in Epitaxial Growth and Erosion", Trofaiach, Austria, 9.6. – 13.6.2002.
15. M. Mühlberger, C. Schelling, G. Springholz and F. Schäffler, "Step-bunching in $Si_{1-x}Ge_x$ layers and superlattices on vicinal Si (001)", poster at the NANO7/ECOSS21, Malmö 2002.
16. J. Myslivecek, C. Schelling, B.Voigtländer, P. Êmilauer, J. Krug, M. Mühlberger, F. Schäffler, "Step-bunching during Si(001) homoepitaxy: The role of the surface diffusion anisotropy", poster at the NANO7/ECOSS21, Malmö 2002.
17. G. Pillwein, A. Prinz, G. Brunthaler, P.E. Lindelof, and J. Ahopelto, "Screening behavior of the two-dimensional metallic state in silicon-on-insulator structures", Poster at the 26th Int. Conf. on the Physics of Semiconductors, Edinburgh, 2002.
18. P. Rauter, T. Fromherz, G. Dehlinger, H. Sigg, D. Grützmacher, G. Bauer, "Voltage tuneable two-band MIR detection based on Si/SiGe quantum well cascade structures", 4th International conference on Low Dimensional Structures and Devices, Fortaleza, Dec. 2002.
19. F. Schäffler, "Spintronics in silicon-based heterostructures: a potential route toward quantum computing", COST P5 Workshop: Mesoscopic Electronics, Catania, Italy 18.10.2002.
20. D. Gruber, M. Mühlberger, T. Fromherz, F. Schäffler, M. Schatzmayr, "SiC Precipitation during Annealing of $Si_{1-x-y}Ge_xC_y$ Epilayers", oral presentation at the MRS Fall Meeting, 02.12.2002, Boston.
21. J. Mysliveček, C. Schelling, M. Mühlberger, F. Schäffler, B. Voigtländer, J. Krug, P. Šmilauer, "Step Bunching during Si(001) Homoepitaxy Caused by the Surface Diffusion Anisotropy", oral presentation at the MRS Fall Meeting, 02.12.02, Boston.

22. H. Lichtenberger, Z. Zhong, M. Mühlberger, G. Bauer, S. Senz, and F. Schäffler, "Transient-Enhanced Surface Diffusion on Native-Oxide Covered Si(001) Nanostructures during Vacuum Annealing", oral presentation at the MRS Fall Meeting, 03.12.2002, Boston.
23. T. Schwarzl, W. Heiss, G. Springholz, "Mid-infrared absorption of highly ordered PbSe/PbEuTe quantum dot superlattices in a high finesse microcavity", MRS Fall Meeting 2002, Boston, USA (December 2 – 6, 2002).
24. T. Schwarzl, W. Heiss, G. Springholz, H. Krenn, T. Fromherz, "Mid-infrared absorption of highly ordered PbSe/PbEuTe quantum dot superlattices in EuTe/PbEuTe microcavities", 26th International Conference on the Physics of Semiconductors (ICPS 2002), Edinburgh, United Kingdom (July 29 - August 2, 2002).
25. M. Simma, A. Raab, T. Fromherz, G. Springholz, G. Bauer , "Lateral photocurrent spectroscopy of self-organized PbSe quantum dot superlattices", poster at the 12th International Winerschool on New Developments in Solid State Physics – Low dimensional Systems from 2D to Molecules, Mauterndorf, Austria, 25.2. – 1.3.2002.
26. T. U. Schülli, M. Sztucki, T. H. Metzger, R. T. Lechner, J. Stangl, G. Springholz, G. Bauer, "Anomalous x-ray diffraction frm IV-VI semiconductor multilayers and quantum dots", talk at the Fall Meeting of the Materials Research Society, 1.-6.12.2002, Boston, USA.
27. G. Springholz, A. Raab, R. T. Lechner, Z. Zhong, V. Holy, P. Mayer, G. Bauer, "Investigation of self-organized later ordering in vertically aligned PbSe/Pb1-xEuxTe quantum dot superlattices", talk at the 26th International Conference on the Physics of Semiconductors, 29.7.-2.8.2002, Edinburgh, UK.
28. G. Springholz, A. Raab, R. Lechner, V. Holy, P. Mayer, and G. Bauer, "The phase diagram of vertical and lateral ordering in self-organized PbSe quantum dot superlattices", talk at the Fall Meeting of the Materials Research Society, 1.-6.12.2002, Boston, USA.
29. K. Wiesauer, G. Springholz, "Dislocation patterning in PbSe7PbTe (100) heteroepitaxy", poster at the 35th IUVSTA Workshop on "Pattern Formation and Atomic Processes in Epitaxial Growth and Erosion", Trofaiach, Austria, 9.6. – 13.6.2002.
30. K. Wiesauer, "Determination of the critical cluster size and diffusion length in PbTe (111) molecular beam epitaxy", oral presentation at the 12th EuroMBE Workshop, Bad Hofgastein, Feb. 2003.
31. K. Wiesauer, "Selbstorganisierte Nano-Musterbildung durch Versetzungen", talk at the NanoForum2002, Linz, Nov. 2002.
32. Z. Wilamowski, W. Jantsch, F. Schäffler, U. Rössler, S.A. Lyon, "Spin properties of two-dimensional electrons in Si/SiGe quantum wells", 26th int. Conf. Physics of Semiconductors (ICPS-26), Edinburgh (July 29 – August 2, 2002).
33. T. Schwarzl, W. Heiss, G. Springholz,
    Mid-infrared absorption of highly ordered PbSe/PbEuTe quantum dot superlattices in a high finesse microcavity,
    MRS Fall Meeting 2002, Boston, USA (December 2 – 6, 2002)
34. T. Schwarzl, W. Heiss, G. Springholz, H. Krenn, T. Fromherz,
    "Mid-infrared absorption of highly ordered PbSe/PbEuTe quantum dot superlattices in EuTe/PbEuTe microcavities",
    26th International Conference on the Physics of Semiconductors (ICPS 2002), Edinburgh, United Kingdom (July 29 - August 2, 2002)

35. W. Heiss, R. Kirchschlager, R. T. Lechner, G. Springholz,
"Giant magneto-optical effects in EuSe epilayers and EuSe/EuTe superlattices" (poster)
26th International Conference on the Physics of Semiconductors (ICPS 2002), Edinburgh, United Kingdom (July 29 - August 2, 2002)

36. Z.H. Chen, W. Heiss, I. Souma, A. Murayama, Y. Oka,
"Anomalous magneto-optical properties of EuTe induced by magnetic polarons (poster)
2nd International Conference on Physics and Applications of Spin Related Phenomena in Semiconductors (PASPS), Würzburg, German (July 23-26, 2002)

37. R. Kirchschlager, W. Heiss, R. Lechner, G. Springholz,
"Strongly magnetic field dependent luminescence transitions in EuSe epilayers and EuSe/EuTe superlattices" (poster)
2nd International Conference on Physics and Applications of Spin Related Phenomena in Semiconductors (PASPS), Würzburg, German (July 23-26, 2002)

38. M. Böberl, W. Heiss, T. Schwarzl, G. Springholz, J. Fürst, H. Pascher,
"IV-VI microcavity lasers for the mid-infrared with a PbTe active region",
Conference on Lasers, Applications and Technologies (LAT 2002), Moscow, Russia (June 22 - 28, 2002)

39. M. Böberl, W. Heiss, T. Schwarzl, G. Springholz,
"Photoluminescence of PbTe/PbEuTe and PbSe/PbEuSe multiquantumwell-structures for use in midinfrared cavity devices" (poster)
International Conference on Superlattices, Nanostructures and Nanodevices (ICSNN 2002), Toulouse, France (22 - 26 July 2002)

40. A. Bonnani, D. Stifter, G. Neuwirt, A. Montaigne-Ramil, K. Schmidegg, K. Hingerl, H. Sitter, "On-line composition determination and growth control of MOCVD-deposited GaN and related ternary compounds via spectroscopic ellipsometry",
6th Int. Workshop on Expert Evaluation and Control of Compound Semiconductor Materials and Technologies, Budapest, Hungary (May 26-29, 2002)

41. C. Teichert, G. Hlawacek, H. Sitter, A. Andreev, G. Matt, N.S. Sariciftci,
"Self-organization in organic semiconductor thin films grown by Hot-Wall Epitaxy",
35th IUVSTA-Workshop on Pattern Formation and Atomic Processes in Epitaxial Growth and Ion Erosion, Trofaiach, Austria (June 9-13, 2002)

42. K. Schmidegg, A. Bonanni, A. Montaigne-Ramil, D. Stifter, K. Hingerl, H. Sitter,
"In-situ growth control and composition determination of MOCVD GaN and related ternary compounds by spectroscopic ellipsometry",
Crystal Growth and Epitaxy, Vienna, Austria (Oct. 20-23, 2002)

43. A. Andreev, H. Sitter, G. Matt, S. Sariciftci, D. Meissner, H. Hope, H. Plank, R. Resel, A. Thierry, B. Lotz
"Oriented organic semiconductor thin films",
E-MRS 2002 Spring Meeting, Strassbourg, France (June 18-21, 2002)

44. H. Sitter, A. Andreev, G. Matt, S. Sariciftci, H. Plank, R. Resel,
"Hot-wall epitaxial growth of highly ordered organic epilayers",
E-MRS 2002 Spring Meeting, Strassbourg, France (June 18-21, 2002)

45. H. Sitter, A. Andreev, G. Matt, N.S. Sariciftci,
"Hot-Wall Epitaxy – the method of choice for the growth of highly ordered organic epilayers", 4th Int. Conf. On Electronic Processes in Organic Materials, Lviv, Ukraine (June 3-8, 2002)

46. A. Andreev, H. Sitter, R. Resel, D.-M. Smiglies, H. Hoppe, G. Matt, N.S. Sariciftci, D. Meissner, D. Lysacek, L. Valek, "Highy ordered organic semiconductor thin films

grown by Hot-Wall Epitaxy", 4th Int. Conf. On Electronic Processes in Organic Materials, Lviv, Ukraine (June 3-8, 2002

47. A. Andreev, H. Sitter, S. Sariciftci, R. Resel, D.M. Smilgies, "Morphology and growth kinetic of molecular organic thin film deposited by HWE", Crystal Growth and Epitaxy, Vienna, Austria (Oct. 20-23, 2002)
48. A. Bonanni, D. Stifter, A. Montaigne-Ramil, K. Schmidegg, K. Hingerl, H. Sitter, "In-situ spectroscopic ellipsometry of MOCVD grown GaN compounds for one line composition determination and growth control", 9th Int. Conference on MOVPE, Berlin, Germany (May 2002)
49. G. Kocher-Oberlehner, W. Jantsch, L. Palmetshofer, A. Ulyashin Luminescence enhancement by hydrogenation of Si:Er,O E-MRS Spring Meeting (June 18 - 21, 2002)
50. Z. Wilamowski, W. Jantsch Spin Relaxation in a 2d electron gas in Si quantum wells 2nd International Conference on Physics and Application of Spin Related Phenomena in Semiconductors, PASPS 2002, Würzburg (July 23 – 26, 2002)
51. Z. Wilamowski, W. Jantsch, N. Sandersfeld, F. Schäffler, S. Lyon Spin-coherance and –manipulation in Si/SiGe quantum wells E-MRS Spring Meeting, SYMPOSIUM Q (June 18 – 21, 2002)
52. B.A. Andreev, W. Jantsch, Z.F. Krasilnik, D.I. Kuritsyn, V.P. Kuznetzov, M.V. Stepikhova, A.N. Yablonsky Quantum efficiency and temperature quenching of the luminescence of uniformely and selectively Erbium-doped silicon structures produced by the sublimation MBE method 26th int. Conf. Physics of Semiconductors (ICPS-26), Edinburgh (July 29 – August 2, 2002)
53. G. Kocher- Oberlehner, W. Jantsch, A. Ulyashin Hydrogen-enhanced luminescence of Erbium doped Silicon 26th int. Conf. Physics of Semiconductors (ICPS-26), Edinburgh (July 29 – August 2, 2002)
54. Z. Wilamowski, W. Jantsch, F. Schäffler, U. Rössler, S.A. Lyon Spin properties of two-dimensional electrons in Si/SiGe quantum wells 26th int. Conf. Physics of Semiconductors (ICPS-26), Edinburgh (July 29 – August 2, 2002)

Diploma Theses

Finished in 2002:

1. Herbert Lichtenberger "Characterization and overgrowth of prestructured silicon-substrates" (June 2002)
2. Böberl Michaela: "Bauelemente mit vertikalen Resonatoren basierend auf Bleisalz-Metallstrukturen"

Current works:

1. Wolfgang Schwinger "*Epitaxial Overgrowth of Fullerenes on Si (100)*" (Technische Physik)
2. Mathias Simma "*Photoleitungsuntersuchungen an Quantenpunkten*"

3. Stefan Griesser
   "*Leitfähigkeitsmessungen an zweidimensionalem Elektronengas"*
4. Benjamin Lindner
   "*Metall-Isolator-Übergang in zweidimensionalen Siliziumstrukturen*"
5. Dietmar Pachinger
   "*High-mobility Si/SiGe heterostructures for spintronic applications*"
6. Patrick Rauter
   "*Intersubbandübergänge in SiGe-Strukturen*"
7. Eugen Wintersberger
   "*Röntgenbeugung und –reflexion an Si/SiGe/GaAs Hetero- und Nanostrukturen*"
8. Kirchschlager Raimund:
   "Magnetooptische Eigenschaften von Eu-Chacogeniden"
9. Roither Jürgen:
   "Mikroresonatoren aus dielektrischen Bragg-Spiegeln für lichtemittierende II-VI-Halbleiterbauelemente"
10. Söllinger Walter:
    "3-D Mikroresonatoren"

Doctor's Theses

Finished in 2002:

1. Dipl.Ing. Adrian Prinz
   "Magnetotransport investigations of the two-dimensional metallic state in silicon metal-oxide-semiconductor structures" (March 2002)
2. M. Sc. Tomas Roch
   "Structural investigations of SiGe cascade multilayers and self-organized SiGe wires using x-ray scattering techniques" (April 2002)

Current works:

1. Dipl. Phys. Anke Hesse:
   "Strukturelle Untersuchungen an Halbleiternanostrukturen"
2. Dipl. Ing. Michael Mühlberger
   "Epitaktisches Wachstum von modulationsdotierten Si/SiGe Si/SiGeC Heterostrukturen"
3. Dipl. Ing. Karin Wiesauer
   "Scanning tunneling microscopy studies of dislocation structures in IV-VI heterostructures"
4. Dipl. Ing. Anneliese Raab
   "Molecular beam epitaxy of self-assembled IV-VI quantum dots"
5. Mag. Rainer T. Lechner
   "Herstellung und Charakterisierung von EuSe- Nanostrukturen"
6. Dipl.Ing. Thomas Berer
   "Electronic and spin properties of Si/SiGe heterostructures"
7. Dipl.Ing. Georg Pillwein
   "Elektrische Untersuchungen von Quanteneffekten an Nanostrukturen"
8. Dipl.Ing. Herbert Lichtenberger
   "Kinetic and strain-induced self-organization of SiGe heterostructures"

9. Mag. Jiri Novak
   "Untersuchung der strukturellen Eigenschaften von Quantenpunkten"
10. Dipl.Ing. Daniel Gruber
    "Two-dimensional electron gases in Si/SiGe for spintronics
11. Dipl.-Ing. Joachim Achleitner:
    "Simulation magnetooptischer Effekte"
12. Dipl.-Ing. Michaela Böberl
    "Elektrooptische Bauelemente aus Bleisalz"
13. Dipl.-Ing. Gernot Fattinger:
    "Methoden zur statistischen und dynamischen Charakterisierung von Mikrostrukturen"
14. Mag. Erich Kaufmann:
    "Laterale Bleisalz-Strukturen"
15. Dipl.-Ing. Gudrun Kocher-Oberlehner:
    "Er-dotiertes Si und SiGe für optoelektronische Anwendungen im Bereich von 1,54 µm"
16. Dipl.-Ing. Hans Malissa:
    "Spin-Eigenschaften in niedrigdimensionalen Systemen"
17. M.Sc. Alberto Montaigne-Ramil:
    "Fabrication and ex-situ characterization of wide band gap semiconductor materials"
18. Dipl.-Ing. Klaus Schmidegg:
    "Growth and optical characterization of GaAlN and GaInN"
19. Dipl.-Ing. Thomas Schwarzl:
    "Vertikal emittierende Bleisalzlaser"

Cooperations

1. Academy of Sciences, Bratislava, Slovakia
2. Aixtron, Aachen, Deutschland
3. Akademie der Wissenschaften, Troitsk, Moskau
4. Akademie der Wissenschaften, Warschau, Polen
5. AMS Unterpremstätten, Österreich
6. Balzers (Unaxis), Trübach, Schweiz
7. Bosch (Stefan Holl), Linz
8. CENG Grenoble, France
9. CNRS-CRMC2-Marseille, France
10. CNRSM-PASTIS, Brindisi, Italy
11. Daimler Benz Reserach Laboratories, Dr. Presting, Dr. König, Ulm
12. DESY, Hasylab, Hamburg, Deutschland
13. E+E Electronic GmbH, Engerwitzdorf, Österreich
14. ELETTRA, Triest, Italy
15. ENEA, Roma, Italy

16. ESRF Grenoble, France
17. ETH, Zürich, Swiss
18. FOM Institute Rijnhuizen, Niederlande
19. FORTH, Crete, Greece
20. Fraunhofer-Institut (IAF) Freiburg (Chiptechnologie), Deutschland
21. Fraunhofer-Institut für Physikalische Meßtechnik (Freiburg, Deutschland)
22. Heriot Watt University, Edinburgh, Scotland
23. High Magnetic Field Lab., Grenoble, France
24. IBM Research Center, Yorktown Heights, USA
25. INFINEON Villach, Österreich
26. INSA, Lyon, France
27. Inst. f. Experimentalphysik I, Universität Bayreuth, Deutschland
28. Institut für Festkörperelektronik, TU Wien
29. Institut für Halbleiterphysik, Frankfurt/Oder, Deutschland
30. Institute for Physics of Microstructures RAS, 603600 Nizhny Novgorod, Russland
31. Institute of Physics, Polish Academy of Sciences, Warschau, POLEN
32. Ioffe Physico-Technical Institute RAS, 194021 St.Petersburg, Russland
33. KEBA, Ing.G.Krippner, Linz, Österreich
34. Lebedev Institut, Russian Academy of Sciences, Moskau, Russland
35. Masaryk University, Brno, Czech Republic
36. Max-Born Institut fuer Nichtlineare Optik, Berlin-Adlershof
37. Max-Planck Institut für Festkörperpforschung, Stuttgart
38. MIT, Cambridge, MA, USA
39. Nanoelectronics Research Center, University of Glasgow, Scotland
40. NIST, Gaithersburg, MD, USA
41. North Carolina State University, NC, USA
42. Ørsted Institut, Kopenhagen, Dänemark
43. Paul Scherrer Institut, Villigen, Schweiz
44. Philips Analytics, Almelo, Niederlande
45. Physics Department, Cornell University
46. Profactor, Steyr, Upper Austria
47. Purdue University, Lafayette, IN, USA
48. Sektion Physik, Ludwig-Maximilians Universität München
49. Sentech, Berlin
50. Siemens München, Zentrale Technik, Bereich Halbleiter
51. ST Microelectronics, Crolles, Grenoble
52. TASC Triest, Italy

53. Thomson, Paris, France
54. Tohoku University, Sendai, Japan
55. TU Berlin, Institut für Festkörperphysik, Deutschland
56. TU-München (Mikrowellentechnik), Deutschland
57. Unipress, High Pressure Research Center, Polish Academy of Sciences, Warschau
58. Universita Padova, Italia
59. Universität Bremen, Deutschland
60. Universität Graz, Institut für Experimentalphysik
61. Universität Paderborn, Deutschland
62. Universität Potsdam, Deutschland
63. Universität Würzburg, Deutschland
64. Université de Montpellier, France
65. Universiteit Instelling, Antwerpen, Niederlande
66. University of Erlangen-Nürnberg, D-91058 Erlangen, Deutschland
67. University of Lund, Solid State Physics, Lund, Sweden
68. University of Maryland, MD, USA
69. University of Southampton, England
70. University of Warwick, Coventry, England
71. Van der Waals-Zeeman Institute, University of Amsterdam, NL
72. VOEST ALPINE, Dr.Angerer, Linz
73. Walter Schottky Institut, TU München, Deutschland

Transient-Enhanced Surface Diffusion on Natural-Oxide-Covered Si(001) Templates during Vacuum Annealing

H. Lichtenberger, M. Mühlberger, C. Schelling, F. Schäffler,

Inst. of Semiconductor and Solid State Physics, Joh. Kepler Univ. Linz

We report on the transient-enhanced shape transformation of nano-structured Si(001) surfaces upon *in vacuo* annealing at relatively low temperatures of 900 – 950 °C for a few minutes. We find dramatic surface mass transport concomitant with the development of low-energy facets on surfaces that are covered by native oxide. The enhanced surface mass transport ceases after the oxide is completely desorbed, and it is not observed on surfaces where the native oxide had been removed by HF before annealing.

Introduction

Commercial ultra-large-scale integrated circuits have reached physical gate lengths well below 100 nm, and self-organization phenomena are explored as an alternative route toward the fabrication of even smaller device structures. However, the fabrication of such small structures is only one precondition for shrinking device dimensions. It is as important to preserve their size, shape and electronic properties during subsequent device processing. Here we concentrate on the shape stability of Si nanostructures during vacuum annealing at around 900 °C for a few minutes. Such thermal steps are typically employed for native oxide desorption prior to epitaxial growth, but similar thermal budgets are frequently required during device processing, e.g. after ion implantation.

While the shape evolution of structured Si surfaces is well described [1], [2], most of the experimental studies employed long-term, high-temperature anneals. Also, quite often exotic annealing procedures (e.g. a flash to 1200 °C [3]) and direct current heating (prone to electro-migration artifacts [4]) were used. Here we employed only cleaning and annealing procedures adapted from standard Si device processes.

Experimental

Sample Preparation

Our studies were concentrated on samples consisting of periodic wire arrays of rectangular cross section fabricated by holographic lithography and subsequent reactive ion etching on Si(001) substrates (Fig. 1 (a)). Periods were varied between 400 – 2000 nm at etch depths of typically 250 nm. After photoresist stripping, the samples underwent an RCA clean with or without a final HF-dip immediately before transfer into the UHV environment of an MBE system.

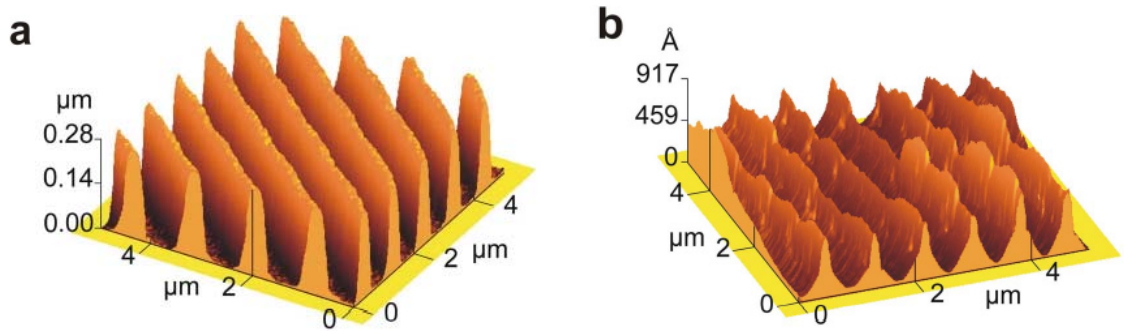

Fig. 1: 3D-AFM images of rectangular wire-template as processed (a) and after 4 min annealing @ 950°C without previous HF-dip (b).

Measurements

In the UHV environment of the MBE system the samples were radiatively annealed for 1 – 5 min at 900 – 950 °C, which corresponds to the standard oxide desorption step prior to epitaxial growth [5], [6]. On all samples covered by native oxide the originally rectangular profiles were transformed into {311}-faceted trapezoids concomitant with a loss of up to 80% of the peak-to-valley modulation (Figs. 1 (b), 2 "RCA"). In contrast, samples that had the native oxide removed by HF showed no significant morphological changes (Fig. 2 "HF").

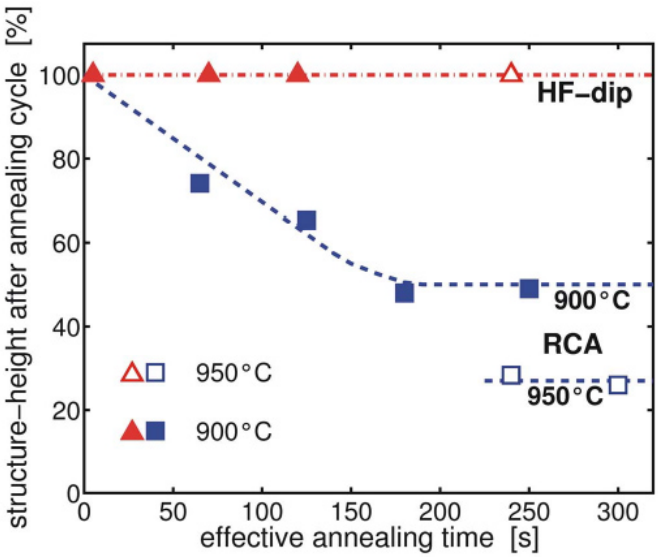

Fig. 2: Reduction of structure-height after different annealing cycles.

We followed the kinetics of faceting as a function of the annealing conditions by high-resolution XTEM imaging (Fig. 3), and compared the results to Monte-Carlo-type simulations that used the surface energies of the {111} and {311} facets as the only input parameters. We found good agreement, which is indicative of a shape transformation that behaves as expected near thermal equilibrium [1], [7], despite the fact that our experiments were conducted 500 °C below the melting point of Si.

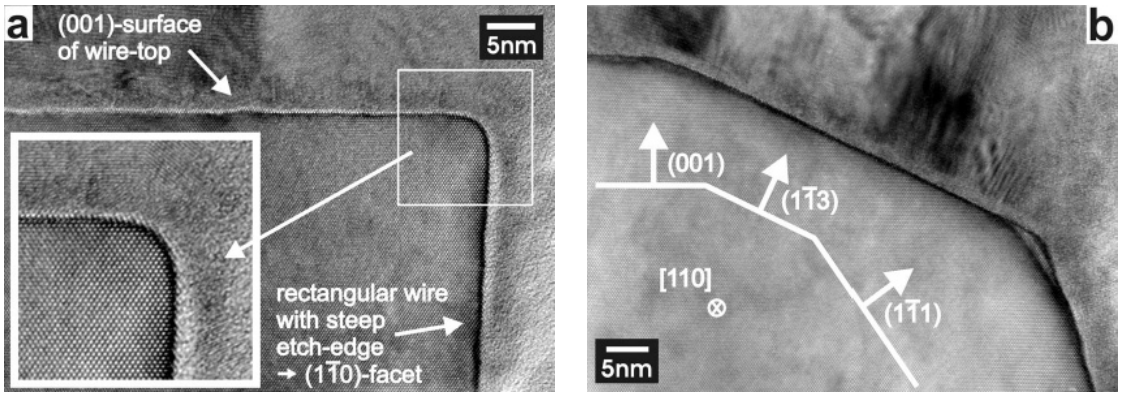

Fig. 3: High-resolution XTEM-images of rectangular and faceted wire-edges, as processed (a) and after 2 min annealing @ 900°C without previous HF-dip (b).

Since only oxide-covered structures reveal the transient enhanced shape transformation, the reaction [8] Si + $SiO_2 \rightarrow SiO\uparrow$, on which thermal oxide desorption at 900 °C is based, is most likely involved in this phenomena. This reaction takes place everywhere at the Si/SiO_2 interface, but it has been found that the oxide desorption reaction occurs mainly at the periphery of voids, which form in the early stages of thermal decomposition in the oxide layer [9]. No correlations between void nucleation and shallow structures at the Si surface have been found yet. However, it is not clear, whether this applies to our nanostructures, which provide almost atomically sharp intersections between two low-index planes (Fig. 3 (a)).

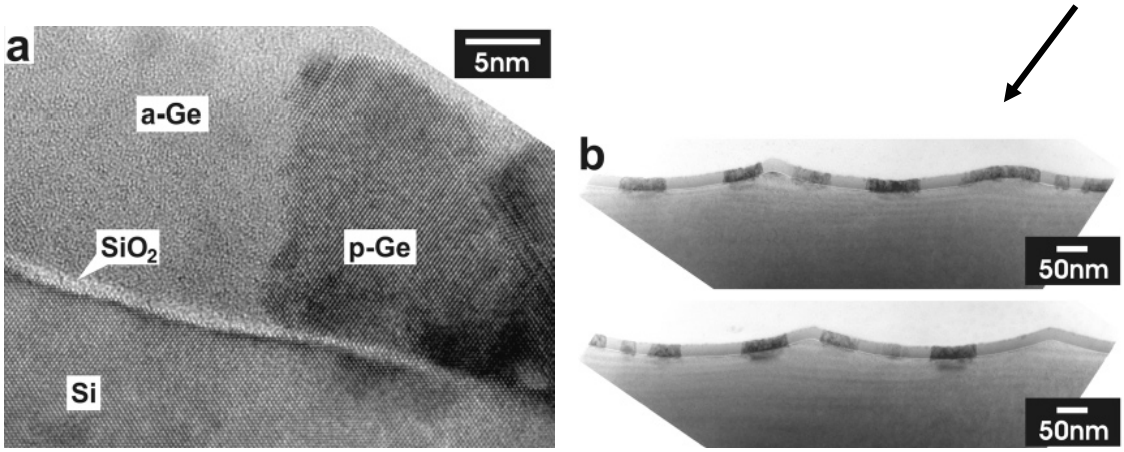

Fig. 4: (a) High-resolution XTEM-image of wire-template with a period of 400 nm after 1 min annealing @ 900 °C with posterior Ge-overgrowth at temperatures below 175 °C. On the SiO_2 covered Si structure amorphous Ge is formed, whereas polycrystalline Ge indicates regions of oxide-desorbed surface parts.
(b) Low resolution TEM images indicate that oxide break-up shows no correlation with the wire template.

In order to distinguish whether the shape transformation is linked to void formation or occurs beneath a still existing layer of oxide, we have developed an XTEM decoration technique. Covering annealed (1 min @ 900 °C) wire templates in situ with low temperature Ge leads to poly-Ge growing in the substrate-exposing voids, and to amorphous Ge on areas that are still covered by native oxide (Fig. 4 (a)). The p-Ge areas can easily be identified in XTEM images because the strain contrast makes them ap-

pear darker (Fig. 4 (b)). In addition, the mass contrast allows a straightforward identification of the SiO_2 layer, which appears as alight stripe.

Figure 4 (b) shows that no correlation whatsoever exists between void formation and the template structure: Most of the remnants of the wires are still buried underneath a continuous SiO_2 film. That means, the shape transformation takes place predominantly below the oxide, and the oxide follows this transformation. The voids do have some influence: The one ridge structure that accidentally coincides with a void in the oxide (arrow in Fig. 4) appears even flatter than the oxide-covered ridges. This effect is most likely responsible for the roughness overall in Fig. 1 (b).

Conclusion

Shrinking the dimensions of semiconductor devices structures to the nanometer range, the preparation and conservation of small morphological features becomes increasingly relevant. The surface free energy of a structured heterosystem is determined by composition, crystal orientation, and strain. The interplay between these parameters is widely exploited for the fabrication of self-organized nanostructures. Pre-patterned substrates can enhance ordering of these sub-micron structures. Here we report on the morphological integrity of such templates under chemical and thermal treatments typically employed during device processing. The results show that even proven and supposedly uncritical process steps can drastically affect the morphology of nanostructures.

Acknowledgements

We thank C. Schelling for his input during the early stages of this study, and A. Halilovic and G. Hesser for template and XTEM preparation, respectively. TEM work was performed at the Technical Services Unit (TSE) of the Johannes Kepler University. This work was financially supported by GMe and FWF (P12143PHY).

References

[1] J. M. Bermond, J. J. Métois, X. Egéa, F. Floret; Surf. Sci. **330** (1995), 48 and references therein

[2] T. Suzuki, J. J. Métois, K. Yagi; Surf. Sci. **339** (1995), 105

[3] S. Tanaka, C. C. Umbach, J. M. Blakely, R. M. Tromp, M. Mankos; J. Vac. Sci. Technol. **A15** (1997), 1345

[4] L. V. Litvin, A. B. Krasilnikov, A. V. Latyshev; Surf. Sci. Lett. **244** (1991), L121

[5] E. Kasper, M. Bauer, M. Oehme; Thin Solid Films **321** (1998), 148

[6] E. A. Gulbransen, S. A. Jansson; Oxid. Metals **4** (1972), 181

[7] M. E. Keeffe, C. C. Umbach, J. M. Blakely; J. Phys. Chem. Solids **55** (1994), 965

[8] R. E. Walkup, S. I. Raider; Appl. Phys. Lett. **53** (1988), 888

[9] D. Jones, V. Palermo; Appl. Phys. Lett. **80** (2002), 673

Laterally Ordered Ge Islands on the Pre-Patterned Si (001) Substrates

Zhenyang Zhong, A. Halilovic, M. Mühlberger, H. Lichtenberger, F. Schäffler, G. Bauer

Inst. of Semiconductor and Solid State Physics, Joh. Kepler Univ. Linz

Ge islands were grown on the pre-patterned Si (001) substrates by solid-source molecular beam epitaxy. The topographies of the islands samples, obtained by atomic force microscopy (AFM), demonstrated that Ge islands tend to grow in the trenches or in the holes on one- or two-dimensionally patterned substrates, respectively. Provided the periodicities of the trenches or the holes originated from the pre-patterns, laterally ordered Ge islands were obtained. The preferential positioning of Ge islands in the trench or in the holes is attributed to a net flux of ad-dimers (or ad-atoms) downwards at the sidewalls, which is related to the growth temperature and the growth rate.

Introduction

Several authors reported the combination of pre-patterning of substrates with self-organized growth to achieve long range ordering of self-assembled islands [1] – [6]. For the growth of Ge islands on (001) Si substrates, so far for their preferential positioning, mainly lithographically defined patterned oxide features have been used. In this fabrication method, the Ge islands are grown preferentially at the edge of the stripes or mesas selectively grown in pre-patterned and etched SiO_2 windows [1] – [4]. By adjusting the size of the SiO_2 windows, a controlled arrangement of the Ge islands could be realized. This local epitaxy works particularly well if gas source (GS) molecular beam epitaxy (MBE) or chemical vapor deposition (CVD) processes are used. However, the remaining SiO_2 layer induces external strain and furthermore complicates the subsequent processes to characterize the properties of Ge islands or to fabricate devices. In this presentation, we show results of ordered Ge islands grown on pre-patterned (one- or two-dimensional (1D or 2D) Si (001) substrates. Our observations demonstrate that the growth kinetics significantly affect the positioning of Ge islands on the pre-patterned substrates without use of SiO_2 windows. In particular, 1D and 2D ordered Ge islands can be realized on these pre-patterned Si (001) substrates.

Experiments

The pre-patterned substrates were fabricated by holographic lithography and reactive ion etching. The orientation of the stripes and the square pattern was chosen to be along <110> directions. Patterns with a periodicity of less or equal than 0.5 µm and a depth of about 50 nm are used. All samples were grown by solid-source MBE. The substrates were cleaned by an RCA cleaning process followed by a HF dip to form hydrogenated surfaces. After desorption of the oxide layer at 900 °C, a Si buffer layer (about 100 nm thick) was deposited at a growth rate of 0.5 Å/s while the growth temperature was ramped from 550 °C to 650 °C. For samples grown on a 1D stripe-patterned substrate, seven monolayers (ML) Ge were then deposited at 650 °C. For the sample grown on a 2D square pattered substrate, 6ML Ge were deposited at 700 °C. For the Ge island growth, a growth rate of 0.04 Å/s was used. We also investigated samples with a stack of three Ge island layers separated by 20 nm Si spacer

layers. In these samples, the upper two Ge islands layers were grown at 650 °C with only 5.7 ML Ge deposition, in order to avoid an increase of the island size. To reduce Ge-Si intermixing, the Si spacer layer was grown at 550 °C. The rather high substrate temperatures for the Ge island growth were chosen to enhance Ge adatom diffusion, which in conjunction with the low growth rates enabled us to achieve the desired ordering. The surface morphology of these samples was investigated after growth in air using a Park Scientific atomic force microscope (AFM).

Results

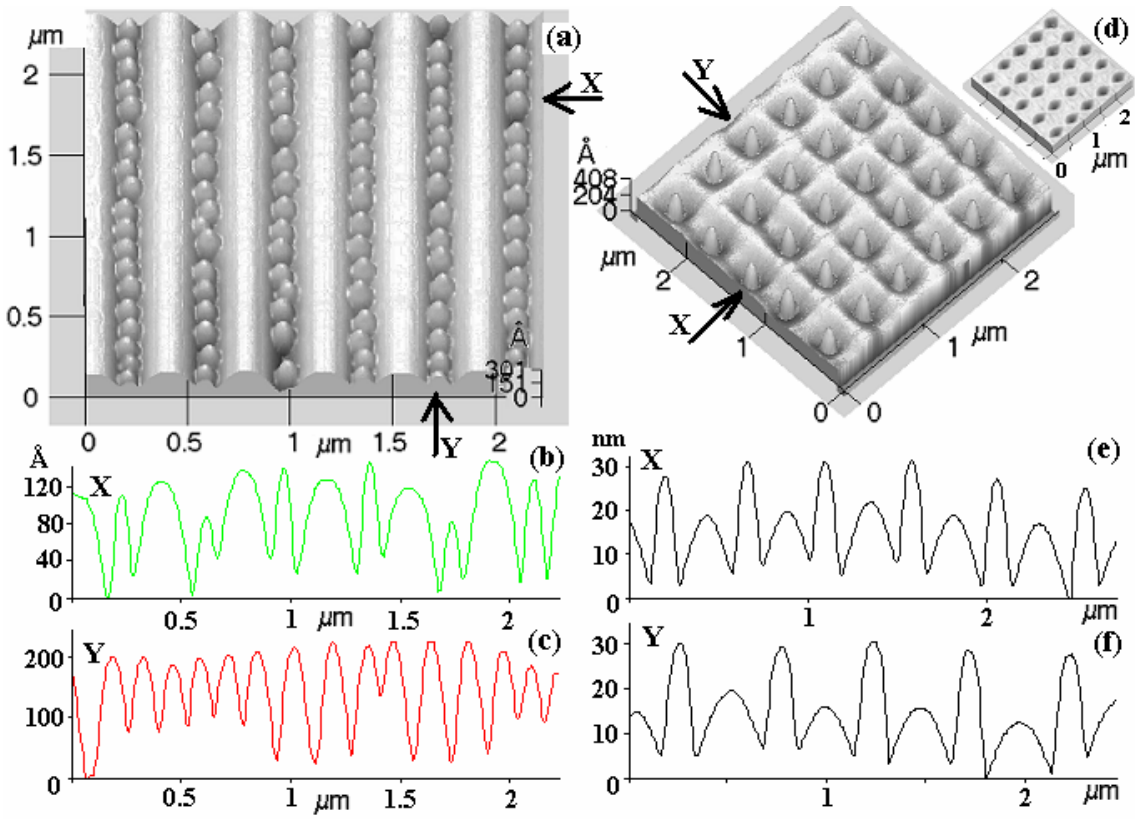

Fig. 1: AFM micrographs of 1D (a) and 2D ordered Ge islands (d), with corresponding line scans (b, c) and (e, f).

The 2D or 3D AFM images of samples A and B are shown in Figs. 1 (a), (b) and (c), respectively. For sample A, which was grown on a 1D patterned substrate, we observe an ordering of the islands along the trenches with a lateral period of 40 nm. In addition, height profiles are shown. Along the trenches (Fig. 1 (b)) and perpendicular to it (Fig. 1 (c)), we observe long range ordering of dome-shaped islands not only for the “one dimensional” sample A but also for the “two-dimensional” sample B. For the square patterned substrate, the Ge islands nucleate in the holes formed by the orthogonally etched trenches and *not* on top of the mesas. This observation differs from previously reported gas source MBE growth of islands on etched mesas [2], [3]. Figures 1 (e) and (f) show line scans, i.e. height profiles of the 2D ordered islands along two orthogonal directions. These line scans reveal both the achieved precision of the two- dimensional lateral positioning as well as size uniformity of the islands.

The nearly perfect lateral ordering of the islands can be used to stack several layers of Ge islands to form a three dimensional island crystal. We chose a Si spacer layer

thickness of 20 nm, which ensures a vertical ordering of the islands, due to the strain fields of the buried ones. Figure 2 shows the surface morphology of samples C and D which consist of a stack of three Ge island layers separated by Si spacer layers, which were grown at 550 °C, These AFM data nicely demonstrate the long range ordering and size homogeneity of the Ge islands. The line scans along two orthogonal <110> directions not only demonstrate the periodicity and the size homogeneity but also the fact that in the stacked island samples the regions in between the islands are flattened through the coverage with Si.

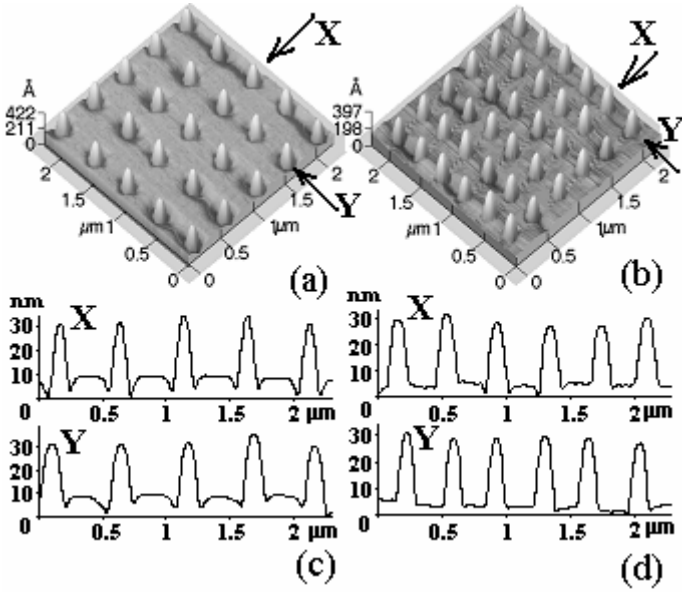

Fig. 2: Surface morphology of three period stacked Ge island samples with a lateral period of 500 nm (sample C, (a)) and 400 nm (sample D, (b)). Line scans along two orthogonal <110> directions marked by X and Y are shown in (c) (sample C) and (d) (sample D).

In samples that were capped with Si we investigated also the photoluminescence (PL). Clear PL signatures both from the islands as well as from the wetting layers were found.

Conclusions

In conclusion, we have demonstrated two-dimensional lateral ordering of Ge islands on pre-patterned Si substrates without the use of patterned oxide layers or of buried stressor layers.

We explain our observations of this two-dimensional ordering by the importance of the growth kinetics of Ge on Si, which primarily affects the preferential positioning of Ge islands on the pre-patterned Si substrates. The formation of Ge islands in the trenches or in these holes is attributed to the accumulation of Ge adatoms migrating downwards from the sidewalls of trenches or holes or even from the neighboring mesas to the bottom. The reason for this downward flux of adatoms is an asymmetry of the activation barrier at steps [7]. The Ge atoms that remain on top of the ridges or mesas form a Ge layer with a thickness less than the critical value for 2D-3D transition, resulting in the absence of islands. This kinetic origin of island formation in trenches or holes agrees with our previous results on the formation of Ge islands on 1D pre-patterned stripes [7].

The growth technique described makes a precise addressing of individual islands possible, a prerequisite for any application of these self-organized Ge nanostructures in electronic or optoelectronic applications.

Acknowledgements

Work supported by FWF, Vienna (Project No 14684), and ECOPRO, EC, Brussels.

References

[1] T.I. Kamins and R. S. Williams, Appl. Phys. Lett. **71**, 1201 (1997).

[2] E.S. Kim, N. Usami, and Y. Shiraki, Appl.Phys. Lett. 72, 1617 (1998).

[3] G. Jin, J. L. Liu, and K. L. Wang, Appl. Phys. Lett. **76**, 3591 (2000).

[4] L. Vescan and T. Stoica, J. Appl.Phys. **91**, 10119 (2002).

[5] O.G. Schmidt, N.Y. Jin-Phillipp, C. Lange, U. Denker, K. Eberl, R. Schreiner, H. Gräbeldinger, and H. Schweizer, Appl. Phys. Lett. **77**, 4139 (2000).

[6] T. Kitajima, B. Liu, S. R. Leone, Appl. Phys. Lett. **80**, 497 (2002).

[7] Zhenyang Zhong, A.Halilovic, M. Mühlberger, F. Schäffler, G. Bauer, Appl. Phys. Lett., ***82,*** 445 (2003).

Growth Instabilities in Si/SiGe Homo- and Heteroepitaxy

M. Mühlberger[1], C. Schelling[1], G. Springholz[1], F. Schäffler[1], J. Mysliveček[2], B. Voigtländer[2], P. Šmilauer[3], J. Krug[4]

[1]Inst. of Semiconductor and Solid State Physics, Joh. Kepler Univ. Linz
[2]Inst. für Schichten u. Grenzflächen ISG 3, Forschungszentr. Jülich, D
[3]Czech Academy of Sciences, Praha, Czech Republic
[4]Fachbereich Physik, Universität Essen, D

We show that for a large set of growth parameters the reason for ripple formation in the Si/SiGe system is the kinetic step-bunching instability found in Si homoepitaxy. Single $Si_{1-x}Ge_x$ layers (with x around 0.5) do not show step-bunching. In superlattices, the instability has a similar behavior as the instability in homoepitaxy. Mainly the growth temperature influences the surface morphology; only little changes can be found when the germanium content in the superlattices is changed. In addition, the increase of ripple height and period with increasing amount of deposited silicon is similar to the one found in homoepitaxy. The more germanium is present in the superlattice the less pronounced the step-bunches appear. In kinetic Monte-Carlo simulations we show that only the interplay between diffusion anisotropy on the (2×1) reconstructed Si(001) surface and the attachment/detachment of adatoms on the step-edges is responsible for the growth instability in Si homoepitaxy.

Introduction

The Si(001) surface is the technologically most important surface for the semiconductor industry. The step-bunching growth instability on vicinal Si(001) is single $Si_{1-x}Ge_x$ layers and Si/SiGe superlattices was often believed to be strain-induced [1]. In fact, it has been found that a step-bunching instability resulting in an indistinguishable surface morphology appears already in Si homoepitaxy [2], where no strain is present.

Experiments

Single SiGe layers and Si/SiGe superlattices (SLs) have been grown by solid source molecular beam epitaxy (MBE) on RCA-cleaned substrates with a miscut of 0.66° in [110] direction to investigate the influence of germanium.

Single $Si_{1-x}Ge_x$ layers (with x around 0.5) do not show step bunching. They replicate the morphology of the underlying buffer layer, which can be chosen as flat or rippled by selecting proper growth conditions. These layers disintegrate into hut-clusters when allowed to reach thermodynamic equilibrium [3].

In superlattices the instability has a similar behavior as the instability in homoepitaxy. When miscut (0.66°) and growth rate (0.2 Å/s) are kept constant, mainly the growth temperature influences the surface morphology, only little changes can be found when the germanium content in the superlattices is changed (see Fig. 1). In addition, the increase of ripple height and period with increasing amount of deposited silicon is similar to the one found in homoepitaxy. Both follow a $y=a \cdot x^b$ type law, with critical exponents of 0.5 and 0.25 respectively. The more germanium is present in the superlattice the less pronounced the step-bunches appear. We attribute this slight decrease with in-

creasing germanium content to changes in surface kinetics, which are due to the segregation of germanium [4].

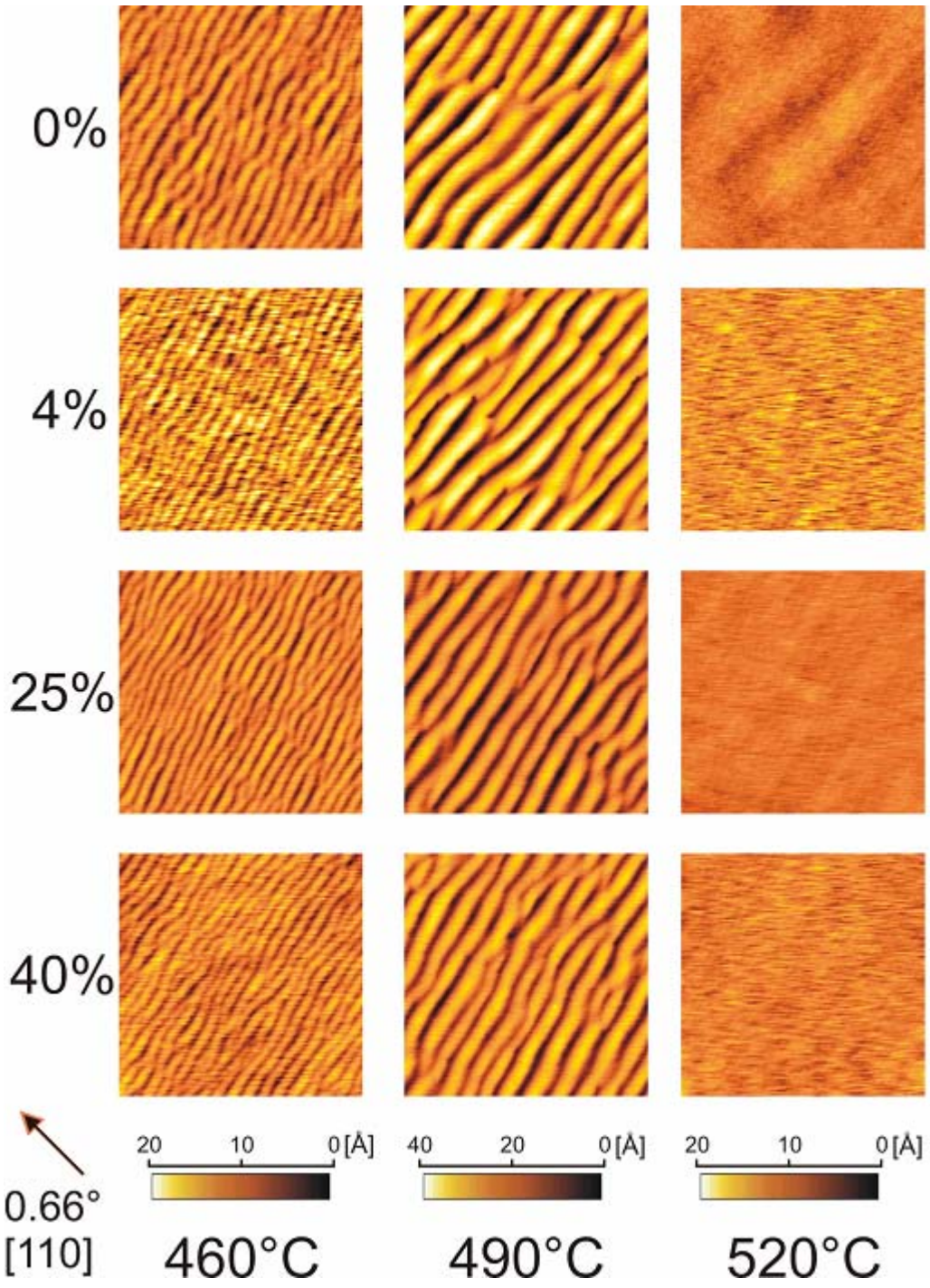

Fig. 1: AFM images of 10× [30Å Si / 300 Å $Si_{1-x}Ge_x$] superlattices grown at various growth temperatures (indicated on the bottom) and Ge-contents (indicated on the left). The miscut direction is given by the arrow on the lower left side. All images are 5×5 µm² in size.

Kinetic Monte-Carlo Simulations

In two-dimensional kinetic Monte-Carlo simulations, we show that growth kinetics is the mechanism, which is relevant for the step bunching. In Si homoepitaxy only the interplay between the diffusion anisotropy on the (2×1) reconstructed Si(001) surface and the attachment/detachment of adatoms on the different S_A and S_B step-edges is responsible for the growth instability in Si homoepitaxy. No step-edge barriers are necessary to explain the experimentally observed morphology [5]. Figure 2 shows images illustrating the time evolution of the sample surface during the simulation.

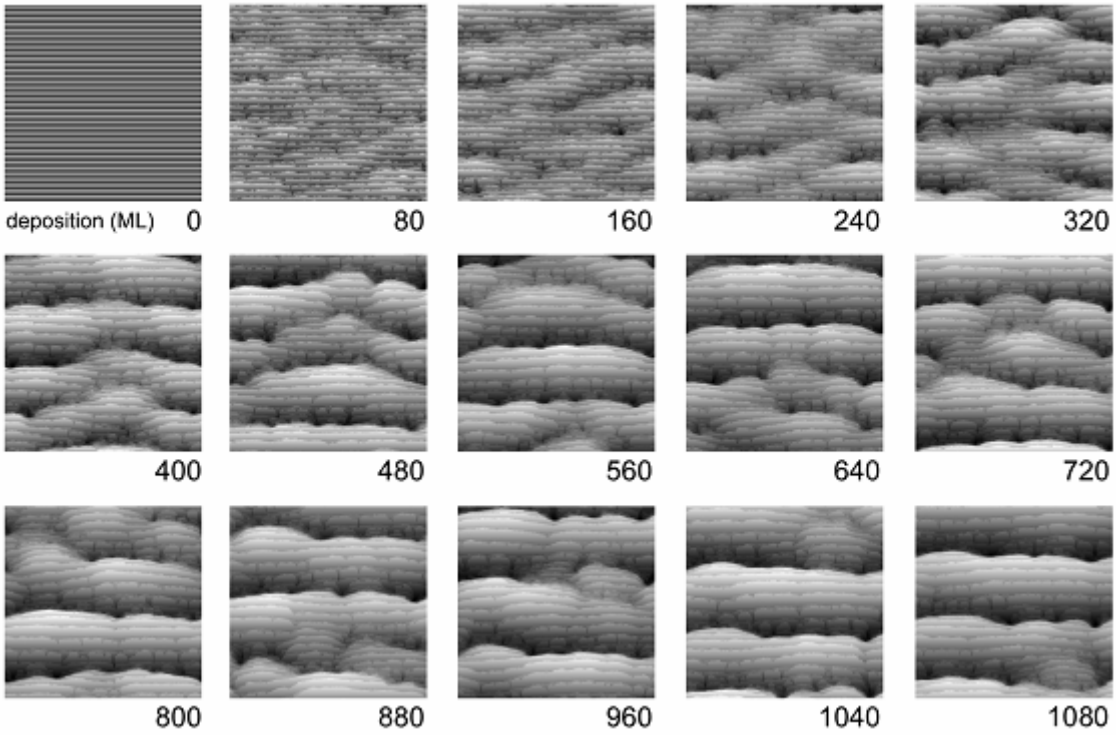

Fig. 2: Results of the two-dimensional kinetic Monte Carlo simulation showing the evolution of the surface. The number of deposited monolayers (MLs) is given for each image.

Conclusion

In conclusion, we show that for a large set of parameters strain-induced step bunching can be excluded with high probability and that the reason for ripple formation in the Si/SiGe system is only the kinetic step bunching instability found in Si homoepitaxy. We find that germanium slightly influences the step bunching in Si due to its segregation but not due to the strain introduced because of the lattice mismatch. Two-dimensional kinetic Monte Carlo simulations give close insight in the atomic mechanisms responsible for this phenomenon.

References

[1] J. Tersoff, Y.H. Phang, Z. Zhang, M.G. Lagally, “Step-bunching instabiliy of vivinal surfaces under stress”, Phys. Rev. Lett. 75, 2730 (1995)

[2] C. Schelling, G. Springholz, F. Schäffler, “Kinetic growth instabilites on vicinal Si(001) surfaces”, Phys. Rev. Lett. 83, 995 (1999)

[3] C. Schelling, M. Mühlberger, G. Sprigholz, F Schäffler, “Si1-xGex growth instabilities on vicinal Si(001) substrates: Kinetic vs. strain-induced effects”, Phys. Rev. B 64, 041301R (2001)

[4] M. Mühlberger, C. Schelling, G. Springholz, F. Schäffler, “Step-bunching in SiGe layers and superlattices on Si(001)”, Surface Science, in print (2003)

[5] J. Mysliveček, C. Schelling, F. Schäffler, G. Springholz, P. Šmilauer, J. Krug, B. Voigtländer, “On the microscopic origin of the kinetic step-bunching instability on vicinal Si(001)”, Surface Science 520, 193 (2002)

Light from Silicon: SiGe Quantum Cascade Structures

T. Fromherz, G. Bauer

Inst. f. Semiconductor- and Solid State Physics, University Linz, Austria

Recently, encouraging results on electroluminescence of valence band SiGe cascade structures in the mid- and far infrared (THz) spectral regions have been reported. In this paper, we review these results an compare them to **kp** bandstructure calculations based on a strain dependent Luttinger Kohn Hamiltonian.

Introduction

The working principle of a quantum cascade (QC) emitter is based on optical transitions of only one type of carrier (uni-polar emitter). Typically, one period of the cascade consists of an active region and of an injector region. The active region is built up of typically 1 – 4 quantum wells (QW) that are designed for intense emission at the target wavelength, for long non-radiative life time in the excited state of the laser transition and for efficient depopulation of the laser-transition ground-state. The injector consists of a chirped superlattice in that the ground states of adjacent QWs become aligned in energy for a certain voltage drop across the cascade period. At this voltage, an energetically flat miniband is formed in the injector superlattice through that the carriers coherently tunnel from the ground state of the active region to the excited state of the active region of the following cascade period. (For an illustration of the QC principle, see for example [1].) Up to now, quantum cascade lasing has been demonstrated only in structures made from III-V materials. In these systems, the quantum cascades are formed in the conduction band.

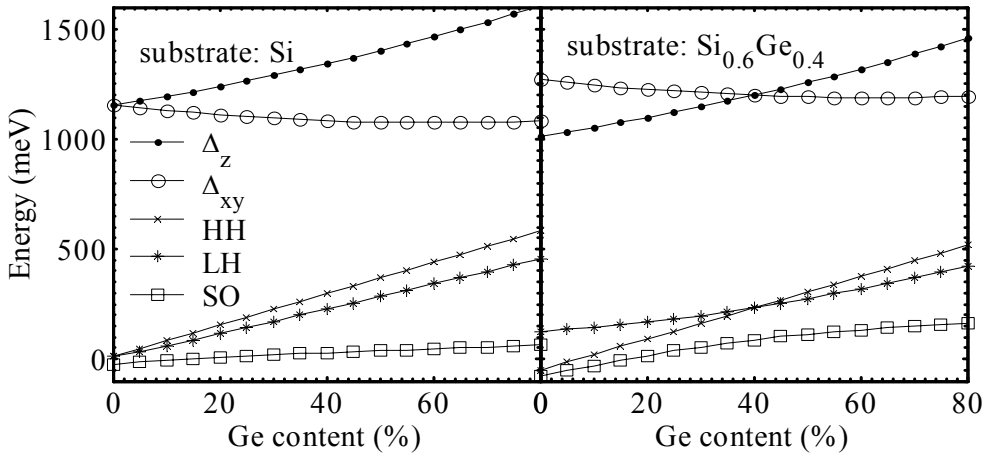

Fig. 1: Calculated band line-up for pseudomorphic SiGe alloys grown on a Si substrate (left panel) and a $Si_{0.6}Ge_{0.4}$.pseudo-substrate (right panel).

Since no optical transitions over the fundamental band gap are involved in the emission process of a quantum cascade device, the QC concept is a promising strategy to achieve light emission also in indirect fundamental band-gap materials like Si and Ge. For the Si/Ge material system, the calculated alignment of the conduction and valence band edges as a function of the SiGe alloy composition is shown in Fig.1. for growth on a Si (left panel) and a $Si_{0.6}Ge_{0.4}$ (right panel) substrate. In the calculations, the parameters given in [2] were used. Due to the uniaxial strain in the epitaxial SiGe layer, the heavy (HH) and light (LH) hole valence band maxima as well as the Δ_{xy} and Δ_z conduction band minima become split. Figure 1 shows that holes are always confined to the Ge rich layers for both types of substrates. The ground states in the valence band QW are HH states, the HH band offset increases by approx. 70 meV per 10% of Ge in the alloy. For electrons, nearly no band offset occurs in the conduction band for growth of SiGe alloys on a Si substrate. For SiGe epitaxy on SiGe substrates, QW are formed in the conduction band of the Si rich layers. The ground states of these QWs are built up from the Δ-valleys in the growth direction. However, the electrons in these valleys have a huge effective mass (0.98 m_0) in the direction of the confinement so the coupling of neighboring QWs is extremely weak. Therefore, all of the work on light emission of SiGe cascades published so far has been performed on valence band QWs.

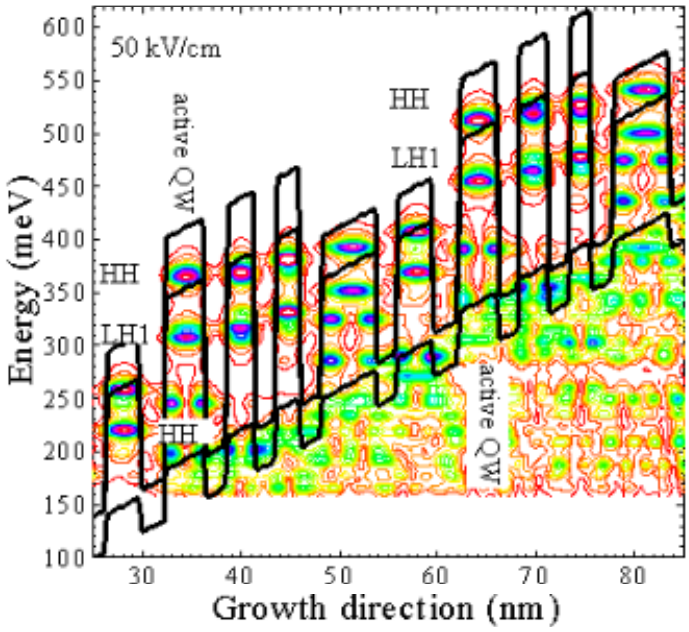

Fig. 2: Valence band potentials, eigenstates and hole wave functions for a typical QC structure grown on Si substrate. The details of the plot are described in the text.

Experimental Results

Mid-infrared emission

Cascade light emission in the mid-infrared spectral region around 150 meV has been reported recently [3] – [6]. In Fig. 2, the band structure of a typical Si/SiGe cascade structure [3] calculated according to [2] is shown. The alignment of the HH, LH and split off (SO) hole bands edges are indicated by the dashed, full and dashed-doted lines, respectively. The moduli of the wave functions are plotted as contour lines centered

around their eigenenergy. The broadening of the contours along the energy axis indicates the broadening of the eigenenergies (assumed to be 5 meV FWHM in the calculations). The emission wavelength is determined by the energy difference between the HH1 and HH2 in the QW labeled “active QW” in Fig. 2. From the HH1 state in the active QW, the holes tunnel via the HH groundstates in the neighboring QWs into the HH2 state of the next active QW.

Unlike in the case of cascade structures in the conduction band, in the valence band additional states exist between the HH2 and the HH1 states. These states are the ground states confined to QWs formed by the LH valence bands (labeled LH1 in Fig. 2). Pump and probe experiments have shown that the holes in the HH2 states are efficiently scattered into the LH 1 states by optical phonon deformation potential interaction reducing the hole life time in the HH2 state to approximately 250 fs [7]. Reducing the LH1-HH2 energy difference by a proper design of the active QW below the energy of an optical phonon blocks this recombination channel and enhances the power efficiency of the QC emission by approximately a factor 100 [3].

The growth of sophisticated cascade structures on Si substrates is limited by the accumulated strain energy in the epitaxial SiGe layers. These limitations can be overcome by growth on SiGe virtual substrates: Intersubband absorption of high quality $Si_{0.2}Ge_{0.8}$ QWs on a $Si_{0.5}Ge_{0.5}$ virtual substrate [8] as well as electroluminescence around 175 meV due to a bound-to-miniband transition in a QC structure consisting of up to 30 cascades each containing 14 $Si_{0.2}Ge_{0.8}$ QWs separated by Si barriers grown on a $Si_{0.5}$ $Ge_{0.5}$ virtual substrate [6] were observed recently.

THz emission

In the THz region, up to now no emission from typical cascades containing an injector and active QW region has been published. However, THz emission from $Si_{0.72}Ge_{0.28}$ multi-QWs separated by Si barriers grown on a $Si_{0.77}$ $Ge_{0.23}$ virtual substrate has been observed [9] under an electrical field parallel to the growth direction. For this sample, the in-plane dispersions in [100] direction of the four hole states within the energy range of the experiments are plotted in Fig. 3.

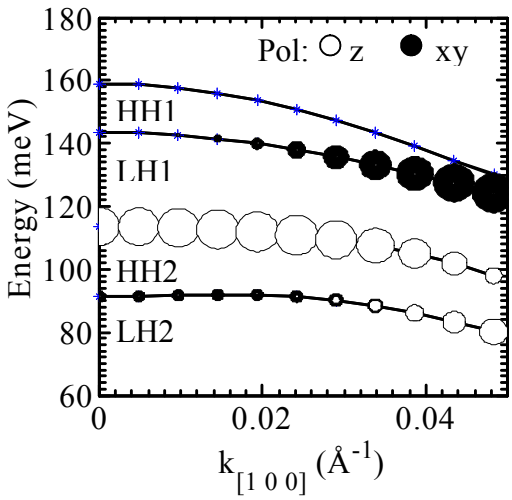

Fig. 3: In-plane dispersion along [100] direction for a $Si_{0.72}Ge_{0.28}$ QW on a $Si_{0.77}$ $Ge_{0.23}$ virtual substrate. The diameters of the symbols indicate the relative size of the optical dipol matrix element for transitions to the HH1 ground state. The open (full) symbols refer to light polarized parallel to z (xy) direction (growth direction: z).

The diameter of the open (full) symbols in Fig. 3 indicates the magnitude of the matrix-element for optical dipole transitions in z (xy) polarization between the HH1 ground and the LH1, HH2, LH2 excited states. Experimentally, the HH1-LH1 as well as the HH1-HH2 emission bands have been observed close to the calculated transition energies (at 10 meV and 40 meV) with the polarization selection rules indicated in Fig. 3 [9]. For the LH2 emission band, the matrix element is calculated to be much smaller than for the LH1 and HH2 bands. Consequently, in the emission experiments, the signal was close to the noise level at the calculated transition energy around 65 meV. In [10], a power conversion efficiency in excess of that observed for III-V *electroluminescence* devices is reported.

Conclusion

Both in the MIR and THz regime encouraging results have been obtained from electro-luminescence experiments. While for the samples emitting in the MIR range, typical QC designs are employed, the samples for THz emission contain a series of uncoupled QWs. The experiments and model calculations indicate that in both spectral regions the realization of Si/Ge based QC lasers appears feasible.

References

[1] F. Capasso, C. Gmachl, D. L. Sivco, A. Y. Cho: “Quantum cascade lasers”, Physics-Today, 55,2002, pp. 34-40.

[2] T. Fromherz, E. Koppensteiner, M. Helm, G. Bauer, J. F. Nützel, G. Abstreiter: „Hole energy levels and intersubband absorption in modulation doped Si/Si1-xGex multiple quantum wells“, Phys. Rev. B, 50, 1994, pp. 15073- 15085, and refs.erences therein.

[3] G. Dehlinger, L. Diehl, U. Gennser, H. Sigg, J. Faist, K. Ensslin, D. Grützmacher, E. Müller: “Intersubband electroluminescence from silicon-based quantum cascade structures”, Science, 290, 2000, pp.2277-2279.

[4] H. Sigg, G. Dehlinger, L. Diehl, U. Gennser, S. Stutz, J. Faist, D. Grützmacher, K. Ensslin, E. Müller: ”Valence band intersubband electroluminescence from Si/SiGe quantum cascade structures”, Physica E, 11, 2001, pp. 240-244.

[5] I. Bormann, K. Brunner, S. Hackenbuchner, G. Zandler, G. Abstreiter, S. Schmult W. Wegscheider: “Midinfrared intersubband electroluminescence of Si/SiGe quantum cascade structures”, Appl. Phys. Lett, 80, 2002,pp. 2260-2262.

[6] L. Diehl, S. Menteşe, E. Müller, D. Grützmacher, H. Sigg, U. Gennser, I. Sagnes, Y. Campidelli, O. Kermarrec, D. Bensahel, J. Faist: “Electroluminescence from strain-compensated Si0.2Ge0.8 /Si quantumcascade structures based on a bound-to-continuum transition”, Appl. Phys. Lett., 25, 2002, pp 4700-4702.

[7] R. Kaindl, M. Wurm, K. Reimann, M. Woerner, T. Elsaesser, C. Miesner, K. Brunner, G. Abstreiter: „Ultrafast Dynamics of Intersubband Excitations in a Quasi-Two-Dimensional Hole Gas”, Phys. Rev. Lett.,86, 2001, pp 1122 -1125.

[8] L. Diehl, H. Sigg, G. Dehlinger, D. Grützmacher, E. Müller, U. Gennser, I. Sagnes, T. Fromherz, Y. Campidelli, O. Kermarrec, D. Bensahel, J. Faist: „Intersubband absorption performed on p-type modulation-doped Si0.2Ge0.8/Si quantum wells grown on Si0.5Ge0.5 pseudosubstrate”, Appl. Phys. Lett., 80, 2002, pp 3274-3276.

[9] S. Lynch, R, Bates, D. J. Paul, D. J. Norris, A. Cullis, Z. Ikonic, R. W. Kelsall, P. Harrison, D. D. Arnone, C. R. Pidgeon, “Intersubband electroluminescence from

Si/SiGe cascade emitters at terahertz frequencies", Appl. Phys. Lett., 81, 2002, pp.1543-1545.

[10] D.J. Paul, S.A. Lynch, R. Batesa, Z. Ikonic, R.W. Kelsall, P. Harrison, D.J. Norris, S.L. Liew, A.G. Cullis, D.D. Arnoned C.R. Pidgeon, P. Murzyn, J.-P.R. Wells, I.V. Bradley: "Si/SiGe quantum-cascade emitters for terahertz applications", Physica E, 2003, in print.

Strained Silicon Above and Below Ge Islands

A. Hesse[1], J. Stangl[1], V. Holý[1], G. Bauer[1], U. Denker[2], O.G. Schmidt[2]

[1]Institute for Semiconductor Physics, Univ. Linz, Austria
[2]Max-Planck-Institute, Stuttgart, Germany

We present a method to realize strained Si without graded SiGe layers. By capping self-organized grown Ge islands at sufficiently low temperatures with Si, above and below Ge-dome shaped islands in-plane strain values of about 0.48% are achieved in Si. These high values of tensile in-plane strain are quite important for confining electrons in Si. The structural properties of the capped islands are almost identical to those of uncapped SiGe islands grown under the same conditions.

Introduction

Recently strained Si has found a lot of interest because of the fact that higher electron mobilities as compared to conventional MOS structures can be obtained. Usually relaxed graded SiGe buffers are used to provide the biaxial tensile strain in the subsequently deposited Si layers. However, the strain values that can be achieved using this approach are limited. Furthermore, threading dislocations from the graded buffer layer penetrate through the active strained Si layer. We investigated another method to realize strained Si, which avoids graded SiGe layers and has the advantage that the active strained Si layer is dislocation free. The time to grow Ge islands is essentially shorter than the one used for the graded buffer layer growth. By capping self-organized grown Ge islands at sufficiently low temperatures with Si, above and below Ge-dome shaped islands in-plane strain values of about 0.48% are achieved in Si. Low temperatures can suppress the usually observed changes in shape, composition and strain [1]. However, the optical and electrical properties can deteriorate with decreasing growth temperatures [2]. Therefore, an optimum between sample quality and structural properties has to be found.

Experimental

Three island samples have been grown by solid source molecular beam epitaxy on Si (001) wafers. After the deposition of a Si buffer layer, 5 monolayers of Ge were deposited at a growth temperature of 630 °C, forming dome-shaped islands. The islands were capped with about 150 nm of Si at different temperatures: for sample A the cap layer was grown at 630 °C, as the islands, whereas for samples B and C the growth temperature was lowered to 540 °C and 460 °C, respectively. In order to investigate the Ge distribution, high-resolution x-ray diffraction experiments were performed. Reciprocal space maps (RSMs) were recorded in a coplanar setup around the asymmetrical (224) and (404) Bragg reflections. Figure 1(a)–(d) shows several measured intensity distributions. Panels (a)–(c) show the RSM around the (224) Bragg reflection of sample A, B, and C, respectively. Panel (d) shows additionally the (404) map of sample C. The intensity distributions in Figs. 1(a)–(c) are quite different. For sample A, a maximum elongated along Q_z but narrow along Q_x is observed very close to the truncation rod. This indicates that the SiGe islands are flat and wide and that the strain *with respect to*

the substrate $\varepsilon_{||} = (a_{||}-a_{Si})/a_{Si}$ is small. On the contrary, for samples B and C peaks wider along Q_x but narrower along Q_z are observed at a larger distance from the truncation rod, corresponding to higher more strained islands with smaller base, especially for sample C.

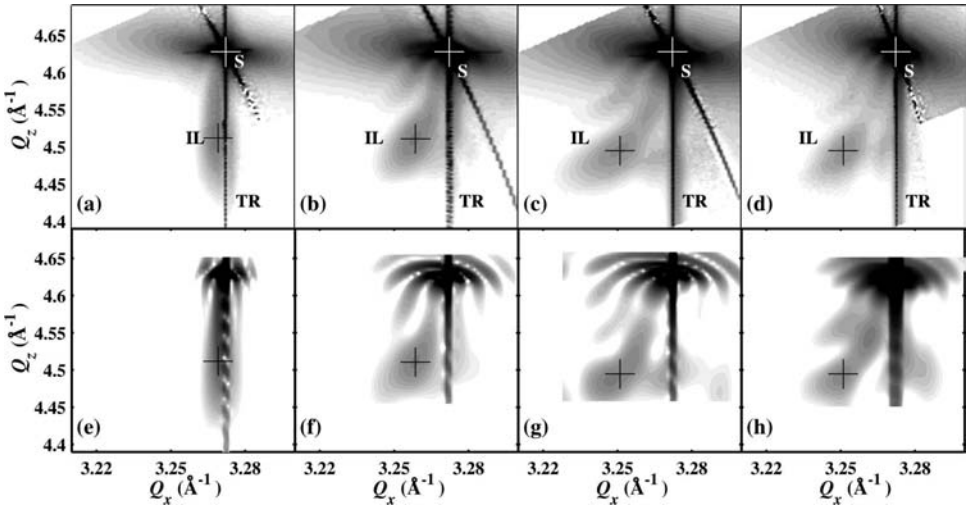

Fig. 1: (a) Measured RSM of sample A around the (224) Bragg reflection of Si. Beside the substrate peak labelled “S” and the crystal truncation rod labelled “TR”, diffuse scattering from the buried SiGe islands labelled “IL” is clearly visible. (b) and (c) (224) measured RSMs of samples B and C, respectively. (d) RSM around the (404) reflection of sample C, with Q_x divided by $\sqrt{8}/4$ for comparison with the (224) RSM. (e),(f), and (g) Simulations of the (224) reflection for samples A, B, C using a parabolic shape. Simulations for sample C using a pyramidal shape are shown as well as (h). 8 contour levels per decade are shown in the RSMs between 10^{-8} and $10^{-5.5}$ relative to the substrate intensity. Crosses denote the position of the maximum scattered intensity.

Figure 1(d) shows the map of sample C recorded around the (404) reflection, i.e., in an azimuth in between the (224) and (2-24) maps. The Q_x-axis in the plot has been rescaled by a factor $\sqrt{8}/4$. Hence the coordinates along Q_x and Q_z correspond to those in the (224) maps. Obviously, the intensity distribution from the SiGe islands in Fig. 1(c) and Fig. 1(d) shows only small differences.

Results

For a quantitative analysis of the x-ray data, we performed a simulation of the diffuse x-ray scattering pattern. Starting from a model of the island shape and the Ge distribution, the strain fields in and around the islands are calculated using an analytical approach. In accordance with our x-ray diffraction data and investigations using AFM of uncapped islands at comparable samples, we assume an approximately rotationally symmetric shape of the islands. The results for samples A, B, and C are shown in Fig. 1 (e)–(g), respectively. A perfectly rotationally symmetric shape is certainly an idealization. Therefore, we performed simulations not only with a rotationally parabolic shape, but also with the shape of a truncated pyramid, with a square base oriented along <110> directions. Figure 1(g), (h) shows the simulations around the (224) reciprocal lattice point for sample C for both types of shape, with a linear Ge profile optimized for each shape, i.e., with the best correspondence of the *peak position* with the experiment. Again, different assumptions on the shape give slightly different results in the Ge

distribution, but within our confidence interval of ± 0.05. It is obvious that the simulated *peak shape* of the diffuse intensity distribution does not perfectly match the experiment (see Fig. 1(c)) in either case, but rather the latter is in between the two simulations. Therefore we conclude that the actual shape of the buried islands is similar to pyramidal islands, but with rounded corners. As the differences in the results are not significant, as far as Ge content and strain values are concerned, we used the values obtained from the parabolic model.

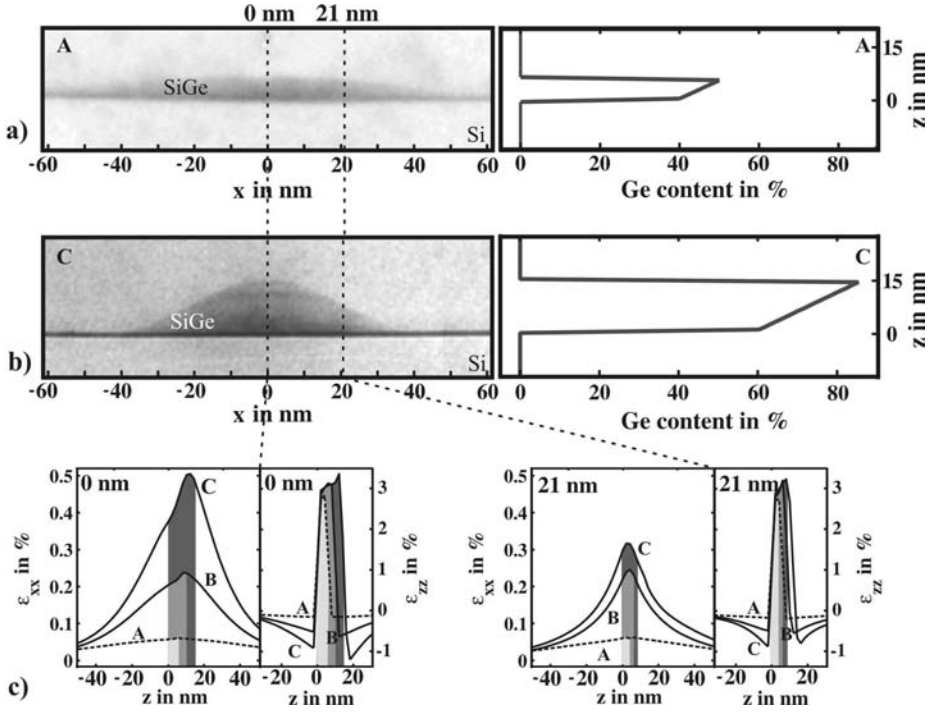

Fig. 2: (a) Cross-sectional transmission electron micrograph of sample A together with Ge composition gradient along height z in the center of the island. (b) as (a) but for sample C. (c) strain tensor components ε_{xx} and ε_{zz} as a function of height z through the center of the island (0 nm) and along a vertical line laterally shifted by 21 nm towards the edge. Note the appreciable amount of in-plane strain above and below the buried island in the tensily strained Si and its drastic decease with increasing Si capping temperature. The z-coordinate=0 in all drawings corresponds to the bottom of the islands. The respective heights of the islands are illustrated by shaded areas.

The results of our analysis are summarized in Fig. 2. For sample A capped at 630 °C we obtain a base width of the islands of about 100 nm and a height of about 6.6 nm. For the in-plane strain ε_{xx} values around 0.06 % without a significant variation within the island. The Ge content varies from 0.4 at the base to 0.5 at the apex of the island, as shown in Fig. 2(a). These values are almost identical to those obtained in a previous study on buried islands [3]. For samples B and C capped at 540 °C and 460 °C, respectively, however, the properties are considerably different: for the lowest capping temperature, the base width and height of the islands are evaluated to be about 70 nm and 15 nm, respectively. The structural properties of the islands capped at low temperatures are almost identical to those of uncapped SiGe islands grown under the same conditions [4]. The prevention of the flattening leads to a much higher lateral strain ε_{xx} in Fig. 2(c) for sample C, i.e., 0.38 % at the base and 0.48 % at the apex. The much larger lateral strain values are a consequence of the higher Ge content within the islands in sample C: We obtain a variation from x=0.6 at the base to 0.85 at the apex

(see Fig. 2(b)), actually close to the properties of uncapped islands grown under the same conditions. For sample B we obtained for the islands values between those of sample A and B, i.e., a base width of 84 nm, a height of 10.5 nm and a Ge content variation between x=0.4 (base) and 0.8 (top). In Fig. 2(c), these strain values ε_{xx} and ε_{zz} are shown for a vertical cross-section along the center of the island and in addition along a vertical line shifted laterally by 21 nm towards the edge of the islands. Our study clearly shows that the shape, strain and Ge distribution of capped islands depends sensitively on the growth temperature used for Si capping. For the lowest capping temperature of 460 °C, the structural properties of the Ge islands are nearly preserved. We would like to point out that the capping temperature has also a drastic influence on the strain status of tensily strained Si up to about 50 nm, i.e., 3 to 4 times the island height, above and below the Ge island. For the lowest capping temperature, the maximum in-plane strain in the Si matrix immediately above the island is as high as 0.48 %. These high values of tensile in-plane strain are quite important for confining electrons in Si.

Conclusion

We have investigated a series of SiGe islands grown on Si(001) and capped with Si at temperatures 630 °C, 540 °C, and 460 °C. The change of shape, strain, and Ge distribution observed at high capping temperatures of 630 °C can be drastically suppressed by lowering the capping temperature to 460 °C. The structural properties of the islands capped at low temperatures are almost identical to those of uncapped SiGe islands grown under the same conditions.

References

[1] A. Rastelli, E. Müller, H. von Känel, Appl. Phys. Lett. **80**,1438 (2002).

[2] O.G. Schmidt, U. Denker, K. Eberl, O. Kienzle, F. Ernst, Appl. Phys. Lett. **77**, 2509 (2000).

[3] A. Hesse, J. Stangl, V. Holý, T. Roch, G. Bauer, O.G. Schmidt, U. Denker, B. Struth, Phys. Rev. B **66**, 085321 (2002).

[4] J. Stangl, A. Daniel, V. Holý, T. Roch, G. Bauer, I. Kegel. T.H. Metzger, Th. Wiebach, O. G. Schmidt, K. Eberl, Appl. Phys. Lett. **79**, 1474 (2001).

High-Mobility Strained Si for Spintronics Applications

M. Mühlberger[1], H. Malissa[1], N. Sandersfeld[1], W. Jantsch[1] and F. Schäffler[1]
A. Tyryshkin[2] and S. Lyon[2]

[1]Inst. of Semiconductor and Solid State Physics, Joh. Kepler Univ. Linz
[2]Electrical Engineering Department, Princeton University, NJ, USA

We have grown modulation-doped $Si_{1-x}Ge_x$ quantum wells ($0 \leq x \leq 0.1$) on relaxed $Si_{1-xs}Ge_{xs}$ buffer layers, and have investigated this system using conduction electron spin resonance (CESR) and conventional Hall measurements. For a pure Si channel, mobilities of up to 341 000 cm²/Vs at carrier densities of $2.8 \cdot 10^{11}$ cm^{-2} were found in Hall measurements under illumination at 1.6 K. In CESR, extremely narrow line widths of down to 40 mG can be observed. In pulsed-ESR experiments, spin lifetimes T_1 and T_2 in the order of microseconds have been found. This is two orders of magnitude longer than the length of the microwave pulses used to flip the spins. The g-factor for the electrons in Si (g = 1.998) and Ge (g = 1.563) is significantly different. We grew samples with $Si_{1-x}Ge_x$ quantum wells with x = 0.05 and x = 0.1. In these samples, a clear shift of the g-factor could be observed although in this first attempt the line width of the CESR signal was significantly increased.

Introduction

Electrons in silicon are very promising for spintronics and quantum information processing. The main reasons are the extremely long spin lifetimes, which are due to silicon's weak spin-orbit coupling, and the suitability of this material system for very large scale integration (VLSI). Especially the spin properties of two-dimensional electron gases (2DEGs) in the Si/SiGe heterosystem have attracted considerable interest recently. [1]

For a quantum computer [2] it would be useful to change the g-factor and therefore the position of the resonance in an electron spin resonance (ESR) experiment. This can be accomplished by using the fact that the g-factor for the electrons in Si (g = 1.998) and Ge (g = 1.563) is significantly different.

Experiments

We have grown modulation-doped $Si_{1-x}Ge_x$ quantum wells ($0 \leq x \leq 0.1$) on relaxed $Si_{1-xs}Ge_{xs}$ buffer layers with $0.20 < x_s < 0.3$. The properties of the two-dimensional electron gases (2DEGs) have been investigated using conduction electron spin resonance (CESR) and conventional Hall measurements.

Growth was performed by solid source molecular beam epitaxy (MBE), and doping with Sb was done at the low growth temperature of 300 °C to suppress the strong segregation. On top of a relaxed buffer layer (3.4 µm linear grading + 0.6 µm constant composition part) the strained $Si_{1-x}Ge_x$ channel was deposited, followed by an undoped spacer layer, the doping layer, and $Si_{1-x}Ge_x$ and Si cap layers.

Results

For a pure Si channel, mobilities of up to 341 000 cm²/Vs at carrier densities of $2.8 \cdot 10^{11}$ cm^{-2} were found in Hall measurements under illumination at 1.6 K (see Fig. 1). In CESR, extremely narrow apparent line widths of down to 40 mG can be observed (see Fig 2).

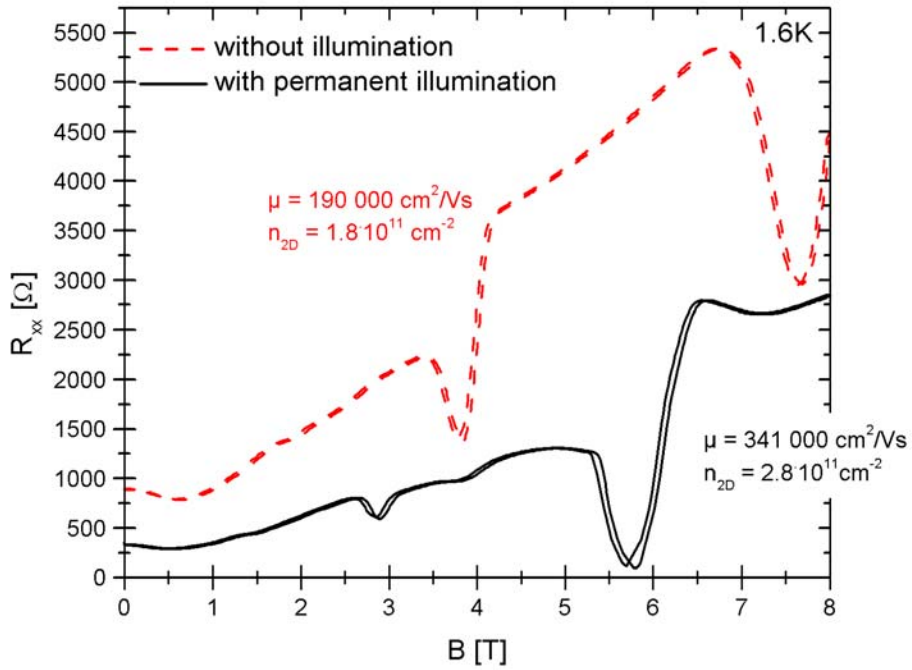

Fig. 1: SdH measured at 1.6 K with (solid line) and without permanent illumination.

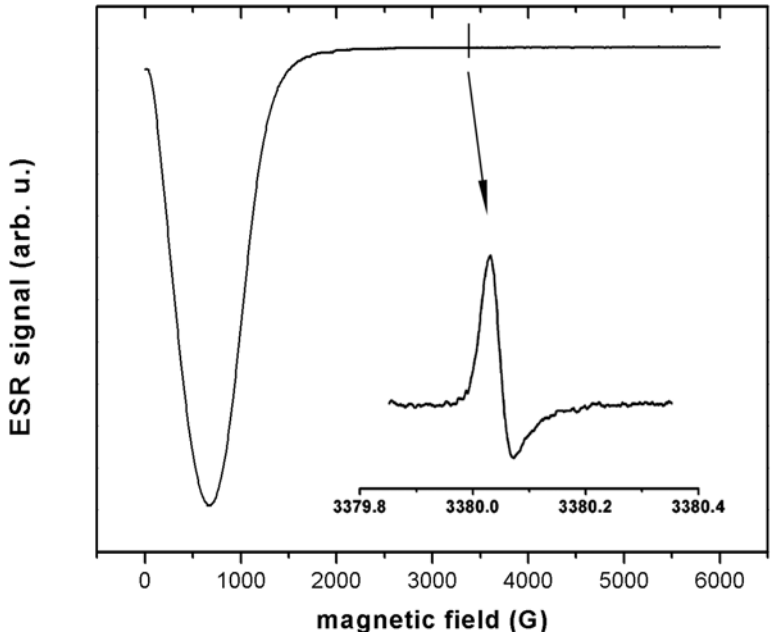

Fig. 2: Cyclotron resonance and CESR signal (inset) measured at 2.5 K. The line width of the CESR signal is only 40 mG.

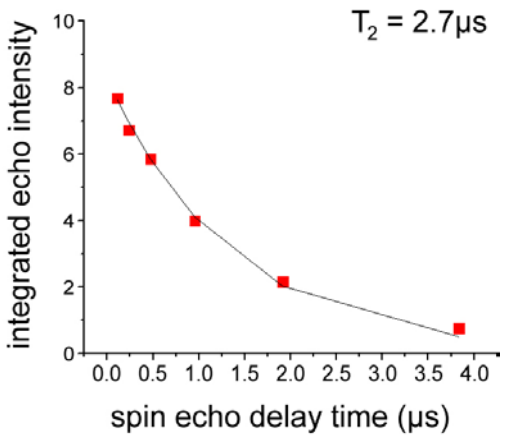

Fig. 3: Determination of T_2 from spin echo experiments [4].

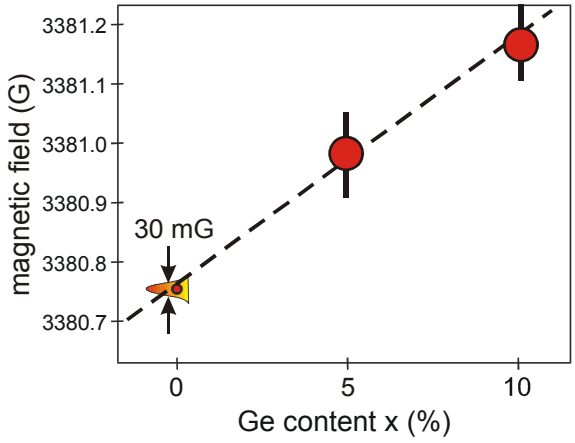

Fig. 4: Change of g-factor of the two-dimensional conduction electrons as a function of Ge-content in the quantum well.

In pulsed-ESR (spin echo) experiments in a comparable sample [3], it was found that the spin-lifetime T_1 (longitudinal relaxation time) and the phase memory time T_2 (transverse time) are both in the order of microseconds (see Fig. 3) [4]. This is two orders of magnitude longer than the length of the microwave pulses used to flip the spins. A typical π-pulse, which flips a spin by 180°, is 10 ns long. Consequently, many coherent spin operations are possible.

The g-factor for the electrons in Si (g = 1.998) and Ge (g = 1.563) is significantly different. Since for a quantum computer [2] it would be useful to change the g-factor and therefore the position of the resonance in a CESR experiment, we grew samples with $Si_{1-x}Ge_x$ quantum wells for the electrons with x = 0.05 and x = 0.1. In these samples, a clear shift of the g-factor could be observed (see Fig. 4), although in this first attempt the line width of the CESR signal was significantly increased.

Conclusion

We have demonstrated the growth of high mobility modulation-doped Si quantum wells with spin lifetimes in the range of microseconds. Furthermore, first steps towards the manipulation of these spins have been made with promising results.

References

[1] W. Jantsch, Z. Wilamowki, N. Sandersfeld, M. Mühlberger and F. Schäffler, “Spin lifetimes and g-factor tuning in Si/SiGe quantum wells”, Physica E **13** (2002) 504

[2] R. Vrijen, E. Yablonovitch, K. Wang, H. W. Jiang, A. Balandin, V. Roychowdhury, T. Mor and D. DiVincenzo, “Electron-spin-resonance transistors for quantum computing in silicon-germanium heterostructures”, Phys. Rev. A **62** (2000) 012306

[3] Z. Wilamowski, N. Sandersfeld, W. Jantsch, D. Többen and F. Schäffler, “Screening Breakdown on the Route toward the Metal-Insulator Transition in Modulation Doped Si/SiGe Quantum Wells”, Phys. Rev. Lett. **87** (2001) 026401

[4] Z. Wilamowski, W. Jantsch, N. Sandersfeld, M. Mühlberger, F. Schäffler, S. Lyon, “Spin relaxation and g-factor of two-dimensional electrons in Si/SiGe quantum wells”, Physica E, in print

Characterization of Lateral Quantum Dots Fabricated by E-Beam Lithography

G. Pillwein[1], G. Brunthaler[1], G. Strasser[2]

[1]Institute for Semiconductor Physics, Univ. Linz, Austria

[2]Institute for Solid State Electronics, TU-Vienna, Austria

Small lateral quantum dots were fabricated from a two-dimensional GaAs/AlGaAs heterostructure by electron beam lithography using a split gate technique, where the geometry of the dot is defined electrostatically by metal gates. The devices were characterized electrically in a ³He cryostat at 300 mK. The measurements show conductance oscillations typical for Coulomb blockade. From the experimental data, the diameter of the dots was estimated to be approximately 125 nm.

Introduction

Artificial semiconductor quantum dots are among the presently discussed options for realizing the quantum entanglement necessary for doing quantum computation [1] and are also a suitable system for possible spintronics devices [2]. Since we are still at the beginning of our research in this field, we have chosen to fabricate single lateral quantum dots in a 2D GaAs/AlGaAs system as an entry point, which acts as a basis for more complicated devices.

A quantum dot can be shortly described as a mesoscopic electronic system coupled weakly to two electronic reservoirs (Fig. 1(a)). Electronic transport through such a structure is inhibited if the energy necessary to add an electron to the dot exceeds the electrochemical potential of the reservoirs and the thermal energy k_BT. This phenomenon is known as the Coulomb blockade. The addition of one electron to a quantum dot of total capacitance C requires the charging energy $E_C = e^2/C$.

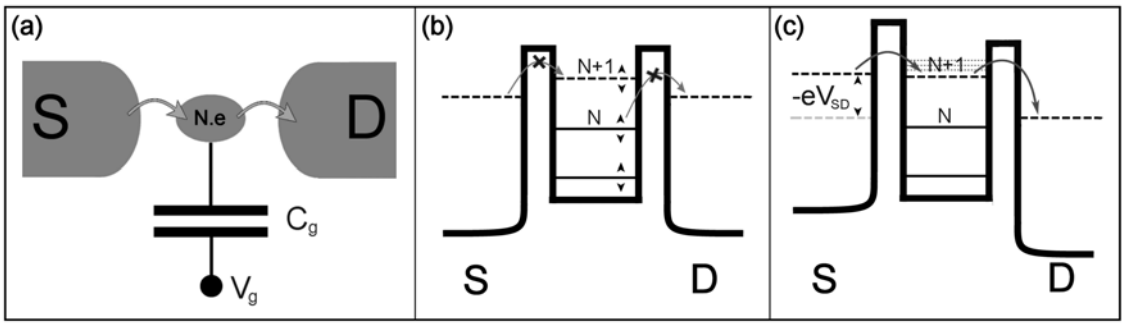

Fig. 1: (a) Schematic representation of a quantum dot. The area in the center is only coupled via tunneling to the source and drain leads. The charge on the dot can only be varied in quantized steps of e. (b) Schematic band diagram of the blocked state; by changing V_G, the energy levels inside the dot can be shifted. (c) A large source-drain voltage allows transport via the N+1 state (dashed line), or its excited states (dotted lines).

By applying a voltage to a gate coupled capacitively to the quantum dot the energy levels inside the dot are shifted with respect to the reservoirs (Fig. 1(b)), which allows changing the number of electrons on the dot one by one. The variation in energy levels amounts to $\Delta E = e\Delta V_G(C_G/C)$, when changing V_G by ΔV_G. Whenever an energy level inside the dot is aligned with the chemical potential in the leads, current flows via sequential tunneling of single electrons into and out of the dot, resulting in periodic peaks in the conductance trace, which are referred to as Coulomb oscillations. The period corresponds to the charging energy E_C, which is equivalent to a period of $\Delta V_G = e/C_G$ in gate voltage units. Transport through the structure can also be achieved by applying a large DC source-drain bias (Fig. 1(c)). Whenever the Fermi level in the biased lead is aligned with one of the dot levels, the conductance increases. When the bias is raised further, the excited states of the dot energy levels also contribute to transport. The I-V characteristic of such a device is thus strongly non-linear.

Experimental

The investigated samples are based on a MBE grown GaAs/$Al_{0.3}Ga_{0.7}As$ heterostructure with a two dimensional electron gas (2DEG), which is situated 70 nm below the sample surface and has a carrier concentration of 2.73×10^{11} cm^{-2} and a mobility of 250000 cm²/Vs. Using standard optical lithography, Hall bar mesas were wet-etched and ohmic contacts were made from an Au/Ni/Ge alloy. The actual quantum dot was defined by e-beam lithography and subsequent deposition of metal electrodes (i.e. the split gates) on top of the hall bars. The optical microscope image in Fig. 2(a) shows the ohmic contacts, the mesa, and the gate electrodes. By applying a negative voltage to the split gates, the 2DEG can be completely depleted. Using three pairs of gate fingers, a quantum dot can be easily defined. The outer pairs of gates define the tunnel barriers, which separate the quantum dot area from the surrounding 2DEG. Besides of defining the dot geometry, the inner gates can be used to change the electrostatic potential of the dot. Usually only one of the inner gates is varied and is then referred to as the plunger gate. A SEM image of this split gate geometry is shown in Fig. 2(b). The quantum dot area defined by the metal gates is approximately circle shaped with a diameter of roughly 260 nm in the investigated sample.

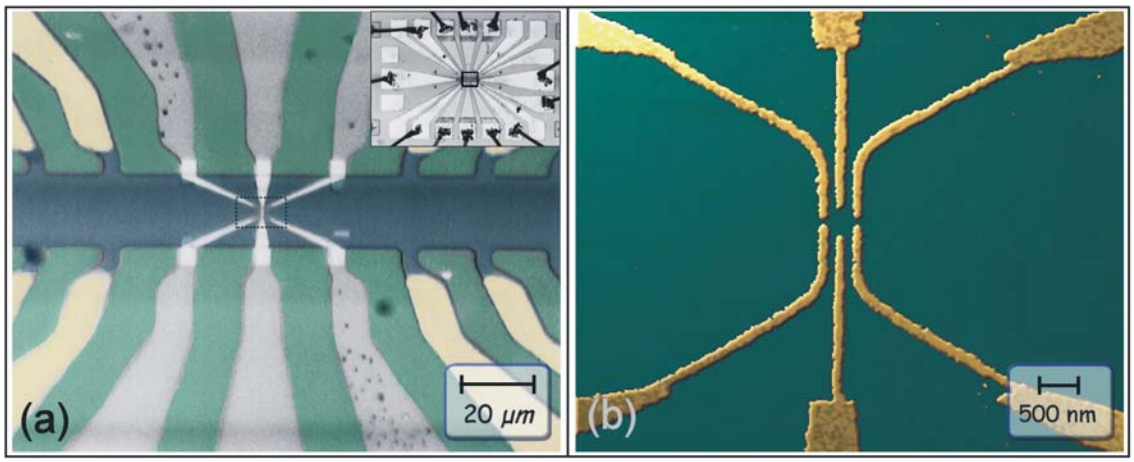

Fig. 2: (a) Shows a part of the hall bar containing the split-gate structure viewed in an optical microscope. The inset shows the entire structure including the bond pads. (b) This image was taken with the electron microscope and shows an enlargement of the center region marked in Fig. 2(a).

Electrical measurements were carried out in a ^{3}He cryostat at a temperature of 300 mK using a low frequency lock-in technique (f = 10 Hz). To avoid heating of the electrons it is important to keep the excitation voltage lower than the thermal energy, which corresponds to 25 μV at 300 mK, thus excitation voltages of 10 μV or below have been used.

The voltages on the split-gates were set to a negative value to ensure that the quantum dot is well defined and that the transport occurs via tunneling through the barriers. Then the plunger gate voltage was swept in order to change the number of electrons in the dot. Such a measurement is shown in Fig. 3(a), where the conductance through the dot is plotted versus the plunger gate voltage. From the period of the conductance peaks a gate capacitance of $C_G = 1.6\times10^{-18}$ F can be calculated. Because the plunger gate voltage also has an influence on the tunnel barriers, the conductance is totally pinched off at about –6.45 V. On the other hand, as V_G increases, conduction also occurs between the peaks (e.g. at –6.17 V), because the tunneling barriers become more transparent. In order to observe more oscillation periods, another split-gate geometry is required, where the plunger gate does not couple so strongly to the tunnel barriers.

By applying a large DC source drain bias, superimposed by a small AC signal, we measured the differential conductance dependent on V_{SD}. This measurement (Fig. 3(b)) clearly demonstrates the nonlinear I-V characteristics of the device. The differential conductance can even become negative, if an excited state has a long lifetime inside the dot and thus blocks transport as long as it is occupied.

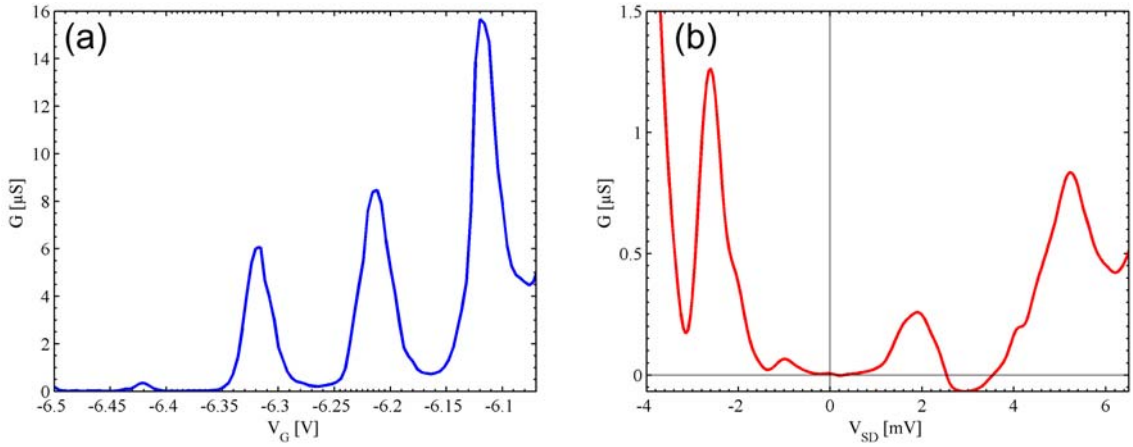

Fig. 3: (a) Coulomb oscillations observed in the conductance G versus plunger gate voltage V_g. The spacing of the peaks gives an estimate of the gate capacitance $C_g = 1.6\times10^{-18}$ aF. (b) Differential conductance G of a large bias V_{SD} measurement, showing nonlinear behaviour.

By combining both of the above measurements, most of the basic properties of the quantum dot can be obtained, including total and source capacitance as well as an estimate of the actual size of the quantum dot. Figure 4 shows a 3D plot of the differential conductance dependent on V_{SD} and V_G viewed from the top. The horizontal axis corresponds to the plunger gate voltage V_G, the vertical axis to the source-drain voltage V_{SD}. The blue (red) areas correspond to low (high) G. In the dark parallelogram-shaped regions, the number of electrons is fixed and no transport is possible due to Coulomb blockade. The features, from which important properties can be obtained, are marked by dotted lines.

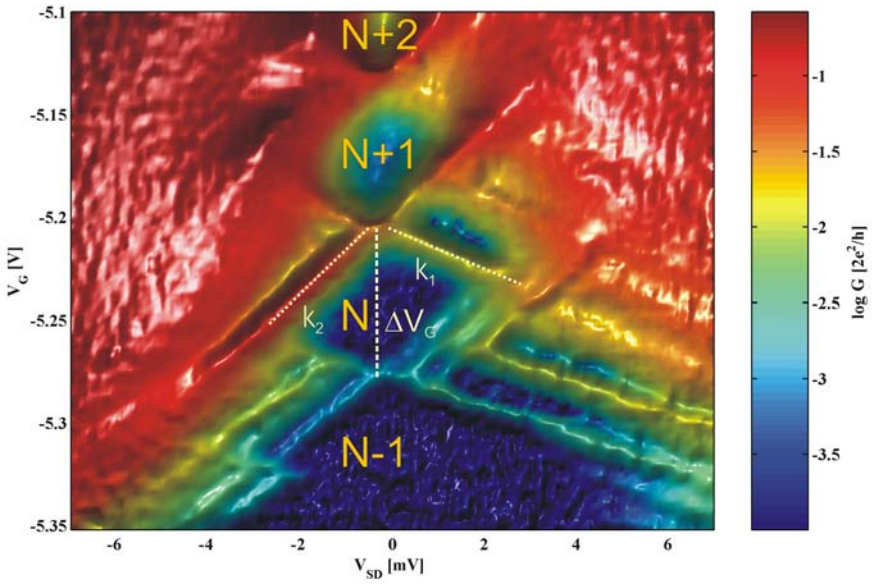

Fig. 4: Differential conductance G versus source-drain voltage V_{SD} and plunger gate voltage V_G. The blue (red) areas correspond to low (high) G. Coulomb blockaded regions are indicated by N–1, N, etc. Dotted lines mark some of the features used for evaluation. A light source illuminates the figure from the bottom to make the contours of peaks more clearly visible.

From the conductance peak spacing ΔV_G at zero source drain voltage the capacitance C_G of the plunger gate can be calculated to be 2.2×10^{-18} F. From the slopes of the peak lines (k_1, k_2) we obtained the total and the source capacitance to be $C = 71\times10^{-18}$ F and $C_S = 24\times10^{-18}$ F. Via the known relation for the charging energy $E_C = e^2/C$ we related the gate voltage scale to an energy scale. From the average vertical spacing of peak lines, corresponding to excited single electron states, we roughly estimated the diameter of the electron island to be about 125 nm. Considering that the depletion region will extend about 70 nm (i.e. the distance of the 2DEG from the surface) around the contours of the split-gates, this is in very good agreement with the structure diameter of 260 nm.

Conclusion

We have successfully fabricated split-gate quantum dots using 2D GaAs/AlGaAs heterostructures and our measurements of the Coulomb diamond demonstrate that they work as intended. Further measurements on these structures will be made to investigate their possible use for quantum information technology or for spintronics devices. Now that we have established this technology in our workgroup, we can further improve our device design and we will be able to fabricate more sophisticated structures such as coupled quantum dots, quantum dot arrays, etc. in the future.

References

[1] D. Loss and D. P. Vincenzo: “Quantum computation with quantum dots”, Phys. Rev. A Vol. 57, 1998, pp. 120 – 126.

[2] G. Burkard, H. A. Engel, and D. Loss: “Spintronics and Quantum Dots for Quantum Computing and Quantum Communication”, Fortschr. Phys., Vol. 48, 2000, pp. 965 – 986.

Enhanced Luminescence of Erbium Doped Silicon Due to Hydrogen

G. Kocher-Oberlehner[1], W. Jantsch[1], L. Palmetshofer[1], A. Ulyashin[1], A. Ulyashin[2]

[1]Inst. of Semiconductor and Solid State Physics, Joh. Kepler Univ. Linz
[2]Univ. of Hagen, Haldener Str. 182, PO Box 940, D-58084 Hagen

Erbium- and oxygen-doped silicon was additionally doped with hydrogen, using plasma-enhanced Chemical Vapor Deposition. Samples treated with solid-phase epitaxy (SPE) before hydrogen doping and annealing at 900 °C after show a large enhancement of the photoluminescence yield. Secondary Ion Mass Spectroscopy gives evidence for an enhanced diffusion of both oxygen and erbium at this temperature towards the surface. This change in local concentration leads to a dominance of the cubic center that is usually only found for lower Er concentrations. Controlled etching shows that the PL does stem from a deeper region with lower erbium concentration. The luminescence yield in the hydrogenated samples is significantly higher even if compared to samples prepared to optimize the cubic center luminescence. We thus conclude that hydrogen can enhance the solubility of the cubic center in Si:Er,O.

Introduction

Erbium (Er) doped semiconductors have attracted a lot of attention as they seem to indicate a way to obtain temperature stable emission at a well defined wavelength [1] – [7]. Furthermore, the wavelength close to 1.5 µm of this emission stemming from an intra-4f-transition coincides nicely with the absorption minimum in conventional optical fibers. The main problem for applying this material system to devices working at room temperature is the temperature induced quenching of the luminescence efficiency. Investigations showed that co-doping of Si with Er and light elements, in particular oxygen (O), leads to a reduction of this quenching [3] and room temperature electroluminescence (EL) and photoluminescence (PL) [4], [5] were subsequently reported.

The low solubility limit of Er in Si necessitates the use of non-equilibrium methods like ion implantation for its incorporation. Because of the required high doses for Er and O, a thermal annealing step for re-crystallization is necessary. To achieve room temperature EL, Er has to be incorporated in $SiO_{2-\delta}$ precipitates, which are formed at high annealing temperatures (> 950 °C) [6]. Both Er and O stay relatively immobile even at temperatures that high. The shallow dopants required for a diode structure, however, show substantial diffusion already at this temperature. [7]

Hydrogen is a very common impurity in all semiconductor materials. Focusing on its positive characteristics – gettering of metal impurities and passivation of residual defects – as well as on the known enhancement of the diffusion of interstitial oxygen [8] and the formation of Er-O complexes and precipitates [9], we expected an overall positive effect on the performance of our structures. We also hoped that hydrogen might decrease the necessary annealing temperature for precipitate formation thus helping to prevent diffusion of the dopants.

Results and Discussion

Samples were prepared from boron doped (10 Ohm·cm) Cz-Si (100) with an oxygen content of approx. 2 x 10^{18} cm^{-3}. Er was implanted at 300 keV with a dose of 1 x 10^{14} cm^{-2} resulting in a peak concentration of 5 x 10^{18} cm^{-3} in 100 nm depth. Oxygen was implanted at 40 keV with a dose of 1 x 10^{15} cm^{-2} resulting in a peak concentration of 5 x 10^{19} cm^{-3}. Both profiles overlap spatially according to TRIM code simulation and SIMS. Two sets of samples were prepared – one treated by SPE (600 °C/15 min. in N_2 atmosphere), the other "as implanted" – and hydrogenated for 1 hour at 260 °C by a hydrogen plasma (110 MHz, 200 sccm hydrogen flux, 400 mTorr pressure) which leads to a hydrogen concentration of about 10^{19} cm^{-3} throughout the wafer [10]. The samples were then annealed at various temperatures in the range between 450 °C and 1000 °C.

In samples not treated with SPE, the effect of hydrogen is rather limited. The Er-related line spectra closely resemble those in samples without hydrogen treatment, although the intensity due to Er-O complexes is smaller in respect to the cubic lines than in non-hydrogenated samples at elevated annealing temperatures. In samples previously treated with SPE, the PL-intensity is slightly higher than in the reference samples at first. The peak PL-intensities of the annealed samples are shown in Fig. 1 as a function of annealing temperature. The difference becomes significant at higher annealing temperatures (800 and 900 °C), where the luminescence yield is about five times bigger than in the non-hydrogenated samples.

Furthermore, we observe a change in the PL spectra. For samples with hydrogen and annealing temperatures larger than 700 °C, the so-called "cubic" center becomes more and more prominent, and it dominates the spectra after annealing at 900 °C. This center is attributed to Er on an interstitial site and was previously only observed in samples with a low concentration of Er, i.e., when the implantation doses are below the amorphisation limit [11]. The lines due to Er-O complexes are completely absent for samples annealed at 900 °C.

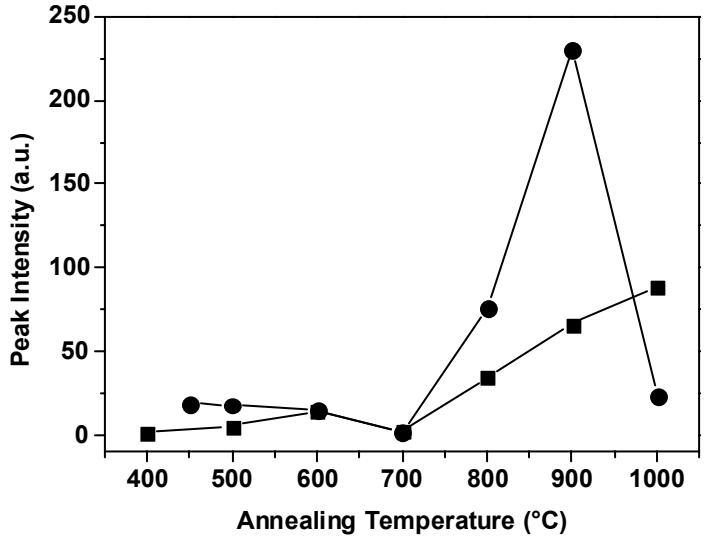

Fig. 1: Peak intensities versus annealing temperatures. Circles show the intensities for the hydrogenated samples, diamond symbols represent the reference samples.

We applied SIMS to gain information on possible changes in local concentration. The results show that hydrogen does not only enhance the diffusion of oxygen but also af-

fects erbium. The usual Gaussian profile is broadened and an accumulation of both species near the surface can be clearly seen. Most of the Er is concentrated within 50 nm of the surface reaching concentrations of up to 1020 cm^{-3}.

To determine the origins of the luminescence we removed 60 nm from the top of the wafer using reactive ion etching. However, although we removed approx. 80 % of the incorporated erbium according to SIMS, the luminescence dropped only by 10 %. This observation points strongly to a PL origin in the region with lower concentration further inside the sample. Using the incorporated doses and the SIMS results as landmarks, we estimate the remaining concentration of erbium in the sample to be approx. 3×10^{12} cm^{-2}. Maximum PL yield for the cubic center is achieved for an implantation dose of 1×10^{13} cm^{-2} and annealing temperatures of 900 °C. Comparing the PL yield to such samples, the intensity is still significantly higher in the hydrogenated samples (Fig. 2). This is an indication for a higher percentage of optically active erbium in our hydrogenated samples.

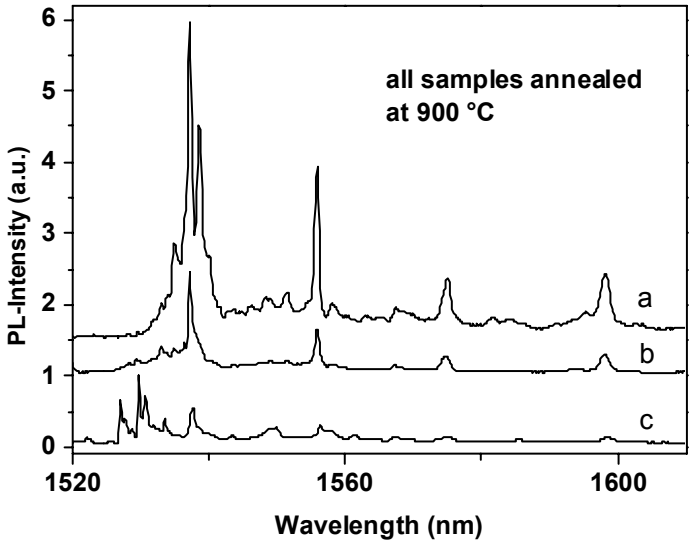

Fig. 2: (a) The cubic lines dominate the PL-spectra in the hydrogenated samples. (b) Spectra of a sample with low Er concentration and (c) of a reference sample (set 4) are shown. The lines at 1.53 µm due to Er-O complexes are absent in the hydrogenated sample. Spectra shifted for clarity.

Studies of power dependence support this interpretation. In the high power regime, the PL-yield I_{Pl} is given by $I_{PL} \propto N_{Er}^{*} / \tau$ with N_{Er}^{*} being the number of optically active erbium and τ being the radiative lifetime. The hydrogenated samples show a higher saturation intensity compared to both the reference sample and samples optimized for cubic center luminescence. The comparison to the reference sample is valid, because although the emitting center is different, the lifetime is identical for both centers [12]. The higher saturation intensity demonstrates a higher number of optically active erbium ions. The “thermal” quenching of the PL intensity with increasing temperature is not influenced by hydrogen. So additional co-doping with hydrogen does not help with room temperature applications. However, it may be advantageous for applications at low temperatures to make use of the higher percentage of optically active erbium and the narrow linewidth [11] of the cubic center.

Conclusion

In summary, hydrogen influences the PL of Si:Er,O indirectly by mobilizing the implanted Er and oxygen. SIMS measurements give evidence for an enhanced diffusion of both species at elevated temperatures towards the surface. Subsequently the local concentration of both dopants is changed. This change in local concentration leads to a dominance of the cubic center, which is usually only found for lower Er concentrations. We find a substantial increase of the luminescence yield for annealing temperatures in the range of 800°C to 900°C. The luminescence yield in the hydrogenated samples is significantly higher even if compared to samples prepared to optimize the cubic center luminescence. Comparing luminescence yield and local concentration, we obtain strong indications for an enhanced solubility of the cubic center in samples co-doped with hydrogen.

Acknowledgements

We thank H. Haselgrübler for expert technical assistance. This work was also supported by the Fonds zur Förderung der Wissenschaftlichen Forschung

References

[1] H. Ennen, J. Schneider, G. Pomrenke, A. Axmann, Appl. Phys. Lett. 43, 943 (1983)

[2] H. Ennen, G. Pomrenke, A. Axmann, K. Eisele, W. Haydl, J. Schneider, Appl. Phys. Lett. 46, 381 (1985)

[3] G. N. van den Hoven, J. H. Shin, A. Polman, J. Appl. Phys. 78, 2642 (1995)

[4] J. Michel, J. L. Benton, R, F, Ferrante, D. C. Jakobson, d. J. Eaglesham, e. A. Fitzgerald, Y. H. Xie, J. M. Poate and L. C. Kimerling, J. Appl. Phys. 29, 2672 (1991)

[5] B. Zheng, J. Michel, F.Y.G. Ren, L.C. Kimerling, D.C. Jacobson, J.M. Poate, Appl. Phys. Lett. 64, 2842 (1994)

[6] W. Jantsch, G. Kocher, L. Palmetshofer, H. Pryzbylinska, M. Stepikhova, H. Preier, Mat. Sci. Eng.B B81, 86 (2001)

[7] G. Kocher, H. Przybylinska, M. Stepikhova, L. Palmetshofer and W. Jantsch, Phys.B 308-310, 344 (2001)

[8] R. Job, W. R. Fahrner, A. I. Ivanov, L. Palmetshofer, A. G. Ulyashin, MRS Proc. 469, 95 (1997)

[9] V. P. Markevich, L. I. Murin, J. L. Lindström, A. G. Ulyashin, R. Job, W. R. Fahrner, V. Raiko, J. Phys.: Condens. Matter 12, 10145 (2000)

[10] A. G. Ulyashin, R. Job, W. Fahrner, D. Grambole, F. Hermann, Solid State Phenomena 82-84, 315 (2002)

[11] H. Przybylinska, W. Jantsch, Yu. Suprun-Belevitch, M. Stepikhova, L. Palmetshofer, G. Hendorfer, A. Kozanecki, R.J. Wilson, B.J. Sealy, Phys Rev. B 54, 2532 (1996)

[12] Sven Lanzerstorfer, “Er-dotierte Materialien für optische und optoelektronische Anwendungen im Infrarot-Bereich bei einer Wellenlänge von 1,54 µm”, PhD. Univ. of Linz (1999)

Comparison of IV–VI Semiconductor Microcavity Lasers for the Mid-Infrared with Active Regions of Different Dimensionality

T. Schwarzl[1], M. Böberl[1], W. Heiss[1], G. Springholz[1], J. Fürst[2], H. Pascher[2]

[1]Inst. of Semiconductor and Solid State Physics, Joh. Kepler Univ. Linz
[2]Experimentalphysik I, Universität Bayreuth, D-95447 Bayreuth, Germany

A comparison between IV-VI vertical-cavity surface-emitting mid-infrared lasers containing active regions of different dimensionality is presented. Optically pumped laser emission is observed at wavelengths between 3.5 and 4.4 µm. The microcavities consist of high-reflectivity EuTe/PbEuTe Bragg mirrors, with active regions consisting of either a self-organized PbSe/PbEuTe quantum-dot superlattice, PbTe/PbEuTe multi-quantum wells or bulk-like PbTe. For the 0D active medium, laser emission is obtained at temperatures up to 150 K. The results for the lasers with 2D active region are similar to those with the 3D bulk-like active region, for which lasing is observed up to 317 K. The threshold pump intensity is only 4 kW/cm^2 at 195 K, and 15 W/cm^2 at room temperature.

Introduction

Coherent emitters for the mid-infrared range are of high interest due to various gas absorption lines in this region allowing high-resolution gas spectroscopy. For these applications, typically edge-emitting semiconductor lasers made from lead salt (IV-VI) compounds are used permitting to access emission wavelengths as long as 30 micron at cw operation temperatures as high as 223 K. Apart from the conventional edge-emitting lasers also surface-emitting lead salt microcavity lasers were recently demonstrated. The surface-emitting microcavity lasers offer several advantages over edge emitters, like small beam divergence, single mode operation, and simplified monolithic integration.

Up to now, different types of IV–VI microcavity lasers have been realized based on bulk material, quantum wells, as well as quantum dots as active regions, and with optically stimulated laser emission observed up to temperatures of 290, 340 [1], and 90 K [2], respectively. However, a direct comparison of the performance of the different types of lasers has been hindered by the fact that different cavity structures as well as different excitation sources have been used in these studies. We have done a comparison between IV–VI vertical-cavity surface-emitting lasers (VCSELs) containing active regions of different dimensionality but with a nearly identical optical design of the cavity [3]. In addition, the same optical set-up as well as pump source was used for laser excitation and characterization. This allows studying the influence of the dimensionality of the active material on the laser properties.

Design and Materials Issues

The multilayer VCSEL samples were grown by molecular beam epitaxy on (111) oriented BaF_2 substrates. The microcavity is formed by a high-reflectivity $Pb_{0.94}Eu_{0.06}Te$/EuTe Bragg mirror with only three layer pairs (bottom mirror) exhibiting a reflectivity above 99 %. This is possible due to the exceptionally high refractive index contrast of

up to 80 % between the mirror materials. In order to make the top mirror transparent for the pump wavelength of 1.907 µm, the Eu-content in the $Pb_{1-x}Eu_xTe$ layers of the top mirrors was increased to 30 %. Thus, four layer pairs have to be used to obtain a reflectivity of about 98 %.

The laser active regions consist either of highly-ordered PbSe/PbEuTe self-organized zero dimensional (0D) quantum dot superlattices [2] with 236 periods of 5 monolayers PbSe and 48 nm $Pb_{1-x}Eu_xTe$ (x = 0.05), two dimensional (2D) PbTe/PbEuTe multiquantum wells [1] with nine 20 nm wide PbTe quantum wells (QWs) embedded in $Pb_{0.94}Eu_{0.06}Te$ barrier layers, or three dimensional (3D) bulk-like PbTe with a thickness of 1115 nm grown on top of a 960 nm $Pb_{0.94}Eu_{0.06}Te$ buffer. The cavities are optimized for a wavelength of 3.7 µm, 3.5 µm or 3.3 µm, which are the spontaneous emission wavelengths of the respective active regions at room temperature.

Results

All samples were characterized by high-resolution Fourier-transform infrared transmission measurements clearly showing narrow cavity resonances with line widths between 1 and 3 meV. The VCSELs were optically pumped with 10 ns pulsed laser excitation at a wavelength of about 1.9 micron. The stimulated type of emission from the cavities is evidenced by a clear threshold behavior [3], a considerably line width narrowing with respect to the resonance line width in the transmission spectra [3] and a strongly forward directed emission profile with a divergence smaller than 1° as shown in Fig. 1.

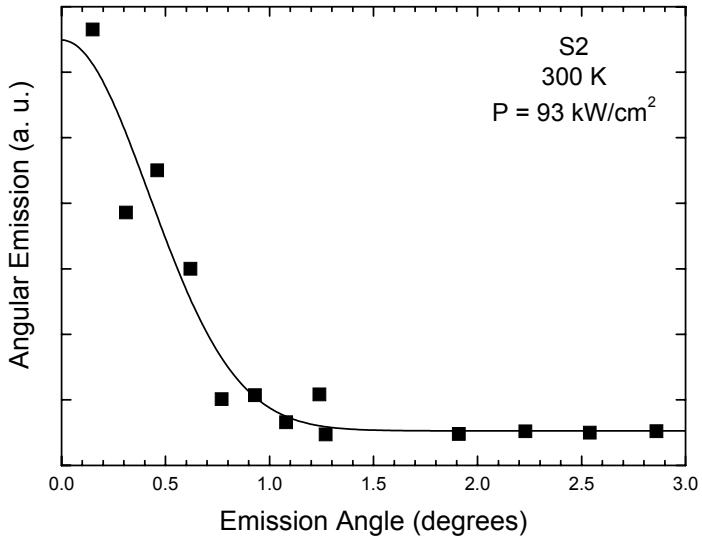

Fig. 1: Laser emission of a QW VCSEL plotted as a function of emission angle at T = 300 K evidencing the strongly forward directed emission with a divergence below 1°.

For the 0D quantum dot active medium, laser emission is obtained between 3.5 and 4 microns at several cavity resonances (due to the large cavity length) at temperatures up to 150 K [3]. The results for the lasers with 2D active regions, as shown in Fig. 2 by the temperature dependence of the laser emission, are similar to those with the 3D bulk-like active regions, for which lasing at 4.4, 3.8 and 3.6 microns is observed up to temperatures as high as 317 K (44 °C) for the 3D active zone and 307 K (34 °C) for the 2D active region. At 307 K the lower edge of the QW gain spectrum shifts out of the cavity resonance frequency and thus the laser operation is quenched as is explained in

detail in [1]. It is noted that a similar QW VCSEL with a central cavity mode at higher energy (400 meV) showed laser emission with fs-pulses up to 338 K (65 °C) [1]. The maximum emission intensity of the 3D VCSEL is of the same order of magnitude as that of the 2D VCSEL. Because the gain width in 2D systems is smaller than in 3D systems, the temperature range in which laser emission is observed is smaller for the 2D VCSEL.

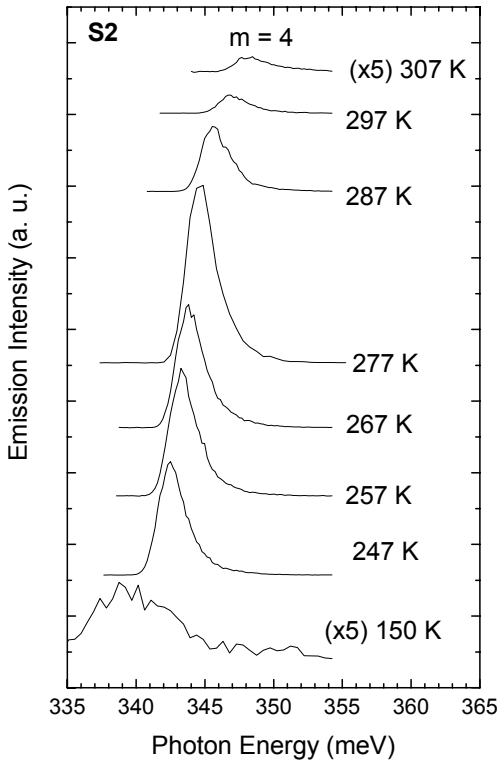

Fig. 2: Emission spectra of the QW VCSEL at various temperatures with constant pump power. The broad emission line at 150 K is due to spontaneous emission.

The threshold pump intensity is only 4 kW/cm^2 at 195 K, and 15.6 kW/cm^2 at room temperature. These values are much smaller than those reported for III-V mid-infrared VCSELs of 235 kW/cm^2 at 260 K, as well as those reported for a bulk-like PbSe VCSEL of about 70 kW/cm^2 at T = 239 K.

Conclusion

In conclusion, above-room-temperature lasing of mid-infrared IV-VI VCSELs with bulk-like PbTe as well as PbTe QWs in the active region was demonstrated up to a temperature of 320 K. The comparison of 0D, 2D and 3D systems in the active region shows that up to now the reduction of the dimensionality does not yield a laser improvement as expected from the squeezing of the wavefunctions. Bulk-like and QW VCSELs show comparable performance. This indicates that the nonradiative recombination losses due to defects are still limiting the laser process. This is obviously more important than the increase of the density of states and localization of carriers in low dimensions.

Acknowledgements

This work is funded by the FWF and the ÖAW.

References

[1] W. Heiss, T. Schwarzl, G. Springholz, K. Biermann, K. Reimann. “Above-room-temperature mid-infrared lasing from vertical-cavity surface-emitting PbTe quantum-well lasers”, Appl. Phys. Lett., Vol. 78, 2001, pp. 862 – 864.

[2] G. Springholz, T. Schwarzl, W. Heiss, G. Bauer, M. Aigle, H. Pascher, I. Vavra. “Midinfrared surface-emitting PbSe/PbEuTe quantum-dot lasers”, Appl. Phys. Lett., Vol. 79, 2001, 1225 – 1227.

[3] J. Fürst, H. Pascher, T. Schwarzl, M. Böberl, W. Heiss, G. Springholz, G. Bauer. “Midinfrared IV-VI vertical cavity surface-emitting lasers with zero-, two-, and three-dimensional systems in the active regions”, Appl. Phys. Lett. Vol. 81, 2002, 208 – 210.

Molecular Beam Epitaxy of $PbSe_{1-x}Te_x$ for Strain Engineering in IV-VI Semiconductor Heterostructures

A. Hallbauer, T. Schwarzl, R. T. Lechner and G. Springholz

Inst. of Semiconductor and Solid State Physics, Joh. Kepler Univ. Linz

Molecular beam epitaxy and the structural and electronic properties of ternary $PbSe_xTe_{1-x}$ layers on BaF_2 (111) for strain engineering of lattice-mismatched IV-VI semiconductor heterostructures is investigated. It is shown that although the ternary lattice constant exactly follows Vegard´s law, the energy band gap as a function of the ternary composition shows a substantial bowing behavior with a negative bowing parameter determined as –62 meV. Furthermore, the threading dislocation density in the layers is also found to depend drastically on the ternary composition due to alloy hardening that hinders the dislocation annihilation processes during strain relaxation. Nevertheless, very high quality layers are obtained for a selenium concentration of 78% for which the ternary compound is exactly lattice-matched to the BaF_2 substrate.

Introduction

The narrow band gap IV-VI semiconductors (PbSe, PbTe, PbS) have long been used for mid-infrared optoelectronic device applications [1]. These structures are usually grown on lattice-mismatched substrates such as BaF_2 or Si with appropriate fluoride buffer layers [1]. In heterostructures, band structure engineering is achieved by alloying with the wide band gap Eu or Sr chalcogenides for increasing the band gap, or with the Sn chalcogenides for reducing the band gap [1]. Because these compounds exhibit a lattice-mismatch of a few percent with respect to their lead salt counterparts, the lattice constants of the ternaries change with changing alloy composition. This can be compensated by admixtures of PbSe and PbTe, because the lattice constant of PbSeTe can be adjusted over a wide range due to the rather large difference of the PbSe and PbTe lattice constants (a_{PbTe} = 6.462Å, a_{PbSe} = 6.124Å). This can be utilized not only for achieving a lattice-matching to various substrate materials, but also for strain engineering in heterostructures as well as growth of high finesse epitaxial Bragg mirrors that are used for IV-VI compound vertical cavity surface emitting laser devices [2].

Experimental

In the present work, the growth behavior and the structural and electronic properties of $PbSe_xTe_{1-x}$ layers grown by molecular beam epitaxy onto (111) BaF_2 substrates was investigated. For this purpose a series of samples was grown at a temperature of 380 °C with ternary compositions adjusted in the range of x = 0 – 100% by controlling the flux rates from the PbTe and PbSe effusion cells. The alloy composition was determined precisely from beam flux rate measurements performed using a quartz crystal microbalance moved into the substrate position. These measurements were calibrated using several PbSe/PbSeTe and PbTe/PbSeTe superlattices in which the layer thicknesses were precisely determined by x-ray diffraction. Thus, a relative precision of the chemical composition of better than +2% could be achieved.

Results

All layers were characterized by high-resolution x-ray diffraction, Fourier transform infrared (FTIR) transmission, and atomic force microscopy (AFM) measurements. The ternary lattice constant was determined precisely from a detailed strain analysis using the asymmetric (264) Bragg reflection. In Fig. 1 (a) the resulting ternary lattice constant is plotted as a function of alloy composition. As indicated by the dashed line, it exactly follows Vegards law, i.e., corresponds exactly. The energy band gap of the ternaries was determined from the fitting of the FTIR spectra using a model dielectric function and the transfer matrix method as illustrated in the inset of Fig. 1 (b). The energy band gaps as a function of ternary composition (Fig. 1 (b)) are found to deviate significantly from a linear behavior, with only a minor change in the PbSeTe band gap as compared to the 325 meV PbTe band gap for Se concentrations up to about 50%. Above this composition, the band gap linearly decreases to the PbSe band gap of 180 meV at 300 K. This can be explained by the fact that the character of the conduction and valence bands of PbTe and PbSe are exchanged. With respect to the refractive index, a linear dependence of n versus x_{Se} was found.

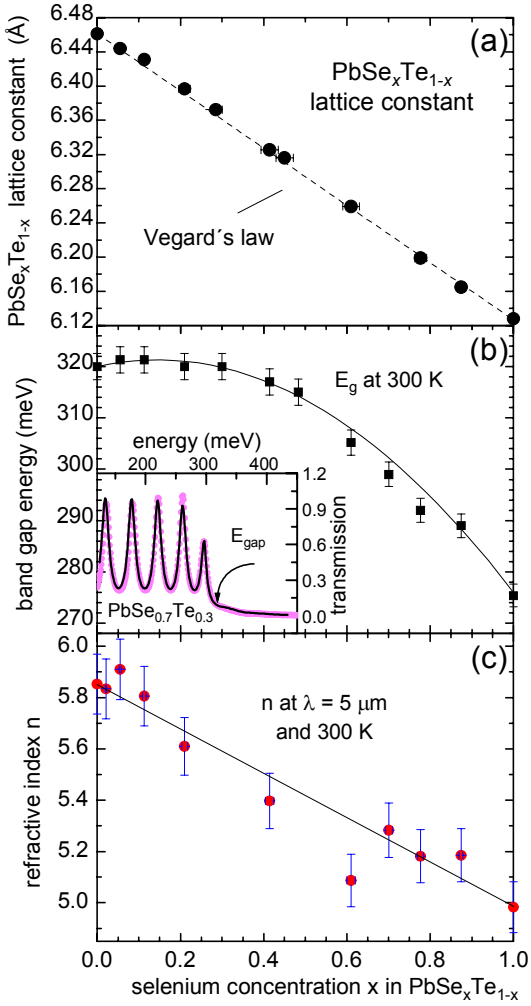

Fig. 1: (a) Lattice constant of $PbSe_xTe_{1-x}$ as a function of Se concentration. The solid line corresponds to the linear interpolation between the PbTe and PbSe bulk lattice constants (Vegard´s law). (b) Energy band gap and (c) refractive index at λ = 5 µm of $PbSe_{1-x}Te_x$ as a function of Se concentration. The insert in (b) shows the FTIR transmission spectrum of a sample with x_{se} = 70%.

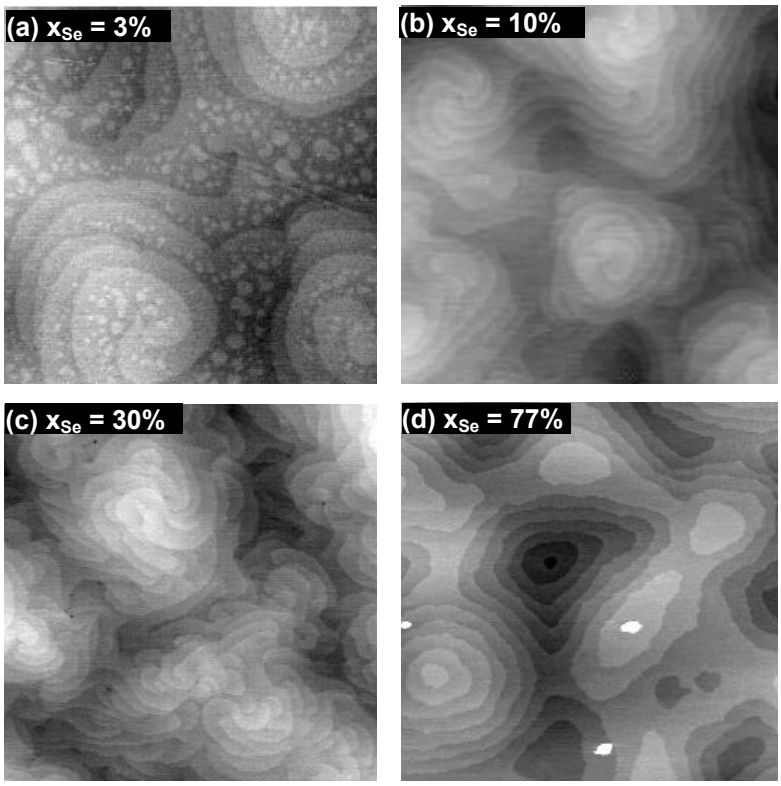

Fig. 2: Atomic force microscopy images (3 x 3 μm^2) of 3 µm $PbSe_xTe_{1-x}$ layers on BaF_2 (111) with different Se concentration.

A particularly interesting effect was observed concerning the structural properties and threading dislocation density of the layers as determined from an analysis of large-scale atomic force microscopy images as shown in Fig. 2. For the pure PbSe and PbTe layers, rather low threading dislocation densities of around 10^7 cm^{-2} were found [3] as well as narrow x-ray rocking curve widths. With increasing alloy composition, however, both parameters drastically increase reaching a maximum for Se concentrations of ~50%. This is shown in detail in Fig. 3, where the threading dislocation density evaluated from the atomic force microscopy images is plotted as a function of the selenium concentration. With increasing selenium concentration, the threading dislocation density more or less increases linearly up to values of around 2 x 10^9 cm^{-2} for selenium concentrations in the range of 20 – 60%.

At higher selenium concentrations, the dislocation density decreases again because the ternary lattice constant approaches the lattice constant of 6.200 Å of the BaF_2 substrate. This is because much less misfit dislocations are required for strain relaxation due to the resulting decrease of the layer/substrate lattice-mismatch. For a selenium concentration of 78%, the ternary layer is exactly lattice-matched to BaF_2. As a result, no dislocations are formed during deposition, and the dislocation density drops by more than two orders of magnitude below 10^5 cm^{-2}. As the selenium concentration further increases, again a lattice-mismatch to the substrate builds up, and the threading dislocation density again increases. However, as the ternary composition approaches pure PbSe, the dislocation density drops again reaching a value of around 10^7 cm^{-2} for pure PbSe. This marked behavior is attributed to a strong alloy hardening effect of the ternary layers, which prevents an efficient relaxation of the layer/substrate lattice-mismatch by glide of dislocations. Therefore, the efficient dislocation annihilation processes known, *e.g.*, for pure PbTe are kinetically suppressed in the ternary layers.

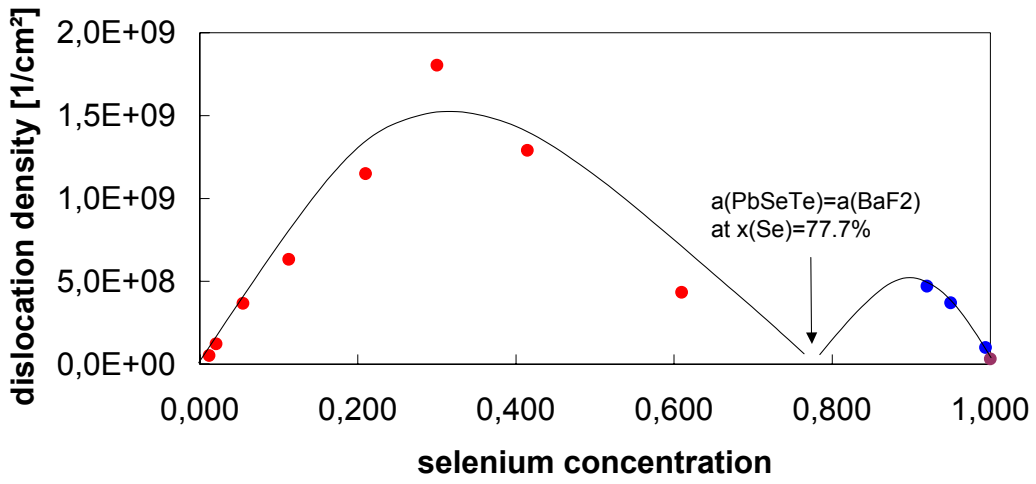

Fig. 3: Threading dislocation density of 2.7 µm $PbSe_{1-x}Te_x$ layers on BaF_2 (111) as a function of Se concentration. A minimal dislocation density is observed for x_{Se} = 78% because of the resulting layer/substrate lattice-match.

Conclusions

From investigation of ternary $PbSe_xTe_{1-x}$ layers grown by molecular beam epitaxy on BaF_2 (111) substrate it is shown that lattice constant exactly follows Vegard´s law, whereas the energy band gap as a function of the ternary composition shows a substantial bowing behavior. Although solution hardening effects in the ternary allows lead to a drastic increase of the threading dislocation density on the ternary composition, very high quality layers are obtained for a selenium concentration of 78% for which the ternary compound is exactly lattice-matched to the BaF_2 substrate. This opens promising perspectives for the growth of dislocation-free IV-VI based optoelectronic devices.

Acknowledgements

This work was supported by the Österreichische Akademie der Wissenschaften (APART) and the Förderungsfonds der Wissenschaftlichen Forschung, Wien.

References

[1] *see, e.g.,* G. Springholz, Z. Shi, and H. Zogg in “Thin Film Heteroepitaxial Systems” eds. W.K. Liu and M. B. Santos (World Scientific, Singapore, 1999) p. 621 – 688, and references therein.

[2] G. Springholz, T. Schwarzl, M. Aigle, H. Pascher and W. Heiss, Appl. Phys. Lett. **76** (2000) 1807-1809.

[3] G. Springholz, A.Y. Ueta, N. Frank and G. Bauer, Appl. Phys. Lett. **69 (**1996) 2822 - 2824.

Intermixing and Shape Transitions of PbSe Quantum Dot during Overgrowth

A. Raab and G. Springholz

Inst. of Semiconductor and Solid State Physics, Joh. Kepler Univ. Linz

The size and shape changes of self-assembled PbSe quantum dots during overgrowth by $Pb_{1-x}Eu_xTe$ barrier layers with different Eu concentrations is investigated using atomic force microscopy and in situ reflection high-energy electron diffraction. It is shown that whereas for overgrowth with pure PbTe a very strong intermixing of the PbSe dots with the cap layer material occurs, this effect is drastically suppressed with increasing Eu concentration in the $Pb_{1-x}Eu_xTe$ cap layers. As a result, the size and shape of the as-grown PbSe dot is essentially conserved during the capping process, which is important for opto-electronic device applications.

Introduction

Self-assembled semiconductor quantum dots synthesized via the Stranski-Krastanow growth mode have attracted great interest due to their excellent electronic and optical properties. For applications, quantum dots have to be embedded in a matrix material to avoid surface recombination effects. However, it is well known that *e.g.* for InAs dots embedded in GaAs there is significant intermixing between dot and matrix material [1] – [4], which leads to remarkable changes in the dot size and shape for the overgrown dots [5]. Similar effects have been also observed for SiGe dots overgrown by silicon layers, and the degree of intermixing was found to depend strongly on the growth conditions [6]. Since the optical and electronic properties depend crucially on size and shape of the embedded dots it is important to gain detailed knowledge about the changes of these parameters due to capping process.

Experimental

In the present work, we have investigated the overgrowth behaviour of self-assembled PbSe quantum dots grown by molecular beam epitaxy (MBE) on PbTe (111). The PbSe dots are formed due to strain-induced coherent islanding (–5.4 % lattice-mismatch) once the critical coverage of 1.5 PbSe monolayers (ML) is exceeded. The surface islands have a well-defined pyramidal shape with triangular base and with (100) side facets. For the overgrowth studies, a series of dot samples was prepared under identical conditions with a total PbSe thickness of 5 monolayers. Then the PbSe dots were overgrown with $Pb_{1-x}Eu_xTe$ cap material of different Eu concentration and different cap thicknesses. The evolution of the surface morphology was determined using *in situ* reflection high-energy electron diffraction (RHEED), as well as *ex situ* atomic force microscopy (AFM) under ambient conditions after rapid quenching of the partially capped samples to room temperature.

Results

In a first set of experiments, the evolution of the RHEED patterns during overgrowth of PbSe quantum dots predeposited on a PbTe buffer layer at Ts = 360 °C was investigated. Figure 1 (a) and (b) shows examples of the RHEED patterns before and after

dot overgrowth. The initial average PbSe dot height of the samples before overgrowth was 105 Å as determined from reference samples. For a more detailed analysis, the integrated intensity of the 3D (224) diffraction spot was measured as a function of cap layer thickness for several different $Pb_{1-x}Eu_xTe$ cap layer compositions as shown in Fig. 1 (c). The exact position of the (224) spot is marked in the RHEED images in (a) and (b). As is evident from Fig. 1 (c), the 3D (224) diffraction spot intensity is maximal for the initial surface with 5 ML PbSe coverage. During overgrowth, the diffraction spot rapidly decreases, and the RHEED patterns transform into the usual streaked diffraction pattern corresponding to the reformation of a planar 2D surface. This indicates that a rapid replanarization takes place in all cases. However, the cap layer thickness required for complete planarization, i.e., the thickness when the 3D spot has disappeared, strongly increases as a function of the Eu content in the ternary cap layer, indicating that the planarization process is much slower for the cap layers with higher Eu content.

Similar results were obtained from the AFM images of the partially capped samples shown in Fig. 2. In this case, the dots were overgrown with different cap layer thickness of $Pb_{1-x}Eu_xTe$, x = 0.065 and pure PbTe, respectively. In Fig. 2, left-hand side, the AFM surface images of PbSe dots overgrown with $Pb_{1-x}Eu_xTe$, x = 0.065 at cap layer thicknesses of 15 Å, 35 Å, 50 Å and 85 Å are shown for (a) – (d), respectively. At a cap thickness of 50 Å, the partially capped quantum dots are still clearly visible. For a cap thickness of 85 Å, the dots are fully overgrown although the initial dot height before overgrowth was 105 Å. This indicates that a certain intermixing between dot material and matrix material takes place and reduces the remaining dot height during capping. A closer look shows that the dots have not only vanished completely, but there are small holes on the surface, which have approximately the same density as the buried dots. From STM studies it is known that these holes are due the lattice deformations, which are caused by the highly strained buried dot.

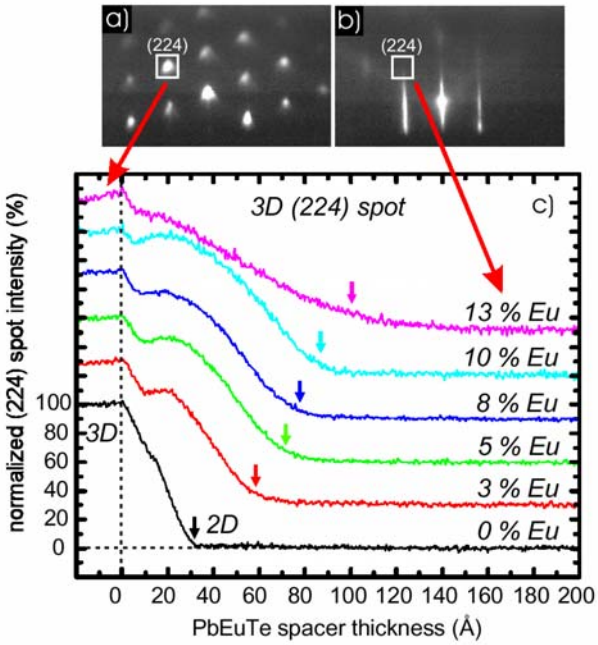

Fig. 1: Top: RHEED pattern of (a) 3D surface with PbSe quantum dots before overgrowth and (b) after complete overgrowth with $Pb_{1-x}Eu_xTe$ spacer layer. Bottom: Normalized intensity of (224) spot as a function of $Pb_{1-x}Eu_xTe$ spacer thickness for x = 0, 0.03, 0.05, 0.08, 0.1, and 0.13. Each curve has a relative offset of 20 for clarity.

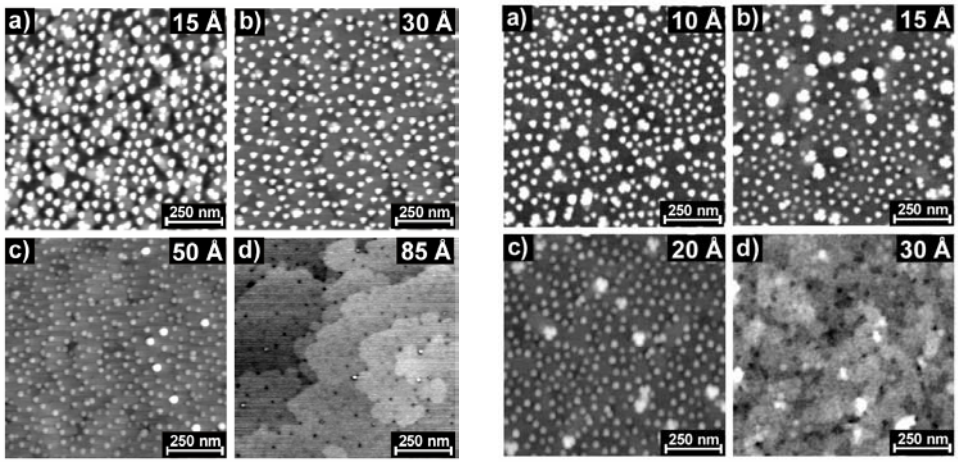

Fig. 2: Left hand side: Atomic force microscopy surface images (1 x 1 μm^2) of 5 ML PbSe quantum dot layer on PbTe buffer layer overgrown with different $Pb_{1-x}Eu_xTe$ (x = 0.065) spacer layer thickness of (a) 15 Å, (b) 35 Å, (c) 50 Å and (d) 85 Å. Right hand side: Atomic force microscopy surface images (1 x 1 μm^2) of 5 ML PbSe quantum dot layer on PbTe buffer layer overgrown with different PbTe spacer layer thicknesses of (a) 10 Å, (b) 15 Å, (c) 20 Å, and (d) 30 Å.

In Fig. 2 right-hand side (a) – (d), AFM surface images of partially overgrown dots with pure PbTe at a cap layer thickness of 10 Å, 15 Å, 20 Å, and 30 Å are shown respectively. In this case, the dots can only be detected up to a cap layer thickness of 20 Å. At 30 Å cap thickness the dots are fully overgrown, indicating that for pure PbTe the intermixing between dot material and matrix material is even more pronounced. Also for pure PbTe there are small holes detected on the surface when the dots are fully overgrown.

From the statistical evaluation of the AFM images, the remaining PbSe island height was determined as a function of the cap thickness, where the result is shown in Fig. 3. The residual dot height is plotted as a function of cap layer thickness d for x = 0, 0.03, 0.065, and 0.1. The dashed line gives the theoretical curve for the dot height, when full shape conservation is assumed and if the $Pb_{1-x}Eu_xTe$ capping material grows only around the dots and not on top. In this case the residual dot height h should be just equal to $h = h_0 - d$ with $h_0 \approx 105$ Å being the initial dot height before capping. Although, in all cases the dot height decreases essentially linearly with increasing cap thickness, the critical cap layer thickness required for planarization increases from only 30 Å for PbTe capping to about 100 Å for capping with $Pb_{1-x}Eu_xTe$ with x_{Eu} = 10%. The data obtained for x_{Eu} = 10% is remarkably close to the theoretical curve, indicating that the dot shape is almost completely conserved. For x = 0.065, there is already a clear deviation from the theoretical curve. The overgrown dots are clearly smaller than what would be expected in the case of shape conservation even for a thin cap layer thickness. It is evident that there is only little overgrowth on the top of the dots, and the intermixing at the dot base leads to further decrease in the remaining dot height. There is no evidence for discontinuities in the overgrowth and intermixing process since the measured residual dot heights follow a straight line. For x = 0.065, the dots have vanished completely after a cap layer thickness of 70 Å was deposited. For Eu contents of x = 0.03 and 0, the dots vanish already at a cap thickness of 56 and 32 Å, respectively. This indicates that while a very strong intermixing and dissolution of the initially 105 Å high dots takes place during pure PbTe overgrowth, this effect is strongly suppressed by the presence of Eu in the cap layer, *i.e.*, for sufficiently high Eu concentrations the dot shape is preserved during the overgrowth process.

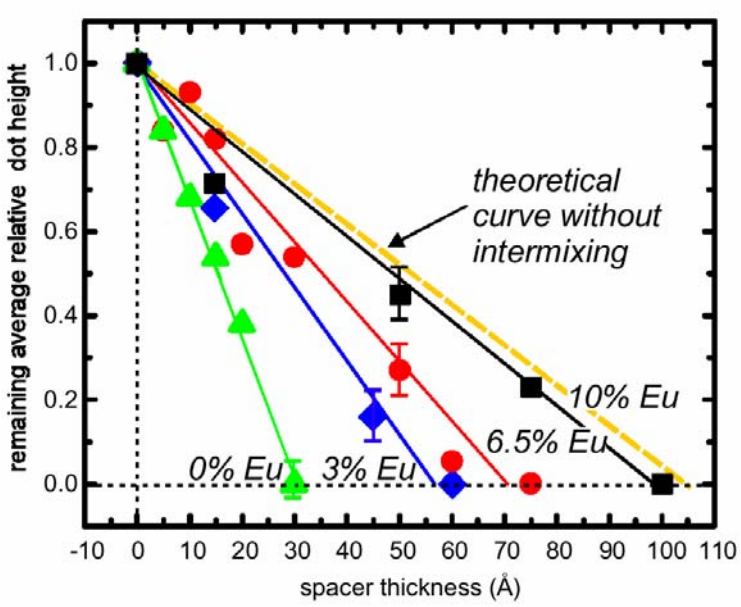

Fig. 3: Remaining average relative dot height as a function of $Pb_{1-x}Eu_xTe$ spacer thickness for different Eu contents of x=0 (▲), x=0.003 (◆), x=0.065 (●), and x=0.1 (■). The dashed curve is the theoretical curve without intermixing.

Conclusions

In conclusion, we have investigated the overgrowth behaviour of self-assembled PbSe quantum dots by $Pb_{1-x}Eu_xTe$ barrier layers with different Eu concentrations. Whereas for overgrowth with pure PbTe a very strong intermixing of the PbSe dots with the cap layer material occurs, this effect is drastically suppressed with increasing Eu concentration in the $Pb_{1-x}Eu_xTe$ cap layers. As a result, in this case the size and shape of the as grown PbSe dot is essentially conserved during the capping process. This is important for optoelectronic device applications.

Acknowledgements

This work was supported by the Österreichische Akademie der Wissenschaften (APART) and the Förderungsfonds der Wissenschaftlichen Forschung, Wien.

References

[1] P. B. Joyce, T. J. Krzyzewski, G.R. Bell and T. S. Jones, Appl. Phys. Lett. 79 (2001) 3615-3617.

[2] J. M. Garcia, G. Medeiros-Ribeiro, K. Schmidt, T. Ngo, J. L. Feng, A. Lorke, J. Kotthaus, and P. M. Petroff, Appl. Phys. Lett. 71 (1997) 2014-2016.

[3] B. Lita and R. S. Goldman, Appl. Phys. Lett. 75 (1999) 2797-2799.

[4] M. O. Lipinski, H. Schuler, O.G. Smith, K. Eberl, N. Y. Jin-Phillipp, Appl. Phys. Lett. 77 (2000) 1789-1791 .

[5] K. Mukai and M Sugawara, Appl. Phys. Lett. 74 (1999) 3963-3965.

[6] A. Rastelli, M. Kummer and H. von Känel, Phys. Rev. Lett 87 (2001) 256101-1.

In-Situ Growth Monitoring and On-Line Composition Determination of MOCVD GaN by Spectroscopic Ellipsometry

K. Schmidegg, A. Bonanni, A. Montaigne Ramil, H. Sitter

Inst. of Semiconductor and Solid State Physics, Joh. Kepler Univ. Linz

In-situ ellipsometry measurements during MOCVD growth of GaN and its ternary compounds AlGaN and InGaN were performed. We show that individual process steps can be identified and resolved with much higher detail than with currently available reflectometry setups. Using the Virtual Interface Approximation (VIA), we are also able to calculate the Al content of the growing layer in real time with good accuracy. For In containing samples we observe a rather large drift originating from a concentration gradient in the layer due to the immiscibility in the GaN/InN system.

Introduction

Group III nitrides have attracted tremendous R&D effort in the past few years resulting in the commercialization of optoelectronic devices operating in the blue and ultraviolet spectral range. Other fields of application include high mobility transistor devices (HEMT's), UV detectors and laser diodes for tomorrow's range of optical storage products [1]. The fabrication of GaN layers is mostly done by Metalorganic Chemical Vapor Deposition (MOCVD), which provides high growth rates and throughput in a non-UHV environment, both of which are well suited for industrial size production. The range of real-time diagnostic tools for MOCVD reactors is however quite limited, as electron diffraction techniques like RHEED (reflection high energy electron diffraction) cannot be used at atmospheric pressure. Optical methods like spectroscopic ellipsometry (SE) or reflection difference spectroscopy (RDS) have been successfully employed for in-situ monitoring of III-V and II-VI compounds. [2], [3]

We show the successful installation of a spectroscopic ellipsometer to a commercial MOCVD reactor and that these measurements have considerable advantages over reflectometry setups regarding sensitivity and an improved signal-to-noise ratio. Our further attention was focused towards the on-line monitoring of ternary alloy compositions in AlGaN and InGaN layers. The Virtual Interface Approximation (VIA) provides an easy and accurate way of determining the dielectric function of a growing layer which can be correlated to a certain Al content by cross-calibration with ex-situ methods like high resolution X-ray diffraction (HRXRD) or secondary ion mass spectroscopy (SIMS).

Experimental Setup

For the growth of group III nitrides, we use a modified commercial AIXTRON AIX200RF-S reactor with extra viewports to accommodate a spectroscopic ellipsometer. Strain free windows are necessary to avoid stress-induced polarization effects on incident and measured light beams. SE measurements were made with an ISA Jobin Yvon ellipsometer operating in the spectral range of 1.5 – 5.2 eV. Additional characterization was done with a laser reflectometer operating at 1.86 eV.

Figure 1 shows reflectivity and kinetic ellipsometry measurements during the growth of a hexagonal GaN layer on sapphire (0001) substrates. Both measurements have been performed below the fundamental absorption edge of GaN to avoid damping of thickness oscillations. We can clearly identify the important steps necessary to achieve high quality layers [2]:

(a) Heating of the substrate to 1200°C: the reflectometry signal increases due to thermal emission of the sample

(b) Desorption under H_2 atmosphere at 1200°C

(c) Decrease of temperature to 540°C for the deposition of low-temperature GaN nucleation layer

(d) Growth of nucleation layer: an islanded film covering the substrate surface is formed and an oscillation representing the first thickness fringe is recorded

(e) Annealing of nucleation layer through increase of the temperature to 1050°C: The behavior of both signals originates from the coalescence of GaN islands and a roughening of the surface. Spectroscopic measurements before and after annealing show layer thicknesses of 50nm and 30 nm respectively.

(f) Growth of GaN at 1050°C with low growth rate (large period oscillations in both reflectometry and SE)

(g) Deposition of GaN with a growth-rate of ~3 µm/h.

It can easily be seen that all the information contained in the reflectometry signal is also contained in the ellipsometry measurement. In this stage, ellipsometry offers the advantage of being independent of absolute intensities (only polarization and phase change are measured), which makes it immune to influences like wobbling of the sample and thermal emission at high temperatures.

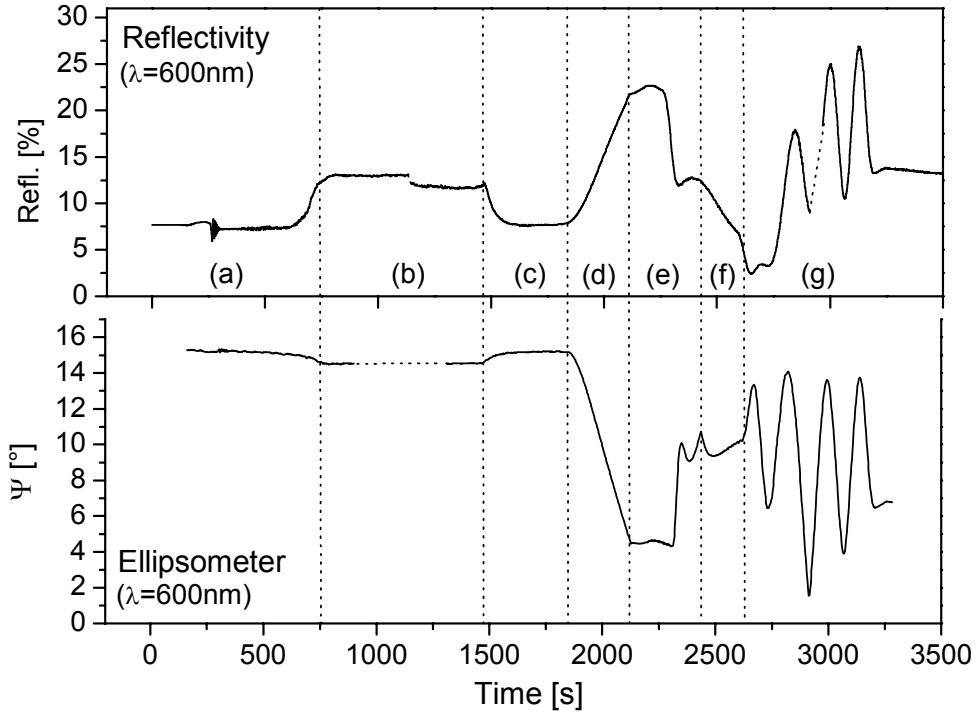

Fig. 1: Reflectometry vs. ellipsometry during the growth of hexagonal GaN layers on sapphire.

Concentration Monitoring

To relate optical information to sample parameters like ternary alloy compositions, it is necessary to perform complementary measurements and relate them to optical data. In our case, we performed high-resolution x-ray diffraction (HRXRD) measurements to gather data about the composition and stress and strain state of the samples. The precision in concentration from these measurements is in the range of ±0.5%.

As there is very little published data of optical constants of these compounds at growth temperature, we had to determine first the dielectric responses of layers with different Al content. Together with the exact concentration values from XRD, it was used as the input data for an algorithm based on the virtual interface approximation (VIA), which determines Al concentrations in real time [4]. The main idea of the VIA is to divide the sample structure into two parts, namely an overlayer and a so-called pseudosubstrate representing the whole structure below. From this 3-layer system (substrate, overlayer, ambient), the dielectric response of the overlayer can be calculated at each time step. The input parameters are the angle of incidence, the monitoring wavelength, the currently measured dielectric function, and its derivative with respect to the thickness of the growing layer. The last point implies the precise knowledge of the growth rate in the case of a measurement with a single wavelength only, which is accomplished by reflectometry in our case.

Figure 2 shows a typical kinetic measurement during the growth of an AlGaN layer. The dielectric function plotted in the complex plane describes an exponential spiral originating from the point for GaN and converging in the point for AlGaN. The inset shows an ellipsometric spectrum at growth temperature.

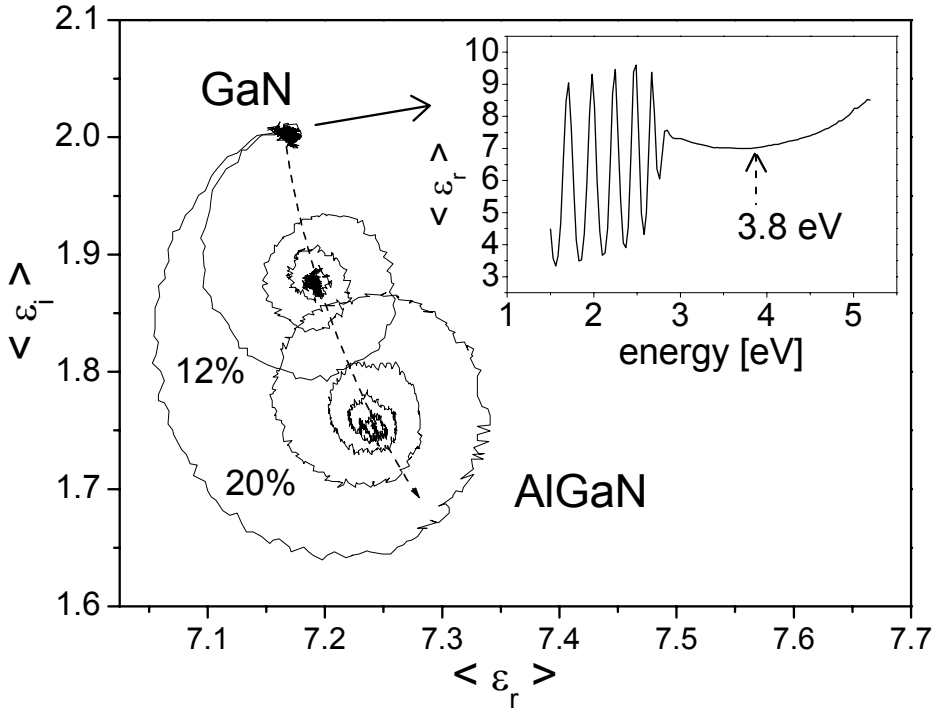

Fig. 2: Evolution of the pseudodielectric function during the growth of AlGaN layers with different Al contents on a GaN buffer. The inset shows a spectroscopic measurement at growth temperature (1050 °C).

A possible application of this method is the monitoring of superlattices as used in devices like vertical emitting laser diodes or transistors. Figure 3 shows the results of a

real-time measurement during the growth of a 30nm/50nm GaN/AlGaN superlattice with 12% Al in the barriers. Also shown in Fig. 3 is a composition profile of a structure with continuously varying Al content.

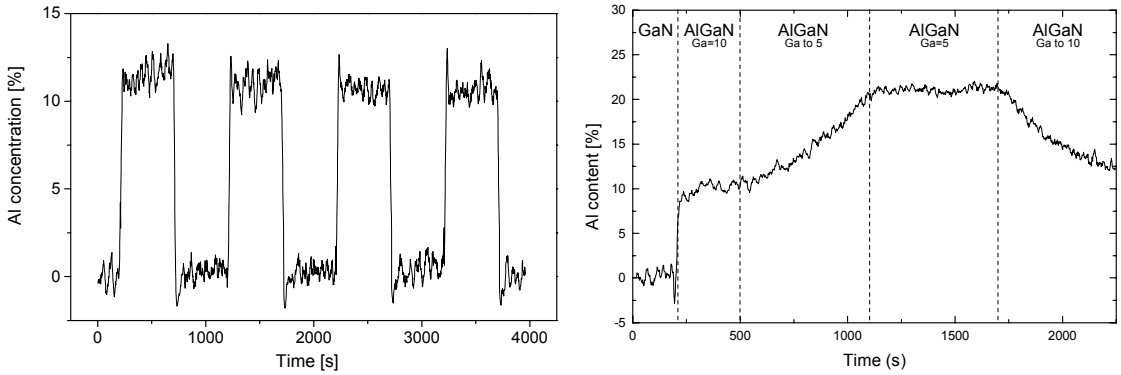

Fig. 3: Left: VIA calculated concentration in a GaN/AlGaN superlattice.
Right: Graded composition layer with Ga fluxes as indicated.

For In containing compounds, concentration monitoring is considerably more difficult. The system GaN – InN has a large miscibility gap resulting in a maximum concentration of a few percent in the crystal. Due to this behavior, InGaN layers also show rather large composition gradients in growth direction [5]. During in-situ measurements, the spirals of the dielectric function do not converge as nicely as for AlGaN compounds. Simulations show that this drift is due to a composition gradient in the layer.

Conclusion

We have demonstrated a method for the optical characterization of MOCVD growth processes of group III nitrides. Characterization of standard growth processes as well as accurate information about ternary layer compositions are obtained in real time thus yielding higher output and enhanced device quality.

Acknowledgements

This work was supported by the European Commission in the 5th Framework Program under the Project number GRD1_1999_10337.

References

[1] S. Nakamura, Science **281**, 951 (1998).

[2] S. Peters, T. Schmidtling, T. Trepk, U.W. Pohl, J.-T. Zettler, W. Richter, J. Appl. Phys. **88**, 4085 (2000).

[3] R.S. Balmer, C. Pickering, A. Mkier, J.C.H. Birbeck, M. Saker, T. Martin, J. Cryst. Growth **230**, 361 (2001).

[4] D.E. Aspnes, Thin Solid Films **233**, 1 (1993).

[5] S. Pereira, M.R. Correia, E. Pereira, K.P. O'Donnell, C. Trager-Cowan, F. Sweeney, E. Alves, Phys. Rev. B **64**, 205311 (2001).

Oriented Organic Semiconductor Thin Films

A. Andreev and H. Sitter

Inst. f. Semiconductor- and Solid State Physics, University Linz, Austria

In this part of our investigations, we use atomic force microscopy and X-ray diffraction to study the growth of para-sexiphenyl (PSP) films on mica. It is shown that self-organization of PSP molecules occurs during the growth controlled by the substrate temperature and deposition time. X-ray diffraction studies confirmed very high crystalline quality of the grown organic films.

Introduction

The ability to control the molecular order in organic thin films consisting of long anisotropic oligomers like *oligo-thiophenes* or *oligo-phenylenes* is essential to study the relation between their structure, surface morphology and their optical and electrical properties. On the other hand, ordered thin films of organic semiconductor *para-sexiphenyl* (PSP) are interesting for the application in organic light-emitting diodes (OLED) with polarized blue light emission [1]. Recently, we reported that a self-organization of PSP molecules occurs during Hot Wall Epitaxy (HWE) on mica resulting in well ordered crystalline needle-like structures with a length to width ratio up to 500 [2], [3]. However, the growth regularities of such highly anisotropic films were not clear yet. In this work, we have used atomic force microscopy (AFM) and X-ray diffraction (XRD) to investigate the morphology, growth kinetic and crystalline quality of these films in the early growth stages, in order to find the process controlling parameters.

Experimental

PSP obtained from Tokyo Chemical Industries was purified by threefold sublimation under dynamic vacuum. HWE was used as evaporation technique [2], [3]. The used substrates were freshly cleaved (001)-oriented mica. The base pressure during growth was about $6x10^{-6}$ mbar and the PSP source temperature was fixed at 240 ºC. The substrate temperature was 90 ºC or 150 ºC, the growth time was varied between 5 sec and 60 min. The film morphology was imaged by AFM using a Dimension 3100 system (Digital Instruments) operated in tapping mode on air. XRD investigations were performed at the F3 station at the Cornell High Energy Synchrotron Source (CHESS). Monochromatic radiation with a wavelength of 1.23985 Å was used in combination with a 4-circle goniometer.

Results

The PSP film morphology with increasing growth time in the range from 5 to 90 sec is shown in Fig.1. The growth temperature was 150 °C. As depicted in Figs.1 (a) and (b), only small uniformly distributed 3D-islands with a compact shape can be detected for the samples grown within 5 – 10 seconds. The surface morphology changes drastically if growth time was increased from 10 to 25 sec: island shape transition occurs resulting in typical needle-like structures with elongated 3D-islands. Figs.1 (c) and (d) show that the islands become thereby progressively longer, quickly reaching a fixed asymptotic width while their height remains much smaller than their length and width. A similar

behavior was found for the samples grown by 90 °C; however, in this case the island shape transition occurs later – between 25 and 45 seconds of growth time.

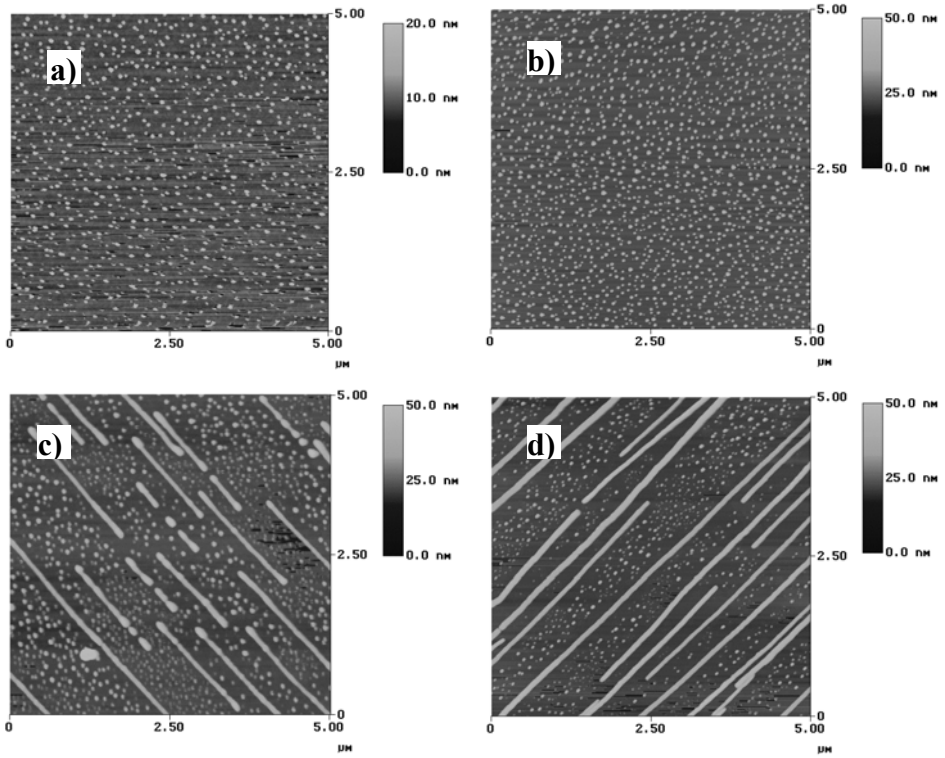

Fig. 1: AFM images of the films grown at 150°C within (a) 5; (b) 10; (c) 25; (d) 90 sec.

Some of these extraordinary features can be explained qualitatively in terms of strain-induced heteroepitaxial island growth, well known in inorganic heteroepitaxy. For example, Tersoff and Tromp [4] have predicted theoretically a strain-induced, spontaneous shape transition from compact square islands to elongated ones of asymptotic constant width. This means that compact 3D-islands grow to a critical size in width and length considerably larger than their height (which remains nearly constant). Above the critical size, the islands grow only in length, but not in width, which converges towards an asymptotic value. Generally, our results agree well with these theoretical predictions.

We performed also XRD measurements in $\Theta/2\Theta$ mode for PSP films of different thickness in order to get information about the variation of interplanar spacing in the growth direction d(11-1) with increasing layer thickness, i.e. about presence of lattice deformation (strain). As shown in Fig.2, the d(11-1) value increases rapidly with increasing needle height approaching the bulk value at a thickness of ≈25 – 30 nm. Such behavior implies that thin PSP layers are strained and this strain is relaxed within the first ≈25 – 30 nm (~60 monolayers) of the film. These observations suggest that weak Van der Waals interactions between the PSP film and the mica substrate are nevertheless strong enough to produce a lattice deformation, which is likely to be the driving force [4], [5] for the needle-like morphology shown in Fig. 1.

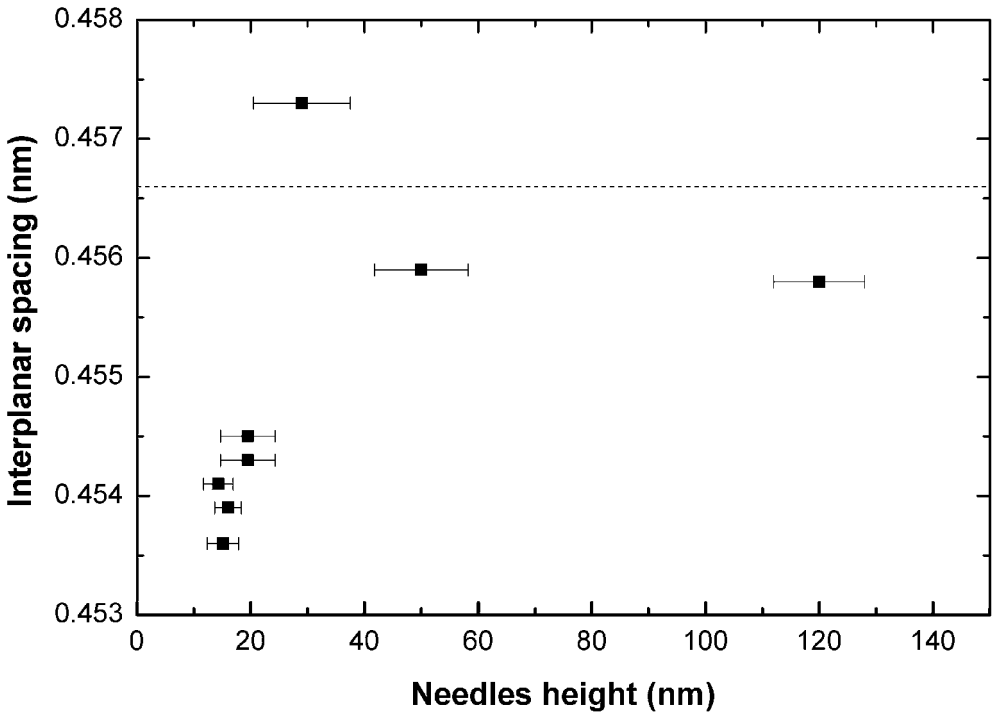

Fig. 2: Interplanar spacing d(11-1) as a function of the average needles height for PSP layers grown at 90°C.

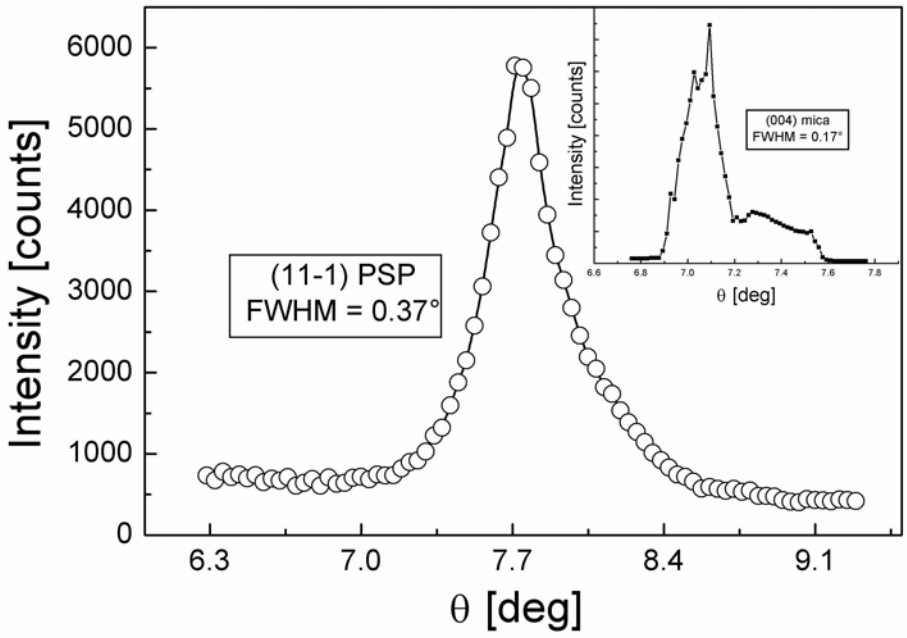

Fig. 3: Rocking curve for the 11-1 reflection of the PSP film. Insert shows corresponding curve for the 004 reflection of the mica substrate.

The so-called Rocking curves (i.e. Θ–scans) provide us a direct measure for the degree of order of the grown films. Additional interest in these investigations arises from the fact that there are only very few papers published, in which rocking curves were reported for organic thin films [5]. Figure 3 shows a typical Rocking curve measured at $2\Theta = 15.67°$ for the characteristic 11-1 reflection of the PSP film grown at 150 °C within 90 sec (see also Fig. 1(d)). The Rocking curve is remarkably narrow for organic films with a FWHM of only 0.37°. For comparison, the Rocking curve of the mica substrate (004) reflection at $2\Theta = 14.26°$ was measured (see inset in Fig.3). The rocking curve of mica shows an irregular shape, which appears often in single crystals of layered compounds like graphite, mica, a.o. The FWHM value of the mica substrate differs not much from the corresponding FWHM of the PSP film itself. These data confirm a very good out-of-plane alignment of PSP crystallites and thus a high degree of order in the film.

Conclusion

The HWE growth of oriented thin films of PSP on mica substrates was investigated. AFM studies of the earlier stage of the growth have clearly shown that self-organization of PSP molecules occurs during HWE resulting in highly anisotropic needle-like structures. XRD investigations using synchrotron radiation confirmed a very high degree of epitaxial order of the films and demonstrated that thin PSP layers are strained and this strain is relaxed within the first ≈25 – 30 nm of the film.

Acknowledgements

We thank R. Resel and D.-M. Smilgies for helping with the XRD experiments. Many thanks also to H. Hoppe for AFM measurements and N.S. Sariciftci for fruitful discussions. Research was supported by the Austrian Foundation for Advancement of Scientific Research (FWF Projects P-15155 and P-15627). Part of this work was performed within the Christian Doppler Society's dedicated laboratory on Plastic Solar Cells funded by the Austrian Ministry of Economic Affairs and Konarka Austria GmbH. We thank also the Cornell High Energy Synchrotron Source (CHESS, Ithaca, USA) for given beam-line time (Project P880).

References

[1] M. Era, T. Tsutsui, S. Saito. “Polarized electroluminescence from oriented p-sexiphenyl vacuum-deposited film”, Appl. Phys. Lett., 67(17), 1995, 2436-2438.

[2] A. Andreev, G. Matt, C.J. Brabec, H. Sitter, D. Badt, H. Seyringer, N. S. Sariciftci. “Highly Anisotropically Self-Assembled Structures of para-Sexiphenyl Grown by Hot-Wall Epitaxy”, Adv. Mat., 12, 2000, 629-633.

[3] H. Plank, R. Resel, S. Purger, J. Keckes, A. Thierry, B. Lotz, A. Andreev, N. S. Sariciftci, H. Sitter. “Heteroepitaxial growth of self-assembled highly ordered para-sexophenyl films: a crystallographic study”, Phys.Rev. B 64, 2001, 235423.

[4] J. Tersoff and R.M. Tromp. “Shape transition in growth of strained islands: spontaneous formation of quantum wires”, Phys. Rev. Lett., 70, 1993, 2782-2785.

[5] S.R. Forrest. “Ultrathin organic films grown by organic molecular beam deposition and related techniques”, Chem. Reviews, 97, 1997, 1793.

3-901578-11-0